

1983

The effect of rare-earth element additions on microstructural properties and irradiation behavior of an Fe-Ni-Cr alloy for LMFBR and fusion reactor applications

Jin-Young Park
Iowa State University

Follow this and additional works at: <https://lib.dr.iastate.edu/rtd>

 Part of the [Nuclear Engineering Commons](#)

Recommended Citation

Park, Jin-Young, "The effect of rare-earth element additions on microstructural properties and irradiation behavior of an Fe-Ni-Cr alloy for LMFBR and fusion reactor applications " (1983). *Retrospective Theses and Dissertations*. 8426.
<https://lib.dr.iastate.edu/rtd/8426>

This Dissertation is brought to you for free and open access by the Iowa State University Capstones, Theses and Dissertations at Iowa State University Digital Repository. It has been accepted for inclusion in Retrospective Theses and Dissertations by an authorized administrator of Iowa State University Digital Repository. For more information, please contact digirep@iastate.edu.

INFORMATION TO USERS

This reproduction was made from a copy of a document sent to us for microfilming. While the most advanced technology has been used to photograph and reproduce this document, the quality of the reproduction is heavily dependent upon the quality of the material submitted.

The following explanation of techniques is provided to help clarify markings or notations which may appear on this reproduction.

1. The sign or "target" for pages apparently lacking from the document photographed is "Missing Page(s)". If it was possible to obtain the missing page(s) or section, they are spliced into the film along with adjacent pages. This may have necessitated cutting through an image and duplicating adjacent pages to assure complete continuity.
2. When an image on the film is obliterated with a round black mark, it is an indication of either blurred copy because of movement during exposure, duplicate copy, or copyrighted materials that should not have been filmed. For blurred pages, a good image of the page can be found in the adjacent frame. If copyrighted materials were deleted, a target note will appear listing the pages in the adjacent frame.
3. When a map, drawing or chart, etc., is part of the material being photographed, a definite method of "sectioning" the material has been followed. It is customary to begin filming at the upper left hand corner of a large sheet and to continue from left to right in equal sections with small overlaps. If necessary, sectioning is continued again—beginning below the first row and continuing on until complete.
4. For illustrations that cannot be satisfactorily reproduced by xerographic means, photographic prints can be purchased at additional cost and inserted into your xerographic copy. These prints are available upon request from the Dissertations Customer Services Department.
5. Some pages in any document may have indistinct print. In all cases the best available copy has been filmed.

**University
Microfilms
International**

300 N. Zeeb Road
Ann Arbor, MI 48106

8323307

Park, Jin-Young

THE EFFECT OF RARE-EARTH ELEMENT ADDITIONS ON
MICROSTRUCTURAL PROPERTIES AND IRRADIATION BEHAVIOR OF AN
IRON-NICKEL-CHROMIUM ALLOY FOR LMFBR AND FUSION REACTOR
APPLICATIONS

Iowa State University

PH.D. 1983

**University
Microfilms
International** 300 N. Zeeb Road, Ann Arbor, MI 48106

PLEASE NOTE:

In all cases this material has been filmed in the best possible way from the available copy. Problems encountered with this document have been identified here with a check mark .

1. Glossy photographs or pages
2. Colored illustrations, paper or print _____
3. Photographs with dark background
4. Illustrations are poor copy _____
5. Pages with black marks, not original copy _____
6. Print shows through as there is text on both sides of page _____
7. Indistinct, broken or small print on several pages
8. Print exceeds margin requirements _____
9. Tightly bound copy with print lost in spine _____
10. Computer printout pages with indistinct print _____
11. Page(s) _____ lacking when material received, and not available from school or author.
12. Page(s) _____ seem to be missing in numbering only as text follows.
13. Two pages numbered _____. Text follows.
14. Curling and wrinkled pages _____
15. Other _____

University
Microfilms
International

The effect of rare-earth element additions on microstructural
properties and irradiation behavior of an Fe-Ni-Cr alloy for
LMFBR and fusion reactor applications

by

Jin-Young Park

A Dissertation Submitted to the
Graduate Faculty in Partial Fulfillment of the
Requirements for the Degree of
DOCTOR OF PHILOSOPHY

Major: Nuclear Engineering

Approved:

Signature was redacted for privacy.

In Charge of Major Work

Signature was redacted for privacy.

For the Major Department

Signature was redacted for privacy.

For the Graduate College

Iowa State University
Ames, Iowa

1983

TABLE OF CONTENTS

	<u>Page</u>
INTRODUCTION	1
General Background	1
Rare-Earth Additions in Austenitic Stainless Steels	10
RADIATION DAMAGE	17
Introduction	17
Point Defect Generation	20
Defect Clusters and Loops, Void Formation, and Swelling	25
Simulation of Neutron Irradiation with Ion Beams	38
EXPERIMENTAL PROCEDURES AND RESULTS	51
Alloy Preparation	51
Structure Analysis and Lattice Parameter Measurements	56
Sample preparation	56
The structure analysis	56
Lattice parameter measurement	64
Hardness Tests	67
General	67
Hardness tests	73
Second Phase Particle Size	74
Ion Beam Bombardment	86
Stacked-edge-on multispecimen assembly preparation	86
TEM specimen preparation	92
Assembly TEM specimens in the specimen holder	96
Particle bombardment facility	102
Irradiations	107
Measurement of Swelling Using Interferometer	112
General	112
Measurement of step height	114
Beam Intensity Distribution	132
Optical Metallographic Examination and Microchemical Analysis	150
Microstructural Analysis	195

DISCUSSION	215
Structure and Lattice Parameter	215
Hardness	215
Second Phase Particles	216
Microchemical Analysis	218
Optical Metallographic Examination	220
Matrix	221
Grain boundary	222
Second phase particle swelling	225
Electropolishing behavior	227
Swelling	229
Microstructure	233
CONCLUSIONS	241
BIBLIOGRAPHY	244
ACKNOWLEDGEMENTS	262
APPENDIX	264

INTRODUCTION

General Background

As the demand for energy increased, cheaper and more abundant sources were sought, and the main source of energy changed successively from biological to fossil energy (oil, natural gas and coal). Now, however, fossil energy reserves are limited and are estimated not to be able to satisfy demand even for the next century (Fig. 1) [1]. Other alternative sources such as wind, solar, geothermal, hydraulic, sea wave and tide, and nuclear energy are in various stages of development.

Considering availability, economics, long-term supply and technology, most countries have recognized the nuclear option and placed it high on the list of alternatives. Nevertheless, supplies of nuclear fuel for thermal nuclear fission reactors (U-235, which is only 0.72% abundant in natural uranium) are not expected to be able to satisfy long-term energy needs. To extend the fission contribution and use other fertile materials (U-238 or thorium), it is necessary to develop the fast breeder reactor (FBR). Judd [2] described briefly the engineering problems for fast reactors. For the longer term, fusion reactors using deuterium and tritium are being developed. The fuel resources are much more abundant and waste problems appear to be more manageable. As an intermediate stage between fast breeder reactors and fusion reactors, fusion-fission (hybride) concepts [3,4] are also being studied in order to use fertile materials more effectively.

Fuel and non-fuel materials play an important role in bringing

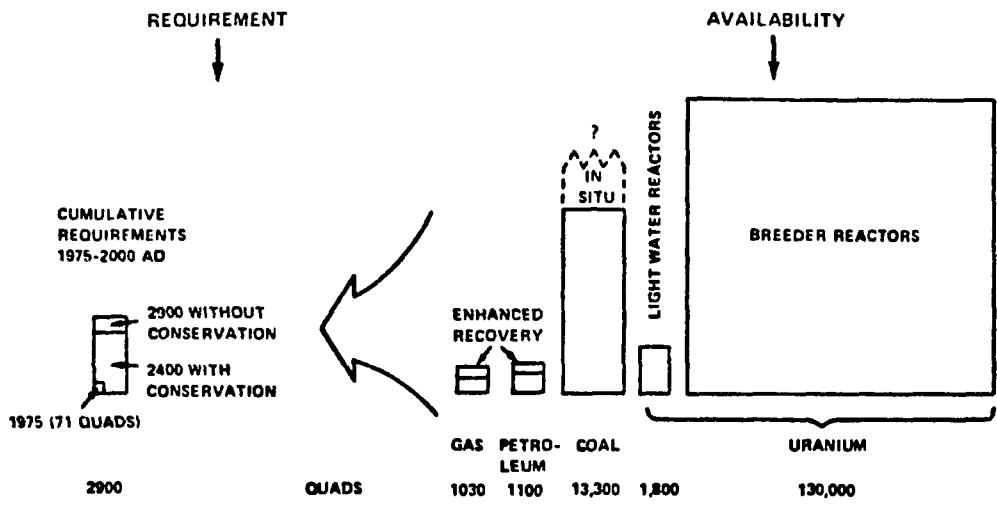


Fig. 1. Energy requirements and availability in quads (10¹⁵ BTU) [1]

advanced fission and fusion options to reality. For the fast breeder reactor, the most important factor in the early days was achieving the necessary high breeding ratio. Another advantage of fast breeder is the high burnup fuel that is possible with reasonable fabrication costs. In the 1960s, however, a serious materials problem became evident. Cawthorne and Fulton [5] reported a transmission electron microscope observation of small voids and helium bubbles in 316 stainless steel cladding irradiated to a fission neutron dose of 6×10^{22} n/cm² at temperatures between 270 to 600°C in the Dounreay Fast Reactor. Since this report, the integrity of structural materials was confirmed to be a problem and much research was done to examine the effect of neutron radiation damage. Most countries dealing with breeder reactors pursued projects to develop better structural materials [6-9].

Bennett and Horton [10] discussed materials requirements for liquid metal fast breeder reactors. Thermal reactor materials require good high temperature tensile, creep and fatigue properties, compatibility with other components, resistance to wear, stress corrosion cracking, crack propagation, and good weldability. Because of their high flux level, the fast breeder reactors require materials with most of the properties cited above, but in addition they must have resistance to radiation embrittlement, swelling and radiation-enhanced creep, good neutronics, and compatibility with fuel and fission products. Bennett and Horton also showed the current status, development goals, schedule, and candidate alloys (Table 1) [10] for liquid metal fast breeder reactors.

Table 1. LMFBR clad/duct materials, (a) current status and development goals, (b) alloy development program, and (c) candidate advanced alloys [After 1 and 10]

(a) LMBFR Clad/Duct Materials. Current status and development goals

Performance Parameter	Reference 316 Current Status	Advanced Alloy Development Goals
Swelling, $\Delta V/V$	18% at 2.5×10^{23} n/cm ²	5% at goal fluence
In-reactor creep rate, 0.45 kg/m ² at 650°C	$>6.2 \times 10^{-7}$ h ⁻¹	$<2 \times 10^{-7}$ h ⁻¹
Rupture stress 20,000 h at 650°C	36 kg/m ²	90 kg/m ²

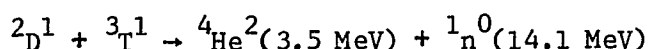
(b) Alloy Development Program Milestones

- o 1976-Complete alloy selections and initiation of EBR-II/PFR test
 - o 1978-Select three candidate alloys
 - o 1980-Start FFTF irradiations
 - o 1982-Select advanced clad/duct alloys
 - o 1985-Complete generation of design data base
-

(c) Candidate Advanced Alloys

Alloy Class	Candidate Commercial Alloy	Candidate Developmental Alloy
Ferritic	HT-9	D57
Solid solution	(316)	D9
Austenitic	310	D11
	330	
Intermediate nickel	A-286	D21
Precipitation	M-813	D25
Strengthened		
High nickel	Nimonic PE16	D66
Precipitation	Inconel 706	D68
Strengthened	Inconel 718	-
	-	D42

McHargue and Scott [11] and Scott [12] discussed materials problems in the TOKAMAK magnetic confined fusion systems (Fig. 2), which also have difficulties because of the hostile environment of high-energy (14 MeV) neutron fluences, high temperatures and large cyclic thermal stresses. At present, the following fusion reaction is assumed to be the most probable:



The energy is released as the kinetic energies of the alpha particles and the neutrons in the plasma region (Fig. 3). The alpha particles are confined within the plasma, but some of the energy of the alpha particles is essentially transferred to the first wall by bremsstrahlung and other radiations (Fig. 3), estimated to be 0.2 to 0.8 MW/m² [12]. As the neutrons have a mean free path of about 0.3 m in the blanket, their energy is deposited throughout the blanket. The total energy density of the neutron current through the first wall is in the range of 1 to 4 MW/m² [12]. The average wall loading is expected to be at the 1 MW/m² level for economic reasons.

The irradiation heat flux due to neutrons, bremsstrahlung, gamma rays and charged particles on the fusion reactor first wall may lead to surface erosion [13], gas absorption, sputtering, blistering, unipolar arcs, and heat pulses. Severe thermal stresses, fatigue, and thermomechanical failure may result due to thermal shock and thermal gradients. Mechanical properties are also affected by radiation-produced defect clusters, voids, and gas bubbles containing helium and hydrogen.

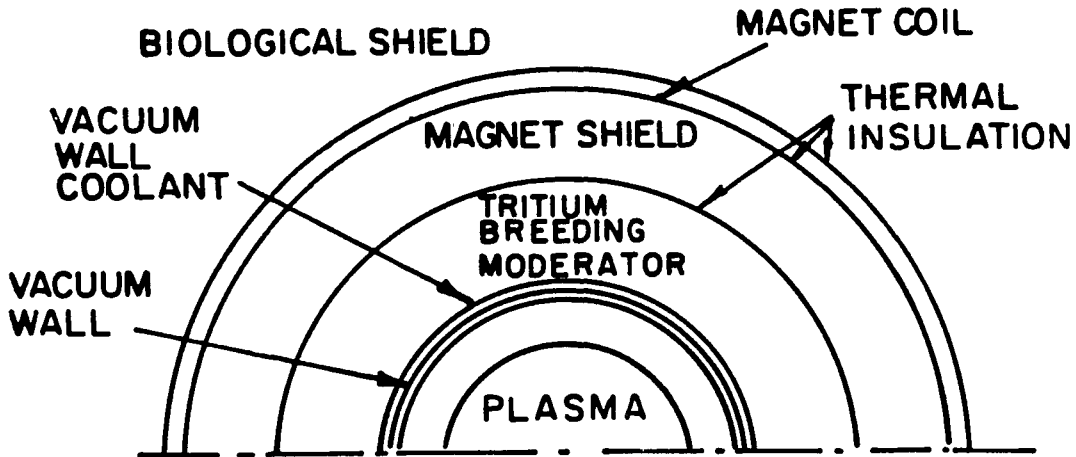


Fig. 2. Typical D-T fusion-reactor configuration employing magnetic confinement

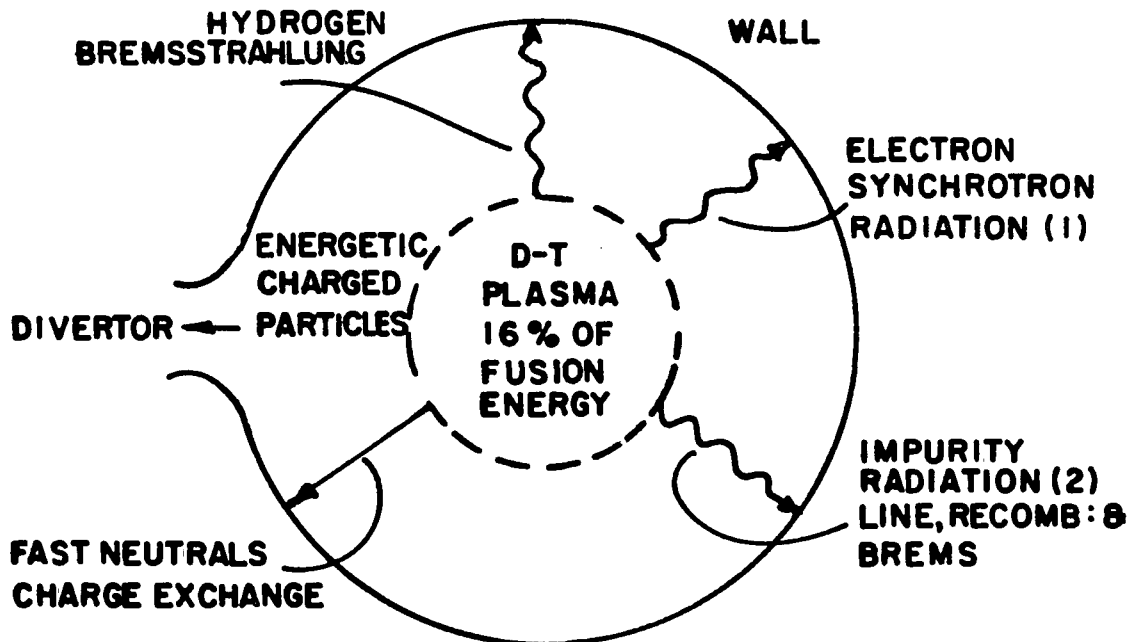


Fig. 3. Mechanisms of energy deposition to the first wall and the divertor

To protect the first wall from the hostile radiation, thin protective coatings of ceramics or other materials are being studied [14], but the major solution depends upon the development of structural materials. Bullough and coworkers [15] discussed and compared the anticipated structural materials requirements, as shown in Table 2. In 1974, the Energy Research and Development Administration (ERDA) established a national program to develop alloys with low swelling characteristics, good resistance to in-reactor creep, and high rupture strength, as shown on Table 1a [10]. The program time schedule is shown in Table 1b [10]. There are sixteen candidate alloys being investigated (Table 1c) [10]. A little later, the Department of Energy submitted a magnetic fusion energy alloy development program based on the following four kinds of alloys: austenitic stainless steels, high-strength Fe-Cr-Ni alloys, reactive and refractory alloys, and advanced materials such as ceramics.

At present, the first wall of the fusion reactor and the cladding and ducts of the liquid metal fast breeder reactor in commercial scale will likely be constructed of an austenitic stainless steel [16]. To survey the low swelling alloys, energetic charged particles (typically, 4 Mev) were used instead of fast neutrons on a range of commercial and synthetic Fe-Cr-Ni alloys (Fig. 4) [17-19]. It was found that the swelling rate decreases rapidly as the nickel concentration increases up to 40% (Fig. 5) [17-19]. Composition appears to be the most potent variable for controlling swelling. But, it can not be neglected that the high nickel concentrations can adversely affect the breeding ratio in fast breeder reactors and produce more helium from (n, α) reactions. Mn

Table 2. Example of anticipate structural materials requirements for fission and fusion reactors [15]

Parameter	Fission breeder (steel)	Magnetically confined fusion	Inertially confined fusion
Temperature (°C)	300-600	300-500(steel) 500-1000(refract.)	300-500(steel) 500-1000(refract.)
Maximum displacement rate (instantaneous dpa/s)	10	(3-10) x 10 ⁻⁷ (mirrors and tokamaks) (1-10) x 10 ⁻⁷ (θ pinch)	~(1-10) x 10 ⁻⁷
Average*(dpa/yr)	50	10-30	10-30
Helium gas production (at.ppm/yr)	10	200-600 (steel) 25-150 (refract.)	200-500 (steel) 25-150 (refract.)
Number of power cycles (yr ⁻¹)	10	~10 (mirror) 10 ³ -10 ⁵ (tokamaks) 3x10 ⁶ (θ pinch)	10 ⁷ -10 ⁹
Stress level (MPa)	60-120	60-120	100-200
Desired lifetime conditions (dpa)	100-150	Acceptable >20	Reactor life 300-1,000
He (at.ppm)	20-30	>400(steel) >50-100(refract.)	6,000-20,000 (800-5000 refract.)
ΔV/V % (lifetime)	<5	<5-10	<10
Creep % (lifetime)	<1	<1	<1
Ductility (% elongation)	>1	>1	>1

*70% Power Factor.

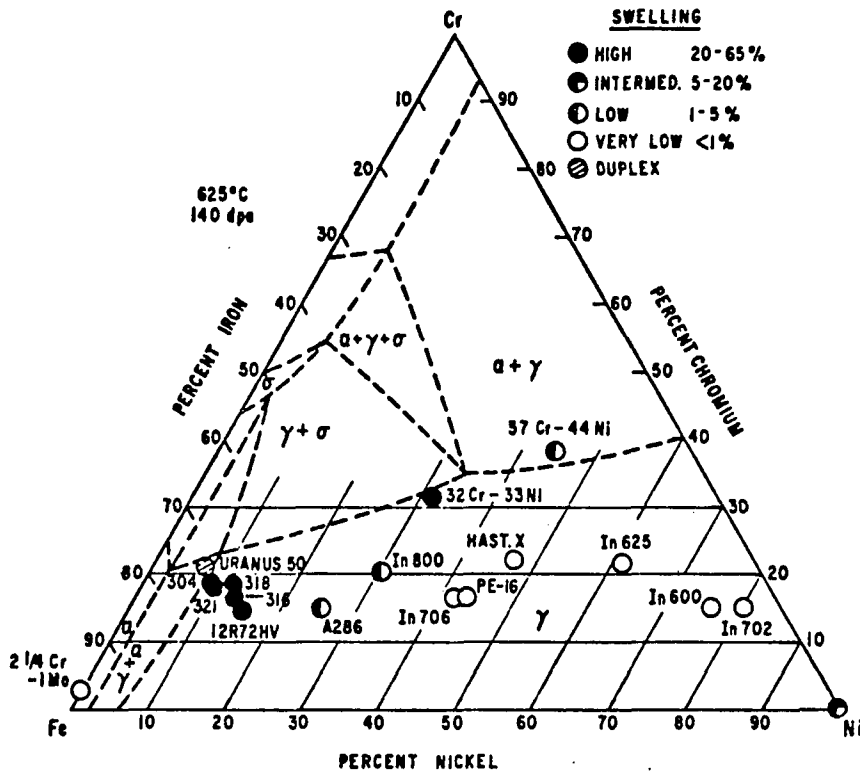


Fig. 4. Relative swelling of commercial alloys ion bombarded to 140 dpa at 525°C. The alloys are plotted on the ternary diagram according to their Cr and Ni contents alone [17-19]

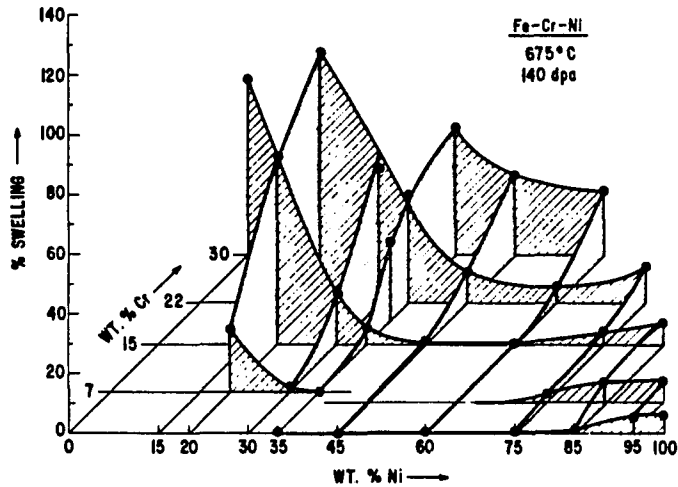


Fig. 5. Swelling of simple ternary alloys of Fe-Cr-Ni bombarded with nickel ions [17-19]

can replace Ni, but a large amount of Mn is apt to reduce ductility. Johnston et al. [17] and Frost [18] discussed the effect of minor additions on the swelling. Combined titanium and silicon additions of 1 wt% reduce drastically the swelling of Type 316 stainless steel (Fig. 6 and 7) [19]. Minor additions of zirconium and niobium can also reduce swelling and improve mechanical properties [20].

For the present work, an intermediate-nickel precipitation strengthened alloy, here designated as AL, was used. The chemical composition of the as-received starting stock is shown in Table 3. The primary approximate composition can be described as Fe-26% Ni-9% Cr. Fig. 8 [21] shows the ternary phase diagrams for the Fe-Ni-Cr system, with the position of the AL indicated. From Fig. 8a, the melting point of the base alloy can be expected to be around 1460°C. As Table 3 shows, Ti and Al are present in the base alloy at concentrations of about 3.3 and 1.65 wt%, respectively. These elements are known to have high affinity for oxygen, thus removing oxygen from solid solution. Oxygen has been observed to stabilize radiation-produced defect clusters in vanadium and thus to retard annealing effects [22].

Rare-Earth Additions in Austenitic Stainless Steels

Besides Ti, Si, Zr and Nb, minor additions of rare earths in stainless steel are known to improve hot workability, ductility and strength, oxidation and scaling resistance at elevated temperatures [23]. Rare-earth additions can also reduce the amount of the nickel used in specific stainless steels while maintaining the same properties [24].

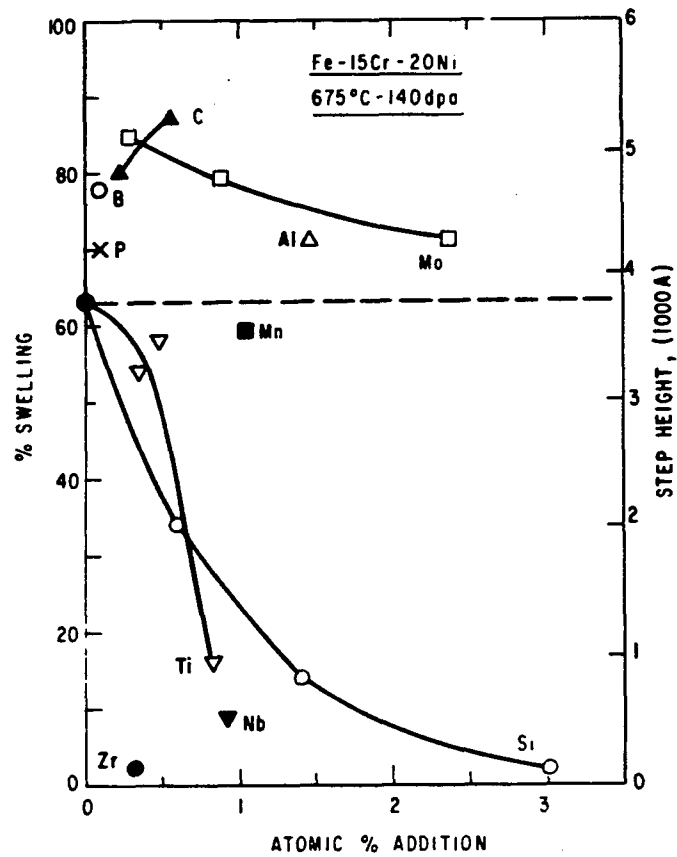


Fig. 6. Effects of individual minor element additions to the base alloy Fe-15Cr-20Ni [19]

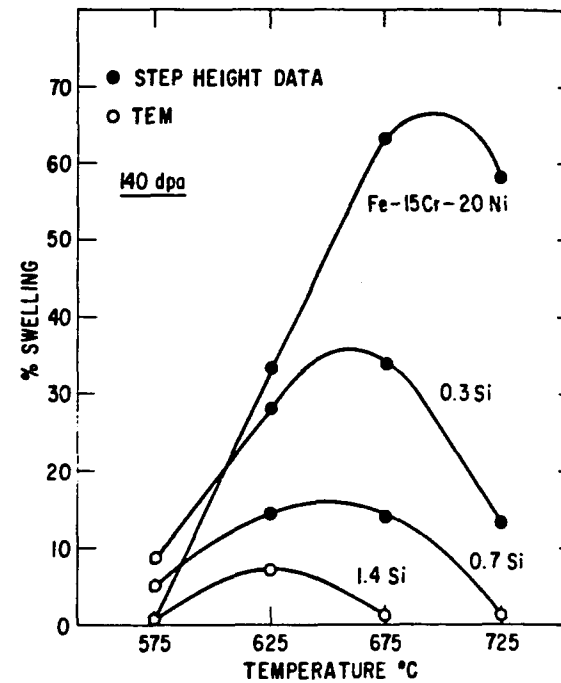


Fig. 7. Temperature dependence of swelling in the simple ternary base alloy, and in alloys with additions of Si [19]

Table 3. Chemical composition of the as-received alloy, AL

Element	Weight Percent
Iron	68.25
Nickel	25.71
Chromium	8.65
Titanium	3.30
Aluminum	1.65
Manganese	0.97
Molybdenum	0.96
Silicon	0.31
Cobalt	0.05
Zirconium	0.05
Carbon	0.046
Copper	0.03
Niobium	0.02
Tantalum	<.01
Vanadium	<.01
Arsenic	<.01
Phosphorus	0.009
Boron	0.004
Sulfur	0.001
Nitrogen	0.001

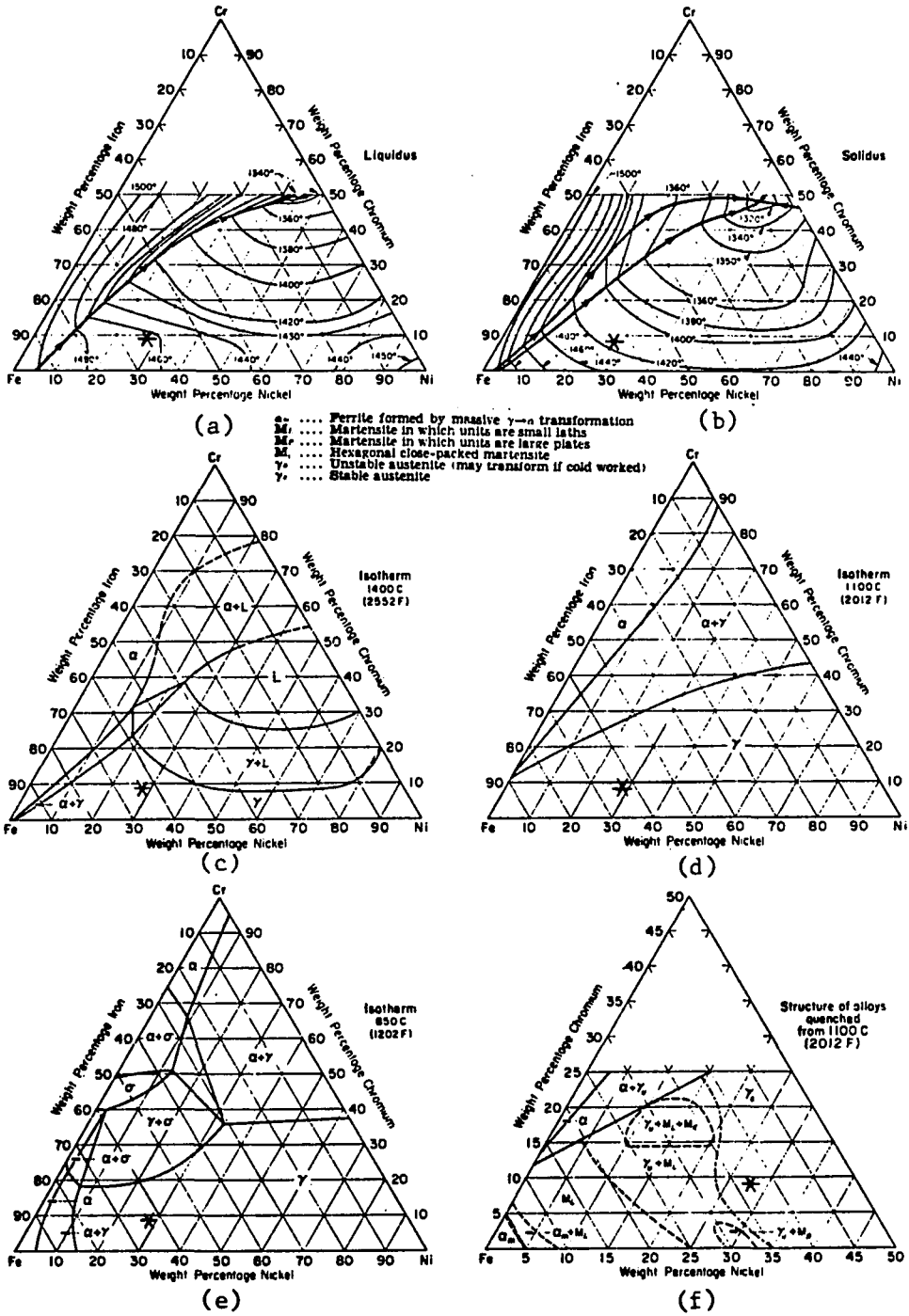


Fig. 8. Ternary phase diagram for the Fe-Cr-Ni systems [21]. *represents the composition of AL alloy

This advantage is very attractive because of the adverse effect on breeding ratio of the nickel in cladding for fast breeder reactors. Under appropriate conditions, rare-earth additions in steel are known to be very reactive, combining readily with oxygen, nitrogen and sulfur, though not with carbon [23,24]. Because of these properties, the rare earths are used in ferrous metallurgical processing for degassing and desulfurizing steels and cast irons. With small amounts of rare-earth additions, lower oxidation at high temperatures was observed and assumed to be due to the result of a compact, nonporous scale layer, which offers resistance to diffusion. Also, rare-earth oxides provide a "keying" effect, which involves the formation of continuous oxide particles in the grain boundaries at the original metal-oxide interface [25,26]. A minor addition of rare-earth elements decreases grain boundary carbide precipitation and the tendency toward sensitization [26]. Chistyakov et al. [27] examined the structure of 0.2% ferrocerium treated Okh23Ni18 steel and found that cerium additions produce a more homogeneous structure rather than large accumulations of segregating elements. They also decrease dendritic nonuniformity with respect to carbon, nitrogen, sulfur and oxygen, and reduce the number of nonmetallic inclusions at the grain boundaries. Gschneidner et al. [28] and Wilson et al. [29] reviewed the type of rare-earth inclusions formed in steel and concluded that the rare earths are strong deoxidizers and desulfurizers in steel and no MnS should remain when the rare-earth content is high enough. The rare earths decrease the grain boundary energy and produce finer, nearly spherical, and stabilized grains [30]. Krivets et al. [31] examined

0.1-0.5% mischmetal-doped Kh18N9T steel (0.07% C, 1.69% Mn, 0.77% Si, 0.018% S, 0.015% P, 18.7% Cr, 10.1% Ni, 0.77% Ti) and found the grains to be fine and equiaxed, and inclusions to be globular shaped. Most of the carbides redistributed within the grains.

Roberts et al. [24] studied irradiated Cr-Al stainless steels used in nuclear reactors, and found that a minor addition of yttrium disperses boron within the grains so that the helium atoms from (n,α) reaction form within the grains and remain isolated, and this prevents embrittlement and swelling. Preliminary work using the ORNL Dual-Beam Van de Graaff accelerator [32,33] has indicated that yttrium additions may improve the swelling resistance of two of the LMFBR developmental alloys [34], while experiments at Ames Laboratory showed that the high temperature tensile properties and hardness in the temperature range of LMFBR interest are not greatly affected [35]. The austenitic stainless steels, like the present AL alloy, are known as precipitation-strengthened alloys and are characterized partially by their second phase precipitations. So, it is not difficult to expect complexity of in-reactor behavior of these second phase precipitates. Lee et al. [36] examined the microstructure of pre- and post-irradiated AISI 316 and Ti-modified stainless steels and concluded that, even though the second phase precipitates are not changed to completely new phases, phase relationships were changed as a result of radiation induced segregation of Ni and Si and enhanced diffusion rates during irradiation. Rowcliffe and Lee [37] performed experiments to correlate the precipitation behavior with swelling behavior and concluded that they are closely linked. As concerns the effect of rare earth

additions in steels, Raman [30] has pointed out that rare earth additions promote a finer grain structure, induce inclusions to be more spherical, and reduce grain boundary precipitation. These changes in microstructure and second phase precipitation tend to improve mechanical properties. The purpose of the present work is to study the effect of rare-earth additions on the mechanical properties, microstructure, and radiation swelling of a particular developmental cladding alloy for LMFBRs. The rare earth additions are yttrium, lanthanum, and cerium.

RADIATION DAMAGE

Introduction

Radiation damage refers to the deviations of the regular arrangement of crystalline solids as a result of irradiation by high energy charged particles, neutrons or electromagnetic radiations. By 1960, neutron irradiation was known to affect the mechanical properties of metals by increasing hardness, yield stress, and sometimes decreasing ductility in a fashion very similar to effects ensuing from cold working. Many theories [38-43] were developed to explain the hardening. These theories referred to point defects migrating to and pinning dislocations (source hardening) or forming clusters which obstruct the movement of dislocations (friction hardening).

As transmission electron microscopy (TEM) was developed, more efforts were applied to investigate the microstructure of radiation damaged metals. Defect clusters were observed as "black spots" in α -iron irradiated to a fission neutron fluence of 5×10^{17} , 5×10^{18} and 1×10^{19} n/cm² by Eyre[44]. This provided evidence for source hardening. A subsequent investigation on molybdenum [45] irradiated to a fission neutron dose of 2×10^{22} n/cm² at 60°C. Each specimen was annealed for 1 hour ranging from 60°C to 800°C and showed a recovery behavior of radiation damaged metal. At this time, microhardness was used as an important indicator of the amount of radiation damage or the post-irradiation recovered state. Eyre and Bartlett [46] used TEM and observed defect clusters in alpha iron

irradiated to about 2×10^{20} n/cm² at 60°C and after annealing up to 500°C. Above 300°C the defect clusters annealed away. The visible defect clusters were believed to be interstitia in nature, the vacancies being trapped by interstitial impurity atoms. The annealing above 300°C was consistent with vacancies breaking away from their traps and recombining with the interstitials in the defect clusters.

By 1966, Cawthorne and Fulton [5,47] found an internal porosity consisting of a distribution of small (smallest resolvable to 1500Å) cavities in 316 stainless steel that had been irradiated in the Dounreay Fast Reactor to a fluence of 6×10^{22} n/cm² at temperatures between 270 and 600°C. Since this finding, radiation damage in nuclear structural materials, especially void swelling, became the subject of intensive investigation, discussed in numerous reviews [48-55] and conferences [56-74]. Void formation has practical implications for fast breeder reactor cladding as well as for the fusion reactor first wall. The large flux of high energy neutrons in a fast reactor core results in a much higher rate of defect production (10^{-6} displacements per atom (dpa) per sec), resulting in void formation and swelling. As the void swelling varies with temperature and neutron fluence, the temperature and flux gradients in the reactor core will result in non-uniform swelling and distortion of structural members. The first wall of a fusion reactor provides the mechanical stability of the torus, contains the vacuum for the plasma chamber, and separates the blanket from the plasma. The fusion energy deposition on the first wall is about 1 Mw/m^2 , and the neutron bombardment produces about 3×10^{-7} dpa/sec, resulting in

void formation. Furthermore, the radiation causes defect segregation to grain boundaries or other potential fracture paths. This may alter the fracture mode and ductility of the first wall material. In addition, sputtering, blistering and evaporation may reduce wall thickness and increase the likelihood of thermomechanical failure. Also, the absorption of the plasma of atoms from the first wall tends to cool the plasma and quench the fusion reaction.

For most metals, the peak swelling occurs in the temperature range 0.3 to 0.55 times the absolute melting temperature. For stainless steels, this temperature range overlaps the operating temperature of the cladding of liquid metal fast breeder reactors [10], as well as the first wall and blanket structural materials of magnetic confinement fusion reactors [11]. The large number of radiation-produced vacancies and interstitials are lost either by recombination or by going to sinks such as the surface, grain boundaries, dislocations or existing voids, but some of them survive and grow. The voids do not grow at low temperature because of low vacancy mobility. The voids also do not form at high temperature because of the high thermal equilibrium vacancy concentration, which reduces the vacancy supersaturation. At medium temperatures, the voids accumulate and grow. Void swelling becomes significant at fast neutron fluences above 20^{22} n/cm² in the 316 stainless steel according to the Appleby et al. [75] and Bates and Korenko [76].

Meanwhile, the surviving interstitials agglomerate into interstitial loops or clusters and become another source of sinks. The neutron

irradiation temperature and total fluence, the neutron flux, major and minor alloy composition [17] and microstructure of the materials, such as dislocation density, grain size and second phases, all influence void formation and swelling.

Point Defect Generation

The primary damage induced by fast neutrons is due to a collision mechanism, producing vacancies and interstitials, and nuclear transmutations. The fast neutron of energy E interacts with solids mainly by making direct billiard-ball collisions with atomic nuclei in the lattice. Through the neutron-atom collision, a sufficient energy, T , may be transferred to the struck atom (primary knock-on atom, PKA) to displace the PKA from its lattice site. An amount of energy, the threshold displacement energy, T_d , of about 13-90 eV is required depending on the physical properties of the atom and displacement direction [55]. Based on irradiations in the high-voltage electron microscope, Makin et al. gave a T_d value of 18 ± 1.5 eV for 316 austenitic stainless steel [77]. In connection with ion bombardment experiments simulating neutron-induced swelling, investigators at the ORNL Van de Graaff accelerator suggest using $T_d = 40$ eV for the AL alloy of the present study [78,79]. If the energy transferred to the PKA is higher than the threshold displacement energy, the struck atom moves as an ion through the lattice. Wechsler [80] reviewed the theoretical and experimental aspects of basic theory of displacement production. If the PKA receives enough energy, it may strike and displace other lattice

atoms and they, in turn, can displace still others by the same collision mechanism. As a result, a displacement cascade is produced. The mean number of displaced atoms, ν , resulting from a single PKA of energy T is approximated by $\nu = T/2T_d$ and the transferred mean energy, T , is approximated by

$$T = \frac{2mM}{(m + M)^2} \cdot E \quad (1)$$

where m and M are the masses of neutron and the target atoms. At low T s, elastic collisions and displacement production predominate. At high T s, more energy is transferred to the electron system producing ionization and electron excitation. Smith [81] summarized the displacement cascade mechanism as shown in Fig. 9 [81]. The mean free path for fast neutron collisions is several cm but the damage produced by a single PKA is generally very concentrated. Therefore, neutron damage consists of numerous regions of high defect density distributed relatively homogeneously throughout the irradiated material. If the PKA receives energy below T_d and is not displaced, the transferred energy winds up as heat, producing a thermal spike. Kinchin and Pease [82], Kelly [55], Billington and Crawford [83] and Thompson [49] discuss overall aspects of these neutron damage mechanisms in solids.

At any temperature above absolute zero, vacancies and interstitials exist in thermal equilibrium. Their concentrations are given by

$$C = C_o \exp \left(- \frac{E_F}{kT} \right) \quad (2)$$

where C_o is a constant of the order of 1-10 [55] and E_F is

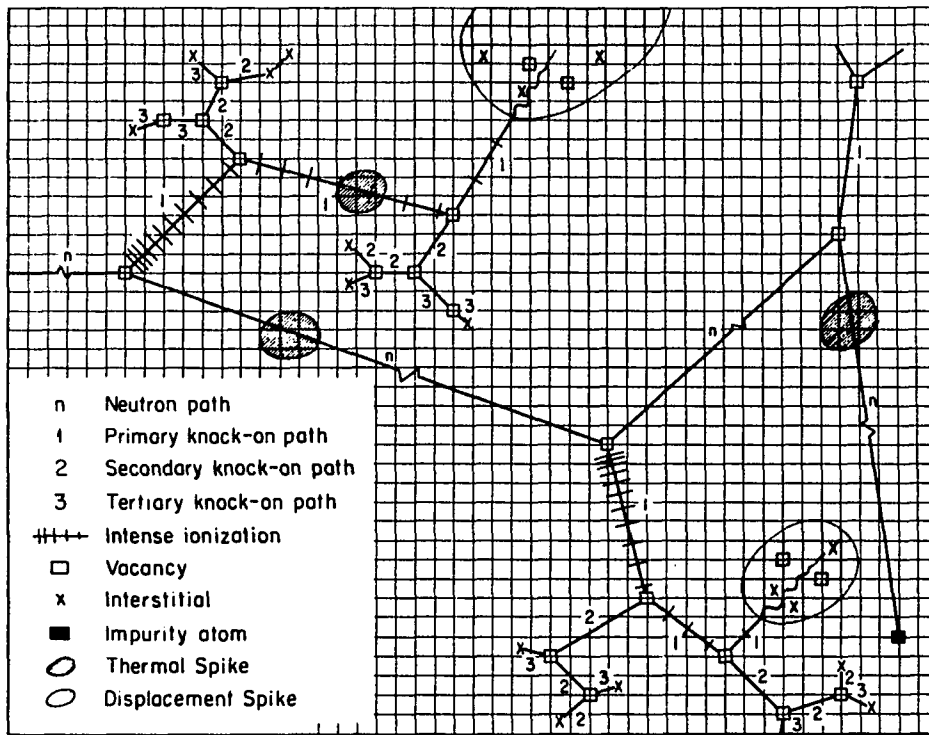


Fig. 9. Schematic diagram of radiation effects in a crystal lattice caused by neutron entering at left [81]

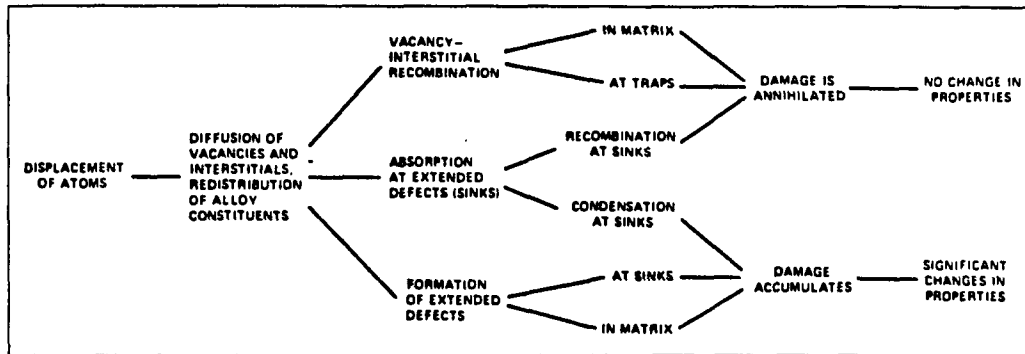
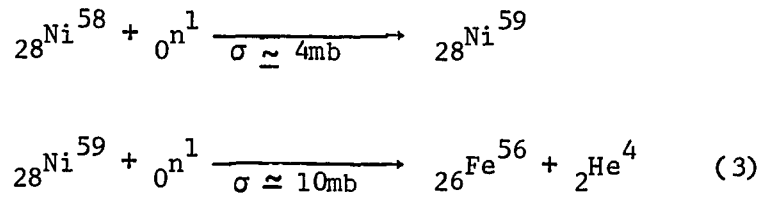


Fig. 10. Flow diagram showing various possible fates of point defects generated by irradiation. Defects may ultimately recombine by several paths, producing no permanent property changes. Defects which accumulate either at existing sinks or precipitates or by forming new sinks produce property changes [89]

activation energy of vacancy or interstitial formation. Besides these thermal equilibrium concentrations, an extra quantity of interstitials and vacancies is produced through irradiation. These radiation-produced defects may anneal out just after the irradiation depending on the energy transferred, defect size, the physical properties of the matrix atom, and especially the matrix temperature. The interstitials are mobile at quite low temperatures (e.g., below about 70°K), and they may combine with vacancies, either during the initial formation of displacement cascade or as a result of thermal motion. If a vacancy and an interstitial recombine, they are mutually annihilated, but if the same kind of defect becomes aggregated, then multiple interstitials and vacancies are formed. These mutual annihilation and aggregation mechanisms of defect are discussed by various authors [50,82-89], and Fig. 10 from [89] illustrates the possible fates of point defects generated by irradiation. Even at low temperature below $0.04 T_m$ (about 70°K for the AL alloy), the interstitials are very mobile and migrate to vacancies to be annihilated, impurity atoms to be trapped, other interstitials to form di-interstitials or higher order three dimensional interstitial clusters, and fixed sinks like grain boundaries, dislocations, and free surfaces [90]. At a temperature above $0.04 T_m$, the interstitials are released from traps and are dissociated from di-interstitials, where upon they move to vacancies and to fixed sinks where they are annihilated. At temperatures above about $0.16 T_m$, (220°K), vacancies begin to move to impurity atoms to be trapped, to other vacancies to form di-vacancies and higher order vacancy clusters, and to fixed sinks to

form higher order vacancy clusters. At temperatures above about $0.22 T_m$ (300°K), vacancies are released from impurity atom trap and di-vacancy pairs dissociate. At temperatures above about $0.3 T_m$ (510°K), all vacancies begin to be quite mobile. Void formation is normally thought to occur in the approximate temperature range $0.3 < (T/T_m) < 0.55$ or for AL alloy $250^\circ\text{C} < T < 680^\circ\text{C}$. This is also the approximate range of service temperatures for reactor structural components. Below this temperature range, vacancies are not sufficiently mobile to agglomerate into voids, and above this range they are not sufficiently supersaturated so, again, the voids do not form. Voids in irradiated metals and alloys have now been widely studied [65], mainly by conventional TEM techniques. Computer simulation studies have also been frequently employed [91-100]. More recently, in-situ electron microscope observations during irradiation have become possible using the high-voltage electron microscope [101-104] and special facilities at Van de Graaff accelerators [105].

Nuclear transmutations also have an important effect on mechanical properties. Gaseous atoms have a particularly significant effect, since they form bubbles that tend to lie along grain boundaries. The most critical of these is helium produced as a product of (n,α) reactions. Thermal neutron (n,α) cross sections may be quite high in special cases (e.g., 4000 barns for the 20% abundant B^{10} isotope), but even for fast neutrons the (n,α) production of helium may be quite significant. One prevalent mechanism for He production in fast-neutron-irradiated Fe-Ni-Cr alloys is based on the reactions [106]



In the iron-nickel base austenite stainless steels, the concentrations of He expected to be produced in one year for fast-breeder reactor cladding and the fusion first wall are 4.7 and 200 appm, respectively. The corresponding concentrations of hydrogen are 270 and 540 appm, respectively [107]. Hydrogen, however, is more mobile than helium, and it is not expected to be as serious a contaminant. Gabriel, Bishop and Wiffen [108] calculated the helium and damage production for important reactor structural materials in various reactor environments as shown in Table 4 [108].

Defect Clusters and Loops, Void Formation, and Swelling

The radiation-produced vacancies and interstitials constitute excess concentrations above the thermal equilibrium amounts. Since the primary collisions occur randomly, vacancy and interstitial production are nonhomogenous on a local scale. These interstitials and vacancies move thermally and annihilate or agglomerate to form vacancy and interstitial defect clusters and voids, as shown in Fig. 11. The nature and concentration of the defects depend on the relative rates of production and removal by annealing. Irradiation temperature and fluence, major and minor chemical composition and stress state of the material influence strongly the radiation-induced microstructure and

Table 4. DPA and helium production per year in an MFR and in fission reactors of interest to fusion reactor alloy development programs (All calculations are for a plant factor of 1.0) [108]

Element or Alloy	Reactor and Position							
	MFR		ORR		HFIR		EBR-II	
	First Wall ^a		C-3 ^b		PTP ^b		Row 2 ^b	
	dpa	He (appm)	dpa	He (appm)	dpa	He (appm)	dpa	He (appm)
Fe	10.6	110.	7.1	2.1	30.9	8.6	37.3	5.7
SS-316 ^c	10.7	155.	7.4	76.9 ^d	32.2	2187. ^d	39.2	15.1
PE-16 ^e	10.8	228.	7.4	258. ^d	32.4	7316. ^d	39.5	37.0
Inconel 600 ^f	10.9	332.	7.5	468. ^d	32.8	13320. ^d	40.4	62.0
Ni	11.2	409.	7.5	626. ^d	33.1	17791. ^d	40.9	81.6
Ti	14.7	105.	11.2	1.1	49.3	4.2	55.1	2.9
V	10.8	47.	8.7	0.16	38.2	0.55	46.0	0.5
Nb	6.7	29.	4.7	0.52	20.2	2.2	27.9	1.4

^aWall loading 1 Mw/m².

^bMaximum flux position.

^cFe, 63.22; Cr, 19.21; Ni, 12.29; Mo, 1.49; Mn, 1.92; Ti, 0.06; Si, 1.58; C, 0.23; Atom %.

^dCalculated from Eq. (1) and does not scale linearly with time! Effective Displacement Energy = 40 eV.

^eFe, 34.62; Cr, 17.77; Ni, 41.12; Mo, 1.87; Ti, 1.38; Al, 2.58; Si, 0.42; C, 0.24. E.D.E = 40 eV.

^fFe, 6.84; Cr, 16.78; Ni, 74.87; Mn, 0.33; Ti, 0.22; Al, 0.15; Si, 0.57; C, 0.24; Atom %. E.D.E. = 40 eV.

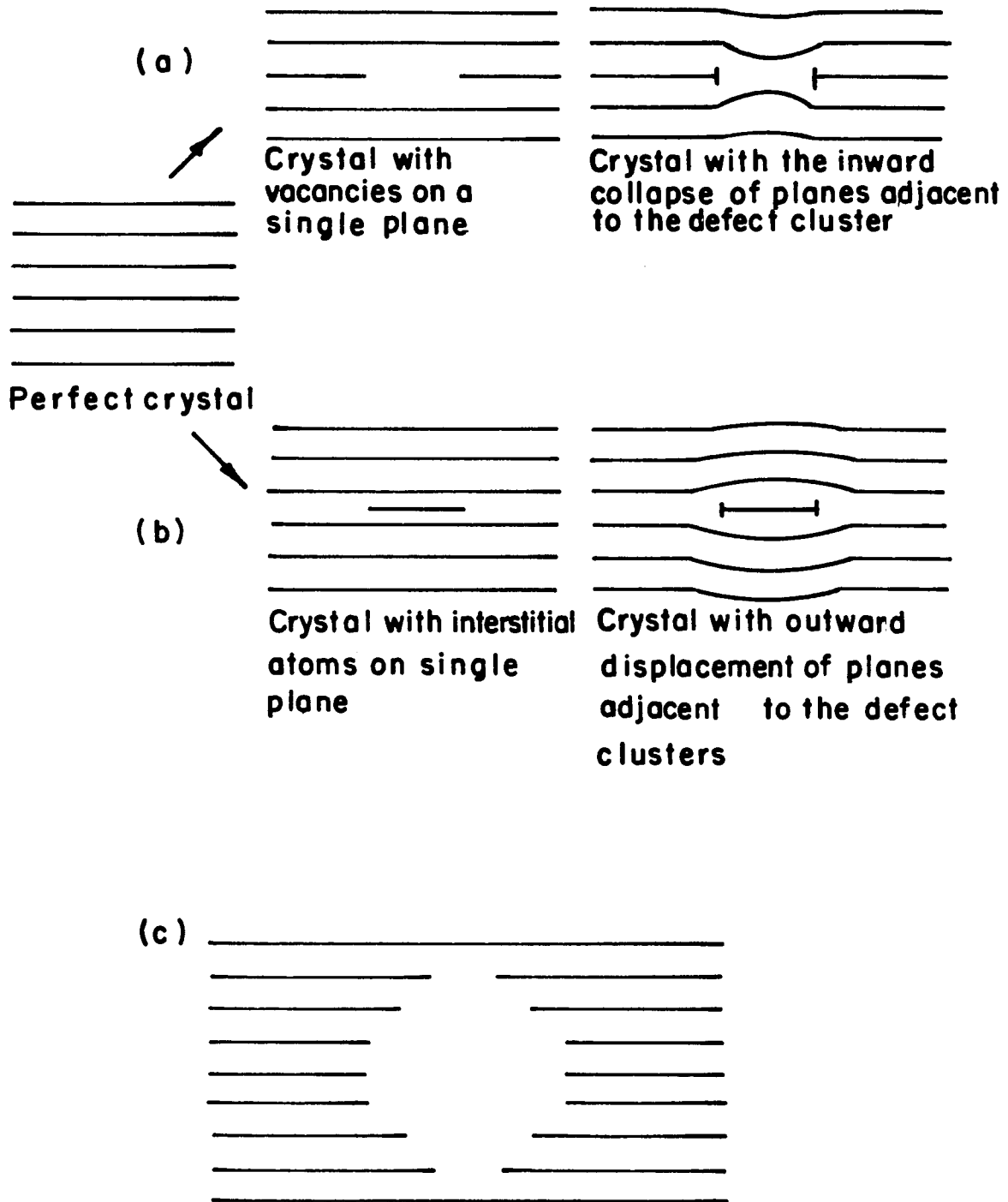


Fig. 11. Defect aggregates: (a) vacancy loop, (b) interstitial loop, and (c) void

especially void formation. Electron microscopy is used to confirm the presence and characterize the defect clusters with diffraction contrast and voids with absorption contrast. The defect clusters and loops are easy to observe and were found much earlier than voids because of their strong strain field [109]. In the face-centered cubic 304 stainless steel irradiated to 1×10^{18} n/cm² at 370°C, defects of about 100Å in diameter were observed [110]. About 75% of them were $a/3 \langle 111 \rangle$ interstitial dislocation loops having a two dimensional strain field, and the remainder were $a/2 \langle 110 \rangle$ dislocation loops and a defect having a symmetrical three dimensional strain field [110]. Gaseous atoms accelerate the formation and stabilize the three-dimensional vacancy clusters against collapse into planar loop aggregates. The structure of voids in austenitic stainless steel is considered as tetrakaidecahedron with [111] and [100] faces, although there is some question as to whether the basic initial shape is a {110} cube with {111} truncation or a {111} octahedron with {100} truncation [111].

Although all commercial stainless steels contain, by virtue of their manufacturing process, hydrogen, nitrogen and oxygen, the effect of the helium gas produced continuously through various (n,α) reactions on void swelling is the most significant. The important role of helium in the formation of voids was proved through pre-injection of He followed by neutron or ion bombardment or by in-situ-injection of helium during neutron and ion bombardment [112-115]. Singh and Foreman [116] reviewed the present theories and experimental results on void formation and suggested that void nucleation is not possible in the absence of gas. In

fusion reactors, the tritium produced in the reactor environment converts to He^3 , which become trapped in the material, and stimulates void formation and swelling [117].

Void development seems to be a two-step process in which helium bubbles about 20 to 100\AA in diameter are formed initially and then consequently are converted to voids about 100 to 1400\AA in diameter as shown in Fig. 12 [118]. Besides void swelling, bubble swelling is another separate phenomenon. Enough helium can cause swelling even under thermal aging with no irradiation. Spitznagel et al. [119], Townsend [120], and Russell [121] discussed the threshold size for the growth or shrinkage of individual cavities and showed that the lower-bound critical cavity size is strongly dependent on helium at elevated temperatures. If a bubble grows eventually bigger than the threshold size, it grows rapidly to a bigger size and becomes a void. The void can be annealed back to a bubble through the same or other mechanism. The Van der Waals equation of state at high pressures is used to derive the number of helium atoms, n , in a spherical cavity of critical radius r_c to be

$$n = \frac{4\pi r_c^3}{3b \left[1 + \left(\frac{r_c}{r_o} \right) \right]} \quad (4)$$

where

- $r_o = 2 \frac{\gamma b}{kT}$ is a characteristic radius
- b = the Van der Waals exclusion volume
- γ = the surface energy
- k = Boltzmann's constant
- T = the absolute temperature.

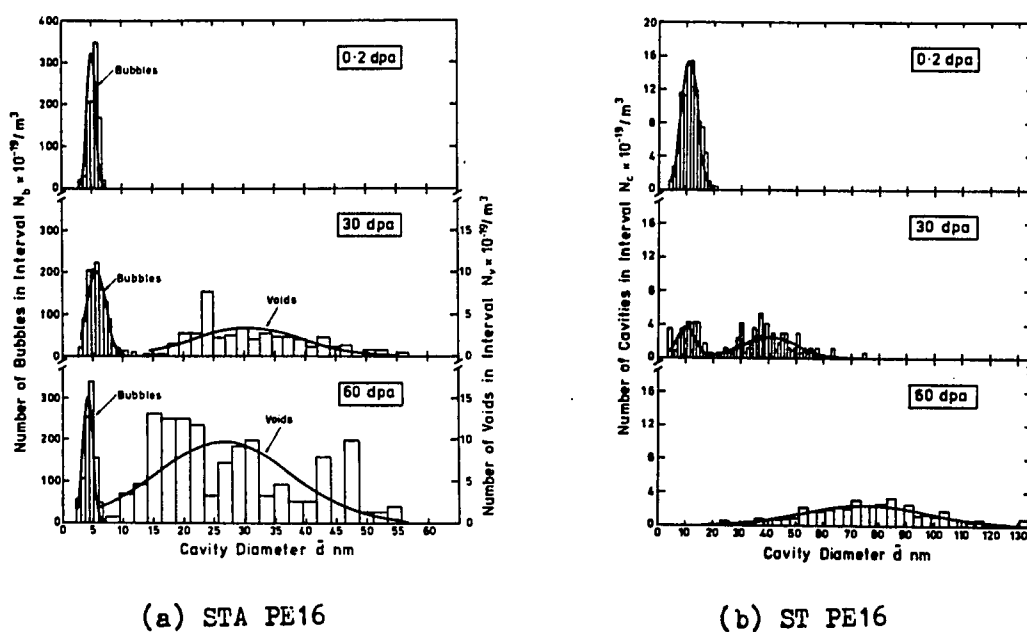


Fig. 12. Histograms of typical cavity distributions in (a) STA PE16 and (b) ST PE16 after 30 and 60 dpa Ni^{6+} irradiation at 625°C following implantation of 100 ppm He at 625°C [118]

Values for these parameters for 304 stainless steel are given [120] as:

$\gamma = 1.25 \times 10^{15} \text{ eV/cm}^5 = 2000 \text{ ergs/cm}^2$, $b = 16 \times 10^{-30} \text{ m}^3 = 16 \times 10^{-24} \text{ cm}^3$
 $= 16 \text{ \AA}^3$, $k = 86.2 \times 10^{-6} \text{ eV/}^\circ\text{K}$, vacancy formation energy = $E_F = 1.6 \text{ eV}$
 (see Equation (2)), and vacancy motion energy = $E_M = 1.3 \text{ eV}$. n in
 Equation (4) can vary from 10 to 10^5 in the temperature range of
 interest, 400–700 $^\circ\text{C}$.

The interaction between radiation-produced He atoms and other gaseous impurities, particularly oxygen and nitrogen, is an important matter that received special attention in the literature recently [122,123]. The principal idea is that these other impurities, perhaps in agglomerated form, may serve as nucleation sites for helium bubbles, which serve, in turn, as nucleation sites for voids. Kenik and Lee [124] studied the influence of He injection on phase stability under ion bombardment of two modified 316 stainless steels. Helium was required to nucleate voids, and for higher He injection rates (up to 20 appm He/dpa) an increase in precipitate density and decrease in precipitate size were observed [125]. Maziasz [126] and Maziasz and Roche [127] discussed the effect of helium content on void formation and solute segregation in austenitic alloys, and showed that bubbles are nucleated on dislocations and precipitates via diffusion of helium atoms and point defects to these sinks.

At relatively low temperature, the helium atoms are at quite high pressure in an equilibrium bubble, but the bubbles do not make a significant contribution to the swelling. At higher temperature, bubbles

grow into voids by thermal vacancy emission at dislocations and vacancy absorption at the bubbles [128]. The formation of helium bubbles is influenced by various factors such as stress, irradiation and annealing temperatures, helium concentration [114,129] and microstructure [36,130-134]. As the helium concentration increases, the bubble size remains fixed, but the bubble concentration increases [129]. As irradiation proceeds, the helium bubble concentration increases rapidly at low dose, and slowly decreases at high dose such as 15 dpa [118,135] for Type 316 stainless steel, as shown in Fig. 12. The size of helium bubbles does not change with dose rate or helium concentration. The bubble size increases with increasing irradiation and annealing temperatures [129].

Bagley et al. [113] reviewed neutron-induced void formation, and suggested that the irradiation temperature is the dominating factor governing the void nucleation and growth. In the majority of metals, void formation temperature is in the range of 0.3 and 0.55 of absolute melting temperature. As the irradiation temperature increases in this range, void concentration decreases and the mean size increases. The total volume of the voids peaks at about 575°C for type 316 stainless steel [89].

The neutron fluence is another important factor. Up to a neutron fluence of order of 10^{22} n/cm², void development in austenitic stainless steels is not significant [89,113]. It is postulated that the swelling induced by the void formation requires an incubation period and is related to the buildup of an appropriate concentration of helium. The

stress state of the material is not significant, as the tensile stress inhibits void formation by encouraging the flow of interstitials to voids, even though it promotes large void diameters ($>200\text{\AA}$) to grow by opposing the surface tension forces tending to minimize void size [113]. The presence of vacancy sinks, promoted by small grain sizes, high dislocation densities, and small precipitates, may reduce swelling [136]. But because of the difficulties in maintaining optimum sink conditions in an irradiation environment at elevated temperature, it does not appear that microstructural modification will be the most practical method for controlling the swelling of commercial reactor alloys [115,137].

The material compositions are another important factor in controlling swelling. In Fe-Ni-Cr austenitic alloys, the highest swelling occurs for low nickel and high chromium (Figs. 4 and 5) [19]. The most swelling resistant simple alloys are those with low chromium and approximately 50 wt % nickel. This high nickel concentration has deleterious effects in producing more helium through various (n,α) reactions. To reduce nickel content and keep the mechanical strength, minor element additions are tried. Minor additions of Si [19,134], Nb [136], Ti [19,136,138-142], zirconium boride [143], V, and Cu [115] cause an appreciable reduction in the peak swelling of the base alloy. The swelling suppression effect of these elements is supposed to be the result of trapping of defects at impurity atoms, but this may not be the entire explanation.

As a result of minor impurities, like carbon, phosphorous and gaseous atoms, the austenitic stainless steels have many kinds of

precipitates forming second phases. Lee et al. [36] and Williams et al. [132] have documented the structures and compositions of second phases in austenitic stainless steels in thermal and irradiation environments. There are several important radiation-induced phenomena such as enhanced diffusion, precipitate nucleation at point defect clusters or loops, segregation resulting from the coupling between solute and point defect fluxes, radiation-induced ordering and disordering, stabilization and destabilization of phases by vacancy fluxes, and cascade dissociation. As a result of these phenomena, the phase mixture which normally develops during thermal aging may be modified [36]. Mansur, Hayns and Lee [130] have classified three general modes of precipitation action: precipitate point defect collection, depletion of point defect traps in the matrix, and changes in overall sink strength or dislocation capture efficiency. Rowcliffe and Lee [37] showed the trappings of helium atoms and point defects at particle-matrix interfaces. Lee, Rowcliffe and Mansur [144] showed the direct effect of the interaction between helium atoms and particles and suggested that a high density of small particles would reduce void swelling. On the other hand, Terasawa et al. [145] maintain that Ni, Ti or C only in solution is effective in reducing swelling and that any precipitation does not suppress swelling.

The concentration of the impurity atoms, such as Mn and V, changes due to radiation-induced nuclear transmutations, and this may affect void swelling [146,147]. These minor impurity elements may change the peak swelling temperature, as shown in Fig. 7 [19]. Odette [148] reviewed the numerous interacting mechanisms that alter both the microstructure and

microchemistry of structural alloys as shown in Table 5.

Most current concepts of a magnetic confinement fusion reactor seem to include a pulsing of the fusion reaction. Lee, Packan and Mansur [149] show that the pulsing refines interstitial loops but not the interstitial networks. It also changes phase stability, makes cavities smaller and suppresses large voids for doses up to 70 dpa. Packan [150] showed that pulsing without helium produces higher swelling, but pulsing with helium reduces the swelling, and slow pulsing (60 sec, on/off) gives slightly greater swelling than fast pulsing (0.5 sec, on/off). Pulsing in the presence of helium is shown to provide the initial burst of interstitial loop nucleation. It results in a finer dispersion of loops, and delays the onset of bias-driven cavity swelling by providing annealing periods for cavity shrinkage closer to the equilibrium size. The pulsing changes the stability of phases and results in different mixtures of coexisting phases.

The reactor grade stainless steels are complex in their chemical composition, microstructure and dynamic behavior in the reactor environment. There are numerous efforts to assess overall aspects of the void swelling [110,113,116,149,151-153], and to evaluate their importance [92,154-157], but still a number of materials parameters need to be better defined. In the past, the microstructural behavior was assumed to evolve homogeneously. In recent years, however, more theoretical attention is being paid to the actual inhomogeneous spatial characteristics of the microstructures and swelling.

Table 5. Some mechanism involved in microstructural evolution [After 48]

-
- A. DEFECT PRODUCTION
 Cascade Clusters and Loops (efficiency)
 Free Defects (fraction/dpa)
 Transmutants
- B. MIGRATION AND RECOMBINATION
 Correlated Diffusion (partial diffusion coefficients including exchange frequencies and correlation factors; activation energy for $\text{He}_S + \text{I} \rightarrow \text{He}_I$)
 Trapping (binding energies, solute clustering, saturability)
 Recombination (recombination volume; sink effects)
 Stress Effects and Free Energy Gradients
- C. SINK STRENGTHS
 Geometric Parameter
 Efficiency (transfer velocity; shell effects-diffusivity, changes and image interaction effects; shape effect; bias factors; stress effects, pinning effects)
 Multiple Sink Correlation (all sink strengths and distribution)
- D. NUCLEATION MECHANISMS
 Homogeneous Nucleation (defect parameters; surface, dislocation and stacking fault energies; segregation; and gas pressure)
 Heterogeneous Nucleation (all above; nucleation sites-cascades, precipitates, bubbles, dislocations)
 Bubble Nucleation (helium diffusivity; trapping; resolutioning; small bubble mobility and driving force)
 Critical Bubbles (He compressibility; surface energy; bubble chemistry; defect fluxes)
 Solute Segregation (see phase instabilities below)
 Precipitate Dissolution (cascade effects)
 Coprecipitation of He, V, I and SA Extended Defect Complexes

Table 5. Continued

E. GROWTH MECHANISMS

Sinks (sink ratios; effective bias factors sink annihilation fractions)

Emission Kinetics (sink chemistry, stress and gas pressure; dislocation interactions and cavity dislocation networks, dislocation evolution, MC evolution)

F. PHASE INSTABILITIES/SEGREGATION

Enhanced Diffusion (vacancy concentrations)

Thermal Instabilities/Segregation

Disorder and Recoil Dissolution (sputtering disorder parameters)

Chemical Vacancies (misfit and defect parameters)

Diffusional Instabilities and Sinkless Segregation

Cascade Microsegregation (cascade physics)

Cascade Amorphization Segregation (partial diffusion coefficients, transport efficiencies, sink structure, solubility limits)

Defect-Precipitate Interactions (dislocation cutting, local sink effects)

Stress Effects

G. ATYPICAL PARAMETERS AND CONDITIONS

Pulsed-Stresses, Temperatures and Fluxes

Near Surfaces; Time Dependent Contamination

Foil Stress State; Damage Gradients

Self-Ion Injection

Simulation of Neutron Irradiation with Ion Beams

Neutron irradiation resistance is one of the most important problems in the development of structural materials for future nuclear reactors. To get the required data, one might perform irradiation experiments with high energy neutrons from such neutron sources as the High Flux Isotope Reactor (HFIR) [158], Rotating Target Neutron Source II (RTNS-II) [158], Fusion Materials Test Facility (FMTF) [158,159], Experimental Breeder Reactor II (EBR-II), and the Fast Flux Tests Facility (FFTF) [10,15] (Tables 1 and 2). But it may not be practical to test with these neutron sources from the point of view of cost, time required, control of temperature, availability of the facilities and handling of the specimens. An alternative is to use high-energy charged particle bombardments [32,33,79,157,158,160,161].

Neutron radiation damage is primarily induced by collisions and nuclear transmutations. Instead of neutrons, electrons or ions can be used to produce similar collision damage. Ion-bombardment facilities can produce displacement concentrations equivalent to LMFBR development goal levels of about 100 dpa (Table 2) in one day, as compared to five years in EBR-II and two years in FFTF [158]. Charged particle bombardments also have the advantage of avoiding problems associated with induced radioactivity. High Voltage Electron Microscopes (HVEM) are used for fundamental radiation damage studies. The radiation damage microstructure can be evaluated for low fluence. The information obtained is useful in testing the validity of theoretical models.

With heavy ions bombardments, high energy primary knock-ons are

generated, which produce displacement cascades. To eliminate complications arising from the introduction of a second element, it is preferable to use bombarding ions of the same species as already present in the target materials. The ion energy should be at least several MeV, so as to deposit damage at least one micron below the incident surface. Three further variables are particularly important. The first variable is the effect of inert gas atoms, particularly He, produced during irradiation. Heavy ion irradiation experiments without He, with He pre-injection and with continuous injection of He ions are carried out to investigate the role of helium on void nucleation and growth. The second variable is the influence of stress during irradiation. The third variable is the effect of pulsed irradiation on the damage structure. Damage structures under different number of pulses, pulse times, and hold times are examined and used to test the validity of existing rate theory models [150].

The use of electron or charged particle bombardments has several problems, such as the limitation in the damage area and volume, the strong depth dependence of the damage and the difficulty in correlating the data obtained from the particle bombardment to the fast neutron irradiation case [162]. Nevertheless, dual beams of nickel (or iron) and helium ions are widely used to simulate the fast breeder and fusion reactor irradiation conditions in the study of swelling in stainless steel. But, it is difficult to correlate the results with those expected upon neutron irradiation [91]. Correlation problems arise from the dose and temperature dependence [163,164], microstructure [133,144,163,165-

167], effects of constituents, and influence of prior cold working. Garner et al. [168], and Farrell [112] compared the high fluence swelling behavior of neutron, electron and ion-beam bombarded stainless steel. The peak swelling temperature is influenced by the physical properties of the bombarding particles, the chemical composition [139,167], stress state, helium injection mode [150,168] and transmutations [139].

In thermal reactors, helium atoms are produced through (n,α) reactions with ^{10}B , ^6Li , ^{14}N , and ^{58}Ni . The helium production is strongly dependent on the (n,α) cross section and the neutron spectrum. For fast neutrons, most metals have cross sections with threshold energies between 1 to 5 MeV. In stainless steel, $\text{Ni}^{58}(n,\gamma)\text{Ni}^{59}(n,\alpha)\text{Fe}^{56}$ is the most important helium generating reaction. To assess the relative importance of transmutation and displacement effects, a ratio of the helium concentration to the displacement concentration, in units of appm He/dpa, is widely used. Gabriel, Bishop and Wiffen [108] calculated this ratio for important reactor structural materials in various reactor environments (Table 4) [108].

The depth dependence of the ion radiation damage is measured using transmission electron microscopy (TEM) or calculated theoretically using the E-DEP-1 [169] code recommended by ASTM E-521 [79]. Farrell, Packan and Houston [170] and Whitley et al. [171] measured the depth dependence of the damage in pure nickel irradiated with 4 MeV Ni^{++} and 0.4 MeV He^+ ions, and they compared the measured and calculated results (Fig. 13) [170]. As input data, 40 eV for the effective threshold displacement energy, T_d , and 0.8 for the atomic interaction correlation factor

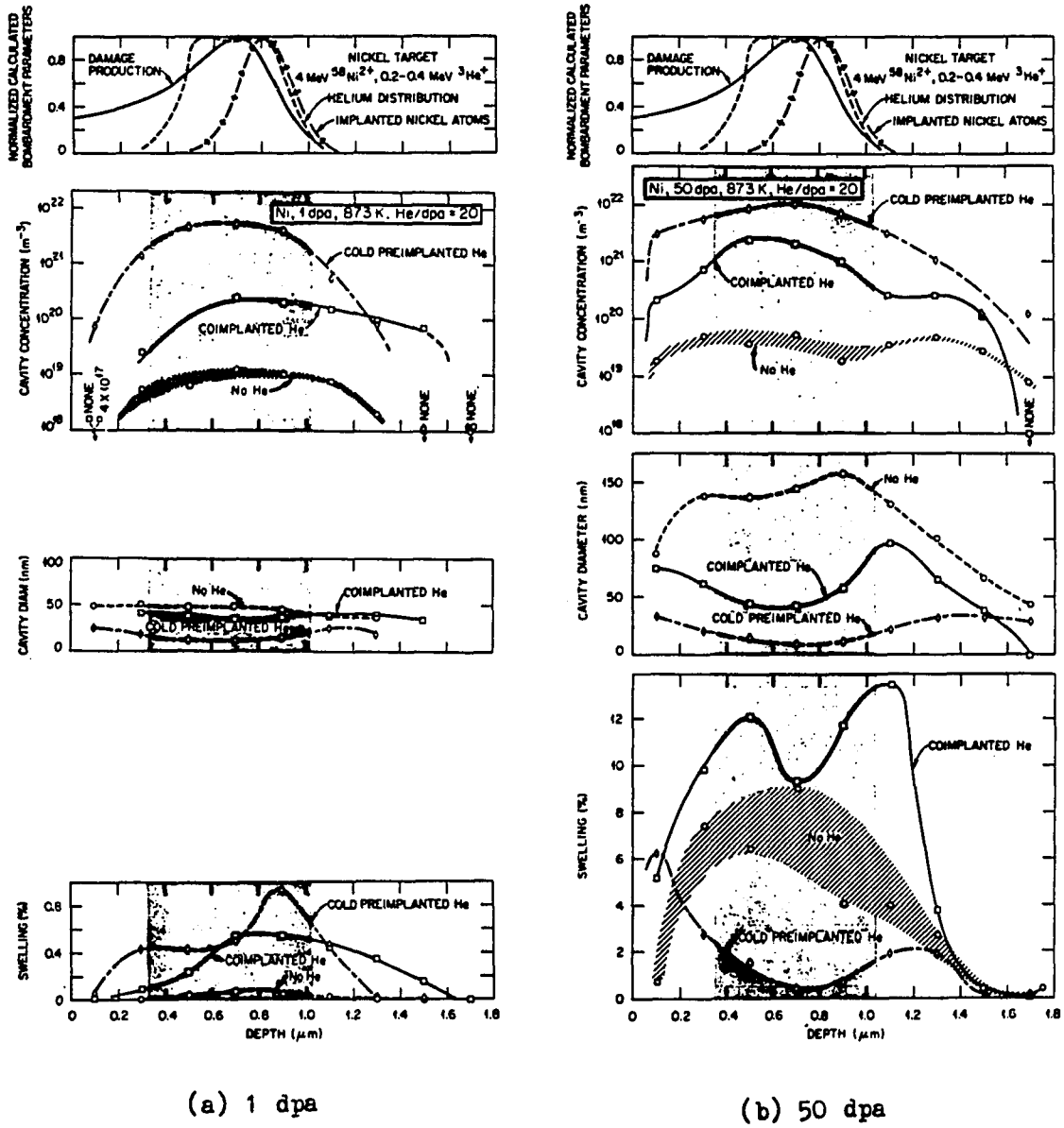
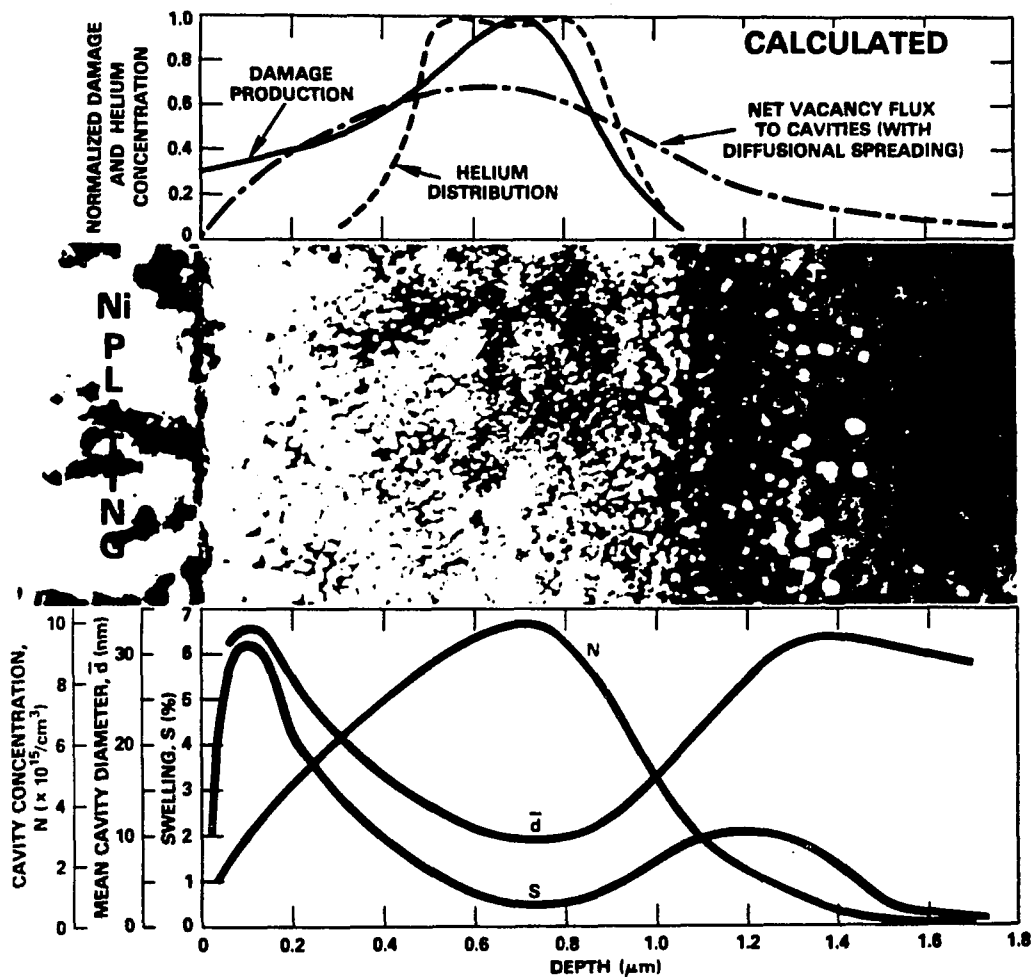


Fig. 13. Cavity-depth data measured for nominal (a) 1 dpa and (b) 50 dpa heavy ion peak doses [170]

were used for stainless steel.

Packan [172] showed the damage depth profile for calculated and experimental results (Fig. 14). Bullough and Hayns [173] calculated the damage depth dependence on ion energy and irradiation temperature (Figs. 15 and 16). Lee, Mansur and Yoo [174] performed ion bombardments on 316 stainless steel samples that were preconditioned by neutron irradiation at 450 and 584 °C. The ratio of the step height to void volume at the peak damage depth was greater for the samples that were neutron irradiated at 584 °C (Fig. 17). Mansur and Yoo [153] suggested certain advances in the theory of void swelling. These include effects due to locally inhomogeneous defect production, mobile helium, and the spacial variation in swelling during charged particle bombardment. Figs. 18 and 19 show a comparison of calculated results with and without the assumption of these advances in the theory.

The chief method for measuring swelling is by TEM. An indirect method, however, is by measuring the step height induced by the swelling and converting to swelling using the ratio of step height to swelling. Johnston et al. [17] measured swelling in Fe-Cr-Ni alloys with these two methods, and suggested that 1% swelling at the peak damage region is equivalent to a surface step of approximately 60Å. At high doses, the swelling appears to increase linearly with increasing fluence [175,176], as shown in Fig. 20 for neutron irradiation [89] and Figs. 21 and 22 for ion bombardment [175].



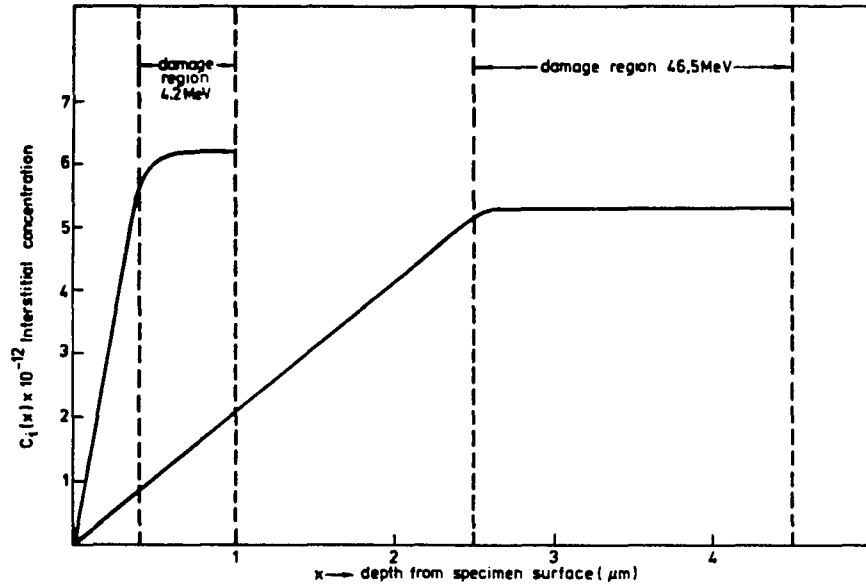
PROBLEM: When heavy ion bombardment is used to rapidly simulate neutron damage, a strong variation of damage arises along the path of the ions within a few microns of the bombarded surface. The challenge is to reveal the microstructural details of the full damage-depth profile. The case of interest was pure nickel, implanted with 1000 atomic ppm He at depths shown in the top figure, and then bombarded at 600°C with 4 MeV Ni^{++} ions to a damage level of 50 displacements per atom.

SOLUTION: Make a sandwich of the bombarded layer and prepare cross-sections for study. The bombarded specimen was cleaned in acetone and, while still wet, immersed in Mohler's ≈ 5 nickel plating bath at 45°C and 25 mA initial plating current. After depositing 2 mm Ni plate, the composite product was sectioned parallel to the ion beam direction and electrothinned using 5% perchloric acid in ethanol at 5°C. Examination was carried out in a 1 MeV electron microscope to minimize image distortions from the ferromagnetic specimen material.

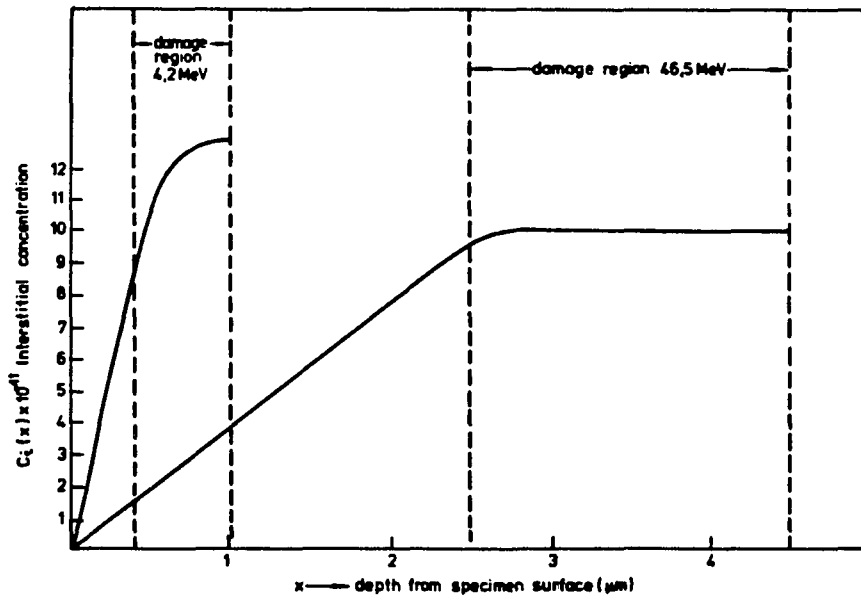
RESULTS: A thin area just at the electroplate/bombarded surface interface yielded the complete damage profile shown above. A diffusion-induced extension of swelling beyond the region of primary damage production is evident. The pronounced effect of helium in stimulating the nucleation of cavities is clearly seen, although swelling is actually diminished due to the reduced cavity size.

CLASS: Electron Microscopy-
Transmission

Fig. 14. Depth profile of swelling in ion-bombarded nickel [172]



(a) Irradiated at 525°C



(b) Irradiated at 700°C

Fig. 15. Fractional interstitial concentration profiles for 4.2 MeV Fe^{++} (at 35 dpa) and 46.5 MeV Ni^{6+} (at 40 dpa) ion irradiations at (a) 525°C and (b) 700°C [173]

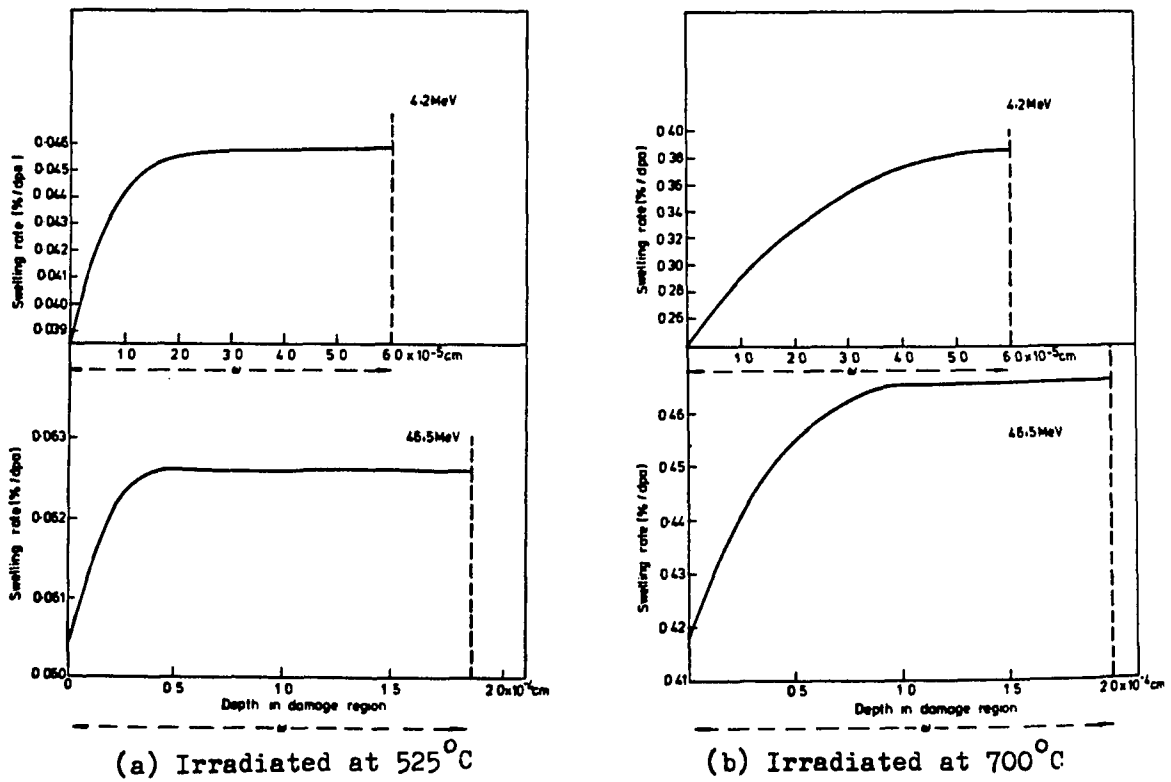
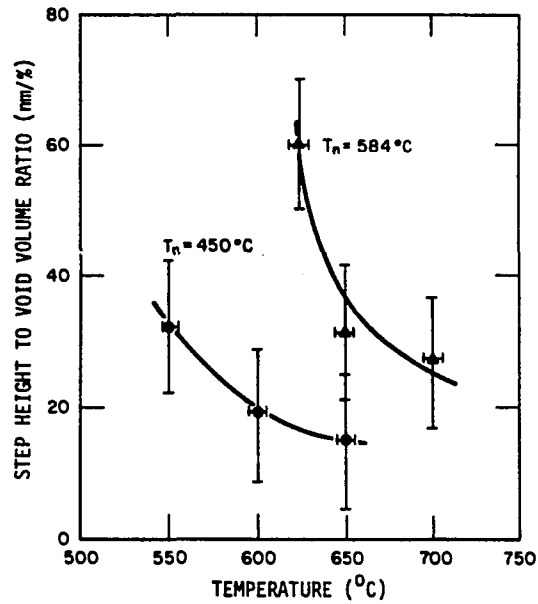
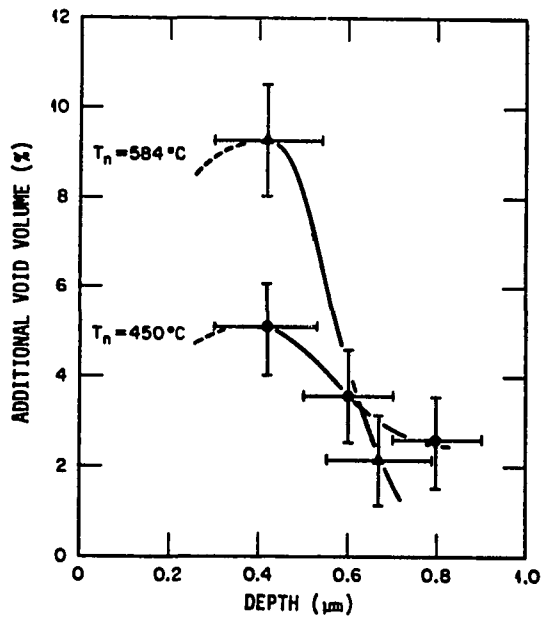


Fig. 16. Calculated swelling rate as a function of depth in the damage region for 4.2 MeV Fe ions (at 35 dpa) and 46.5 MeV Ni ions (at 40 dpa) irradiations at (a) 525°C and (b) 700°C. These results are for a constant dislocation density of 10^9 cm^{-2} . Dotted lines denote the limit of the damaged region [173]



(a)



(b)

Fig. 17. (a) The ratio of step height to measured void volume and (b) the measured additional void volume with depth for SA316 stainless steel neutron irradiated to 8×10^{26} n/m² at 450 and 584°C (T_n) and ion irradiated to 60 dpa at 600 and 625°C [174]

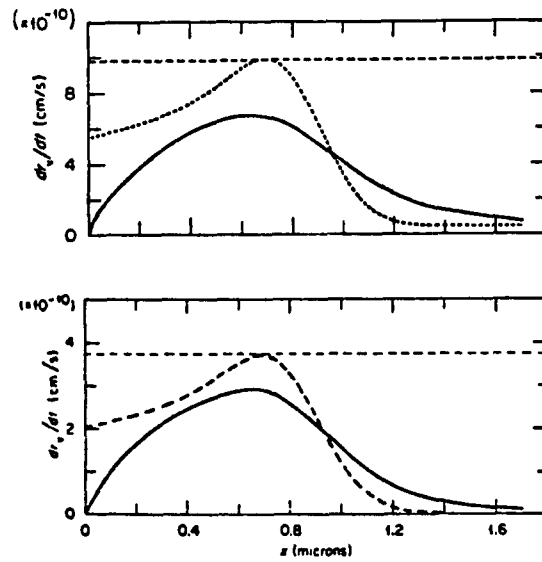


Fig. 18. Calculation of the void growth rate illustrating diffusional spreading. Dashed horizontal line is the infinite medium void growth rate. Dotted curved line is the void growth rate profile obtained from the point defect generation profile when diffusion is ignored. The solid curve is calculated using the spatially dependent theory. The upper part shows results for 650°C and the lower part shows results for 550°C [153]

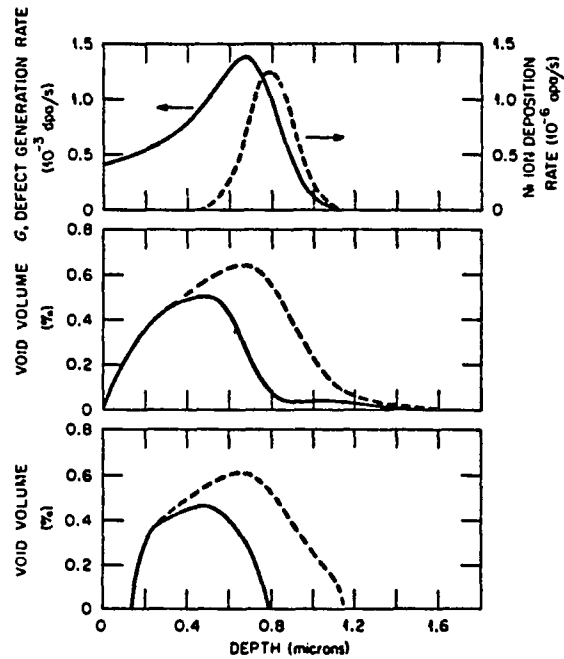


Fig. 19. The reduction of void volume caused by injected interstitials. The dashed curves show the void volume without injected interstitials. The solid curves show the void volume when injected interstitials are included. The upper part shows point defect generation and ion deposition profiles, the middle part shows the void volume at 600°C, and the bottom part shows the void volume at 700°C [153]

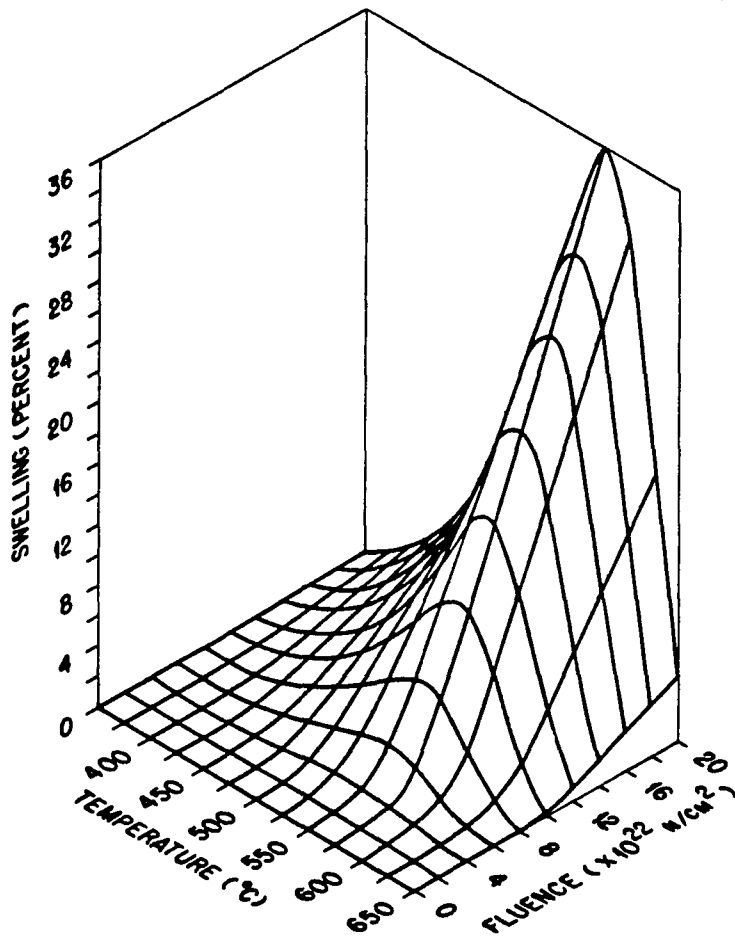


Fig. 20. Smoothed representation of experimental data on swelling of 316 stainless steel irradiated in EBR-II, as a function of temperature and dose, in a plot developed by Stiegler from equations in Ref. 76 [89]

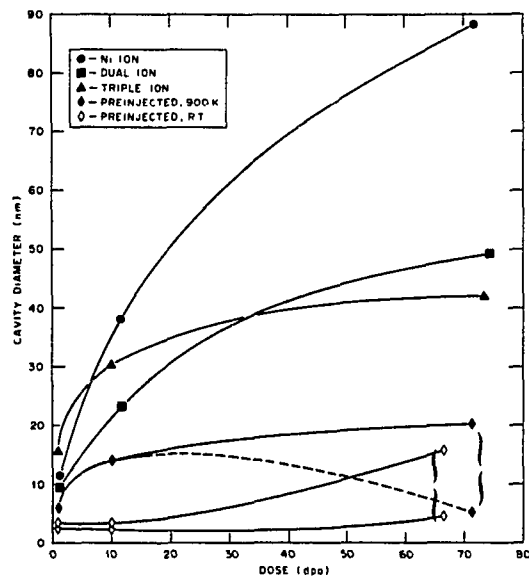


Fig. 21. Dependence of swelling upon dose for the gas injection methods studied [175]

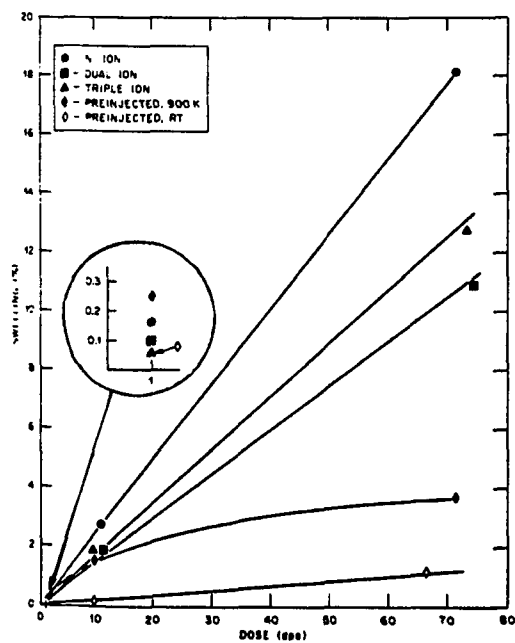


Fig. 22. Diameter of a cavity of mean volume as a function of dose. Certain preinjection conditions give rise to bimodal size distributions, indicated here by pairs of data points [175]

EXPERIMENTAL PROCEDURES AND RESULTS

Alloy Preparation

As a starting material for the specimens used in this experiment, austenitic Fe-Ni-Cr alloy of composition Fe-25.7%-8.7% Cr (Table 3) was supplied in the form of 1 5/16" diameter bar stock by the Hanford Engineering Development Laboratory (HEDL). The rare-earth additions, yttrium (Table 6), lanthanum (Table 7) and cerium (Table 8) were supplied by Ames Laboratory, USDOE.

The alloy bar was sliced into approximately 1.1 cm long lengths. The sliced lengths were cleaned thoroughly with a solution of 80% H₂O, 10% HNO₃, 2% HF and 1% HCl to remove stain during the saw cutting and well cleaned ultrasonically with methanol and acetone. They were weighed and found to be approximately 80 grams. Relating to the weight of slices, the desired quantities of rare-earth yttrium, lanthanum and cerium were determined and the alloys were prepared to contain 0.05, 0.1, 0.5 and 1 weight percent of rare-earth element. The alloys were arc-melted and cast into a finger shape of dimensions of approximately 3.8" long x 0.8" wide x 0.4" thick (Fig. 23). A total of thirteen alloy fingers (undoped, and 0.05, 0.1, 0.5 and 1 weight percent of yttrium, lanthanum, and cerium doped alloys) were prepared. The fingers were sliced as shown in Fig. 23 and ultrasonically cleaned with acetone and a solution of 80% H₂O, 10% HNO₃, 2% HF and 1% HCl. They were given a homogenizing anneal in the NRC 3500 furnace for 16 hours at 1150°C at a vacuum of less than 5×10^{-6} torr. Sections #1 and #9 of each

Table 6. Spark source mass spectrometric analysis of the yttrium

Element	Composition in wt.ppm	Element	Composition in wt.ppm
Ag	<.03	Na	.09
Al	.4	Nb	<1
As	<.02	Nd	.3
Au	<.08	Ni	.8
B	<5	Os	<.5
Ba	<.03	P	<.07
Be	<.05	Pb	<.07
Bi	<.04	Pd	<.2
Br	<2	Pr	1.1
Ca	<.03	Pt	<.3
Cd	<.01	Rb	<.02
Ce	4	Re	<.4
Cl	1	Rh	<.08
Co	<.04	Ru	<.1
Cr	<.04	S	.1
Cs	<.03	Sb	<.009
Cu	1.3	Sc	<.06
Dy	<.4	Se	<.01
Er	<.6	Si	2.4
Eu	<.1	Sm	<.3
Fe	8.3	Sn	<.03
Ga	<.02	Sr	<.02
Gd	<3	Ta	3000
Ge	<.04	Tb	1.5
Hg	<.07	Te	<.01
Hf	<1	Th	<.5
Ho	<.2	Ti	<.2
I	<.03	Tl	<.05
In	<.01	Tm	<.1
Ir	<.2	U	<.2
K	<.03	V	<.05
La	.30	W	<1
Li	<.1	Y	Bal.
Lu	<.3	Yb	<.3
Mg	<.02	Zn	<.02
Mn	<.02	Zr	<2
Mo	<1		

Table 7. Spark source mass spectrometric analysis of the lanthanum

Element	Composition in wt.ppm	Element	Composition in wt.ppm
Ag	<.03	Na	.5
Al	5.0	Nb	<10
As	<.03	Nd	2.2
Au	<.05	Ni	<1
B	.1	Os	<.5
Ba	<3	P	<.2
Be	<.005	Pb	.1
Bi	<.03	Pd	<.1
Br	<.03	Pr	1.0
Ca	<.3	Pt	.60
Cd	<.04	Rb	<.007
Ce	10	Re	<.4
Cl	4	Rh	<.06
Co	<.03	Ru	<.2
Cr	2.0	S	<1
Cs	<20	Sb	<.04
Cu	7.0	Sc	<.09
Dy	<.5	Se	<.05
Er	<.4	Si	<.3
Eu	<.1	Sm	<.1
Fe	80	Sn	<.09
Ga	<.1	Sr	<.02
Gd	15	Ta	<.07
Ge	.16	Tb	1.0
Hg	<.06	Te	<.05
Hf	<.6	Th	<.4
Ho	<.2	Ti	<.3
I	<.03	Tl	<.04
In	<.02	Tm	<.1
Ir	<.2	U	<.1
K	<1	V	<.1
La	Bal.	W	<1
Li	.02	Y	24
Lu	<.2	Yb	<.08
Mg	<1	Zn	<.07
Mn	.20	Zr	<.2
Mo	<.5		

Table 8. Spark source mass spectrometric analysis of the cerium

Element	Composition in wt.ppm	Element	Composition in wt.ppm
Ag	<.02	Na	<.8
Al	7.0	Nb	<10
As	<.03	Nd	2.0
Au	.30	Ni	2.0
B	.1	Os	.97
Ba	<1	P	.2
Be	<.002	Pb	<.3
Bi	<.03	Pd	<.09
Br	<.03	Pr	4.0
Ca	<.7	Pt	100
Cd	<.05	Rb	<.007
Ce	Bal.	Re	<1
Cl	9	Rh	.58
Co	<.05	Ru	<.2
Cr	1.0	S	.5
Cs	<.01	Sb	<.04
Cu	2.8	Sc	.50
Dy	<.3	Se	<.09
Er	<.5	Si	8.0
Eu	<.08	Sm	<.7
Fe	33	Sn	<.1
Ga	<70	Sr	<.02
Gd	<9	Ta	15
Ge	<.09	Tb	1.0
Hg	<.06	Te	<.05
Hf	<.5	Th	<.3
Ho	.80	Ti	<.2
I	<.03	Tl	.40
In	<.02	Tm	<.1
Ir	<.4	U	<.2
K	<.07	V	<.05
La	17	W	<2
Li	<.001	Y	2.8
Lu	<.3	Yb	<.2
Mg	<.5	Zn	.054
Mn	1	Zr	<.3
Mo	<.4		

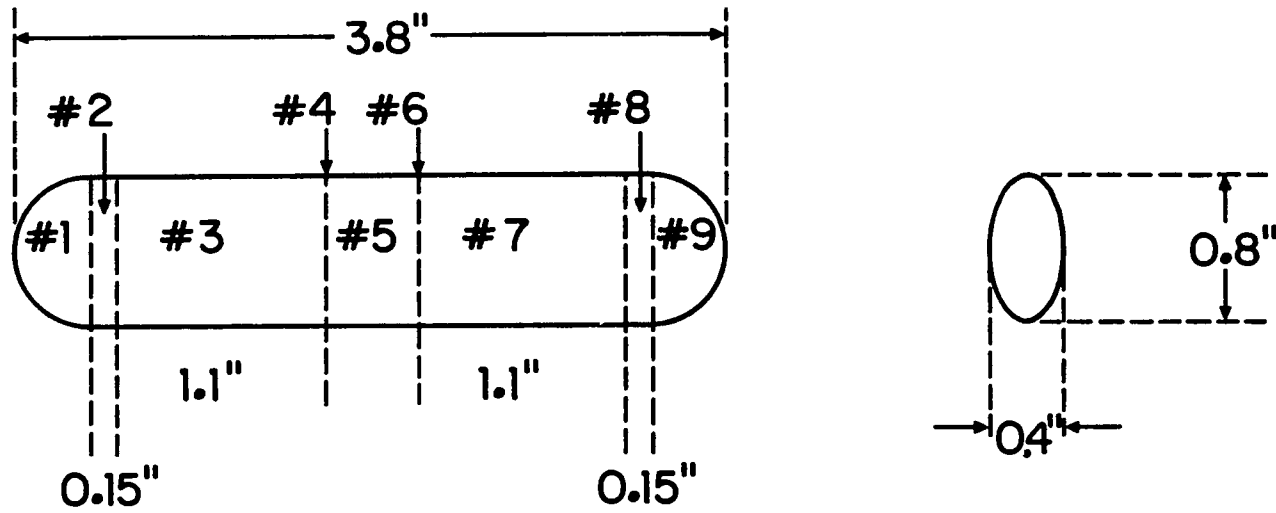


Fig. 23. Typical slicing schedule for the rare-earth doped and undoped AL alloy fingers (all dimensions are approximate)

finger alloy were stored as spares. Sections #2 and #8 were used for metallography, second phase particle size analysis and hardness tests. A part of sections #3 and #7 was used for lattice parameter measurement. A part of sections #3 and #7 was also used for chemical analysis using a wet chemical quantitative analysis method to make sure of the concentrations of rare-earth additions in the alloys after arc-melting, casting and annealing (Table 9). The other parts of sections #3 and #7 and section #5 were used for the ion bombardment experiments. The bombarded specimens were of two types: stacked-edge-on specimens and transmission electron microscope (TEM) disk-shaped specimens.

Structure Analysis and Lattice Parameter Measurements

Sample preparation

A part of sections #3 and #7 of the annealed finger alloy (Fig. 23) was cut into powder as fine as possible with a surface cutting machine. The metallic powder was screened manually to get the finer particles. The powder was ultrasonically cleaned with acetone for 15 minutes and methanol for 20 minutes and well dried. It was put in tantalum cans, numbered to identify each sample, and the cans were put in a bigger can and loaded in the NRC 3500 high vacuum furnace. The powder was annealed for 2 hours at 700°C and slowly cooled. The vacuum during annealing was 5×10^{-6} torr or better.

Structure analysis

The prepared sample powder was dispersed on the surface of a glass plate (3/64" thick x 1 13/16" long x 1 1/8" wide). The glass plates with

Table 9. Chemical analysis of as-homogenized doped alloys

Alloy	Doped Rare-Earth	Nominal Composition(wt%)	Measured Composition(wt%)		Averages (wt%)
AL-1 ^a					
AL-2	yttrium	0.05	0.056	0.056	0.056
AL-3	yttrium	0.10	0.091	0.094	0.093
AL-4	yttrium	0.50	0.47	0.46	0.47
AL-5	yttrium	1.00	0.98		0.98
AL-6	lanthanum	0.05	0.054		0.054
AL-7	lanthanum	0.10	0.10		0.10
AL-8	lanthanum	0.50	0.53		0.53
AL-9	lanthanum	1.00	0.90		0.90
AL-10	cerium	0.05	0.05		0.05
AL-11	cerium	0.10	0.10	0.11	0.105
AL-12	cerium	0.50	0.48	0.50	0.49
AL-13	cerium	1.00	0.99	1.02	1.01

^aArc-melted and annealed for 2 hours at 1200°C.

sample powder were loaded on the sample holder of the Picker powder x-ray diffractometer. Peak positions and relative intensities of each peak were determined from the diffractometer chart traces. The samples were assumed to be face-centered cubic structure, which is the characteristic structure of the austenitic stainless steel. For the standardization of the 2θ angle, lithium fluoride was used. It has the same crystal structure as the sample alloy and its peak positions are well known. The lattice parameter and peak positions of the lithium fluoride were obtained from the "1980 Powder Diffraction File, Inorganic Phases" [177]. Stanolind Petroleum (Snow White, U.S.P. ALBA, Standard Oil Company) was used to immobilize the combined sample alloy powder and lithium fluoride powder together on the glass plate and to avoid segregation from each other because of the vibration of the diffractometer during the measurement scanning. The Miller indices of the sample peaks were decided according to the diffraction 2θ angles and their relative intensities compared with the peaks of lithium fluoride (Figs. 24-27). The target of the x-ray generator was molybdenum, for which the characteristic wave lengths are as follows [178]:

$$\lambda_{K\alpha_2} = 0.713590 \text{ \AA}$$

$$\lambda_{K\alpha_1} = 0.709300 \text{ \AA}$$

$$\lambda_{K\beta_2} = 0.632872 \text{ \AA}$$

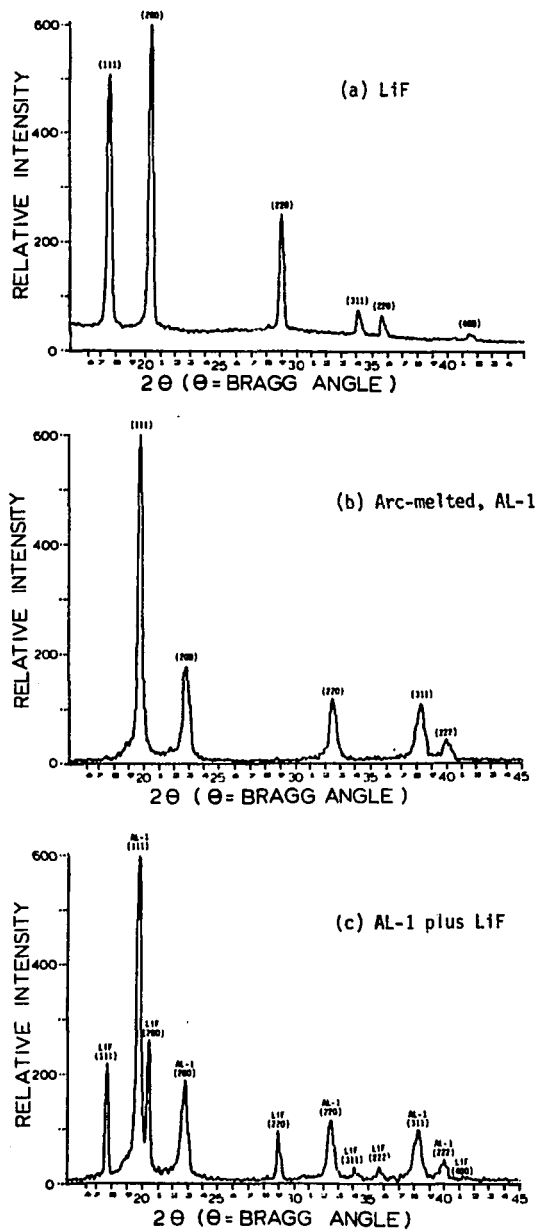


Fig. 24. Relative intensity versus 2θ for various X-ray diffraction peaks, as indicated for (a) AL-1, (b) LiF, and (c) AL-1 plus LiF

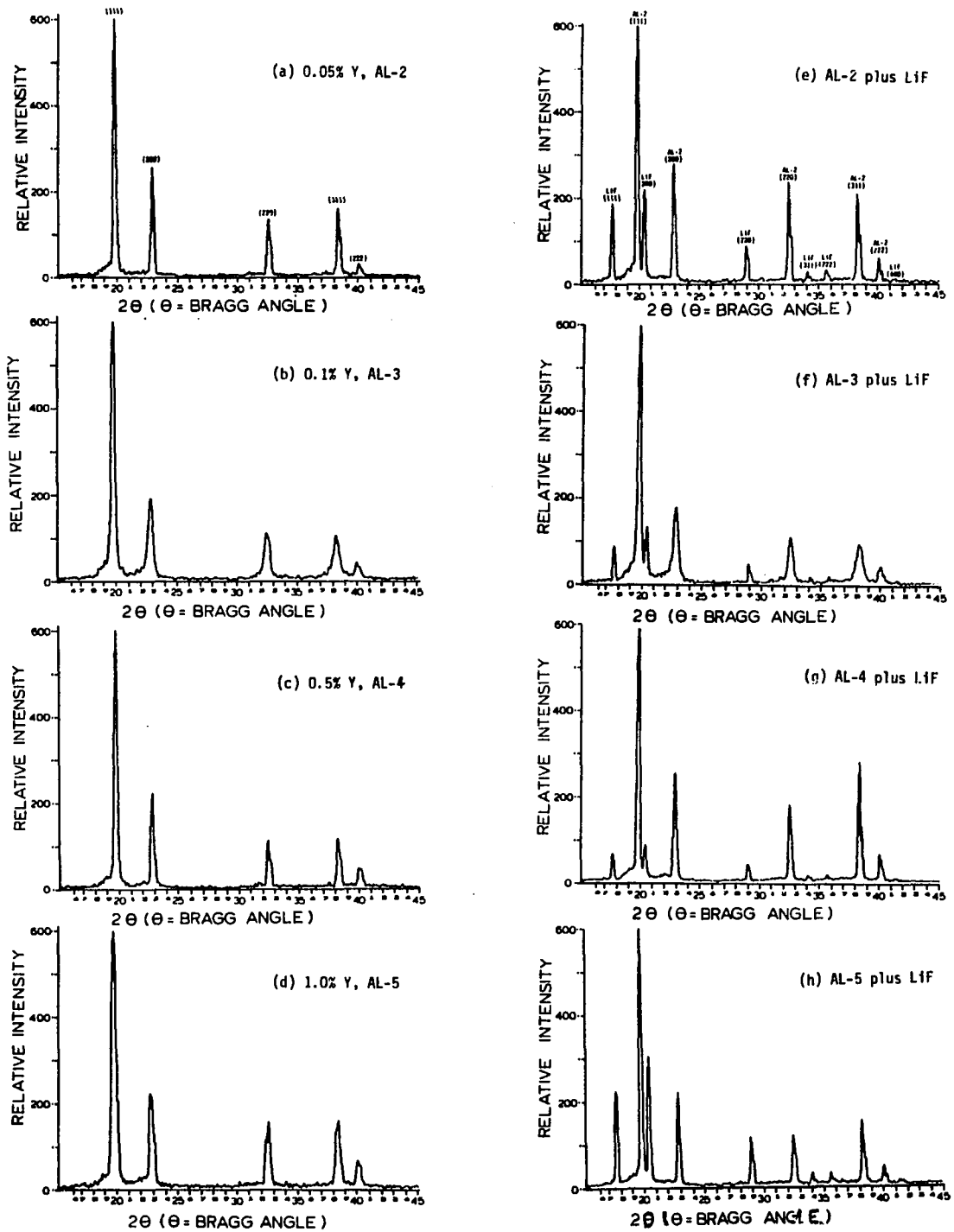


Fig. 25. Relative intensity versus 2θ for various X-ray diffraction peaks, as indicated for (a) 0.05% (AL-2), (b) 0.1% (AL-3), (c) 0.5% (AL-4), and (d) 1.0% (AL-5) yttrium-doped alloys and (e), (f), (g) and (h), alloy plus LiF

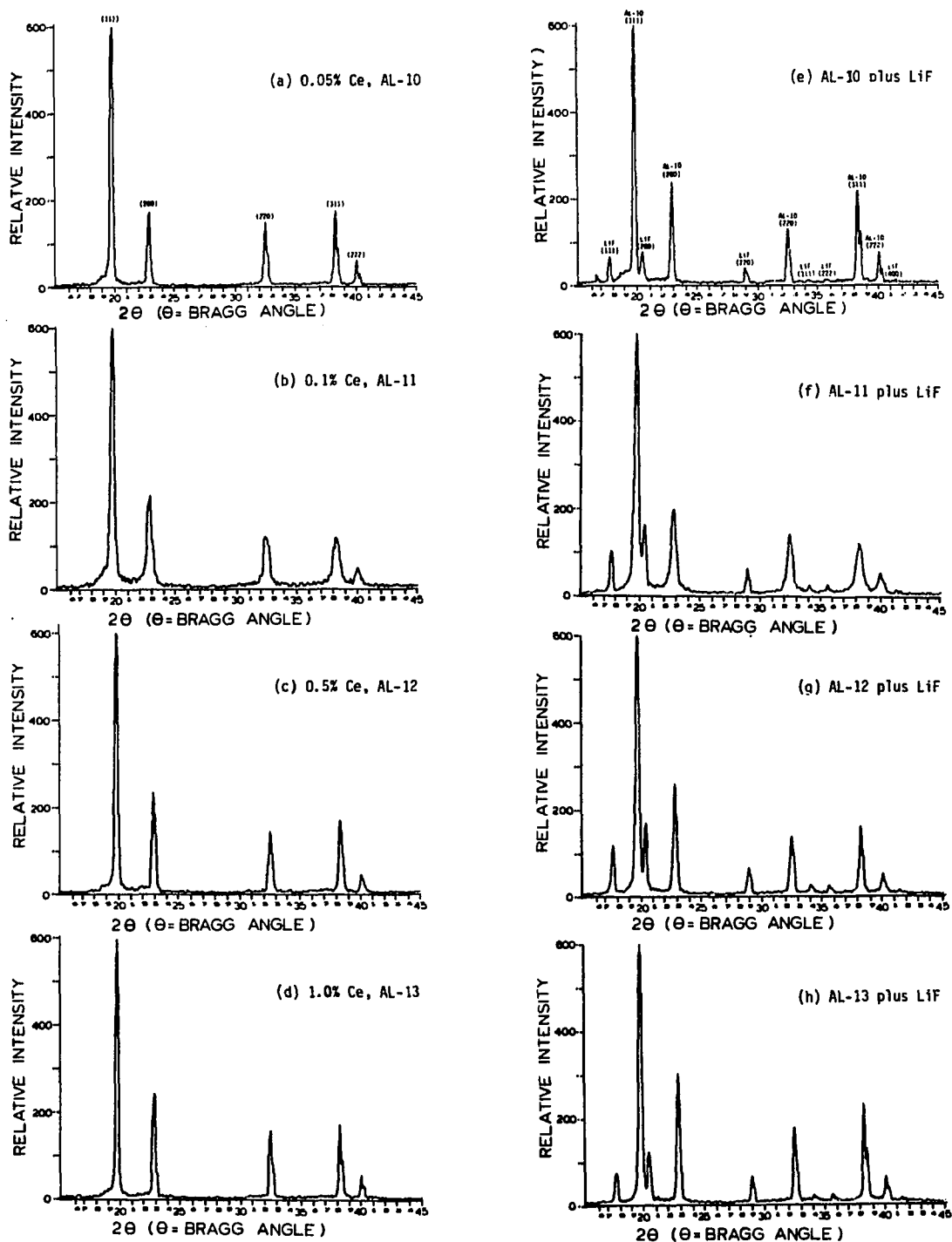


Fig. 26. Relative intensity versus 2θ for various X-ray diffraction peaks, as indicated for (a) 0.05% (AL-6), (b) 0.1% (AL-7), (c) 0.5% (AL-8), and (d) 1.0% (AL-9) lanthanum-doped alloys and (e), (f), (g) and (h), alloy plus LiF

$$\lambda_{K\beta_1} = 0.632288 \text{ \AA}$$

The filtering material was zirconium.

The intensity of each 2θ angle was measured by a scintillation counter and recorded by computer. The range of the scanned diffraction angle, 2θ , was from 17.30° to 53° . The step of each measurement of 2θ was 0.02° . The time of measurement at each diffraction angle 2θ was 5 seconds. The peaks of lithium fluoride and sample were scanned together and separated into two groups: peaks for lithium fluoride and peaks for the sample. The computer program printed out the following information: (1) 2θ values, (2) diffracted x-ray beam intensity at the 2θ angles, and (3) the mean of the intensities for $(2\theta)_{i-1}$, $(2\theta)_i$, $(2\theta)_{i+1}$ in order to give smoothed intensity values. 10 to 20 smoothed 2θ values around each peak were taken to decide the peak position (2θ angles) using the center of inertia method, as follows:

$$2\theta = \frac{\sum I_i^2 (2\theta)_i}{\sum I_i^2} \quad (5)$$

where $2\theta_i$ = measured i 'th 2θ angle around the peak

I_i = the mean intensity of 3 points, $2\theta_{i-1}$, $2\theta_i$, $2\theta_{i+1}$
at i 'th 2θ angle.

A least-squares method was applied to get a correlation equation between measured 2θ angles for the lithium fluoride peaks, as shown in the following equation:

$$(2H)_j = [AX(2\theta')_j] + B \quad (6)$$

where

$$A = \frac{N \times \sum [(2\theta)_i \times (2T)_i] - \sum (2\theta)_i \times \sum (2T)_i}{N \times \sum (2\theta)_i^2 - [\sum (2\theta)_i]^2} \quad (7)$$

$$B = \frac{\sum (2\theta)_i^2 \times \sum (2T)_i - \sum (2\theta)_i \times \sum [(2\theta)_i \times (2T)_i]}{N \times \sum (2\theta)_i^2 - [\sum (2\theta)_i]^2} \quad (8)$$

$(2\theta)_i$ = measured 2θ angle of i 'th peak of LiF

$(2T)_i$ = recommended standard 2θ angle of i 'th peak of LiF

N = number of peaks considered

$(2\theta')_j$ = measured 2θ angle of j 'th peak of the alloys

$(2H)_j$ = modified 2θ angle of j 'th peak of the alloys

Based on the modified 2θ angles of the alloys, the Miller indices were decided as (111), (200), (220), (311), (222) and (400), as shown in the Figs. 24-27.

Lattice parameter measurement

The annealed powder samples were screened with U.S. standard screen, size number 200, to get fine powder. The refined powder was sealed into 0.3 mm diameter glass capillaries. Using a Debye-Scherrer camera, the diffracted pattern was photographed for 12 hours. From the exposed film, 2θ angles were measured. Cobalt radiation was used for which the characteristic wave lengths are as follows [178]:

$$\lambda_{K\alpha_2} = 1.792850 \text{ \AA}$$

$$\begin{aligned}\lambda_{K\alpha_1} &= 1.788965 \text{ \AA} \\ \lambda_{K\beta_2} &= 1.790260 \text{ \AA} \\ \lambda_{K\beta_1} &= 1.62079 \text{ \AA}\end{aligned}$$

The range of the measured angles of 2θ was from 45° to 130° . The interplanar spacings, d , were calculated using the simplified equation, $d = 2d \sin\theta$ and the observed 2θ angles. Since the crystal structure is FCC, the value of the lattice constants corresponding to each diffraction angle 2θ was calculated from the following equation:

$$a_0^2 = d^2(h^2 + k^2 + l^2) = d^2Q \quad (9)$$

To reduce experimental error, an approximate value of a_0 was obtained using an extrapolation procedure in which the apparent a_0 was plotted versus the Nelson-Riley function [179]:

$$X = \frac{1}{2} \left(\frac{\cos^2\theta}{\sin\theta} + \frac{\cos^2\theta}{\theta} \right) \quad (10)$$

It was assumed that if the apparent lattice constants determined by each reflection are plotted versus Nelson-Riley function, an extrapolation to the zero of the function, or $2\theta = 180^\circ$, gives the most accurate value of a_0 . A least-square method was applied to get modified lattice parameters from the approximately calculated lattice parameters and the

value of the function X of eq. (10) corresponding to each diffraction angle, as shown in the following equation:

$$Y_i = A X_i + \bar{a} \quad (11)$$

where,

$$A = \frac{N \times \sum X_i a_i - \sum X_i \times \sum a_i}{N \times \sum X_i^2 - (\sum X_i)^2} \quad (12)$$

= slope of the modified function obtained by the least-square method

X_i = the value of the Nelson-Riley function corresponding to the i'th 2θ angle

a_i = apparent lattice parameter calculated using i'th diffraction angle, 2θ

N = number of 2θ angle considered.

Y = modified lattice parameter obtained from the least squares method and i'th diffraction angle, 2θ

$$\bar{a} = \frac{\sum X_i^2 \times \sum a_i - \sum X_i a_i \times \sum X_i}{N \sum X_i^2 - (\sum X_i)^2} \quad (13)$$

This value of \bar{a} is the lattice parameter corresponding to $2\theta = 180^\circ$ where the major errors disappear. The standard error of estimation, E, is calculated from the following equation:

$$E = \frac{1}{N} \sqrt{N \times \sum a_i^2 - (\sum a_i)^2 - \frac{N \times \sum X_i a_i - \sum X_i \times \sum a_i}{N \times \sum X_i^2 - (\sum X_i)^2}} \quad (14)$$

The results are summarized on Table 10 and shown in Fig. 28 for the yttrium-doped and undoped alloys, Fig. 29 for the lanthanum-doped and undoped alloys, and Fig. 30 for the cerium-doped and undoped alloys.

Hardness Tests

General

The hardness is generally conceived as a quality of matter having to do with solidity and firmness of outline and resistance to permanent indentation under static loads. Williams [180] states that hardness is a measure of the resistance to permanent deformation of the solid. Since the indentation process involves plastic deformation, some relationship between the hardness (DPH) and flow stress (γ) can be expected. Tabor [181] tried to establish a relationship between the ultimate tensile strength and hardness using Mayer's power relation for the ball hardness test as

$$P = ad^m \quad (15)$$

where P is load, d is the diameter of the impression, and a and m are constants. George et al. [182] estimated yield strength from hardness data. But, the relationship, Eq. (15), is not applicable to every material since P is a function of many variables. For example, Tate [183] showed the effect of surface condition on the apparent Vickers and Knoop hardness for several materials. Many attempts have been made to calculate the functional form for various indenter shapes to correlate

Table 10. Lattice parameters of rare-earth-doped and undoped AL alloys

Alloy	Composition	Lattice Parameter (\AA)	Standard error of estimation (\AA)
AL-0 ^a	as-received	3.5929	± 0.0007
AL-1 ^b	arc-melted	3.5920	± 0.0005
AL-2	AL + 0.05% Y	3.5915	± 0.0003
AL-3	AL + 0.1 % Y	3.5924	± 0.0007
AL-4	AL + 0.5 % Y	3.5929	± 0.0002
AL-5	AL + 1.0 % Y	3.5923	± 0.0005
AL-6	AL + 0.05% La	3.5917	± 0.0011
AL-7	AL + 0.1 % La	3.5922	± 0.0007
AL-8	AL + 0.5 % La	3.5906	± 0.0010
AL-9	AL + 1.0 % La	3.5929	± 0.0005
AL-10	AL + 0.05% Ce	3.5928	± 0.0004
AL-11	AL + 0.1 % Ce	3.5923	± 0.0007
AL-12	AL + 0.5 % Ce	3.5932	± 0.0003
AL-13	AL + 1.0 % Ce	3.5926	± 0.0010

^aAs-received and annealed for 1 hour at 950°C as bulk alloy and 2 hours at 700°C as powder.

^bArc-melted and annealed for 2 hours at 1200°C as bulk alloy and 2 hours at 700°C as powder.

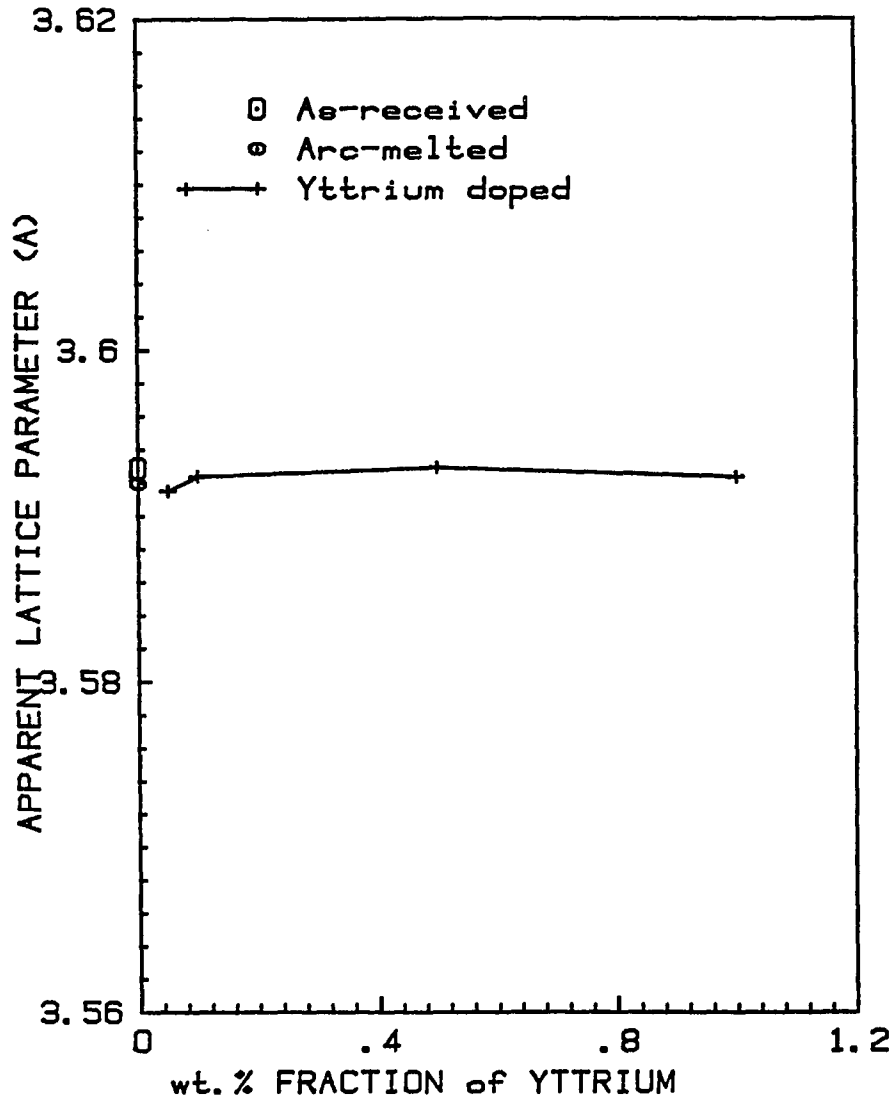


Fig. 28. Lattice parameters of the as-received (AL-0), arc-melted (AL-1), 0.05% (AL-2), 0.1% (AL-3), 0.5% (AL-4), and 1.0% (AL-5) yttrium-doped alloys

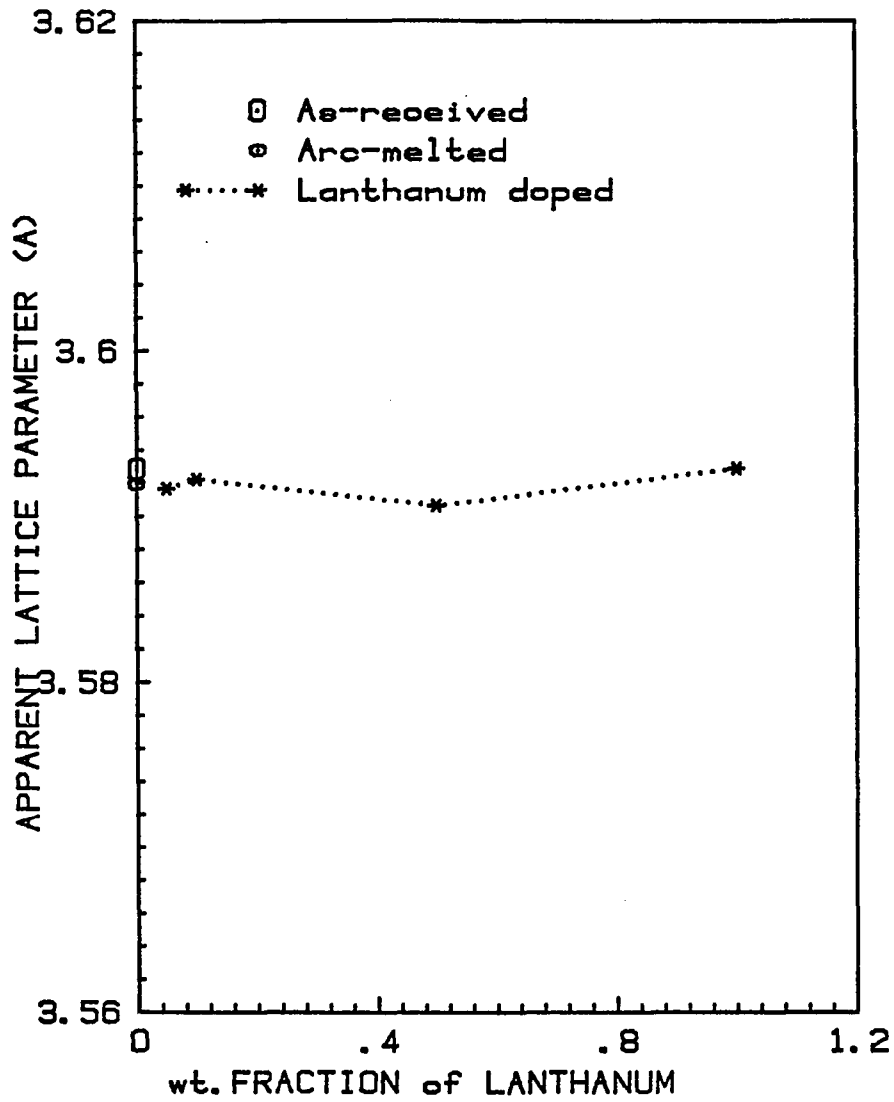


Fig. 29. Lattice parameters of the as-received (AL-0), arc-melted (AL-1), 0.05% (AL-6), 0.1% (AL-7), 0.5% (AL-8), and 1.0% (AL-9) lanthanum-doped alloys

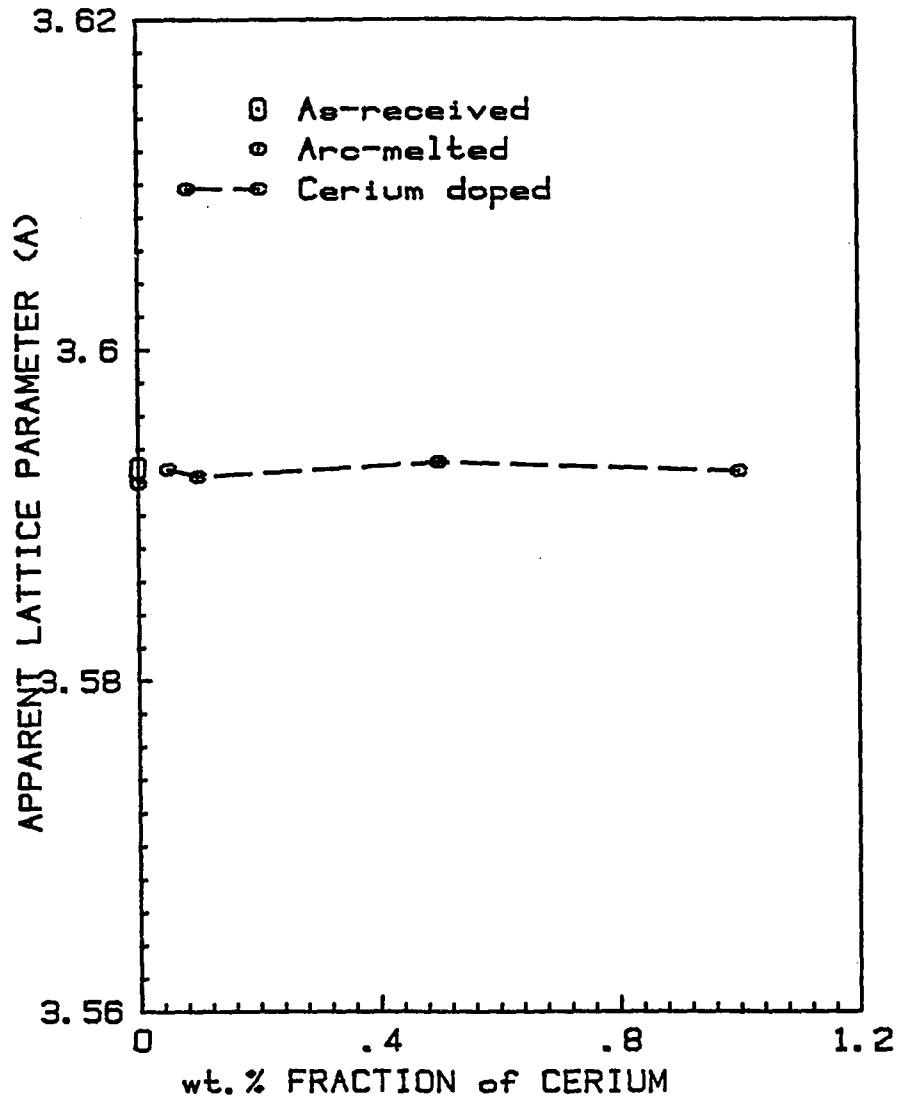


Fig. 30. Lattice parameters of the as-received (AL-0), arc-melted (AL-1), 0.05% (AL-10), 0.1% (AL-11), 0.5% (AL-12), and 1.0% (AL-13) cerium-doped alloys

the yield stress [180,182,184] and creep rate [185-187] with the hardness. Temperature dependence of hardness is also important from the point of view of application, but only empirical expressions are available in a limited temperature range on limited materials [188,189]. Many observations of microhardness on neutron irradiated materials at elevated temperature were done by Kamphouse et al. [190]. But, no experiments were done to establish a correlation between radiation fluence and hardness.

Some early work examined the region beneath the hardness indentation and found evidence of dynamic recrystallization, and Hill and Rowcliffe [191] tried to prove the physical process involved in the hardness test using microscopic examinations. Most of the evidence tends to show that the hardness test is complex, and the fundamental physics of hardness is not yet clearly understood. However, the hardness test is used because of the ease in specimen preparation and simplicity of measurement. A change in minor element concentration is not expected to cause a large change in mechanical properties. Similar materials may be graded and compared to each other on the basis of hardness. Also, the quality and uniformity of materials or products may be checked using hardness tests following various treatments such as forming, alloying, heat treatment or case-hardening. By establishing a correlation between hardness and some other desired property, simple hardness values may serve to indicate rapidly the value and the uniformity of the property.

Although a number of testing methods relating to the shape of

indenter, applied load and dynamic or static conditions [192-195] are available, the Vickers hardness test was used for this study. A Tukon tester was employed. This tester has a 136° Vickers diamond pyramid indenter, consisting of a square pyramid with 136° between faces. A load of 1 kg was used. The indenter under load produces a permanent deformation in the shape of a square inverted pyramid on the surface of the specimen. The diagonals of the impression are measured in filar units from the microscope eyepiece. The filar units are converted into millimeters. The diamond pyramid hardness (DPH) values were calculated as the load per unit of surface contact in kilograms per square millimeter.

Hardness tests

The same specimens of rectangular shape (0.1" thick, 0.2" wide and 0.3" long) used for metallography and second phase particle size analysis were used for the hardness tests. After polishing, the specimens were demounted from the bakelite mounts and annealed for 2 hours at 1200°C in the NRC 3500 furnace at a vacuum below 5×10^{-6} torr. A load of 1 kilogram was used for the hardness tests. About ten indentations on the surface of each alloy specimen were made, and the two diagonal lengths of each indentation were measured in filar units. The measured values were converted into millimeters and statistically handled to obtain the averages and standard deviations. Then, the diamond pyramid hardness (DPH) values were evaluated using the following equation:

$$H = \frac{P}{A} = \frac{2P}{d^2} \cdot \sin \frac{\theta}{2} \quad (16)$$

where H = diamond pyramid hardness, DPH

A = unrecovered projected area of indentation (mm^2)

d = mean diagonal length of indentation in mm

θ = the included face angle of the indentation = 136 degrees.

The results are shown in Table 11 and Fig. 31.

Second Phase Particle Size

Sections #2 and #8 of the finger alloys (see Fig. 23) were used for the photomicrographs and second-phase particle size analysis and hardness tests. They were machined to a rectangular shape (0.1" thick, 0.2" wide and 0.3" long) and mounted in bakelite. The mounted specimens were ground using up to 600 grit silicon carbide paper and polished with a Syntron vibratory lapping machine with a wax base. Two abrasives were used to produce the final polished surface: $0.3 \mu\text{m Al}_2\text{O}_3$ (Linde A), removing 2-3 mils, and $0.05 \mu\text{m Al}_2\text{O}_3$ (Linde B), removing 2 mils.

After ultrasonic cleaning, the specimen surface was photographed at a magnification of 1000X, 400X or 200X, depending on the second phase particle size. The diameter distributions of the second phase particles on the photomicrographs were analyzed using a TG23 (Zeiss) particle size analyzer. The measured results of the diameter distribution analysis are shown in Fig. 32 for the as-received and arc-melted alloys. Fig. 33 shows similar results for the 0.05, 0.1, 0.5 and 1 weight percent yttrium-doped alloys, Fig. 34 for the 0.05, 0.1, 0.5 and 1 weight percent lanthanum-doped alloys and Fig. 35 for the 0.05, 0.1, 0.5 and 1 weight percent cerium-doped alloys. The integrated areal distributions (Figs.

Table 11. Microhardness of the rare-earth-doped and undoped AL alloys

Alloy	Composition	No. of indention	Mean Filar Unit	Observed Length (μm)	Hardness (DPH)
AL-0	AL ^a	10	186.20	85.09 \pm 0.81	256.7 \pm 4.9
AL-1	AL ^b	10	169.95	77.67 \pm 0.51	307.8 \pm 4.1
AL-2	AL+0.05% Y	10	169.40	77.42 \pm 0.25	309.5 \pm 2.0
AL-3	AL+0.1 % Y	10	169.30	77.37 \pm 0.13	309.8 \pm 1.0
AL-4	AL+0.5 % Y	9	175.20	80.08 \pm 0.77	289.8 \pm 5.3
AL-5	AL+1.0 % Y	10	182.70	83.49 \pm 1.24	267.5 \pm 7.6
AL-6	AL+0.05% La	10	175.05	80.00 \pm 0.58	290.2 \pm 4.1
AL-7	AL+0.1 % La	10	171.00	78.15 \pm 0.77	304.5 \pm 6.2
AL-8	AL+0.5 % La	10	168.45	76.98 \pm 0.67	313.6 \pm 5.5
AL-9	AL+1.0 % La	9	169.60	77.51 \pm 0.49	308.9 \pm 3.8
AL-10	AL+0.05% Ce	10	176.30	80.57 \pm 0.68	286.2 \pm 4.7
AL-11	AL+0.1 % Ce	10	166.70	76.18 \pm 0.47	319.8 \pm 3.9
AL-12	AL+0.5 % Ce	11	168.73	77.11 \pm 0.20	311.9 \pm 1.6
AL-13	AL+1.0 % Ce	10	169.10	77.28 \pm 0.62	311.0 \pm 4.6

^aAs received and annealed for 1 hour at 950°C.

^bArc-melted and annealed for 2 hours at 1200°C.

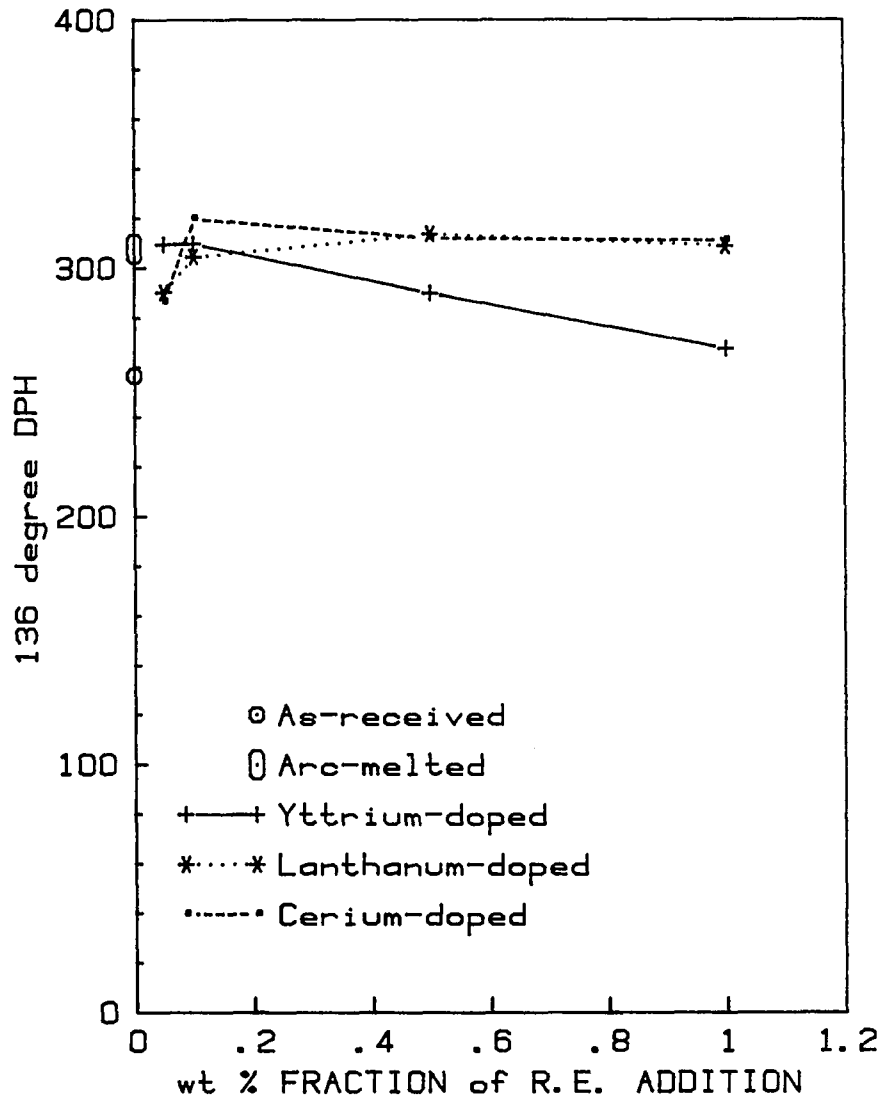


Fig. 31. Microhardness of the rare-earth doped and undoped AL alloys

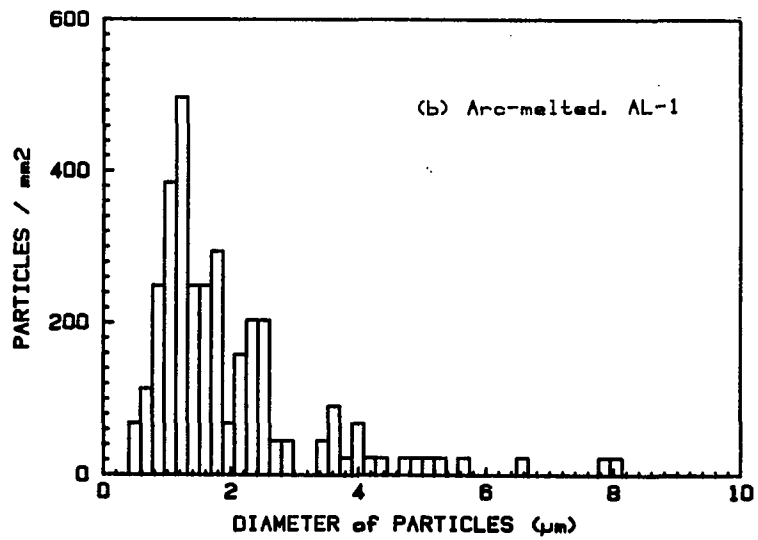
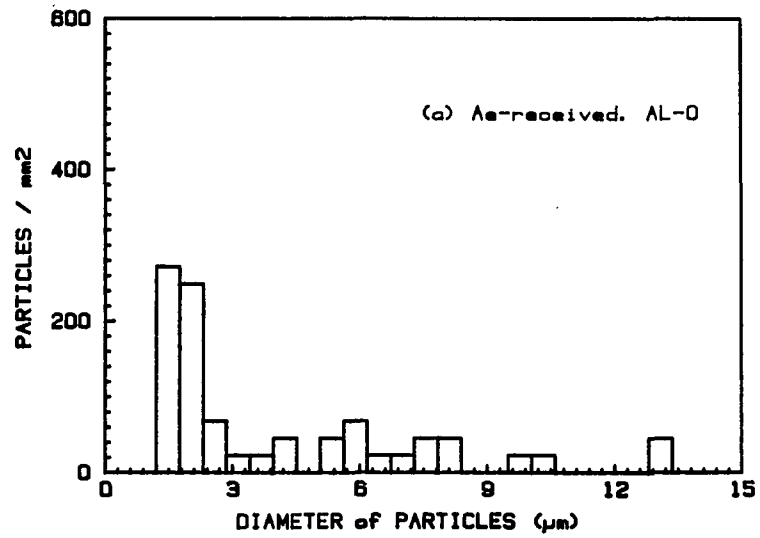


Fig. 32. Particle size analysis for (a) as-received (AL-0) and (b) arc-melted (AL-1) alloys

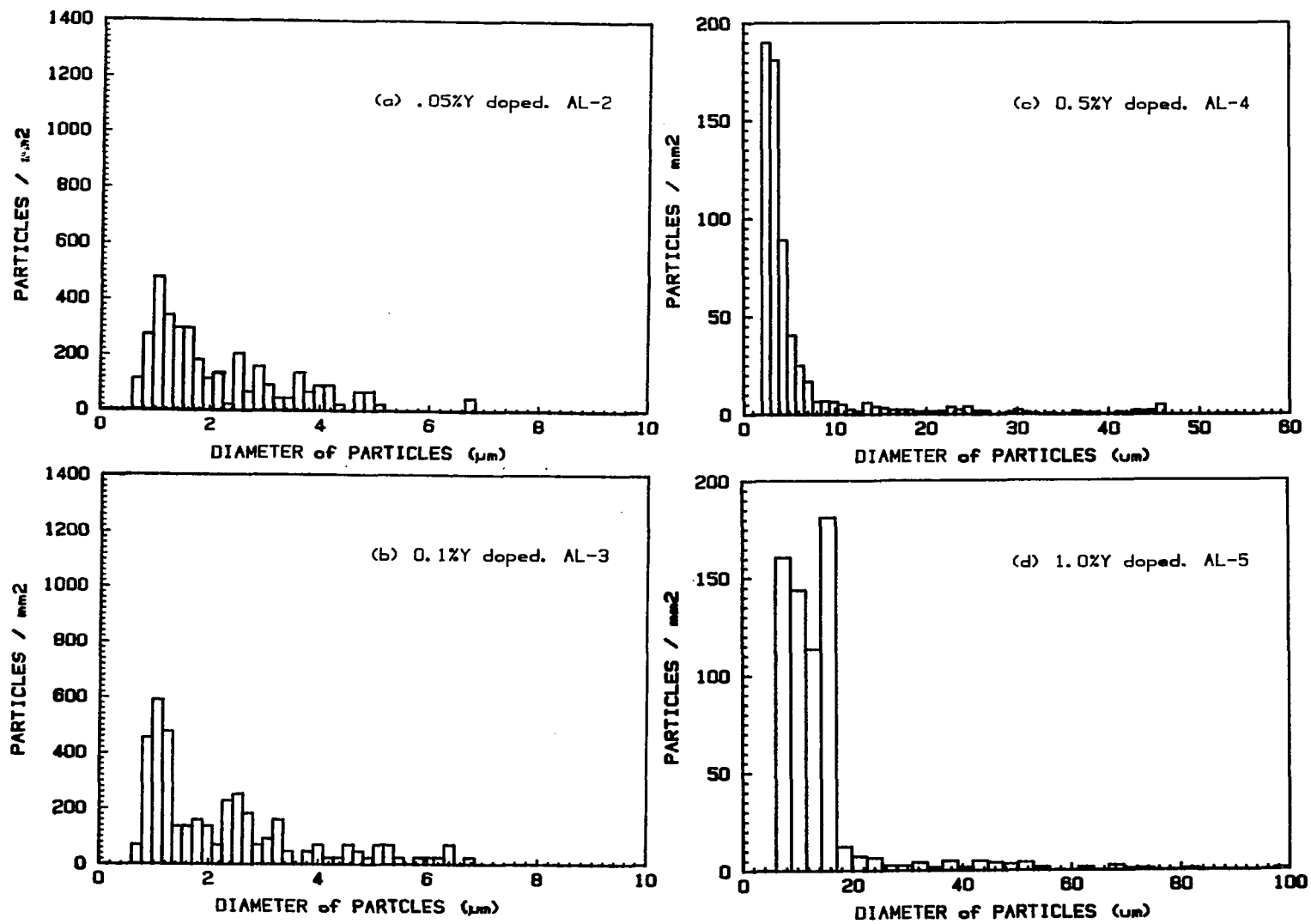


Fig. 33. Particle size analysis for (a) 0.05% (AL-2), (b) 0.1% (AL-3), (c) 0.5% (AL-4) and (d) 1.0% (AL-5) yttrium-doped alloys

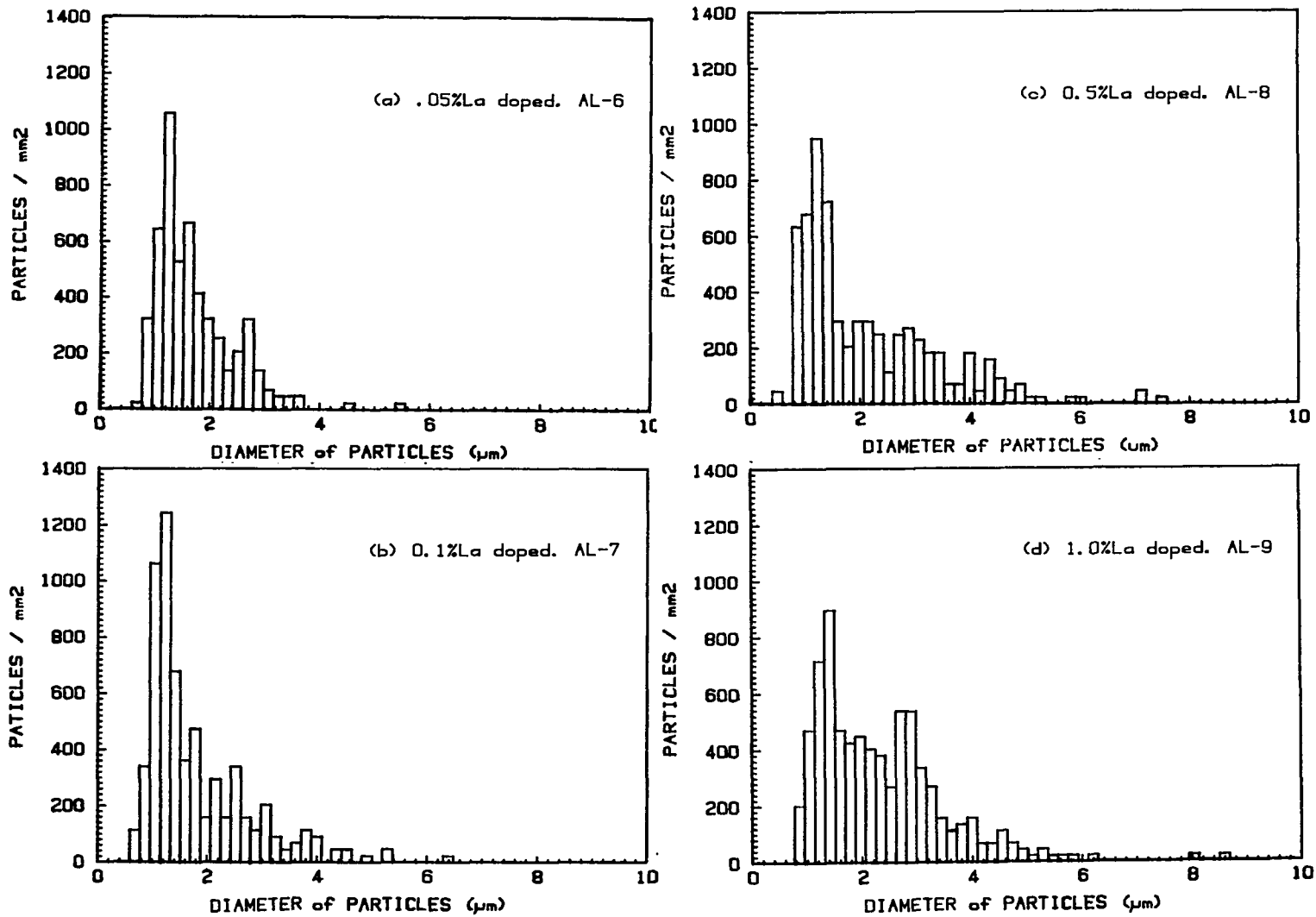


Fig. 34. Particle size analysis for (a) 0.05% (AL-6), (b) 0.1% (AL-7), (c) 0.5% (AL-8) and (d) 1.0% (AL-9) lanthanum-doped alloys

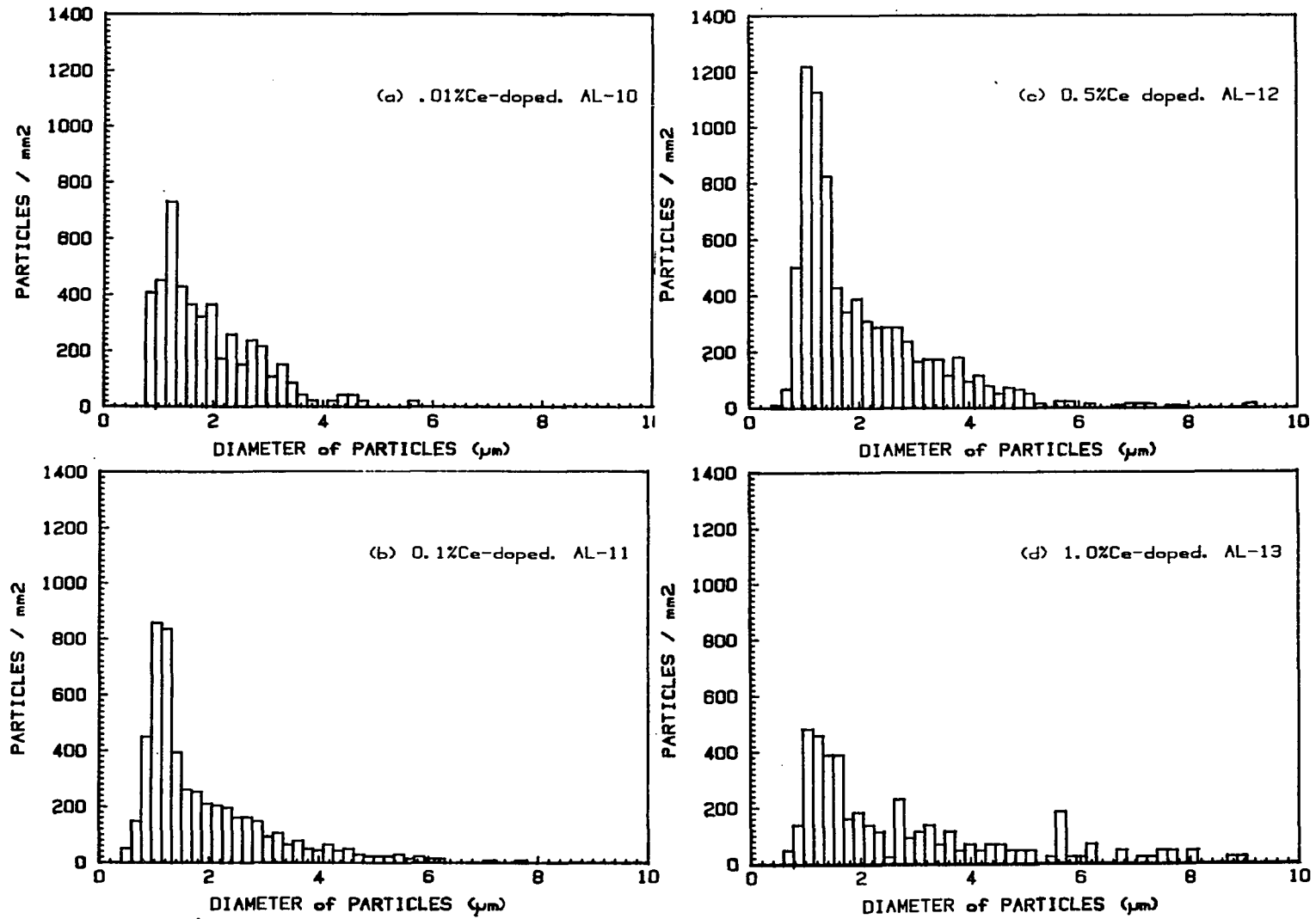


Fig. 35. Particle size analysis for (a) 0.05% (AL-10), (b) 0.1% (AL-11), (c) 0.5% (AL-12) and (d) 1.0% (AL-13) cerium-doped alloys

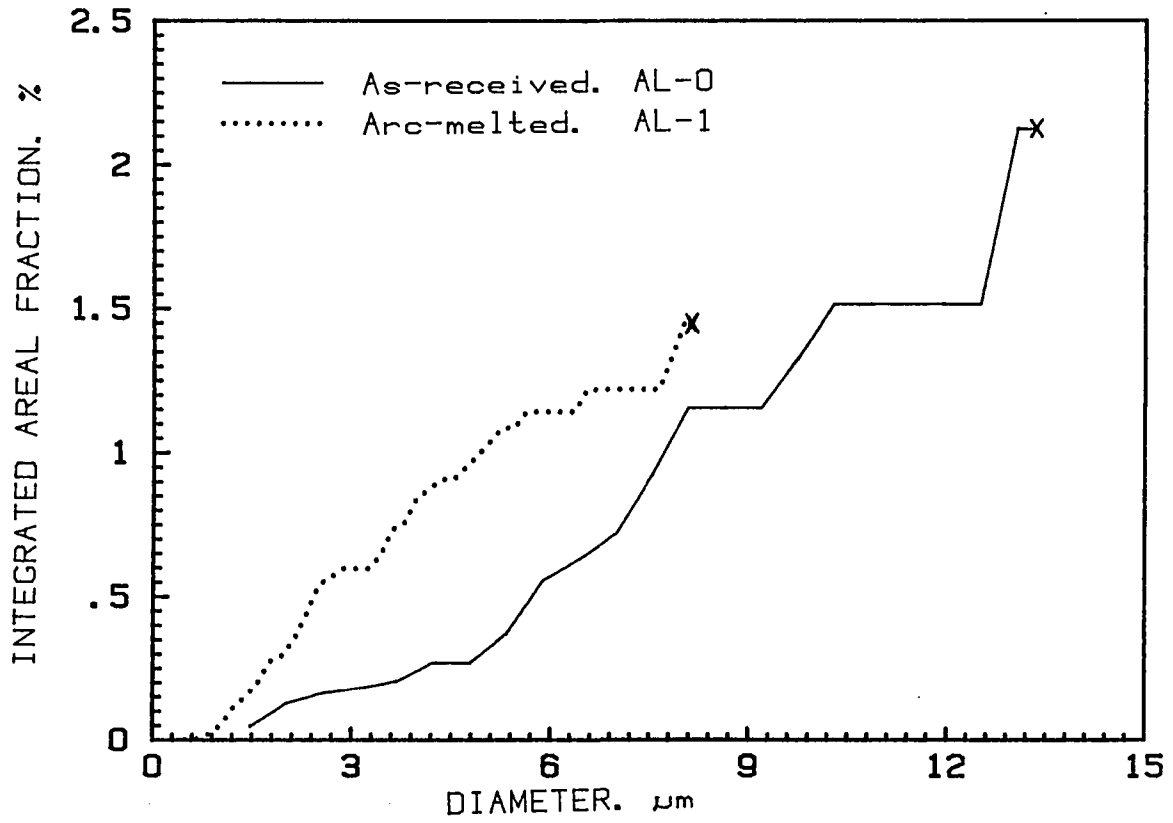


Fig. 36. Integrated areal distribution of particles for as-received (AL-0) and arc-melted (AL-1) alloys

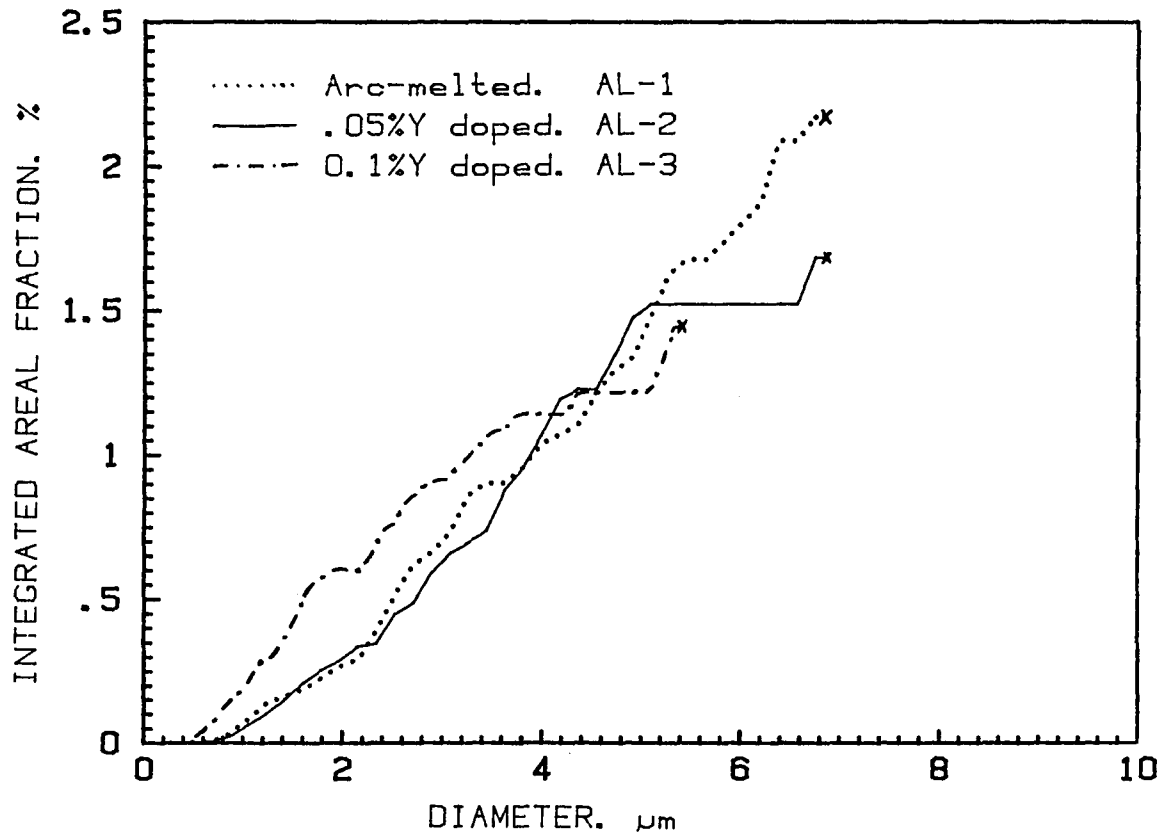


Fig. 37. Integrated areal distribution of particles for arc-melted (AL-1), 0.05% (AL-2) and 0.1% (AL-3) yttrium-doped alloys

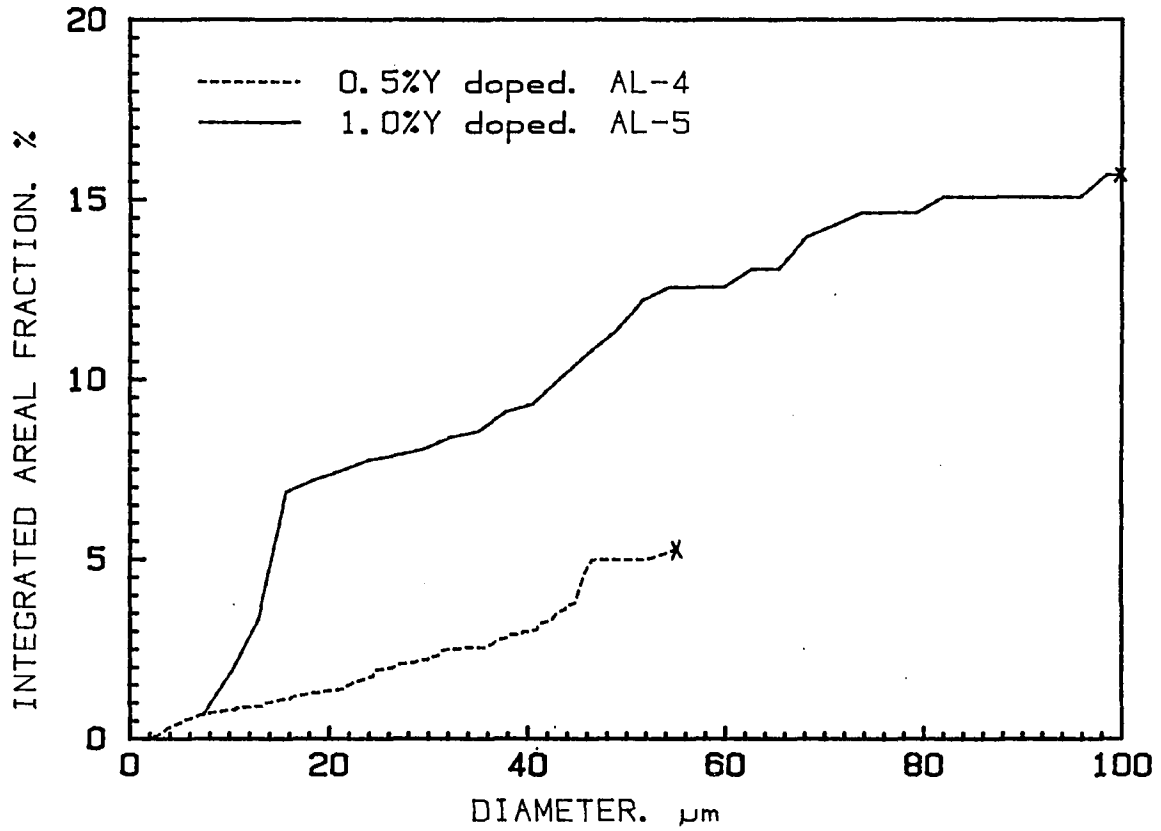


Fig. 38. Integrated areal distribution of particles for 0.5% (AL-4) and 1.0% (AL-5) yttrium-doped alloys

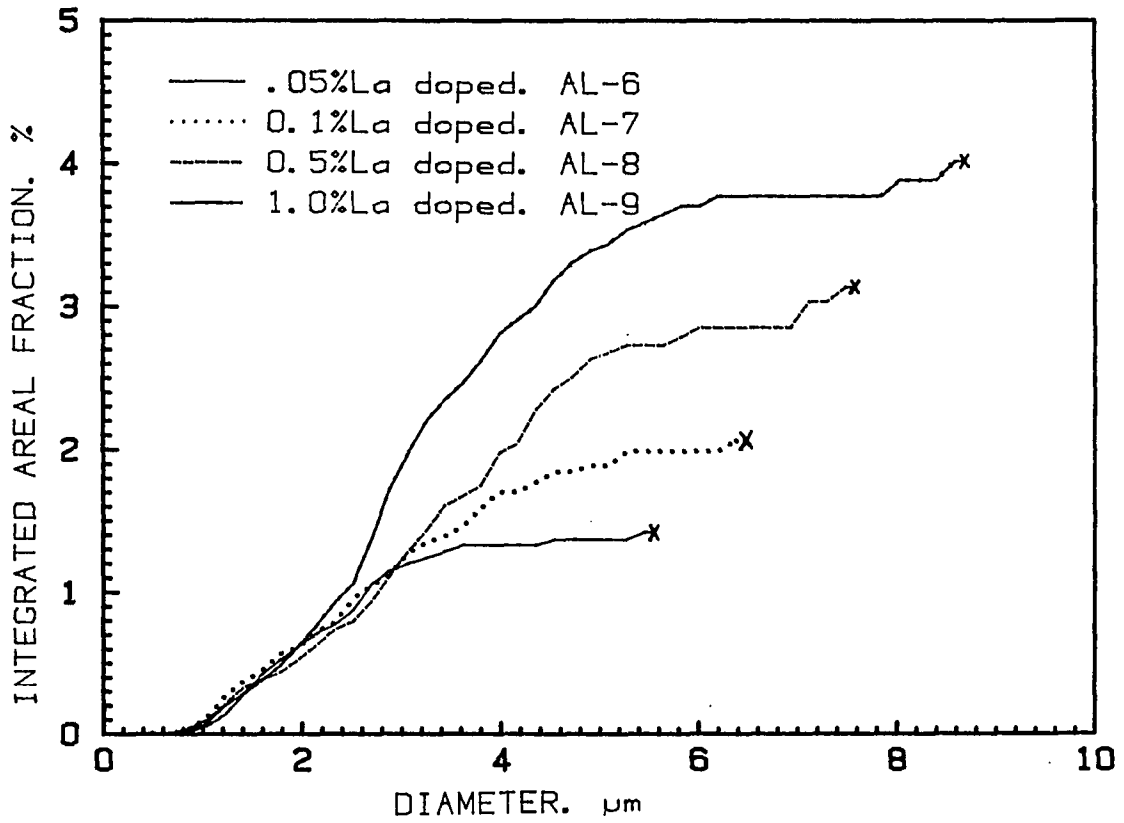


Fig. 39. Integrated areal distribution of particles for 0.05% (AL-6), 0.1% (AL-7), 0.5% (AL-8) and 1.0% (AL-9) lanthanum-doped alloys

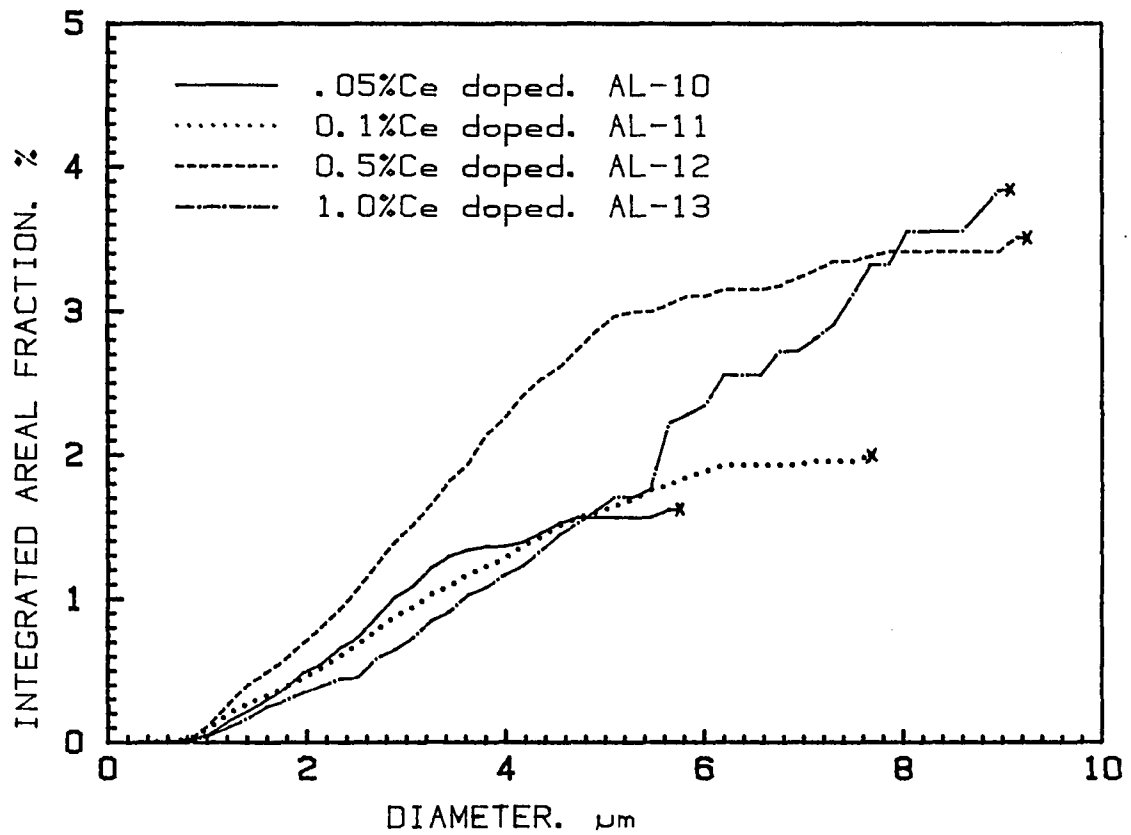


Fig. 40. Integrated areal distribution of particles for 0.05% (AL-10), 0.1% (AL-11), 0.5% (AL-12) and 1.0% (AL-13) cerium doped alloys

36-40) were evaluated from the following equation, based on the diameter distribution data:

$$A_i = \sum_{j=1}^i \frac{\pi}{4} d_j^2 \times N_j \quad (17)$$

where A_j = the integrated areal function of particles of diameter up to

d_j = mean diameter of j'th group of particles

N_j = number density of j'th group of particles

The total areal fractions of second phase particles in each alloy were calculated, as shown in Table 12 and Fig. 41.

Ion Beam Bombardment

Stacked-edge-on multispecimen assembly preparation

Sections #3 and #7 of the arc-melted finger alloys (Fig. 23) were used to prepare the stacked-edge-on specimens for examination of the ion beam bombarded surface condition. The sections were sliced with an Isomet diamond cutting saw to get 0.65 mm thick plates. These plates were ground through 600 grit silicon carbide powder. A Syntron lapping machine with a wax base using a 0.3 μm Al_2O_3 (Linde A) abrasive was then used to remove about 1-2 mils and to produce a plate, approximately 0.5 mm thick with two parallel surfaces. The plates were carefully machined to a rectangular shape (0.5 mm thick, 3 mm wide and 4 mm long). Care was exercised to keep internal stresses as low as possible. A standard P7 stainless steel, (Table 13) supplied by ORNL, was also machined to the same shape and size. This material is known to

Table 12. Second phase particle size analysis on microphotographs of rare-earth-doped and undoped AL alloys

Alloy	Composition	Measured total area ($10^3 \mu\text{m}^2$)	Particle total area (μm^2)	Area fraction of particle in %
AL-0	AL ^a	44.2	938	2.12
AL-1	AL ^b	44.2	627	1.42
AL-2	AL+0.05 % Y	44.2	743	1.68
AL-3	AL+0.1 % Y	44.2	957	2.17
AL-4	AL+0.5 % Y	1840	94100	5.11
AL-5	AL+1.0 % Y	1210	192200	15.85
AL-6	AL+0.05% La	44.2	617	1.40
AL-7	AL+0.1 % La	44.2	886	2.00
AL-8	AL+0.5 % La	44.2	1383	3.13
AL-9	AL+1.0 % La	44.2	1786	4.04
AL-10	AL+0.05% Ce	44.2	752	1.70
AL-11	AL+0.1 % Ce	132.7	2828	2.13
AL-12	AL+0.5 % Ce	132.7	4698	3.54
AL-13	AL+1.0 % Ce	44.2	2016	4.56

^aAs-received and annealed for 1 hour at 950°C.

^bArc-melted and annealed for 2 hours at 1200°C.

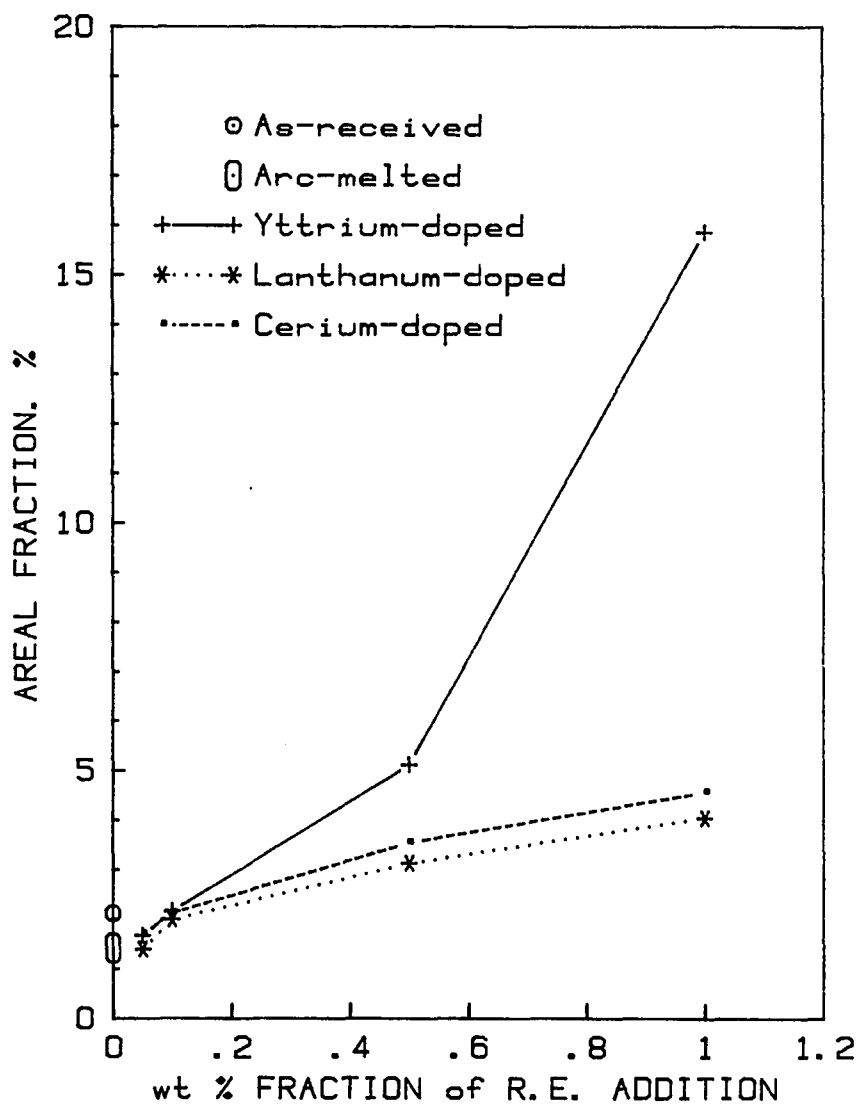


Fig. 41. Areal fraction of the precipitate particles of rare-earth doped and undoped AL alloys

Table 13. Chemical composition of standard stainless steel, P7

Element	Composition (wt%)	Element	Composition (wt%)
Fe	Balance	Co	0.03
Cr	17.0	Cu	0.02
Ni	16.7	Zr	<0.001
Mo	2.5	W	0.0068
Si	0.1	V	<0.001
Mn	0.03	C	0.005
Ti	0.01	O	0.03
Al	0.02	N	0.004
Nb	0.02	H	0.001

undergo large swelling, and thus it provides a measure of the flux distribution within the beam. Both large surfaces (3 mm x 4 mm) of each specimen were identified with a tungsten carbide marker.

Three stacked-edge-on specimens of each of the following 15 types of AL alloys were prepared: as-received, annealed, arc-melted undoped, and 12 arc-melted rare-earth doped alloys (3 dopants, Y, La, and Ce, each in 4 compositions, 0.05, 0.1, 0.5, and 1.0 wt%). In addition, 9 standard P7 stainless steel specimens were included. The 54 specimens were loaded in the inner holders shown in Fig. 42 and listed in Table 14. The specimens were fixed in the holder with set screws from two sides on the holder (Fig. 42a). The surfaces of the specimens in the holders were ground with a surface grinder and polished using a Syntron vibratory lapping machine with a wax base and using two abrasives. The abrasives were $0.3 \mu\text{m Al}_2\text{O}_3$ (Linde A) removing about 2-3 mils and $0.05 \mu\text{m Al}_2\text{O}_3$ (Linde B) removing about 2 mils to produce the final polished surface. At each step of polishing, the specimens were ultrasonically cleaned with acetone and examined at a 500X magnification or surface smoothness using a stereomicroscope. Surfaces found to be acceptable by this procedure were examined using an interference microscope and found to be smooth to within the limit of measurability of the microscope. The assemblies were wrapped with tantalum sheets and annealed for 1 hour at 950°C in the NRC 3500 high vacuum furnace at a pressure below 10^{-6} torr to produce a stress-free condition. One chromel-alumel thermocouple was spot-welded on the surface of one of the specimens of each assembly for irradiation temperature reading. Target assemblies were assembled in the order:

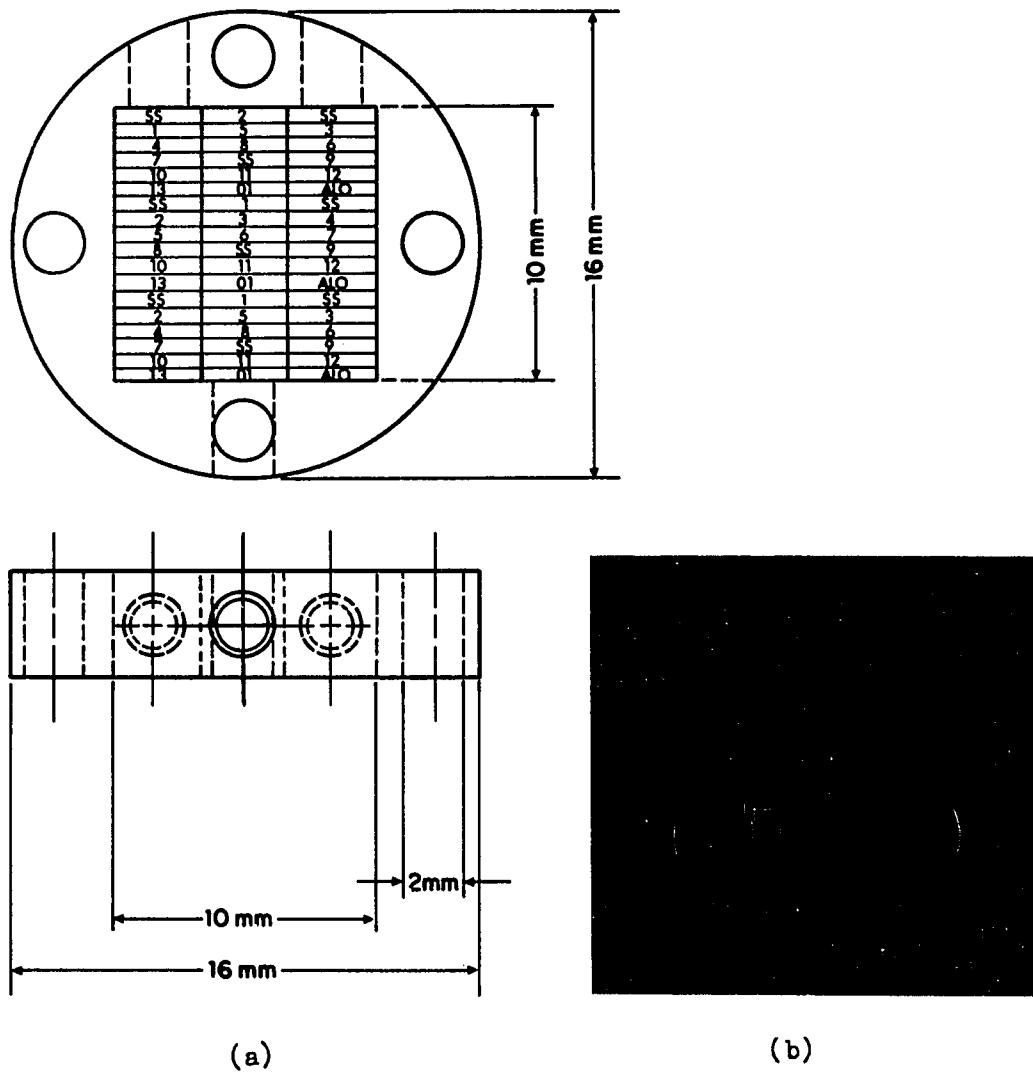
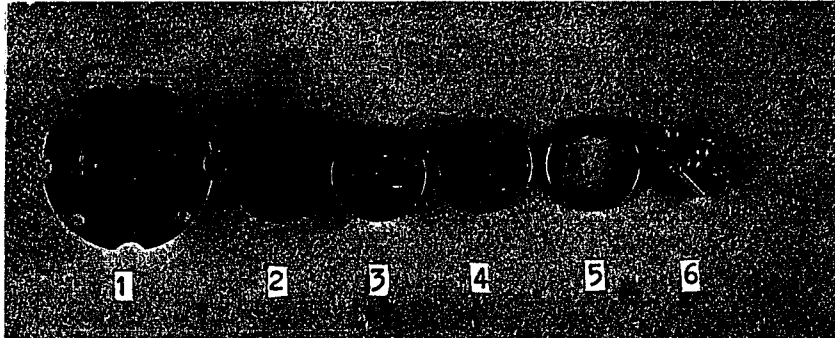


Fig. 42. Stacked-edge-on specimens, (a) dimensional configuration and (b) three sets of specimens in the inner holders

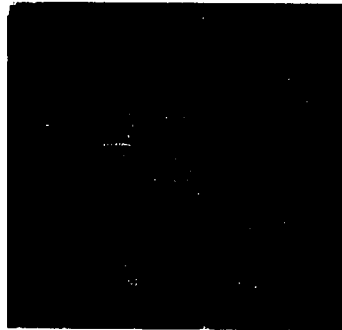
stainless steel thermalizer holder (Item A), tantalum sheet disk (Item B) in the bottom of the thermalizer, specimens in the inner stainless steel holder (Item C) on the tantalum sheet disk, bar mask grid (Item D) on the surface of the specimens, and holding grid (Item E) on the mask grid. The target assembly was tightened with three screws (Item F), as shown as Assembly B in Fig. 43. The bottom holder had three holes to hold thermocouples. In addition, a fourth thermocouple was spot-welded on the surface of one of the specimens of each assembly. Three stacked-edge-on specimen assemblies (Table 14) were prepared for ion beam bombardment.

TEM specimen preparation

Section #5 of the arc-melted finger alloys was used to prepare TEM specimens for the ion beam bombardment experiment. They were sliced with an Isomet diamond cutting saw to get 0.5 mm (20 mil) thick plates. They were punched out into a disk shape of 3 mm diameter. The specification of requirements and preparation procedures for the TEM specimens to be ion bombarded are well described in references 79 and 196. For example, the TEM specimens should be flat to a tolerance $\ll 1 \mu\text{m}$, of the correct size to fit the ORNL 6 MeV Van de Graaf accelerator target holder and for the post-irradiation studies, of the desired phase state for the experiment, of uniform thickness, and with a defect-free surface. After punching, each disk was deburred by sanding or filing. About 30 specimens were mounted on each Corning micro glass slide with Aremco crystal bond. One side of the disk was ground with 600 grit silicon carbide paper. Then, the disks were demounted upside down on stainless steel blocks (2 inch diameter x 0.5 inch high) with Aremco crystal bond,



(a)



(b)

Fig. 43. Target assembly B, (a) disassembled; 1 stainless steel thermalizer, 2 tantalum sheet disk, 3 specimens in the inner holder, 4 mask grid, 5 holding grid, and 6 screws, and (b) assembled

Table 14. Stacked-edge-on specimens (front view of the holder)

	Assembly A			Assembly B			Assembly C		
1	SS-2	2-A	SS-1	SS-12	2-D	SS-10	S-21	2-1	SS-20
2	3-1	5-1	1-A	3-5	5-D	1-D	3-9	5-G	1-G
3	6-A	8-1	4-1	6-D	8-4	4-6	6-G	8-6	4-15
4	9-1	SS-3	7-A	9-4	SS-13	7-E	9-7	SS-2	7-H
5	12-1	11-1	10-1	12-4	11-4	10-4	2-7	11-7	10-7
6	0-3	01-1	13-1	0-9	01-4	13-4	0-2	01-7	13-7
7	SS-5	1-B	SS-4	SS-15	1-E	SS-14	SS-24	1-H	SS-23
8	4-4	3-2	2-B	4-11	3-6	2-E	4-16	3-10	2-2
9	7-B	6-B	5-B	7-F	6-E	5-E	7-4	6-H	5-H
10	9-2	SS-6	8-2	9-5	SS-16	8-5	9-8	SS-25	8-8
11	12-2	11-2	10-2	12-5	11-5	10-5	12-8	11-8	10-8
12	0-5	01-2	13-2	0-11	01-5	13-5	0-10	01-8	13-8
13	SS-8	1-C	SS-7	SS-18	1-F	SS-17	SS-27	1-I	SS-26
14	4-5	3-3	2-C	4-13	3-8	2-F	3-11	5-I	2-6
15	7-C	6-6	5-C	7-G	6-F	5-F	6-I	8-9	4-17
16	9-3	SS-9	8-3	9-6	SS-19	8-7	9-9	SS-28	7-6
17	12-3	11-3	10-3	12-6	11-6	10-6	2-9	11-9	10-9
18	0-6	01-3	13-3	0-4	01-6	13-6	0-12	01-9	13-10

Sample Designation Key

Example: 1-A, A represents the sample number for a given alloy
and 1 represents the alloy number

Code:

0: as-received and annealed for 1 hour at 950^o
01: as-received and, annealed for 2 hours at 1200^oC
1: AL arc-melted
2: AL+0.05 w/o Y
3: AL+0.1 w/o Y
4: AL+0.5 w/o Y
5: AL+1.0 w/o Y
6: AL+0.05 w/o La
7: AL+0.1 w/o La
8: AL+0.5 w/o La
9: AL+1.0 w/o La
10: AL+0.05 w/o Ce
11: AL+0.1 w/o Ce
12: AL+0.5 w/o Ce
13: AL+1.0 w/o Ce
SS: standard P7 stainless steel

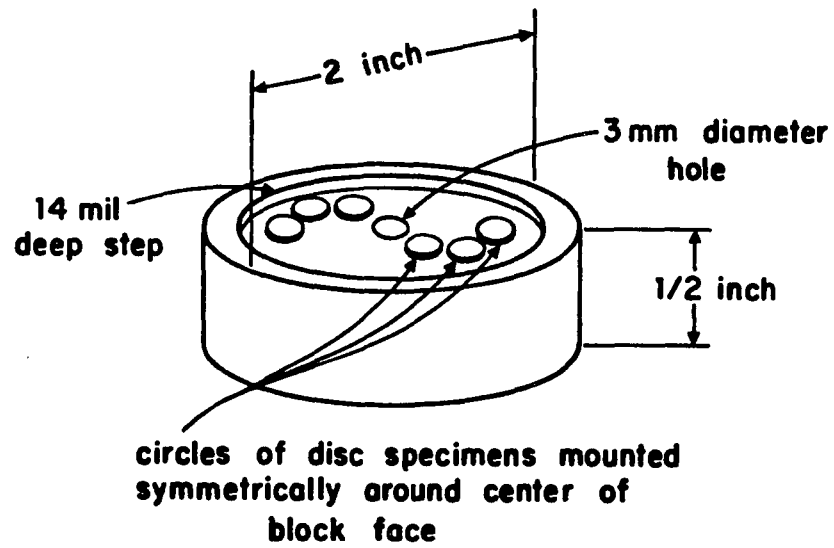
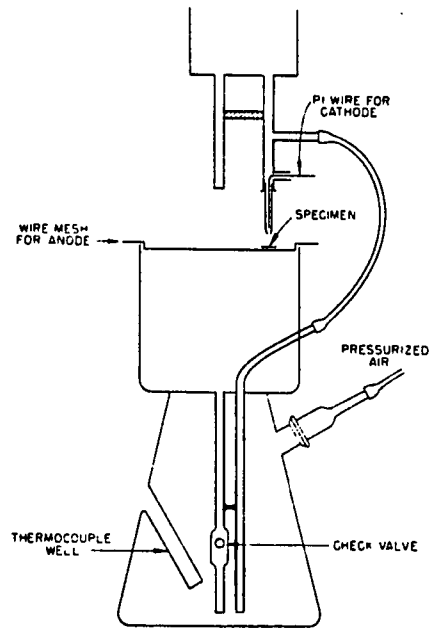


Fig. 44. Specimens mounted on a polishing block. The 14 mil deep step is to produce 14 mil thick specimens with two flat and parallel surfaces

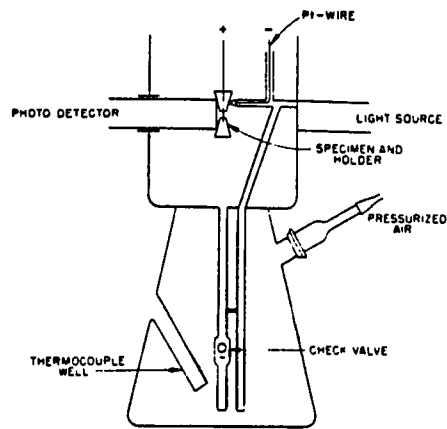
as shown in Fig. 44. The blocks are designed to produce flat and parallel surfaces with a 14 mil deep groove. The specimens on the block were polished flush using 600 grit silicon carbide paper. The surface preparation was done on a Syntron vibratory polishing machine with wax base using $0.3 \mu\text{m Al}_2\text{O}_3$ (Linde A) abrasive removing 1-2 mils, and $0.05 \mu\text{m Al}_2\text{O}_3$ (Linde B) abrasive, removing 2 mils, to produce the final polished surface. Then, the disks were demounted and washed in an ultrasonic bath with acetone for 20 minutes and methanol for 20 minutes. The disks were wrapped separately with tantalum sheets, loaded in a tantalum can and annealed in the NRC 3500 high vacuum furnace for 1 hour at 950°C at pressure below 10^{-6} torr. After the mechanical polishing, the surfaces of the disks were electropolished with a jet surface polishing rig (Fig. 45), as suggested by Lee and Rowcliffe [197]. The disk specimen was loaded on the stainless steel grid and an electrolyte solution of 10% perchloric acid and 90% methanol was uniformly flowed over the surface of the specimen through a 2.3 mm diameter glass tip. The flow rate and jet height were carefully controlled to maintain a uniform flow on the surface of the specimen. Then, a pulse mode current of 200 mA was supplied for 10 seconds at room temperature. The voltage during current supply was about 40 volts. Through this polishing procedure, a $2-3 \mu\text{m}$ layer of the surface was removed. After electropolishing, the specimens were cleaned with methanol and acetone to remove residual acid.

Assembly of TEM specimens in the specimen holder

The procedure and equipment for assembling are well described in the



(a)



(b)

Fig. 45. Constructions of (a) jet surface polishing rig and (b) jet back thinning rig [196]

references 32, 33 and 34. All the parts of the assembly were ultrasonically cleaned with methanol. The face plate made of Kulite-112 machinable tungsten alloy (item a, Fig. 46) was placed beam side down in the loading jig. On the back of the face plates, the area round each hole is recessed to position a 3 mm diameter specimen over the hole. A one-mil-thick molybdenum bar mask (item b, Fig. 46) was used to produce a post-bombardment step height between the shielded and unshielded region. The vertical orientation prevents shadowing of the light ion beam that impinges upon the target at a 15° angle. A crushable ring of annealed 0.1-0.2 mm thick platinum wire (item c, Fig. 46) was placed and then the specimens were loaded so that the platinum wire accommodated the small variation in specimen-to-specimen thickness and none was loose in the holder. A five-mil thick chromel-alumel thermocouple was spot-welded on the surface of one of the nine specimens, and the specimen was loaded at the upper right position of the back side of the face plate. The thermalizer block (item f, Fig. 46) was carefully placed over the samples without dislodging them. Applying the holddown clamp (item g, Fig. 46), rotating the swivel stage upside down, and inspection of the sample were conducted to insure that the masks were oriented properly, thermocouple leads were properly situated, and samples were suitably seated. A clamping force of about 60 kg was applied by a modified toggle-clamp tool (item g, Fig. 46) to partially compress the platinum gaskets. The four 2-56 socket-head screws (item l, Fig. 46) were inserted in the target holder and tightened to maintain the clamp pressure. Four TEM ion bombarding specimen holders were prepared (Table 15 and Fig. 47).

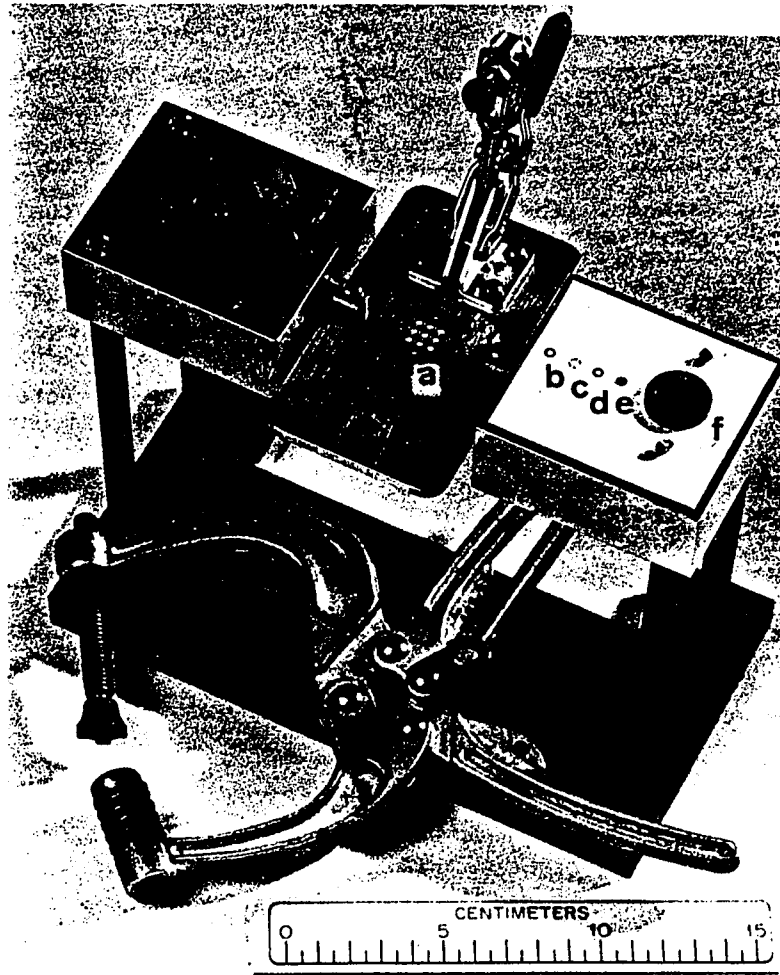


Fig. 46. Disassembled specimen holder in the loading jig. Components are: (a) face plate, (b) miniature bar mask, (c) platinum wire gasket, (d) optional 0.05 mm-thick oxidized stainless steel spacer, (e) specimens, and (f) thermalizer block [32]

Table 15. TEM specimens array (front view of the holder)

Assembly D:	13-10	6-V	8-h
	13-13	6-W	5-R
	1-B	1-C	5-S
Assembly E:	2-G	8-q	11-5
	3-J	4-M	11-2
	3-K	2-F	4-P
Assembly F:	7-e	10-t	10-y
	7-Y	12-8	9-s
	4-N	9-q	12-9
Assembly G:	6-x	1-A	5-Q
	1-*	5-T	13-11
	13-12	6-U	8-m

Sample Designation Key

Example: 13-10, 10 represents the sample number for a given alloy and 13 represents the alloy number as shown on Table 14

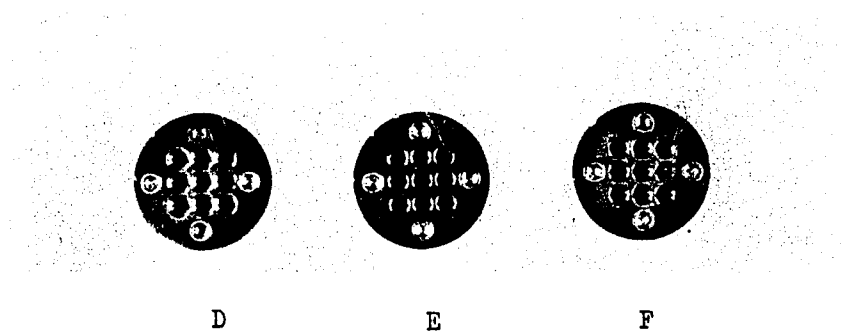


Fig. 47. TEM specimen target assemblies, D, E, and F, bombarded with dual beam of 4 MeV Ni^{++} and 0.4 MeV He^+ ions

Particle bombardment facility

The dual-beam irradiation technique allows the simultaneous bombardment of specimens with energetic heavy ions and helium ions. The facility used to perform the dual-beam irradiations for this study was the ORNL 6 MeV dual Van de Graaff accelerator, as described by Lewis et al. [32], Packan and Buhl [33], Farrell et al. [160] and Lewis et al. [198]. The dual beam irradiation is used because fast neutrons fission and fusion reactors produce not only displacements, but also helium as a result of (n,α) reactions. The Van de Graaff dual beam accelerator was developed for the purpose of more closely simulating the effect of neutron-induced damage in reactor materials.

The ORNL irradiation facility consists of two Van de Graaff accelerators, as shown in Fig. 48 [32]. The heavy ions are accelerated to 4 MeV by a vertical Van de Graaff accelerator (item a, Fig. 48) equipped with a Model 910 Physicon ion source. The ion beam from the ion source is focused by a three-barrel einzel lens into a Wien velocity filter (mass analyzer) to allow only the metal ions to pass. The 4 MeV M^+ ions are stripped to charge state +2 by a differentially pumped argon gas-filled tube. The beam divergence is reduced to obtain a 1 cm^2 uniform beam area by a specially designed Johnson split-field lens [199].

A 0.4 MeV horizontal Van de Graaff accelerator is used to accelerate helium ions and implant them about $0.7 \mu\text{m}$ below the metal surface in the region where the peak of the radiation damage caused by the heavy ions occurs. The entire system is pumped to a base pressure below 10^{-5} Pa

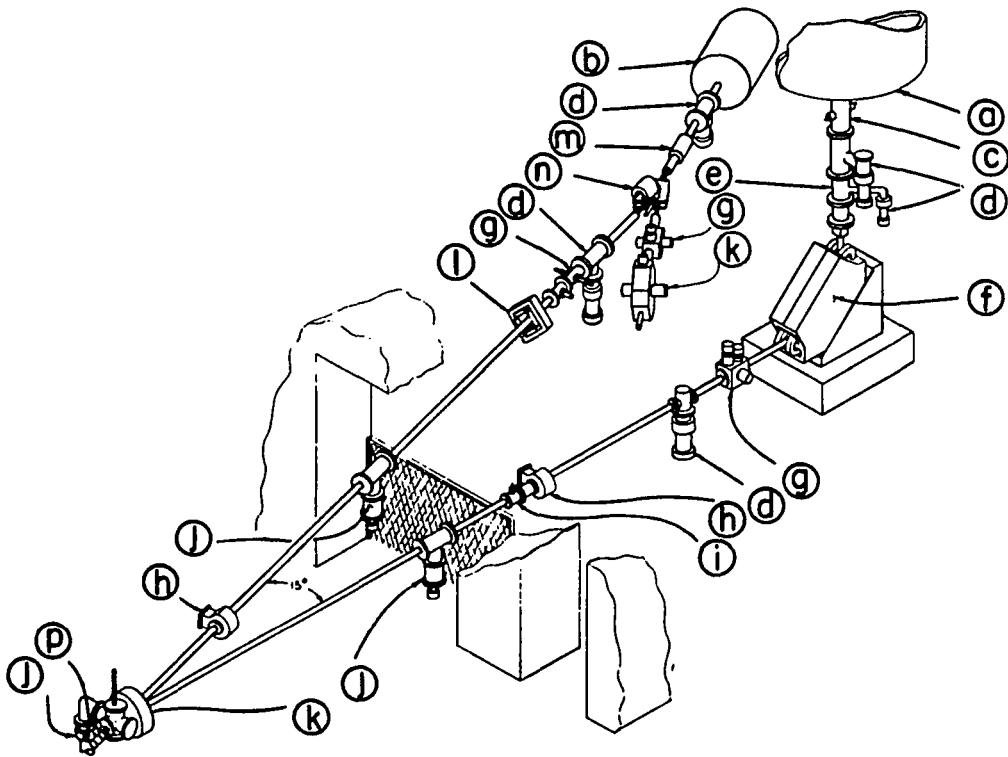


Fig. 48. Schematic of the two accelerators and their respective beam lines to the radiation damage target chamber (lower left) [32 and 33]. (a) CN Van de Graaff accelerator (4 MeV), (b) AN accelerator, (c) steerer, (d) diffusion pump, (e) gas stripper, (f) 90° magnet, (g) beam stop and control slits, (h) beam scanner, (i) Johnson lens, (j) cryo pump, (k) experiment chamber, (l) quadrupole, singlet lens, (m) double transmitting Faraday cup, (n) 90° magnet, (p) Faraday cups

(10^{-7} torr).

To cover a relatively large target area with a beam as uniform as possible, beam detection devices are traversed along the heavy-ion beam in the following order: An X-Y profile monitor (Fig. 49), a removable assembly with nine miniature Faraday cups (Fig. 50), a removable aperture mask (not used for this study), the target assembly (Figs. 49, 51 and 52), and finally, a deep Faraday cup. The helium beam has its own profile monitor (located about 1 m ahead of the target surface) and its own deep Faraday cup.

Specimens are loaded in the target assembly (Fig. 52) in the damage chamber (Fig. 49) to face normal to the heavy-ion beam. The helium beam was incident at a 75° angle. The back pressure in the chamber is kept below 10^{-6} Pa (10^{-8} torr). The specimen temperature is monitored by three thermocouples and an infrared pyrometer. One thermocouple is spot-welded on the surface of the specimens at the lower right corner position as viewed in the direction of the beam. Another two thermocouples fit in recessed holes on the side of the thermalizer block. One of the thermocouples is connected to a temperature controller to control the specimen temperature. The pyrometer moves to each specimen location by a pre-set electronic positioning system. The temperature of all positions on the surface of the specimen holder can be read.

The target assembly (Figs. 51 and 52) consists of six specimen holder and heater stations. Each station holds a specimen holder and is bombarded separately and allows up to six "runs" with different

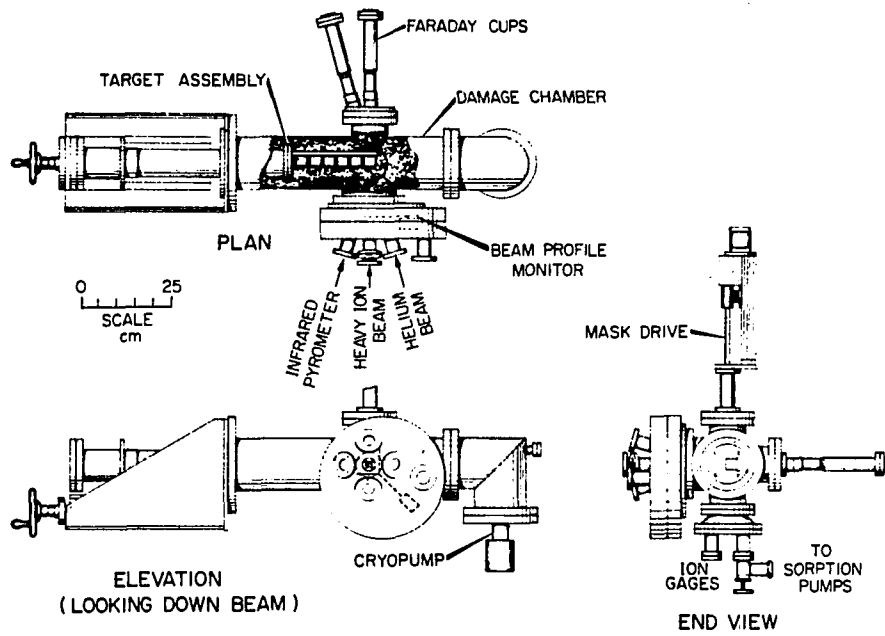


Fig. 49. Layout of the radiation damage target chamber [32]

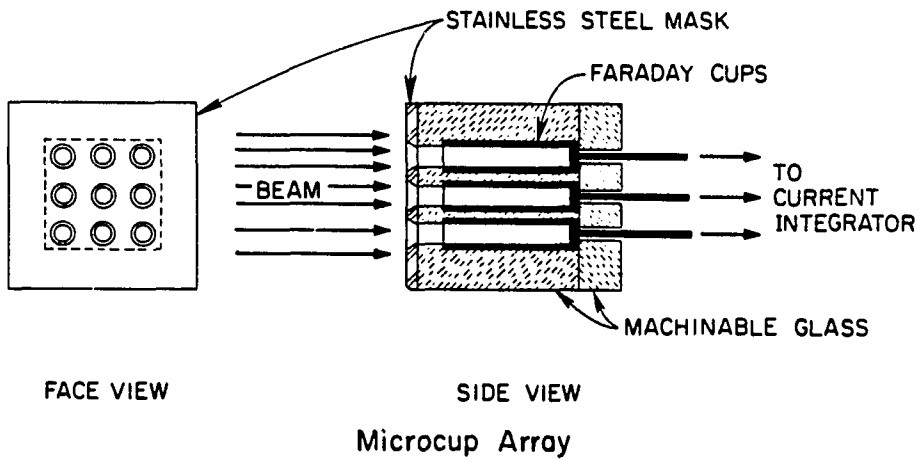


Fig. 50. Two schematic views of the nine-hole miniature Faraday cup array used to assess the true beam intensity on each target disk [32]

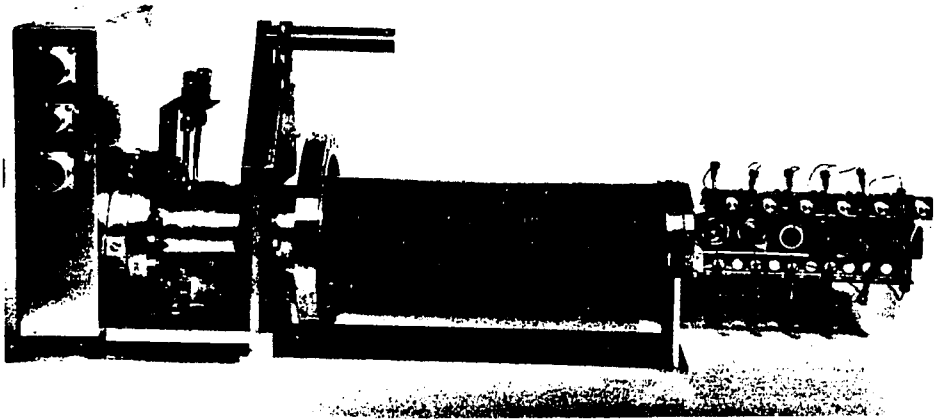


Fig. 51. One of the target assemblies, removed from the damage chamber [32]

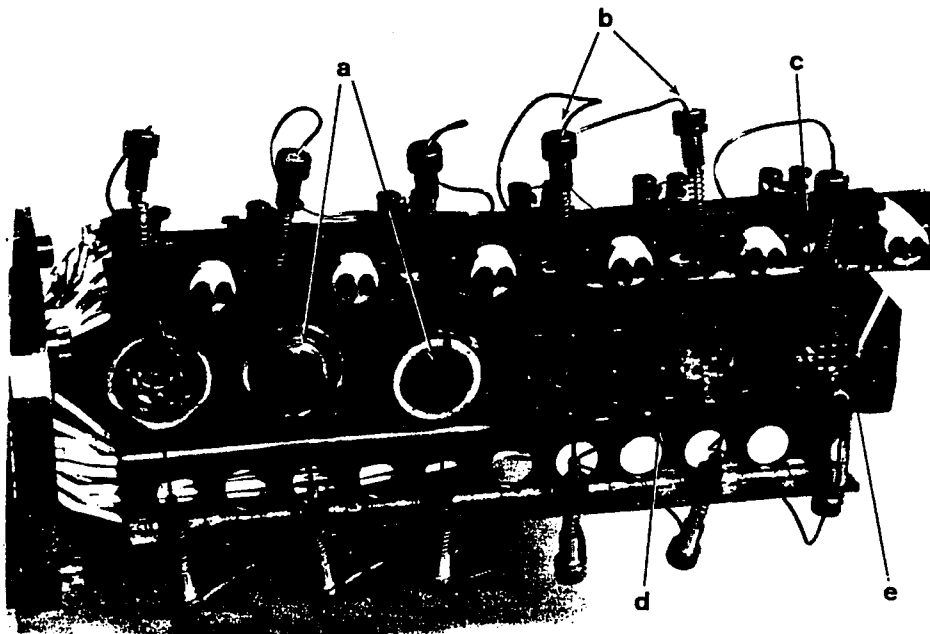


Fig. 52. Detailed view of the target assembly showing the six heater stations in progressive stages of assembly from left to right, including: (a) electron guns; (b) spring-loaded thermalizer block thermocouples; (c) nine disk specimen holder; (d) tantalum heater shield; and (e) specimen thermocouple [32]

irradiation conditions without reloading specimens. Specimens are heated by dispenser cathode-triode electron gun assemblies at each station. Up to 52 specimens of a rectangular shape (0.5 mm thick x 3 mm wide x 4 mm long) are loaded in a stacked-edge-on specimen holder (Fig. 43). The holder consists of stainless steel bottom thermalizer holder, tantalum sheet disk, inner specimen stainless steel holder, mask grid, holding grid and three screws. The bottom holder has three recessed holes to load thermocouples. The TEM specimen holder consists of a face plate with a 3 x 3 array of ~2 mm diameter holes to load 9 TEM specimens and a thermalizer block (Figs. 46 and 47).

Ion beam control and detection are achieved by using the equipment shown in the block diagram of Fig. 53. A TP-50 (Tennecomp Products) minicomputer is used for data acquisition and control. It controls the valves in the beam line (for starting and stopping the run), performs beam current monitoring and mask movement, and prints out details such as the dpa/specimen, the ion current/specimen, the projected time at each measurement, and the end of the run. The temperatures of the specimens are recorded manually.

Irradiations

Table 16 shows the characteristics for the single beam 4 MeV Fe^{++} ion bombardment of Assembly A, the dual beam 4 MeV Ni^{++} and 0.4 MeV He^+ ion bombardment of Assembly B and the dual beam 4 MeV Fe^{++} and 0.4 MeV He^+ ion bombardment of Assembly C. Each assembly consisted of 54 stacked-edge-on specimens in three rows, each containing 18 specimens, as shown in Table 15 and Fig. 40. Assemblies A and C were

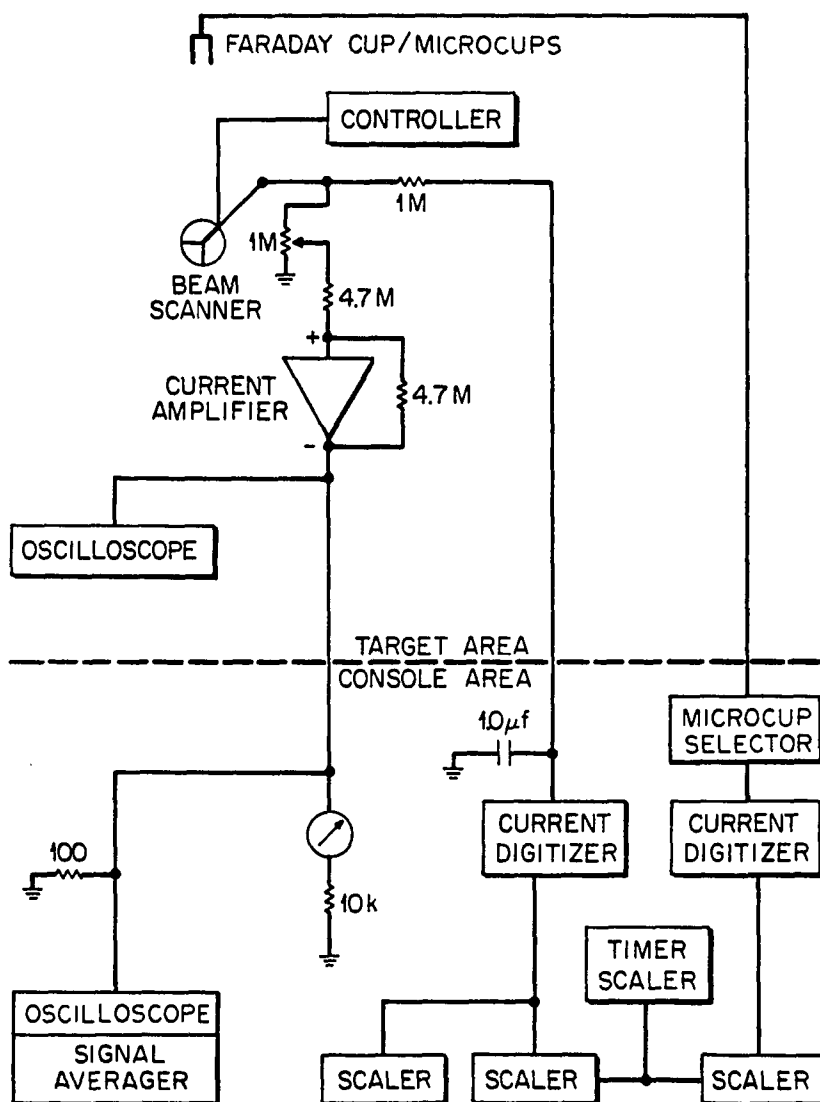


Fig. 53. Block diagram of electronics for the beam monitoring system. Signals originate at the beam scanner (continuously in service) or at the Faraday cup or microcups used at selected times. The current signals are then routed to measurement devices located at the Van de Graaff console area [32]

Table 16. Ion bombardment parameters, stacked-edge-on specimens

	Assembly A	Assembly B	Assembly C
Bombarding ions	4MeV Fe ⁺⁺	4MeV Ni ⁺⁺ + 0.4MeV He ⁺	4MeV Fe ⁺⁺ + 0.4MeV He ⁺
Bombarding time	549 min	238 min	446 min
Temperature (°C)	603±25	570±10	600±25
Displacement concentration (dpa) in the 3x3 matrix ^a	99 97 84 108 121 108 109 94 79	94 117 90 87 123 107 78 105 99	91 94 69 125 140 93 103 106 71
Relative He concentration	0.9±0.2 appm He/dpa		

^a3 x 3 matrix as viewed by beam covering 1.1 x 1.1 cm² area

irradiated in two steps, separated by a cool-down beam-off interval, and Assembly B was continuously irradiated in a single day. The accumulated displacements per atom (dpa) were calculated based on 40 MeV for the displacement energy, 0.8 for the atomic interaction correlation factor and the E-DEP-1 computer code, which uses a modified Kinchin and Pease atomic displacement model [82]. This is discussed further below. For the dual beam bombardments (Assemblies B and C), the relative helium concentration was controlled to be 0.9 ± 0.2 appm He/dpa.

In addition to the three stacked-edge-on assemblies, there were four ion bombarded TEM specimen assemblies (Assemblies D, E, F, and G), as shown in Table 17. The irradiation temperature, T_i , was controlled to be 570°C with the control thermocouple located in one of the holes under the thermalizer block. However, the temperature of the surface of each specimen as measured using a pyrometer is indicated in Table 17. Table 17 also shows the dpa for each sample within each assembly. However, only average He concentrations are available for each assembly. For Assemblies E, F, and G, the appm/dpa ratio was constant during the entire bombardment period, with the average He concentrations as shown in Table 17. For Assembly C, the He flux was inadvertently increased during the last 15 min. or 5.7% of the bombardment period. For the initial 94.3% period, the accumulated He concentration averaged over the assembly was 81 appm He; for the second 5.7% period, it was 465 appm He.

Table 17. Ion bombardment parameters, TEM specimens

	Specimen ^a	Position	T _i (°C)	dpa
Assembly D	13-10	11	562	89
	6-V	12	557	83
	8-h	13	560	45
	13-13	21	560	134
	6-W	22	548	141
	5-R	23	561	86
	1-B	31	556	57
	1-C	32	559	124
	5-S	33	563	66
Average accumulated helium concentration, 81 appm He for first 248 min plus 456 appm He for last 15 min				
Assembly E	2-G	11	573	71
	8-q	12	574	90
	11-5	13	547	66
	3-J	21	569	106
	4-M	22	563	149
	11-2	23	575	116
	3-k	31	573	73
	2-F	32	566	135
	4-p	33	569	84
Average accumulated helium concentration, 102 appm He				
Assembly F	7-e	11	563	80
	10-t	12	563	95
	10-y	13	563	60
	7-y	21	563	140
	12-8	22	563	140
	9-s	23	563	88
	4-N	31	563	102
	9-q	32	563	135
	12-9	33	563	60
Average accumulated helium concentration, 85 appm He				
Assembly G	6-X	11	556	106
	1-A	12	664	115
	5-Q	13	558	84
	1-*	21	550	96
	5-T	22	600	117
	13-11	23	560	96
	13-12	31	547	88
	6-U	32	580	141
	8-m	33	557	82
Average accumulated helium concentration, 104 appm He				

^aFor key, see Table 14.

Measurement of Swelling Using Interferometer

General

The irradiated specimens swell and topographic steps are produced at the boundary between masked (unirradiated) and unmasked (irradiated) surfaces of the specimens. Attempts were made to measure the amount of the swelling using stereo scanning methods [74,139,200-202], a Sloan profilometer [139,202,203], and an interferometer technique [34]. The Sloan profilometer technique was found to be not sufficiently precise for small step heights as low as 500 Å. Therefore, the Carl Zeiss interferometer was used for the measurement of swelling induced by irradiation.

Interferometry is known to be the most sensitive and accurate optical method of measuring the microtopography of surfaces. Two interference methods are commonly used in metallography: the two-beam and the multiple-beam. The procedures for step height measurement are well described in the references of 34, 204 and 205. For the two-beam interference method, a monochromatic beam from a thallium or sodium light source or a beam passed through a monochromatic filter is split into two beams in the microscope (Figs. 54 and 55) [204]. For this study, a thallium monochromatic light source of wave length $\lambda = 5400 \text{ Å}$ was used. One beam passed through the microscope objective to the specimen and was reflected back through the objective and into the eyepiece. The other beam passed through an identically matched objective, onto an optically flat reference plate, back through the same objective, and then was directed by the beam splitter to the eyepiece. If the optical path

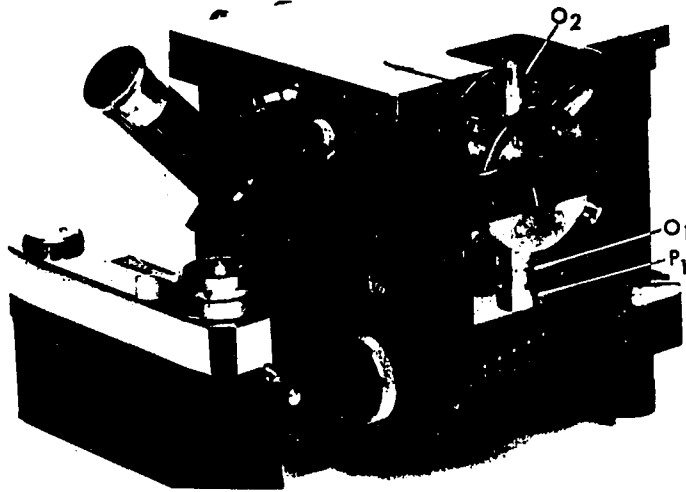


Fig. 54. The Zeiss-Linnik interferometer, for which Fig. 55 is the schematic arrangement. The notation used is the same as in Fig. 55 [204]

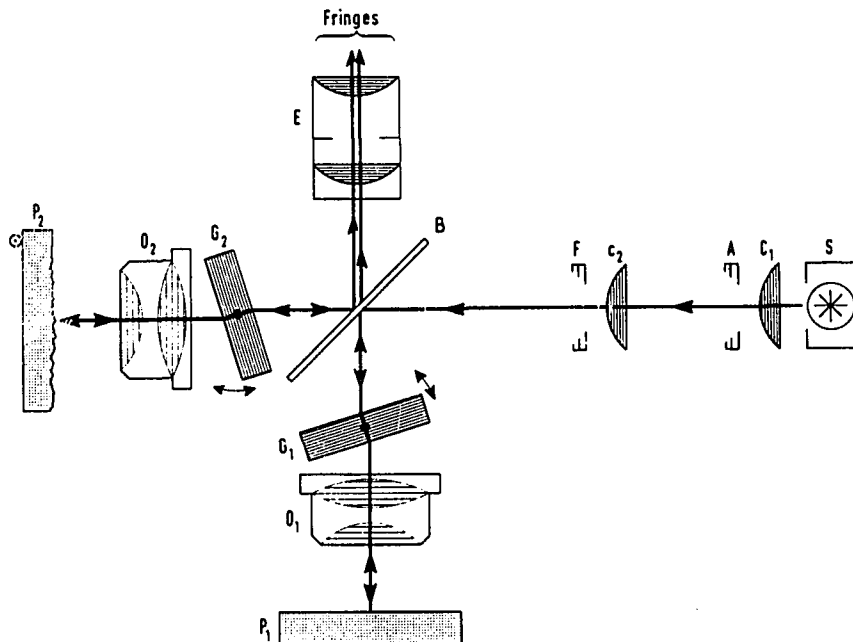


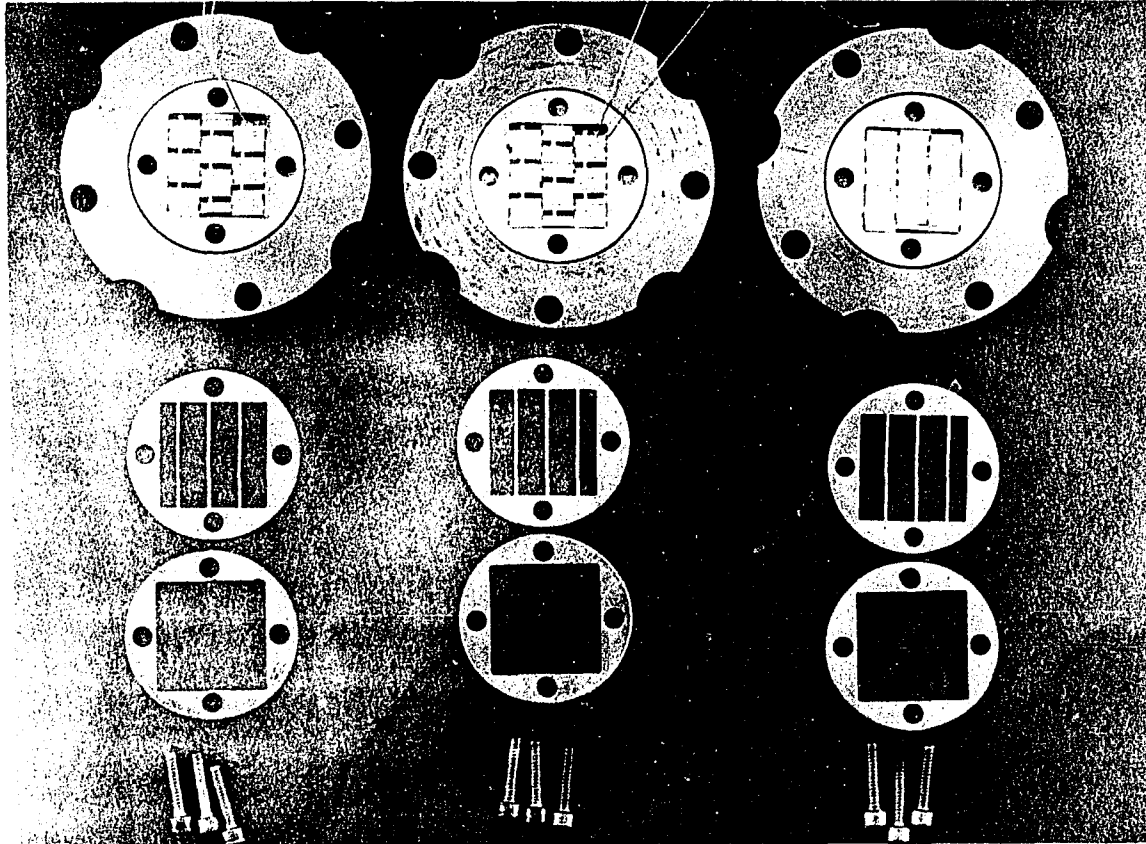
Fig. 55. A two-beam interferometer for use with reflecting specimens, known as a Linnik-type interferometer. The specimen P_2 and the reference plate P_1 are viewed by separate matched objectives O_2 and O_1 . Fringe spacing and inclination are controlled by movements of the glass blocks G_1 and G_2 [204]

difference between the two beams is equal to or a multiple of half the wave length of the monochromatic light, the beams reinforce each other. If not, the beams interfere with each other. Through this process, contour lines or fringes are formed connecting points at the same topographic level. The step height is calculated from the relative change in the spacing of the fringes [34]. Usually, a precision of 1/10 of a fringe spacing can be achieved which corresponds to step height differences of about 270 \AA using a thallium light source. For this study, each step height value was obtained from an average of about 20 measurements of the relative change in fringe spacing. A typical standard deviation was about 60 \AA .

Measurement of step height

The ion beam bombarded stacked-edge-on specimen assemblies (Fig. 56) and TEM specimen assemblies (Fig. 47) were disassembled. The surfaces of the irradiated specimens were observed in a Carl Zeiss interferometer and then photographed at a magnification of 360X. The boundary between masked and irradiated surfaces was located at the center of the photomicrographs. The shifts of the fringes were measured using a Kirem coincidence master rule, which is normally used to measure 2θ angles on Debye-Scherrer x-ray film.

Step heights of the specimens from Assembly B were measured (Table 18). As discussed earlier, the helium ions were simultaneously implanted at an angle of 15° to the vertical, whereas the Ni ions were directed vertically, as shown in Fig. 57. Because of the oblique angle for the He



Assembly A

Assembly C

Assembly B

Fig. 56. Stacked-edge-on specimen target assemblies following partial disassembly. Assembly A bombarded with Fe^{++} ions only, Assembly B before bombardment with dual beam of 4 MeV Ni^{++} and 0.4 MeV He^{+} ions, Assembly C bombarded with dual-beam of 4 MeV Fe^{++} and 0.4 MeV He^{+} ions to 100 dpa, nominal

Table 18. Swelling in the rare-earth doped and undoped AL alloys irradiated with 4 MeV Ni⁺⁺ and 0.4 MeV He⁺ ions at 570°C, nominal (Stacked-edge-on specimens)

Alloy	Specimen	Dose	Step Height (Å)			Swelling, As-observed (equivalent to h ₃)	$\frac{\Delta V/V}{\text{Normalized}}$ (%) to 100 dpa
			h ₃ ^a	h ₁ ^b	h ₂ ^c		
As-received	ALO-9	95	247	193	54	4.1	4.0%
	ALO-11	104	235	192	43	3.9	
	ALO-4	78	137	-d		2.3	
As-received and annealed	AL01-4	112	319	146	164	5.2	5.1%
	AL01-5	116	362	284	78	6.0	
	AL01-6	86	278	155	123	4.6	
Arc-melted, undoped	AL1-D	103	223	177	46	3.7	3.2%
	AL1-E	115	334	158	176	5.6	
	AL1-F	112	245	-d		4.1	
AL+0.05% Y	AL2-D	83	291	201	90	4.9	5.2%
	AL2-E	112	360	218	142	6.0	
	AL2-F	103	290	181	109	4.8	
AL+0.1% Y	AL3-5	72	186	-d		3.1	3.9%
	AL3-6	118	383	160	223	6.4	
	AL3-7	110	138	-d		2.3	
AL+0.5% Y	AL4-6	109	87	81	6	1.5	0.9%
	AL4-11	102	55	-d		0.9	
	AL4-13	98	50	-d		0.8	
AL+1.0% Y	AL5-D	90	232	-d		3.9	2.8%
	AL5-E	121	184	69	115	3.1	
	AL5-F	96	91	89	2	1.5	

^aStep height between masked and dual beam bombarded areas, h₃.

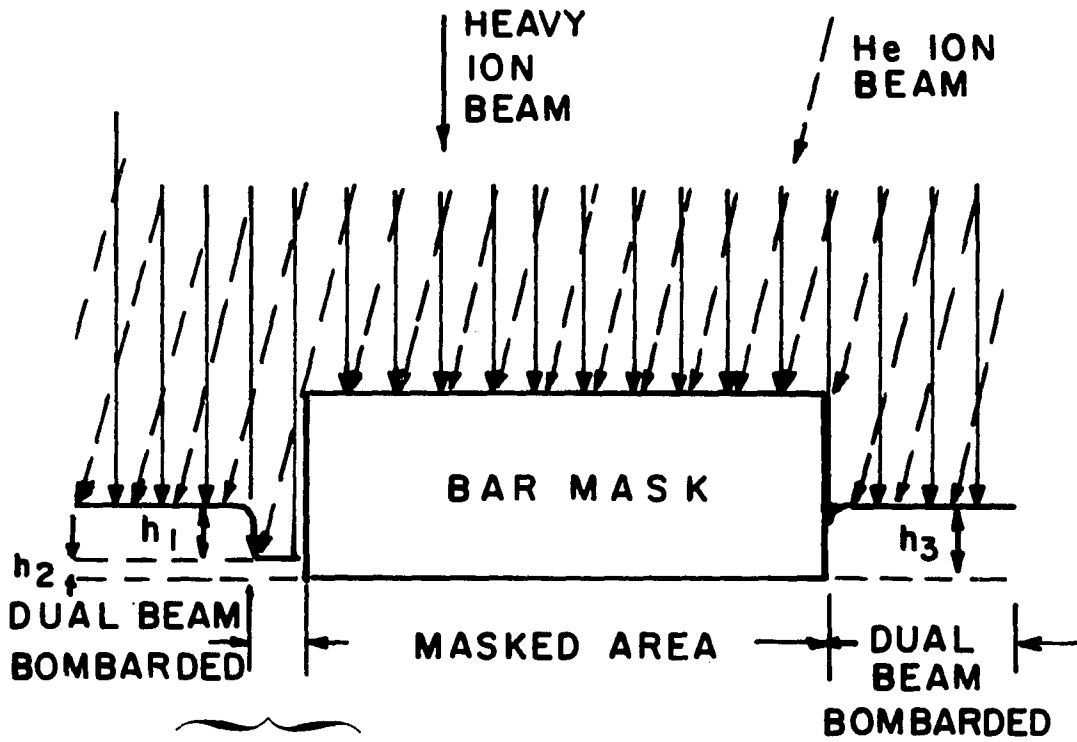
^bStep height between dual-beam bombarded and single beam bombarded areas, h₁.

^cStep height between masked and single beam bombarded areas, h₂ = h₃ - h₁.

^dStep height is smaller than the limit of resolution, about 60 Å.

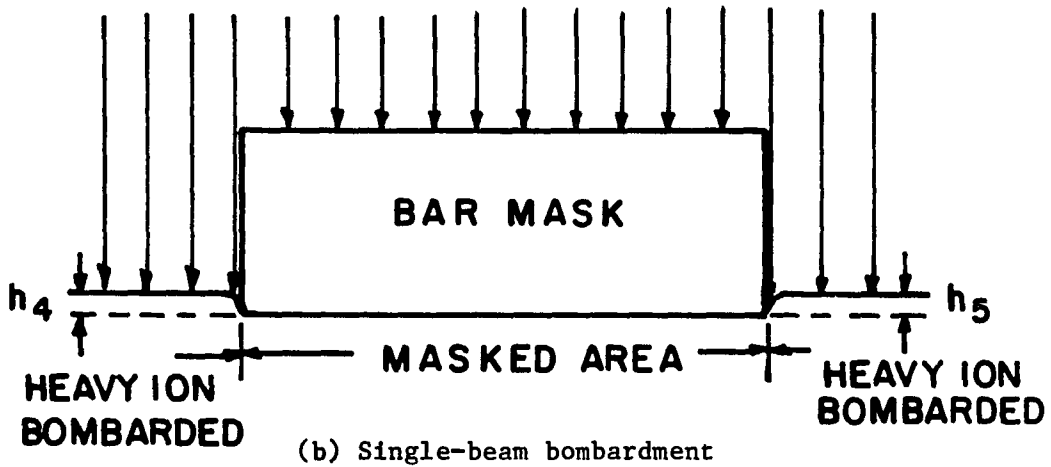
Table 18. Continued

Alloy	Specimen	Dose (dpa)	Step Height (Å)			Swelling, As-observed (equivalent to h_3)	$\frac{\Delta V}{V}$ (%) Normalized to 100 dpa
			h_3^a	h_1^b	h_2^c		
AL+0.05% La	AL6-D	79	190	131	59	3.2	4.1%
	AL6-E	120	314	123	191	5.2	
	AL6-F	102	242	132	110	4.0	
AL+0.1% La	AL7-E	113	347	313	34	5.9	4.0%
	AL7-F	104	282	163	119	4.7	
	AL7-G	96	198	-d		3.3	
AL+0.5% La	AL8-4	97	348	232	116	5.8	5.6%
	AL8-5	120	431	278	153	7.2	
	AL8-7	89	267	124	143	4.5	
AL+1.0% La	AL9-4	84	230	171	59	3.8	3.8%
	AL9-5	105	253	196	57	4.2	
	AL9-6	90	155	-d		2.6	
AL+0.05% Ce	AL10-4	117	319	275	44	5.3	4.9%
	AL10-5	117	275	177	98	4.6	
	AL10-6	82	277	-d		4.6	
AL+0.1% Ce	AL11-4	108	293	105	98	4.9	3.8%
	AL11-5	119	254	-d		4.2	
	AL11-6	93	190	115	75	3.2	
AL+0.5% Ce	AL12-4	89	207	93	114	3.5	3.3%
	AL12-5	105	208	193	23	3.5	
	AL12-6	85	114	-d		1.9	
AL+1.0% Ce	AL13-4	119	357	250	107	6.0	4.4%
	AL13-5	114	317	186	131	5.3	
	AL13-6	74	146	-d		2.4	
Standard P7 stainless steel	SS-10	97		801			
	SS-12	67	795	835			
	SS-13	103	1230	1481			
	SS-14	121	1990	1979			
	SS-15	98	937	953			
	SS-16	120	1936	1228			
	SS-17	109	1643	1777			
	SS-18	102	919	1052			
	SS-19	99	1326	1244			



SHADOWED AREA,
HEAVY ION BOMBARDED
ONLY

(a) Dual-beam bombardment. He^+ ions (dotted lines) are directed at angle of 15° to the vertical direction. Solid lines indicate heavy ions



(b) Single-beam bombardment

Fig. 57. Configuration of (a) dual-beam bombardment and (b) single-beam bombardment

beam, a shadowing effect occurred at one side of the bar mask grid. At the shadowed surface, only Ni ions are assumed to reach the surface of the sample. The step heights, h_2 (Fig. 57), at the boundary between masked and Ni ion bombarded areas were too small to be directly measured. At the boundaries between the shadowed area (bombarded with Ni ions only) and the dual-beam-bombarded area, the step heights, h_1 , were measured and compared with the step heights, h_3 , between masked and dual-beam-bombarded areas. The step heights, h_2 , induced by the single Ni ion beam were derived from the differences between h_3 and h_1 , e.g., $h_2 = h_3 - h_1$. Based on the correlation, 60 \AA corresponding to 1% swelling [17], equivalent percent swellings were calculated. The swelling was assumed to have a linear relationship with dpa values at high dose [89,175]. The normalized percent swelling equivalent to 100 dpa for each alloy was evaluated using the least-squares best fit to observed swelling versus dpa data. The values of swelling and dpa for each specimen of each alloy in the Assembly B are summarized in Table 18 and Fig. 58.

The TEM specimens from Assemblies D, E, and F were also used to measure the step heights induced by irradiation. The results of step height measurement and the equivalent swelling of the stacked-edge-on specimen and the TEM specimens are together summarized on the Table 19 and Figure 59.

The specimens from Assemblies A and C showed surface deformation but the step heights were below the limit of resolution of the microscope. This low swelling is assumed to be because of the higher irradiation

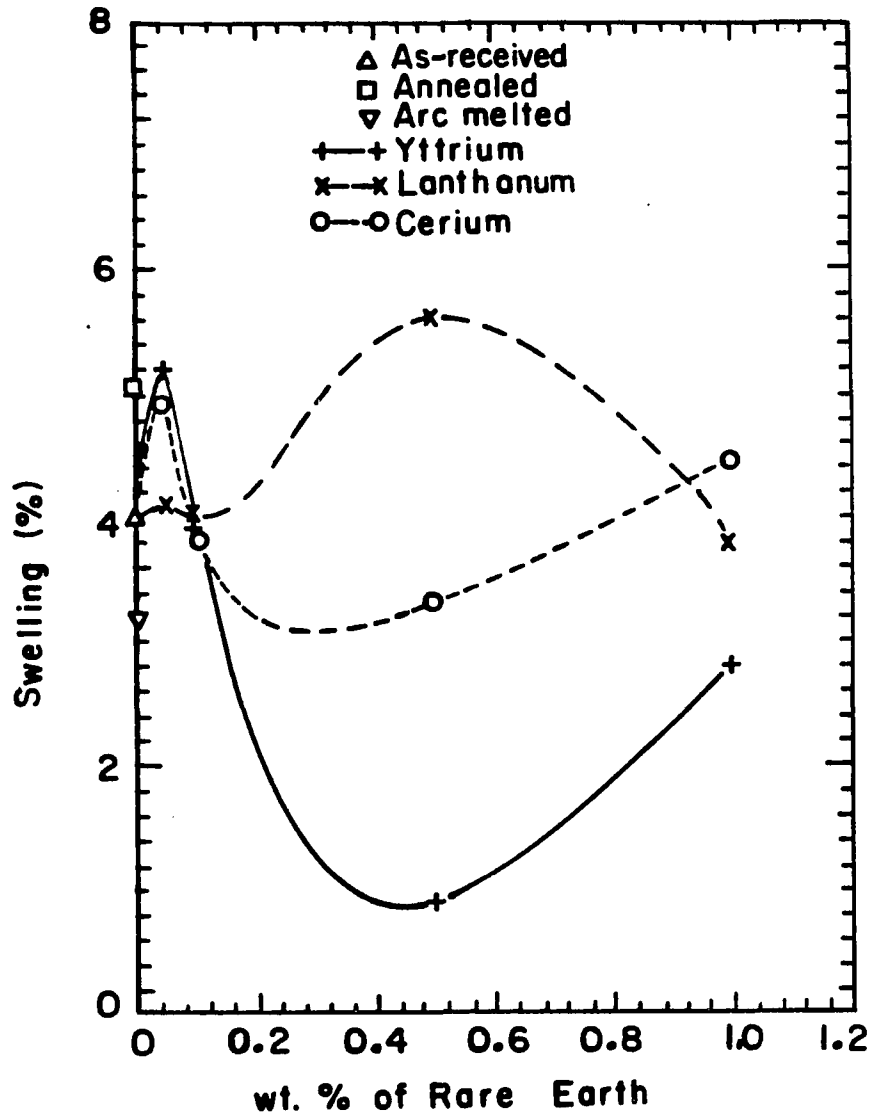


Fig. 58. Swelling in the rare-earth doped and undoped AL alloys irradiated with 4 MeV Ni^{++} and 0.4 MeV He^+ ions to 100 dpa at 570°C, nominal (stacked-edge-on specimens)

Table 19. Irradiation parameters and swelling measurement for the rare-earth doped and undoped AL alloys

Alloy	Specimen	Bombarding position	T_I (°C)	Implanted He (appm)	Dose (dpa)	Step height (Å)	Swelling, $\frac{\Delta V}{V}$ (%)	
							As-observed	Normalized to 100 dpa
As-received	AL0-9	B,6,1	570	94	95	247	4.1	
	AL0-11	B,12,1	570	94	104	235	3.9	4.0%
	AL0-4	B,18,1	570	94	78	135	2.3	
As-received and annealed	AL01-4	B,6,2	570	94	112	310	5.2	
	AL01-5	B,12,2	570	94	116	362	6.0	5.1%
	AL01-6	B,18,2	570	94	86	278	4.6	
Arc-melted, undoped	AL1-D	B,2,3	570	94	103	223	3.7	
	AL1-E	B,7,2	570	94	115	334	5.6	3.8%
	AL1-F	B,13,2	570	94	112	245	4.1	
	AL1-*	G,2,1	664	104	96	230	3.8	
	AL1-A	G,1,2	550	104	116	a		
	AL1-B	D,3,1	556	546	57	178	3.0	5.2%
	AL1-C	D,3,2	559	546	124	391	6.5	
AL+0.05% Y	AL2-D	B,1,2	570	94	90	291	4.9	
	AL2-E	B,8,3	570	94	142	360	6.0	
	AL2-F	B,14,3	570	94	109	290	4.8	5.8%
	AL2-G	E,1,1	573	102	71	419	7.0	
	AL2-F	E,3,2	566	102	135	391	6.5	

AL+0.1% Y	AL3-5	B,2,1	570	94	72	186	3.1	3.1%
	AL3-6	B,8,2	570	94	118	383	6.4	
	AL3-8	B,14,2	570	94	110	138	2.3	
	AL3-J	E,2,1	569	102	106	113	1.9	
	AL3-K	E,3,1	573	102	73	<u> </u> b		
A1+0.5% Y	AL4-6	B,3,3	570	94	109	87	1.5	2.3%
	AL4-11	B,8,1	570	94	102	55	0.9	
	AL4-13	B,14,1	570	94	98	50	0.8	
	AL4-M	E,2,2	563	102	149	401	6.7	
	AL4-P	E,3,3	569	102	84	203	3.4	
	AL4-N	F,3,1	563	85	102	224	3.7	
A1+1.0% Y	AL5-D	B,2,2	570	94	90	232	3.9	2.8%
	AL5-E	B,9,3	570	94	121	184	3.1	
	A15-F	B,15,3	570	94	96	91	1.5	
	AL5-Q	G,1,3	558	104	84	<u> </u> a		
	AL5-T	G,2,2	560	104	117	<u> </u> a		
	AL5-R	G,2,3	561	546	86	<u> </u> b		
	AL5-S	D,3,3	563	546	66	<u>278</u>	4.6	
A1+0.05% La	AL6-D	B,3,1	570	94	79	190	3.2	6.1%
	AL6-E	B,9,2	570	94	120	314	5.2	
	A16-F	B,15,2	570	94	105	242	4.0	
	A16-X	G,1,1	556	104	106	<u> </u> a		
	AL6-U	G,3,2	580	104	141	<u> </u> a		
	AL6-V	D,1,2	557	546	83	<u>354</u>	5.9	
	A16-W	D,2,2	548	546	141	389	6.5	

^aStep height is not measured.

^bStep height is smaller than the limit of resolution, about 60Å^o.

Table 19. Continued

Alloy	Specimen	Bombarding position	T _I (°C)	Implanted He (appm)	Dose (dpa)	Step height (Å)	Swelling, $\frac{\Delta V}{V}$ (%)	
							As-observed	Normalized to 100 dpa
AL+0.1% La	AL7-E	B,4,3	570	94	113	347	5.8	
	A17-F	B,9,1	570	94	104	282	4.7	
	AL7-G	B,15,1	570	94	96	198	3.3	4.2%
	AL7-e	F,1,1	563	85	80	211	3.5	
	AL7-y	F,2,1	563	85	140	292	4.9	
AL+0.5% La	AL8-4	B,3,2	570	94	97	348	5.8	
	AL8-5	B,10,3	570	94	120	431	7.2	
	AL8-7	B,16,3	570	94	89	267	4.5	6.5%
	AL8-q	E,1,2	574	102	90	504	8.4	
	AL8-m	G,3,3	557	104	82	a		
	A18-h	D,1,3	560	546	45	381	6.4	
AL+1.0% La	AL9-4	B,4,1	570	94	84	230	3.8	
	AL9-5	B,10,1	570	94	105	253	4.2	
	AL9-6	B,16,1	570	94	90	155	2.6	5.2%
	AL9-S	F,2,3	563	85	88	509	8.5	
	AL9-q	F,3,2	563	85	135	412	6.9	
AL+0.05% Ce	AL10-4	B,5,3	570	94	117	319	5.3	
	AL10-5	B,11,3	570	94	117	275	4.6	
	AL10-6	B,17,3	570	94	82	277	4.6	5.0%
	AL10-t	F,1,2	563	85	95	261	4.4	
	AL10-y	F,1,3	563	85	60	391	6.5	

Al+0.1% Ce	AL11-4	B,5,2	570	94	108	293	4.9	4.5%
	AL11-5	B,11,2	570	94	119	254	4.2	
	AL11-6	B,17,2	570	94	93	190	3.2	
	AL11-5	E,1,3	547	102	66	249	4.2	
	AL11-2	E,2,3	575	102	116	363	6.1	
Al+0.5% Ce	AL12-4	B,5,1	570	94	89	207	3.5	3.1%
	AL12-5	B,11,1	570	94	105	208	3.5	
	AL12-6	B,17,1	570	94	85	114	1.9	
	AL12-9	F,3,3	563	85	60	179	3.0	
	AL12-8	F,2,2	563	85	140	641	10.7	
AL+1.0% Ce	AL13-4	B,6,3	570	94	119	357	6.0	4.4%
	AL13-5	B,12,3	570	94	114	317	5.3	
	AL13-6	B,18,3	570	94	74	146	2.4	
	AL13-11	G,2,3	560	104	96	_a		3.9%
	AL13-12	G,3,1	547	104	98	_a		
	AL13-10	D,1,1	562	546	89	210	3.5	
AL13-13	D,2,1	560	546	134	_b			
Standard P7 stainless steel (Assembly A)	SS-1	A,1,3	600	--	91	2840	47	53%
	SS-2	A,1,1	600	--	104	2440	41	
	SS-3	A,4,2	600	--	115	2340	39	
	SS-4	A,7,3	600	--	106	2930	41	
	SS-5	A,7,1	600	--	106	3340	56	
	SS-6	A,10,2	600	--	118	3130	52	
	SS-7	A,13,3	600	--	106	3450	58	
	SS-8	A,13,1	600	--	91	3580	60	
	SS-9	A,16,2	600	--	102	3980	66	

Table 19. Continued

Alloy	Specimen	Bombarding position	T ₁ (°C)	Implanted He (appm)	Dose (dpa)	Step height (Å)	Swelling, $\frac{\Delta V}{V}$ (%)	
							As-observed	Normalized to 100 dpa
Standard P7 stainless steel (Assembly C)	SS-10	B,1,3	570	94	97	a		
	SS-12	B,1,1	570	94	67	800	13	
	SS-13	B,4,2	570	94	103	1230	21	
	SS-14	B,7,3	570	94	121	1990	33	
	SS-15	B,7,1	570	94	98	940	16	
	SS-16	B,10,2	570	94	120	1940	32	22%
	SS-17	B,13,3	570	94	109	1640	27	
	SS-18	B,13,1	570	94	102	920	15	
	SS-19	B,16,2	570	94	99	1330	22	
Standard P7 stainless steel (Assembly B)	SS-20	C,1,3	600	100	92	2840	47	
	SS-21	C,1,1	600	100	79	3830	64	
	SS-22	C,4,2	600	100	124	2750	46	
	SS-23	C,7,3	600	100	118	2590	43	
	SS-24	C,7,1	600	100	116	3000	50	56%
	SS-25	C,10,2	600	100	135	3020	50	
	SS-26	C,13,3	600	100	95	3520	59	
	SS-27	C,13,1	600	100	100	3660	61	
	SS-28	C,16,2	600	100	90	3970	66	

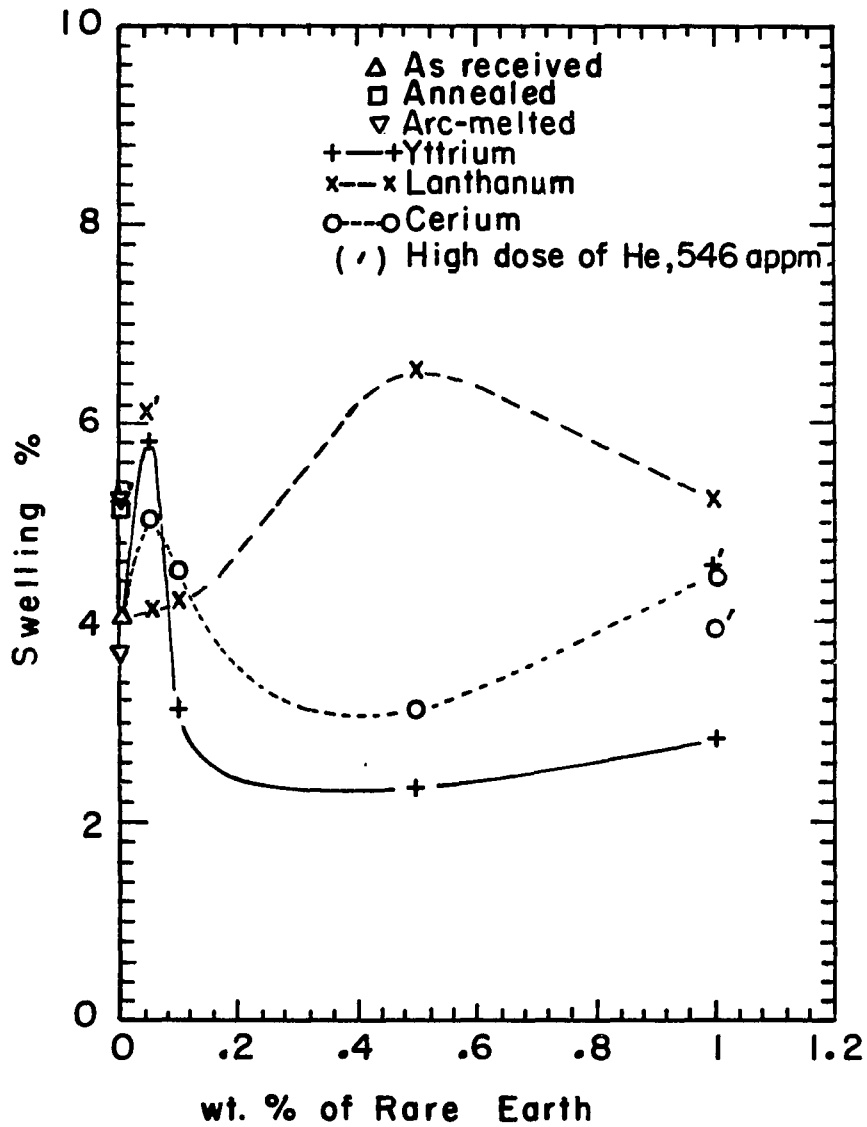


Fig. 59. Swelling in the rare-earth doped and undoped AL alloys irradiated with 4 MeV Ni^{++} and 0.4 MeV He^+ ions to 100 dpa at 570° , nominal (stacked-edge-on and TEM specimens)

temperature, $600 \pm 25^{\circ}\text{C}$, as compared to $570 \pm 15^{\circ}\text{C}$ for Assembly

B. The peak a swelling temperature of the AL alloy is assumed to be about 570°C [34].

Fig. 60 shows a sectional diagram of a TEM specimens of AL-1 alloy used for the measurement of step heights induced by irradiation and electropolishing. The specimen was masked with a miniature molybdenum bar mask and irradiated with the dual beam of 4 MeV Ni and 0.4 MeV He ions up to an accumulated dose of 96 dpa. Then, a part of the specimen surface was lacquered and the sample was electropolished. From the specimen surface, sections of irradiated and lacquered (areas #1 and #3), masked and lacquered (area #2), irradiated and electropolished (areas #4 and #6), and masked and electropolished (area #5) can be observed. Through optical observations at 60X (Fig. 61a) and 360X (Fig. 61b) magnification, the boundaries of each section are clearly defined. Interference fringes were vertically (Fig. 62a) and horizontally (Fig. 62b) applied on the 360X magnified images, and photographed. The shifts of the fringes at the boundaries between sections #1 and #4, #2 and #5, and #3 and #6 in Fig. 62a and #1 and #2, #2 and #3, #4 and #5, and #5 and #6 in Fig. 62b were measured and the corresponding step heights were calculated (Table 20). With the same procedure, the other TEM specimens from the assemblies D, E and F were analyzed to evaluate the step height induced by dual beam bombardment and the corresponding percent swelling.

At the boundary between the masked (#2 and #5) and irradiated (#3 and #6) areas (Figs. 60 and 62), another section #5' was revealed after electropolishing, and the presence of the section #3' was able to be

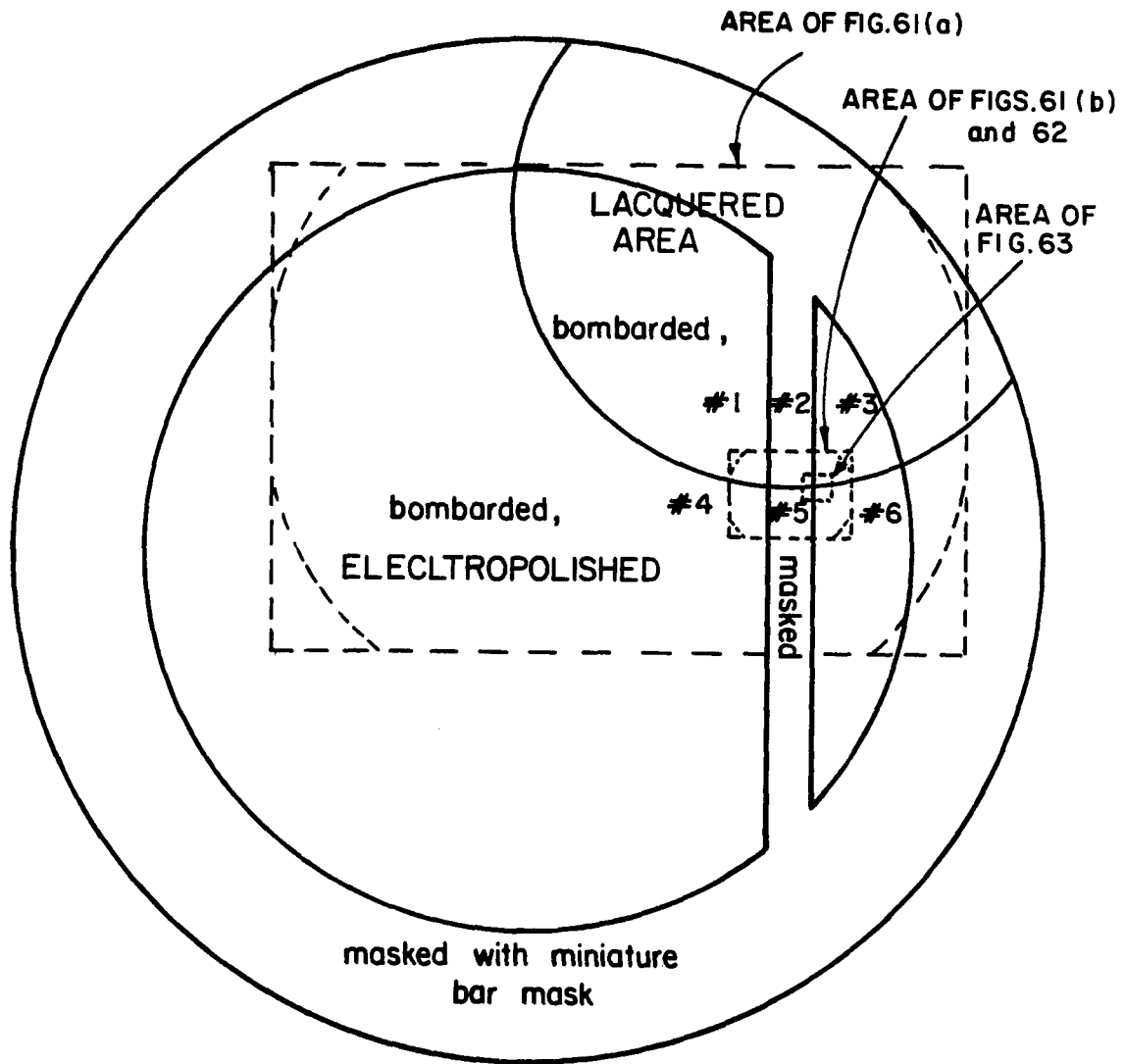


Fig. 60. Sectional diagram of a TEM specimens, #1 and #3 ion bombarded and lacquered, #2 masked and lacquered, #4 and #6 ion bombarded and electropolished, and #5 masked and electropolished areas

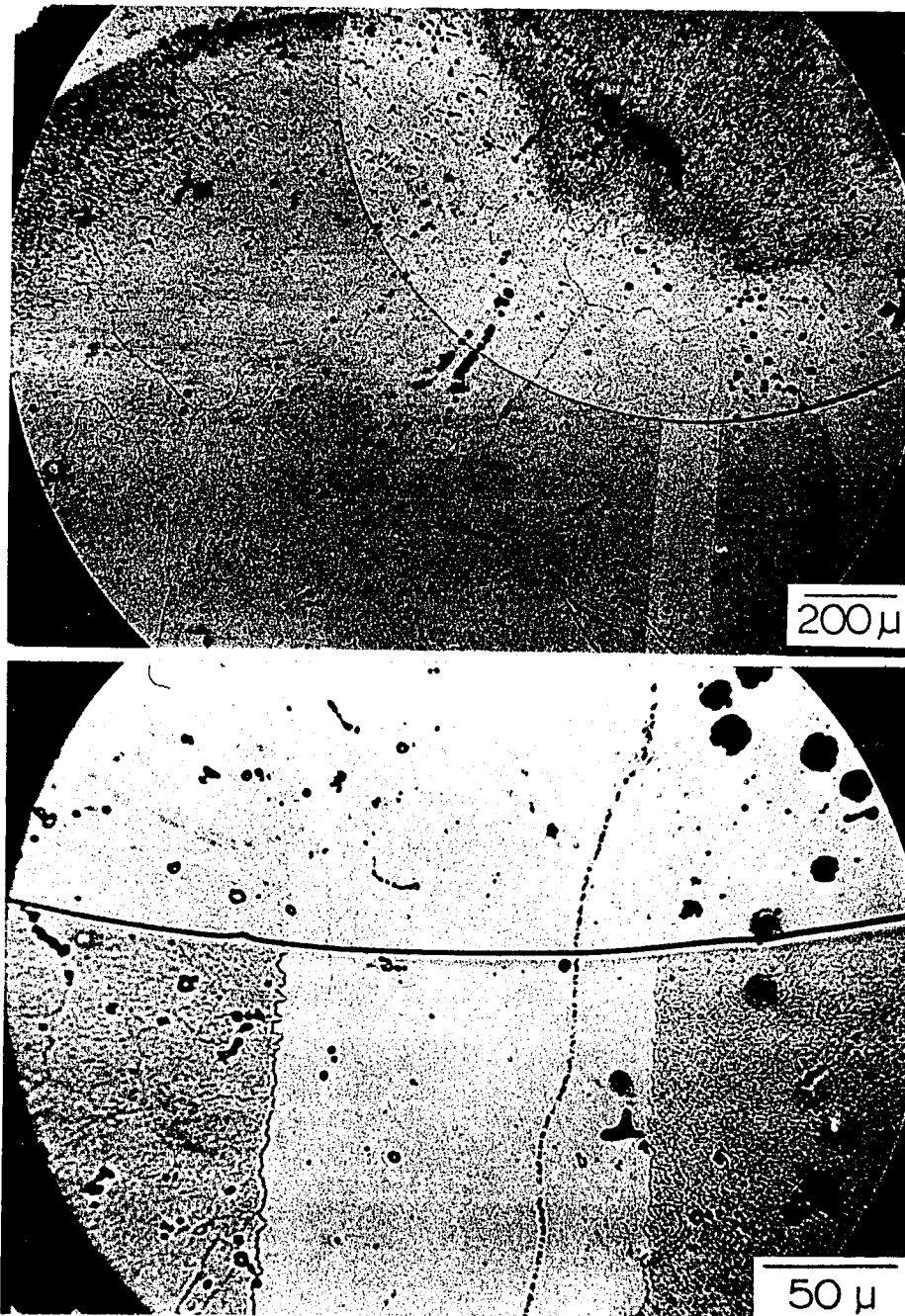


Fig. 61. Masked with a miniature bar mask, ion bombarded, lacquered, and electropolished TEM specimen of AL-1 alloy at (a) 60X and (b) 360X magnification

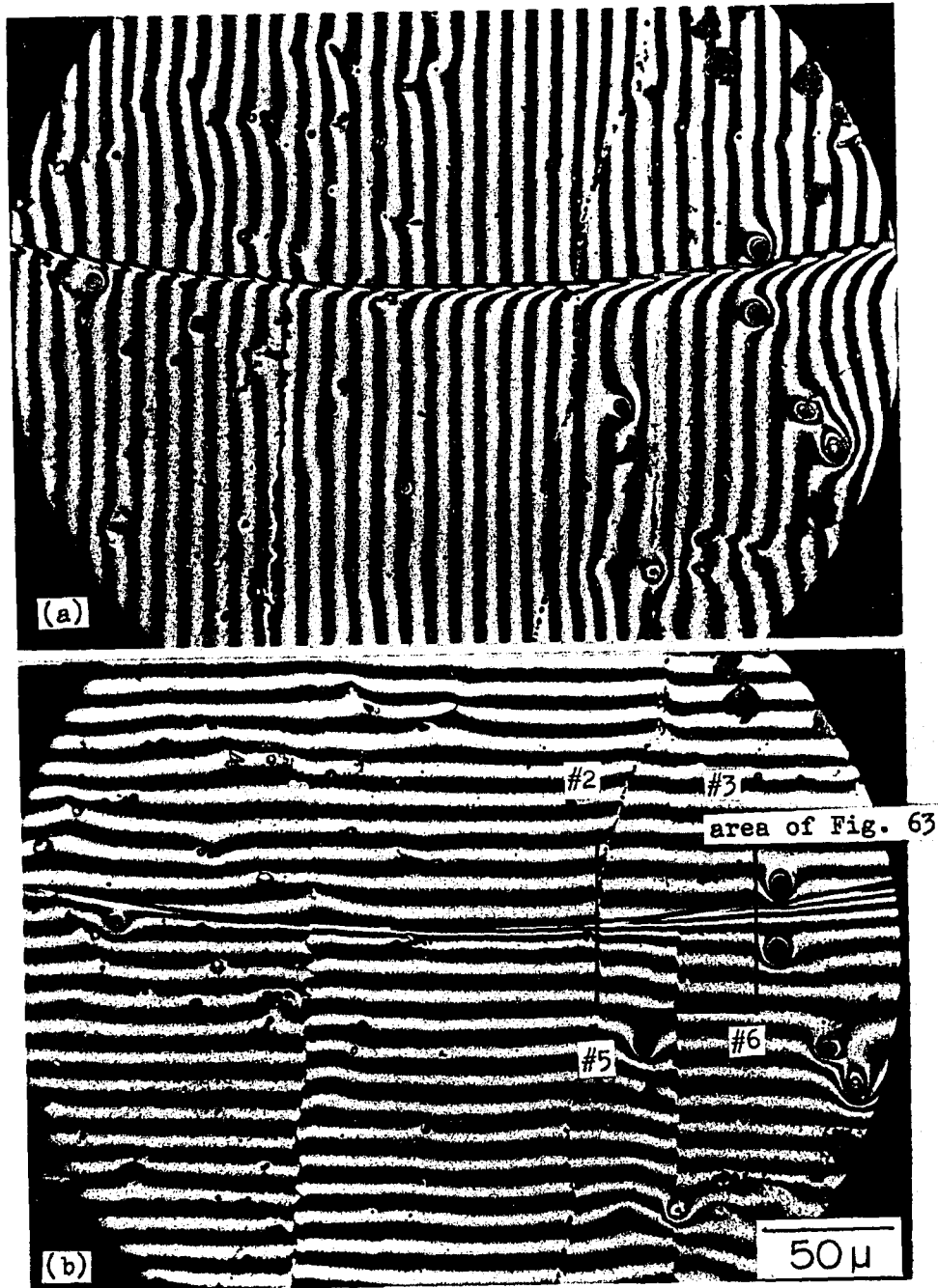


Fig. 62. Masked, ion bombarded, lacquered and electropolished TEM specimen of AL-1 alloy with (a) vertical and (b) horizontal interference fringes

inferred (Fig. 63), but not clearly identified. The width of these subsections was measured to be about 3% of the bar mask width, about 0.13 mm. The boundary between subsections #5' and #6 was clearly defined. Due to the electropolishing, the boundary between sections #5' and #6 was revealed. The sections #3' and #5' are believed to be the shadowed areas; He ions injected at 15° to the vertical direction were shadowed by the miniature bar mask, and hence, Ni ions only reached the sample.

Fig. 64, drawn from the results of the step-height measurements (Table 20), shows an illustrative topography for the unpolished (lacquered) surface and the electropolished surface. The sections #2, #3' and #3 are preferentially swelled according to the nature of the irradiation at each section, and steps are developed at the boundaries between the areas. Sections #2 and #5 were not irradiated and no defects were produced. Defect clusters and voids are assumed to have accumulated and induced swelling at sections #3' and #5', but no helium bubbles were formed as no helium was implanted. However, at sections #3 and #6, a high density of helium bubbles is expected to have accumulated in addition to defect clusters and voids. These sections appear to have experienced the same amount of swelling, as is seen in Figs. 63 and 64 from the fact that the contour lines do not change when the boundary between sections #3' and #3 is crossed. Also, Figs. 63 and 64 show that section #6 experienced much less removal of material upon electropolishing than did section #5'. This may be due to an increased resistivity for section #6 due to the small helium bubbles, which contain



Fig. 63. Enlargement of Fig. 62(b), showing masked areas #2 and #5, shadowed areas #3' and #5' (areas irradiated by Ni^{++} ion beam only), and dual-beam-bombarded areas #3 and #6. The top area #2, #3' and #3 were lacquered after bombardment, and the bottom areas #5, #5', and #6 were not lacquered. Therefore, only area #5, #5', and #6 were electropolished. The lacquer was removed, and the sample was cleaned following the electropolishing

helium gas at high pressure. The increased resistivity causes the electropolishing rate to be reduced, thus producing the 930 \AA step between sections #5' and #6 shown in Fig. 64. By comparison, the boundary between sections #5 and #5' is not sharp, which suggests that the electropolishing rate and the electrical resistivity were about the same for sections #5 and #5'.

Another comment concerning Figs. 60-64 is that the dual-beam-bombarded and then electropolished sections #4 and #6 have much rougher surfaces than the other areas (See particularly Figs. 62 and 63). This is a further indication that the helium bubbles produced a change in electropolishing characteristics.

Beam Intensity Distribution

Beam control and diagnostics apparatus is intended to facilitate the irradiation of a large number of specimens. To do this, a relatively large target area with a reasonably uniform beam is achieved using the unique split field lens described by Johnson [199]. However, to be successful these techniques require thorough monitoring and analysis of the beam in the target region. Diagnostic equipment is traversed by the heavy-ion beam in the following order: a beam profile monitor, a movable assembly of nine miniature Faraday cups, a movable aperture mask, the target, and, finally a deep Faraday cup. The light-ion beam (for this study, He^+ beam) has its own beam profile monitor (located about 1 m ahead of the target plane) and its own deep Faraday cup.

The beam that enters the damage chamber is defined by an 11 x 11 mm

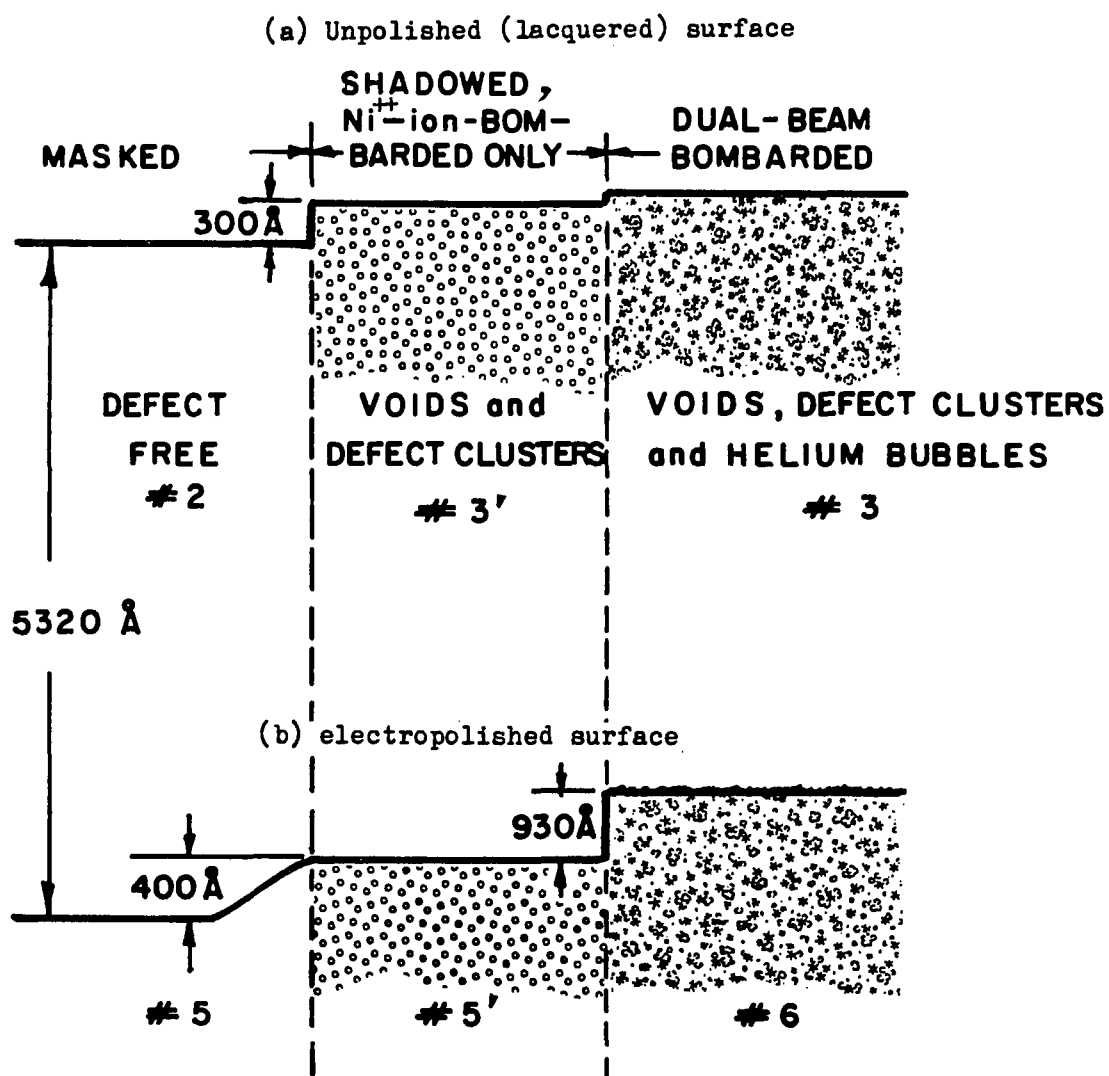


Fig. 64. Topographic configuration of the cross section of the masked (unbombarded), shadowed (bombarded by Ni⁺⁺ ions only), and dual-beam-bombarded areas. (a) Unpolished (lacquered) surface, and (b) electropolished surface. See Table 20 and Fig. 63

Table 20. Step heights at the boundaries between lacquered and electropolished and masked, single beam and dual beam bombarded areas of the TEM specimen. See Fig. 62

Boundary	Step-height
#1-#4	$3508 \pm 68\text{\AA}$
#2-#5	$5319 \pm 64\text{\AA}$
#3-#6	$4284 \pm 56\text{\AA}$
#1-#2	$156 \pm 13\text{\AA}$
#2-#3	$305 \pm 26\text{\AA}$
#4-#5	$928 \pm 48\text{\AA}$
#5-#6	$931 \pm 25\text{\AA}$
#1 and #3:	ion beam bombarded and lacquered areas
#2:	masked and ion beam bombarded
#4 and #6:	ion beam bombarded and electropolished areas
#5:	masked and electropolished area

fixed square aperture behind a pneumatically actuated gate valve. The ion beam uniformity and intensity are monitored during each bombardment run by a nine hole miniature deep Faraday cup array. The deep Faraday cups are positioned in front of the target holder in the beam line every 10 minutes for approximately 20 seconds. The information gathered by the deep Faraday cups is sent to an ion beam current integrator, which assists in the maintenance of a bombardment run log, listing beam currents and accumulative beam displacement concentrations for each of the nine targets being bombarded. Once pre-programmed displacement concentration levels are reached, the ion beam is automatically terminated. The accumulated ion fluences are recorded in dpa values. But, for the stacked-edge-on multi-specimen assembly, the dpa data could not be used directly since the array orientations of the nine miniature Faraday cups (Fig. 50) and the multi-specimen array (Fig. 56) traversed to the beam direction were not coincident.

To evaluate the accumulated ion-beam fluence for each of the 54 specimens of the assembly, the areal distribution of the dpa values is assumed to be described by a two-dimensional function, as follows:

$$D = D_0 \exp\{ - \vec{\bar{X}} \cdot \vec{\bar{Q}} \cdot \vec{\bar{X}} \} \quad (18)$$

where, D = dpa value at position (X_1, X_2)

D_0 = calculated peak dpa value at position (α_1, α_2)

$\vec{\bar{X}}$ = transposed vector of \vec{X}

$$\vec{X} = \begin{pmatrix} x_1 - \alpha_1 \\ x_2 - \alpha_2 \end{pmatrix} \quad (19)$$

$$Q = \begin{pmatrix} Q_{11} & Q_{12} \\ Q_{21} & Q_{22} \end{pmatrix} \quad (20)$$

= intensity shape matrix where $Q_{12} = Q_{21}$

α_1, α_2 = the peak position of the dpa values.

The six constants, D_0 , α_1 , α_2 , Q_{11} , Q_{12} and Q_{22} in Eq. (18) can be obtained using the data of dpa values measured by the nine miniature Faraday cups and the non-linear regression, modified Gauss-Newton method programmed in the statistical analysis system known as SAS [206]. Eq. (18) with the constants obtained (Table 16) gives a series of contour curves (ellipses of constant dpa) as shown in Fig. 65a for the case of assembly B. The orientations of the principal axes of the dpa-ellipses are known relative to the array axes of the nine Faraday cups, but not relative to the bombarded samples.

In a similar way, the step height measurements on the nine P7 stainless steel reference samples in the stacked-edge-on array give a series of ellipses of constant step height. The orientations of the principal axes of these ellipses are known relative to the row and column directions in the stacked-edge-on array. The distribution of step heights is assumed to obey a function similar to that in Eq. (18), namely

$$S = S_0 \exp \{-\tilde{\vec{Y}} \cdot \bar{\bar{R}} \cdot \vec{Y}\} \quad (21)$$

where S = step height of P7 sample at position (y_1, y_2)

S_0 = calculated peak step height at position (β_1, β_2)

$$\vec{Y} = \begin{Bmatrix} y_1 - \beta_1 \\ y_2 - \beta_2 \end{Bmatrix}$$

$\tilde{\vec{Y}}$ = transpose vector of \vec{Y}

$$\bar{\bar{R}} = \begin{Bmatrix} R_{11} & R_{12} \\ R_{21} & R_{22} \end{Bmatrix} = \text{step height shape matrix, where } R_{12} = R_{21}$$

β_1, β_2 = the peak position of the step height.

The six constants, S_0 , β_1 , β_2 , R_{11} , R_{12} and R_{22} were obtained from the nine measured step heights of the nine standard P7 stainless steel samples. The non-linear regression modified Gauss-Newton method was again used, as programmed in the statistical analysis system, SAS [206]. The constant step height ellipses are shown in Fig. 65 (b) for Assembly B. The assumption is then made that the directions of the principal axes in Fig. 65 (a) (dpa ellipses) and Fig. 65 (b) (step height ellipses) should be coincident.

The determination of the principal axes for the dpa ellipses was carried out as follows. For a constant value of D , equation (18) can be written

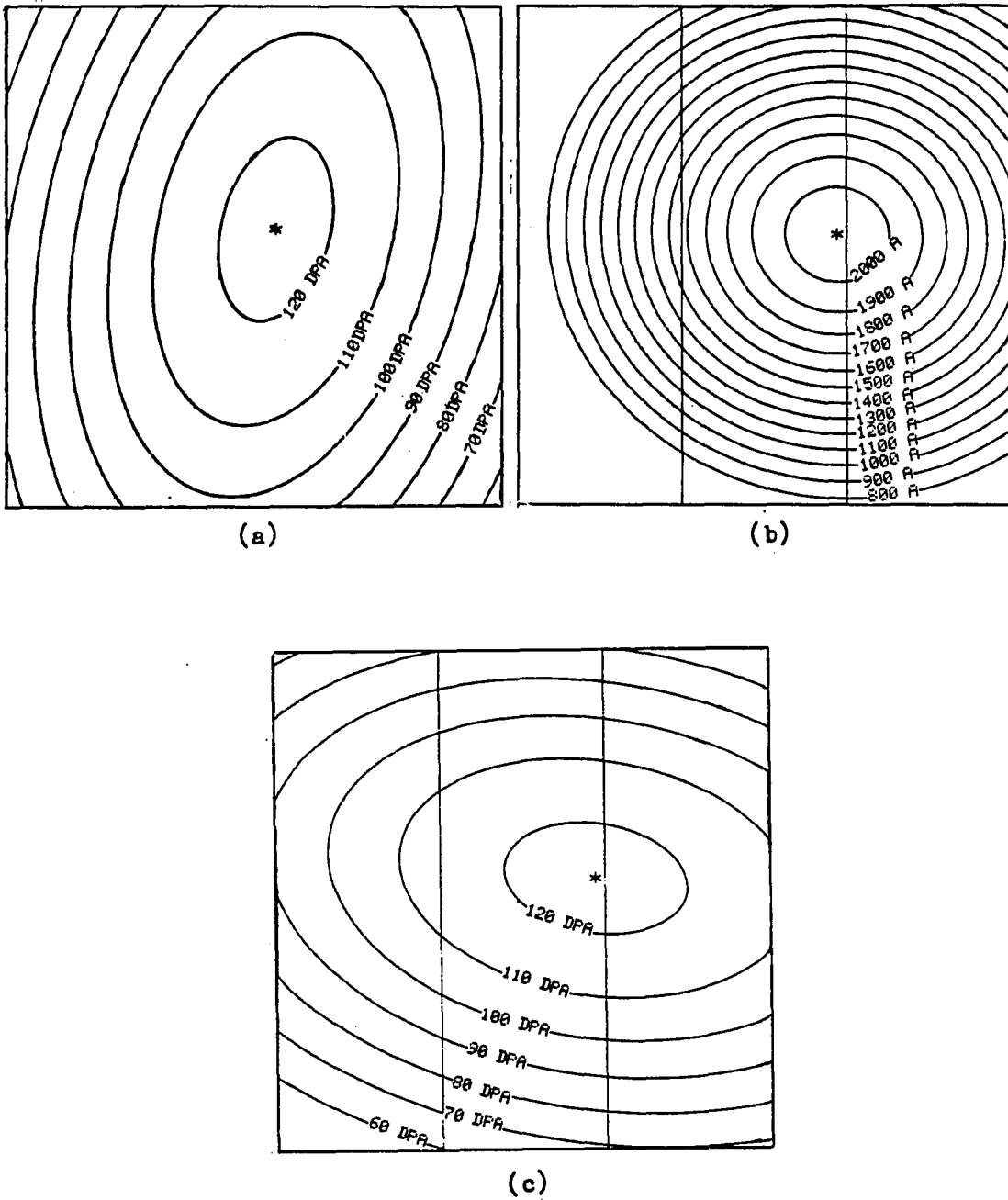


Fig. 65. Contour curves of (a) the irradiated dose in dpa from the measurements using the nine miniature Faraday cups, (b) step heights from the measurements of the pure stainless steel, P7, and (c) modified irradiation dose in dpa of the assembly B

$$\ell_n \frac{D_o}{D} = c = (x_1 - \alpha_1, x_2 - \alpha_2) \begin{Bmatrix} Q_{11} & Q_{12} \\ Q_{21} & Q_{22} \end{Bmatrix} \begin{Bmatrix} x_1 - \alpha_1 \\ x_2 - \alpha_2 \end{Bmatrix} \quad (22)$$

Let $x_1' = x_1 - \alpha_1 = r \cos\theta$ and $x_2' = x_2 - \alpha_2 = r \sin\theta$. Then Eq.

(22) gives

$$\frac{c}{r^2} = Q_{11} \cos^2\theta + 2Q_{12} \sin\theta \cos\theta + Q_{22} \sin^2\theta$$

The principal axes are oriented at angles such that

$$\frac{d}{d\theta} \left(\frac{c}{r^2} \right) = 0$$

which gives

$$\tan 2\theta_{1,2} = \frac{2Q_{12}}{Q_{11} - Q_{22}} \quad (23)$$

where the two values, θ_1 and θ_2 are 90° apart. Equation (23) gives

$$\tan\theta_1 = \frac{1}{2Q_{12}} (Q_{22} - Q_{11} + \sqrt{(Q_{22} - Q_{11})^2 + 4Q_{12}^2})$$

$$\tan\theta_2 = \frac{1}{2Q_{12}} (Q_{22} - Q_{11} - \sqrt{(Q_{22} - Q_{11})^2 + 4Q_{12}^2})$$

To determine the angle between the x_1 -axis and the major-axis of the ellipse, the value of $\frac{d^2}{d\theta^2} \left(\frac{c}{r^2} \right)$ is examined as follows

$$\frac{d^2}{d\theta^2} \left(\frac{C}{r^2} \right) = 2(Q_{22} - Q_{11}) \cos 2\theta - 2Q_{12} \sin 2\theta \quad (24)$$

Applying θ_1 and θ_2 to Eq. (24), the angle that makes $\frac{d^2}{d\theta^2} \left(\frac{C}{r^2} \right)$ positive is the angle between the major axis and the x_1 axis. Let that angle be θ_d .

With the same procedure and Eq. (21), the angle, θ_s , between major axis of the step height ellipse and the x axis can be obtained. To make the axes coincident for the dpa distribution function and the step height distribution function, the major axis of the dpa distribution function should be rotated through angle $\theta_0 = \theta_s - \theta_d$ by operating by a rotation matrix

$$S = \begin{pmatrix} \cos\theta_0 & \sin\theta_0 \\ -\sin\theta_0 & \cos\theta_0 \end{pmatrix} \quad (25)$$

and by moving the peak dpa point to the peak stepheight point (β_1, β_2) .

This gives

$$\begin{aligned} & D(x_1, x_2) \\ &= D_0 \exp\{-\vec{X} \cdot \vec{S} \cdot \vec{Q} \cdot \vec{S} \cdot \vec{X}\} \\ &= D_0 \exp \left[- \begin{pmatrix} x_1 - \beta_1 \\ x_2 - \beta_2 \end{pmatrix} \begin{pmatrix} \cos\theta_0 & \sin\theta_0 \\ -\sin\theta_0 & \cos\theta_0 \end{pmatrix} \begin{pmatrix} Q_{11} & Q_{12} \\ Q_{21} & Q_{22} \end{pmatrix} \begin{pmatrix} \cos\theta_0 & \sin\theta_0 \\ -\sin\theta_0 & \cos\theta_0 \end{pmatrix} \begin{pmatrix} x_1 - \beta_1 \\ x_2 - \beta_2 \end{pmatrix} \right] \end{aligned} \quad (26)$$

Using the dpa distribution function (26) the accumulated ion dose for each specimen is calculated. These computational procedures are programmed in basic language (Fig. A.1) and the results are shown in Figs. 65c, 66 and 67 for Assembly B, and Figs. 68a, 69 and 70 for Assembly A.

For Assembly C, the angle of rotation was reported to be 15° and the center of peak position of the ion beam was calculated using the center-of-area equation following

$$\beta_1 = \frac{\sum x_{1i} S_i}{\sum x_{1i}} \quad (27)$$

$$\beta_2 = \frac{\sum x_{2i} S_i}{\sum x_{2i}} \quad (28)$$

where β_1, β_2 = peak position of step height

x_{1i} = position along x-axis of the i'th measured step height

x_{2i} = position along x-axis of the i'th measured step height

The areal distribution function of the dpa values on Assembly C was obtained using the shape matrix calculated from the dpa values measured by the nine miniature Faraday cups, above calculated peak position and rotation angle 15° as shown in Fig. 71. The dpa values of each position on the specimens are calculated (Figs. 68b and 72).

```

=====
ASSEMBLY # 2
=====
STEP-HEIGHT SHAPE-MATRIX : S-6
  Q11 = .02754 , Q12 = 1.008E-03
  Q21 = 1.008E-03 , Q22 = .03387

THETA1 = 1.41663302 RAD : 81.1670929 DEG
THETA2 = -.154163354 RAD : -8.83290953 DEG
D↑2(C/R↑2)THETA1 = -.0126747734
D↑2(C/R↑2)THETA2 = .0126747732

ANGLE BTWN MAJOR- & X-AXIS : -.154163354 RAD
-----
DPA SHAPE-MATRIX ; FARADAY CUP
  Q11 = .01931 , Q12 = -3.22E-03
  Q21 = -3.22E-03 , Q22 = 7.765E-03

THETA1 = -.254412556 RAD : -14.5767657 DEG
THETA2 = 1.31638377 RAD : 75.4232343 DEG
D↑2(C/R↑2)THETA1 = -.023302156
D↑2(C/R↑2)THETA2 = .023302156

ANGLE BTWN MAJOR- & X-AXIS : 1.31638377 RAD
-----
TRANSFORM-ANGLE : -1.47054712 RAD
TRANSFORM-MATRIX (IN RAD) ;
  COS(-1.47054712 ) SIN(-1.47054712 )
  -SIN(-1.47054712 ) COS(-1.47054712 )
  OR
  .100081371 , -.994979256
  .994979256 , .100081371
=====
TRANSFORMED SHAPE-MATRIX
  7.23934993E-03 , 2.00585689E-03
  2.00585689E-03 , .0198356501

THETA1 = 1.41663297
THETA2 = -.154163355

ANGLE BTWN MAJOR- AND X-AXIS IS
-.154163355 RAD

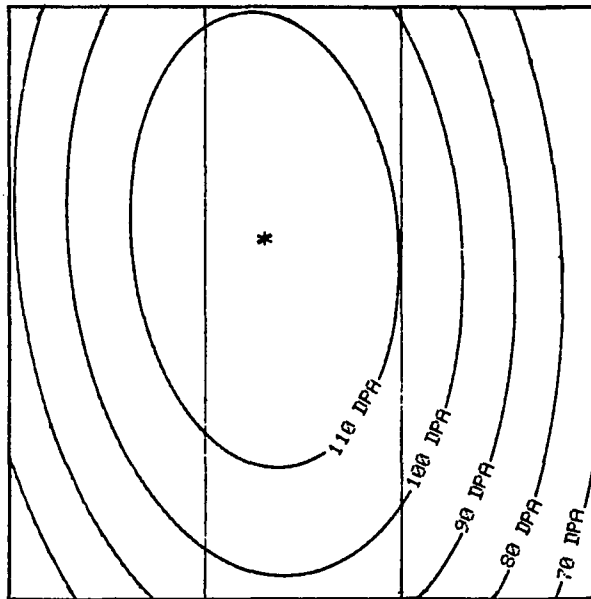
PEAK PT.OF STEP-HEIGHT ( 6.4755 , 4.5897 )
PEAK VALUE OF DPA : 122.94

```

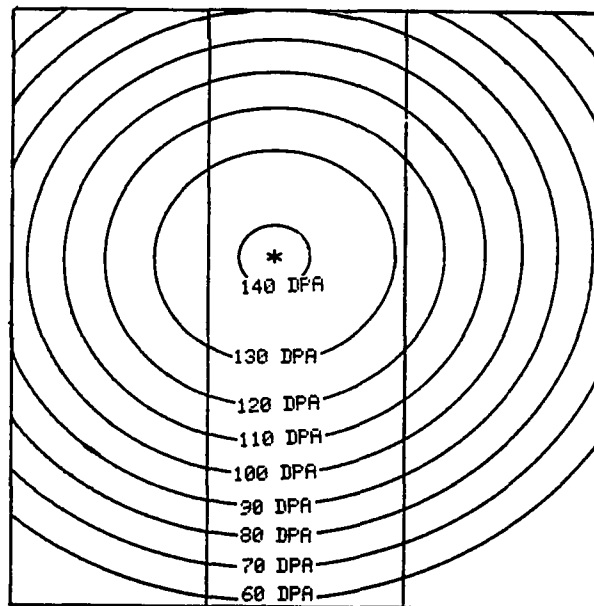
Fig. 66. Input and calculated values of the areal distribution function of the step height and irradiation dose in dpa of the assembly B

#	X1	X2	DPA	X1	X2	DPA	X1	X2	DPA
1	1.98	.691	67	4.86	.531	83	7.35	.861	97
2	1.98	1.16	72	4.86	1.06	90	7.35	1.42	103
3	1.98	1.68	79	4.86	1.56	97	7.35	1.94	109
4	1.98	2.15	84	4.86	2.06	103	7.35	2.39	113
5	1.98	2.65	89	4.86	2.54	108	7.35	2.86	117
6	1.98	3.25	95	4.86	3.07	112	7.35	3.31	119
7	1.98	3.72	98	4.86	3.47	115	7.35	3.81	121
8	1.98	4.31	102	4.86	4.08	118	7.35	4.29	122
9	1.98	4.75	104	4.86	4.79	120	7.35	4.77	121
10	1.98	5.31	105	4.86	5.31	120	7.35	5.21	120
11	1.98	5.81	105	4.86	5.79	119	7.35	5.81	117
12	1.98	6.39	104	4.86	6.31	116	7.35	6.31	114
13	1.98	6.91	102	4.86	6.84	112	7.35	6.82	109
14	1.98	7.51	98	4.86	7.18	110	7.35	7.38	103
15	1.98	7.87	96	4.86	7.64	105	7.35	7.97	96
16	1.98	8.47	90	4.86	8.14	99	7.35	8.51	89
17	1.98	8.97	85	4.86	8.67	93	7.35	8.96	82
18	1.98	9.59	78	4.86	9.23	86	7.35	9.52	74

Fig. 67. Calculated values of dpa at the boundary of the masked and dual beam bombarded areas of the stacked-edge-on specimens in the assembly B



(a) Assembly A



(b) Assembly C

Fig. 68. Contour curves of the calculated dose in dpa of (a) Assembly A and (b) Assembly C

```

=====
ASSEMBLY # 1
=====
STEP-HEIGHT SHAPE-MATRIX :S-S
  Q11 = .01342 ,Q12 = 3.678E-04
  Q21 = 3.678E-04 ,Q22 = 9.373E-03

THETA1 = .08990065 RAD : 5.15092783 DEG
THETA2 =-1.48089567 RAD :-84.8490718 DEG
D12(C/R12)THETA1 =-8.09506896E-03
D12(C/R12)THETA2 = 8.09506895E-03

ANGLE BTWN MAJOR- & X-AXIS :-1.48089567 RAD
-----
DPA SHAPE-MATRIX ; FARADAY CUP
  Q11 = 5.865E-03 ,Q12 = 1.965E-03
  Q21 = 1.965E-03 ,Q22 = .0154

THETA1 = 1.3753214 RAD : 78.8001115 DEG
THETA2 =-.195474932 RAD :-11.1998886 DEG
D12(C/R12)THETA1 =-.0191287136
D12(C/R12)THETA2 = .0191287136

ANGLE BTWN MAJOR- & X-AXIS :- .195474932 RAD
-----
TRANSFORM-ANGLE :-1.28542074 RAD
TRANSFORM-MATRIX (IN RAD) ;
  COS(-1.28542074 ) SIN(-1.28542074 )
 -SIN(-1.28542074 ) COS(-1.28542074 )
  OR
  .281517869 ,-.959555985
  .959555985 , .281517869
=====
TRANSFORMED SHAPE-MATRIX
  .0157059486 , 9.22171689E-04
  9.22171689E-04 , 5.55905141E-03

THETA1 = .0899006634
THETA2 =-1.48089567

ANGLE BTWN MAJOR- AND X-AXIS IS
-1.48089567 RAD

PEAK PT.OF STEP-HEIGHT ( 4.3476 , 3.9372 )
PEAK VALUE OF DPA : 119.32

```

Fig. 69. Input and calculated values of the areal distribution function of the step height and irradiation dose in dpa of the assembly A

#	X1	X2	DPA	X1	X2	DPA	X1	X2	DPA
1	1.34	.311	104	4.28	.311	108	7.24	.801	91
2	1.34	.851	106	4.28	.861	111	7.24	1.32	94
3	1.34	1.41	107	4.28	1.38	113	7.24	1.81	97
4	1.34	1.92	107	4.28	1.86	115	7.24	2.31	100
5	1.34	2.44	107	4.28	2.37	117	7.24	2.84	102
6	1.34	3.02	107	4.28	2.93	118	7.24	3.38	104
7	1.34	3.61	106	4.28	3.43	119	7.24	3.88	106
8	1.34	4.16	104	4.28	3.88	119	7.24	4.42	107
9	1.34	4.68	103	4.28	4.45	119	7.24	4.97	108
10	1.34	5.19	100	4.28	5.06	118	7.24	5.48	108
11	1.34	5.73	98	4.28	5.61	116	7.24	6.03	108
12	1.34	6.34	94	4.28	6.16	114	7.24	6.56	107
13	1.34	6.93	91	4.28	6.68	112	7.24	7.07	106
14	1.34	7.46	87	4.28	7.19	109	7.24	7.55	105
15	1.34	8.01	83	4.28	7.75	106	7.24	8.01	103
16	1.34	8.54	79	4.28	8.31	102	7.24	8.53	101
17	1.34	9.06	75	4.28	8.82	99	7.24	9.04	98
18	1.34	9.66	70	4.28	9.34	95	7.24	9.54	95

Fig. 70. Calculated values of dpa at the boundary of the masked and dual beam bombarded areas of the stacked-edge-on specimens in the assembly A

```

=====
ASSEMBLY # 3
=====
STEP-HEIGHT SHAPE-MATRIX :S-S
=====
ASSEMBLY # 3
=====
DPA SHAPE-MATRIX : FARADAY CUP
  Q11 = .01958   , Q12 = 9.729E-04
  Q21 = 9.729E-04 , Q22 = .02567

THETA1 = 1.41616831 RAD : 81.1404674 DEG
THETA2 = -.154628021 RAD : -8.85953298 DEG
D12(C/R12)THETA1 = -.0121943883
D12(C/R12)THETA2 = .0121943883

ANGLE BTWN MAJOR- & X-AXIS :-.154628021 RAD
-----
TRANSFORM-ANGLE : .244346095 RAD
TRANSFORM-MATRIX (IN RAD) :
  COS( .244346095 ) SIN( .244346095 )
 -SIN( .244346095 ) COS( .244346095 )
  OR
  .970295726   , .241921895
 -.241921895   , .970295726
=====
TRANSFORMED SHAPE-MATRIX
  .0194796757   , -5.70521195E-04
 -5.70521195E-04 , .0257703243

THETA1 =-1.48107825
THETA2 = .0897181093

ANGLE BTWN MAJOR- AND X-AXIS IS
-1.48107825 RAD

PEAK PT.OF STEP-HEIGHT ( 4.45 , 4.1372 )
PEAK VALUE OF DPA      : 141

```

Fig. 71. Input and calculated values of the areal distribution function of the step height and irradiation dose in dpa of the assembly C

#	X1	X2	DPA	X1	X2	DPA	X1	X2	DPA
1	1.5	.411	79	4.5	.321	98	7.36	.721	92
2	1.5	.911	87	4.5	.831	107	7.36	1.26	100
3	1.5	1.43	94	4.5	1.36	116	7.36	1.86	107
4	1.5	1.97	102	4.5	1.87	124	7.36	2.36	112
5	1.5	2.52	108	4.5	2.39	130	7.36	2.84	115
6	1.5	3.11	113	4.5	2.92	135	7.36	3.34	118
7	1.5	3.66	116	4.5	3.44	139	7.36	3.84	118
8	1.5	4.24	118	4.5	4.01	140	7.36	4.36	118
9	1.5	4.79	117	4.5	4.69	139	7.36	4.84	116
10	1.5	5.29	116	4.5	5.36	135	7.36	5.36	112
11	1.5	5.81	112	4.5	5.86	130	7.36	5.91	107
12	1.5	6.38	107	4.5	6.38	124	7.36	6.39	101
13	1.5	6.94	100	4.5	6.91	116	7.36	6.86	95
14	1.5	7.42	94	4.5	7.43	107	7.36	7.38	87
15	1.5	7.93	86	4.5	7.99	97	7.36	7.98	78
16	1.5	8.49	78	4.5	8.33	90	7.36	8.58	68
17	1.5	9.08	68	4.5	8.83	81	7.36	9.12	59
18	1.5	9.67	59	4.5	9.53	68	7.36	9.64	51

Fig. 72. Calculated values of dpa at the boundary of the masked and dual beam bombarded areas of the stacked-edge-on specimens in the assembly C

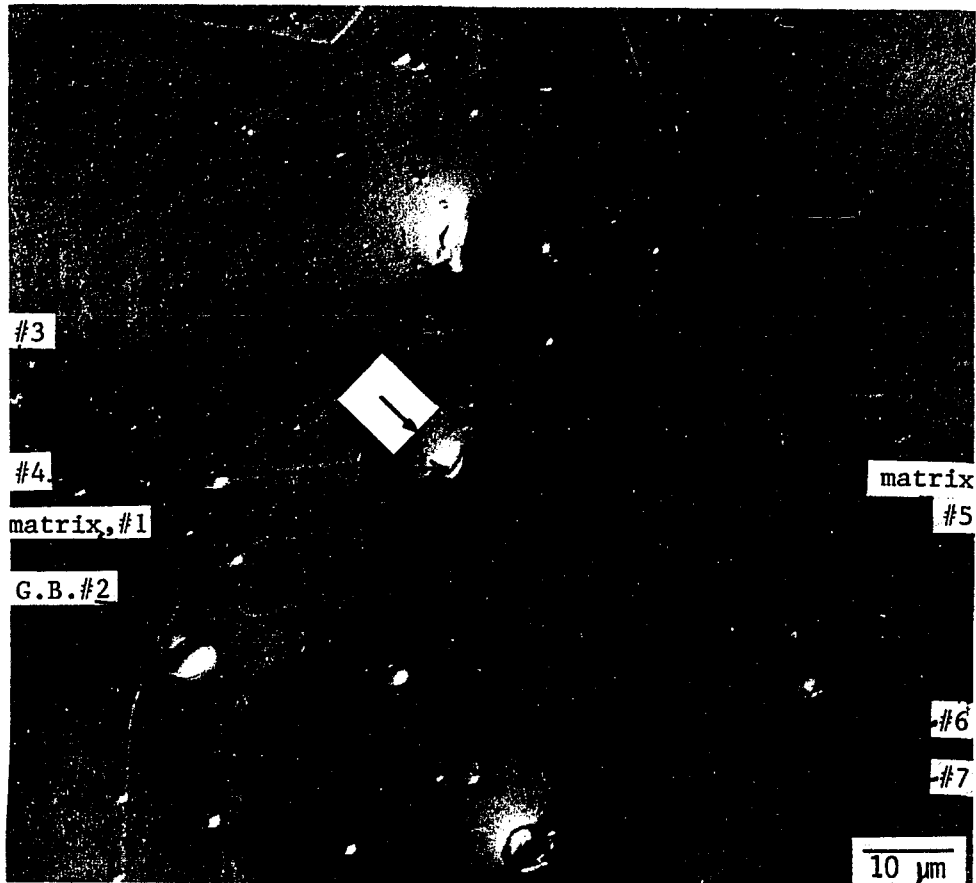
Optical Metallographic Examination and
Microchemical Analysis

Optical metallographs were taken at 1250X magnification of the single-beam-bombarded (Figs. 73-86) and the dual-beam-bombarded (Figs. 87-115) alloys using an Nomarski diffraction interference contrast microscopy. Since the helium ion beam direction was tilted 15° from the vertical direction, the thickness of the bar mask induced a shadowing of the helium beam in the case of the dual beam bombardment, as illustrated in Fig. 57. The shadowed area, shielded from the helium ion beam during the dual beam bombardment, is called the "shadowed single-beam-bombarded area." Thus, there are four types of areas: (1) masked or unbombarded, (2) single-beam-bombarded, (3) shadowed single-beam-bombarded, and (4) dual-beam-bombarded. Figs. 73-115 show the photomicrographs. They are arranged as follows. Figs. 73-86 refer to single-ion-bombarded and masked areas, Figs. 87-101 refer to masked, shadowed single-ion-bombarded, and dual-beam-bombarded areas, and Figs. 102-115 refer to masked and single-ion-bombarded areas.

Surfaces of the single beam bombarded alloys were microchemically analyzed using the electron microprobe (EMP) and the x-ray dispersive analyzer (EMX), consisting of a Tracor Northern Model NS-880 multichannel analyzer with a Kevex Model S101 Si(La) energy dispersive spectrometer. Matrix regions, grain boundaries, and a few typical precipitate particles in the ion-bombarded and masked areas of each alloy were analyzed (Figs. 73-86 and Tables 21-34), and some of the typical precipitates are summarized for their chemical formulas on Table 35. Since oxygen is not

Table 21. Microchemical analysis of heavy ion (Fe^{++}) bombarded AL-01 alloy with EDAX. As-received undoped AL

	original composition wt%	Ion bombarded region				Masked region		
		matrix #1	G.B. #2	pt. #3	pt. #4	matrix #5	pt. #6	pt. #7
Fe	58.35	59.37	59.45	57.23	22.91	50.65	1.59	0.11
Ni	25.63	24.44	25.38	25.77	9.45	25.24	0.66	0.66
Cr	8.66	10.16	9.85	9.36	4.52	9.82	0.42	0.42
Ti	3.28	3.14	3.30	3.33	43.10	3.18	76.53	76.57
Al	1.64	0.03	0.03	0.07	0.01	0.03	0	0
Mn	0.97	1.19	1.14	1.11	0.59	1.16	0	0
Mo	0.96	0.99	0.99	0.88	2.11	0.98	0	0
Si	0.31	0.32	0.34	0.39	0.21	0.39	0.12	0.12
remainder	0.21							
Total	100.01	99.64	100.48	98.13	82.88	91.46	79.32	77.88

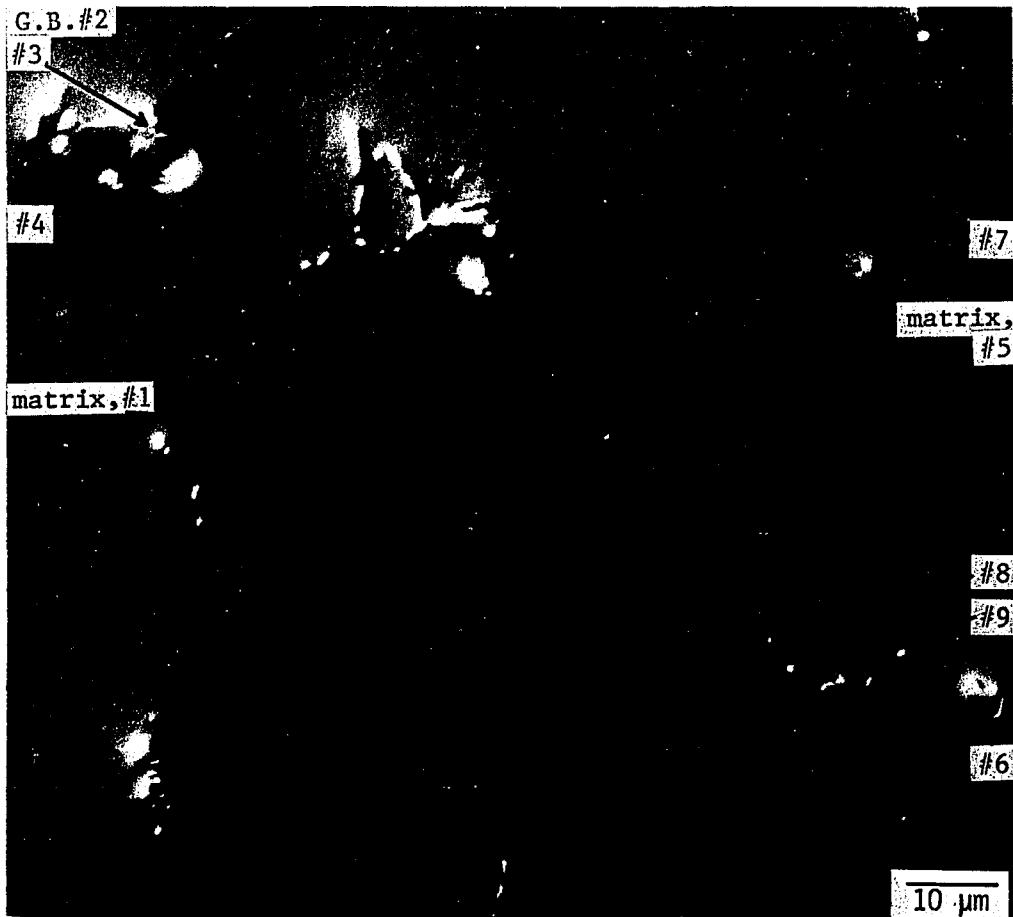


ion bombarded area ↑ masked area
boundary of mask

Fig. 73. AL-01, as-received, partially masked and bombarded with 4 MeV Fe^{++} ions to 114 dpa at 600°C

Table 22. Microchemical analysis of heavy ion (Fe^{++}) bombarded AL-1 alloy with EDAX. Arc-melted AL

	original composition wt%	Ion bombarded region				Masked region				
		matrix #1	G.B.#2	pt.#3	pt.#4	matrix #5	pt.#6	pt.#7	pt.#8	pt.#9
Fe	58.35	58.62	58.85	16.66	55.03	57.98	16.89	19.67	30.70	32.68
Ni	25.63	26.32	26.71	6.30	25.70	26.69	7.14	8.26	40.27	15.05
Cr	8.66	7.86	8.18	3.07	7.35	8.04	2.76	3.29	3.21	4.84
Ti	3.28	3.07	3.06	50.84	8.28	3.16	51.16	42.99	4.38	14.87
Al	1.64	0.03	0.03	0.01	0.03	0.03	0.01	0.11	0.05	0.35
Mn	0.97	1.02	1.08	0.25	1.04	1.07	0.40	0.46	0.73	0.66
Mo	0.96	0.97	1.06	4.91	1.20	1.02	2.88	2.63	1.16	1.34
Si	0.31	0.32	0.31	0.19	0.37	0.44	0.23	0.45	0.13	0.61
remainder	0.21									
Total	100.01	98.19	99.27	82.22	98.98	98.43	81.46	77.85	80.64	70.39

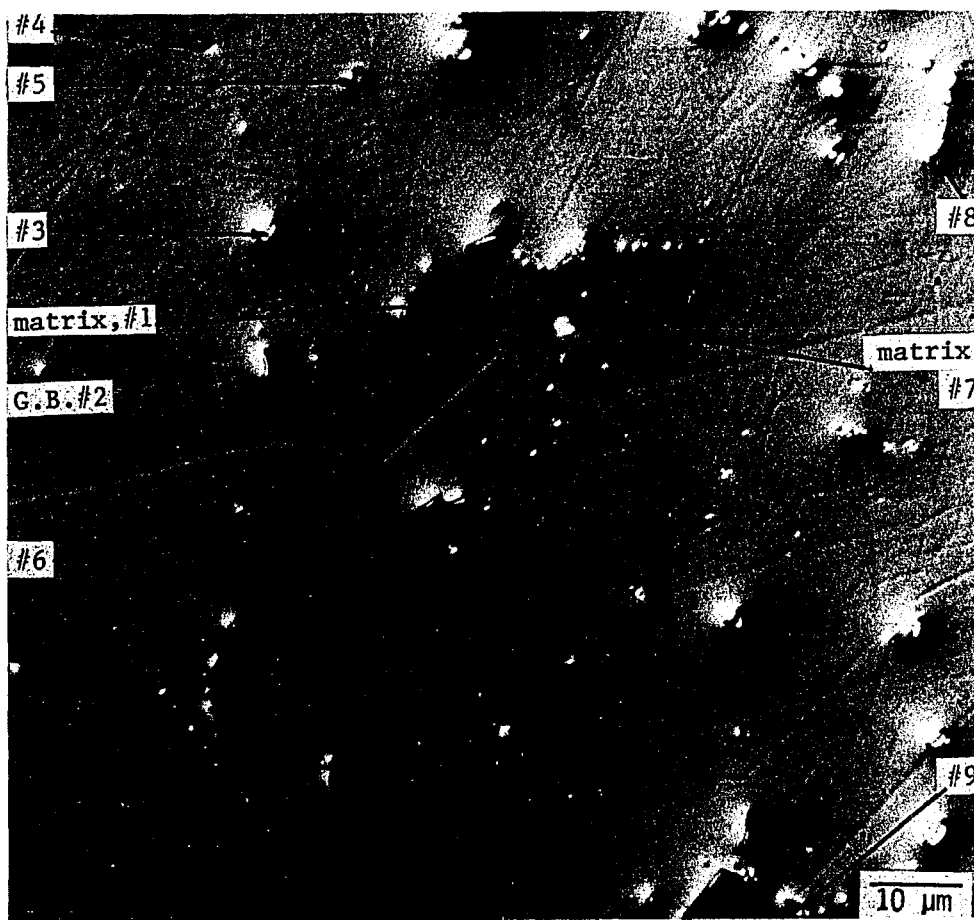


ion bombarded area | masked area
 boundary of mask

Fig. 74. AL-1 alloy, arc-melted, partially masked and bombarded with 4 MeV Fe^{++} ions to 119 dpa at 600°C

Table 23. Microchemical analysis of heavy ion (Fe^{++}) bombarded 0.05 % of Y doped, AL-2 alloy with EDAX

original composition wt%	Ion bombarded region						Masked region			
	matrix #1	G.B.#2	pt.#3	pt.#4	pt.#5	pt.#6	matrix #7	pt.#8	pt.#9	
Fe	58.35	57.15	57.01	23.85	24.97	9.59	47.49	56.86	24.42	9.24
Ni	25.63	23.97	25.84	9.95	10.63	6.07	19.85	24.68	9.62	10.60
Cr	8.66	9.02	8.95	4.01	3.82	1.77	7.12	8.87	4.59	1.24
Ti	3.28	2.83	2.97	4.10	3.32	55.02	2.45	2.92	44.11	1.09
Al	1.64	0.03	0.03	0.94	0.92	0.01	0.36	0.03	0.01	0
Mn	0.97	1.22	1.16	0.35	0.32	0.27	1.00	1.21	0.47	0.28
Mo	0.96	1.08	0.90	1.20	1.28	2.84	0.82	0.84	3.13	11.35
Si	0.31	0.39	0.35	0.21	0.45	0.27	0.28	0.34	0.23	0
Y	0.05	0	0	0	0.23	0	0	0	0	50.35
remainder	0.21									
Total	100.06	95.68	97.23	44.59	45.93	75.83	79.36	95.74	83.58	84.04

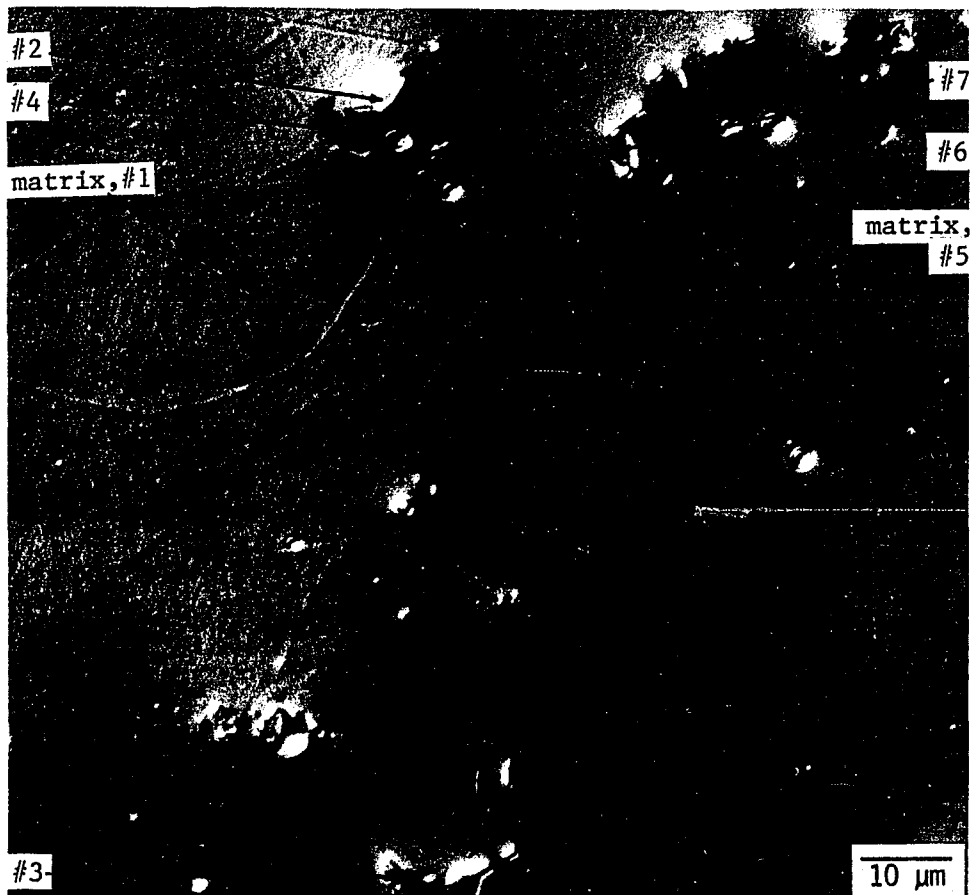


ion bombarded area | masked area
 boundary of mask

Fig. 75. AL-2 alloy, 0.05% yttrium-doped, partially masked and bombarded with 4 MeV Fe^{++} ions to 107 dpa at 600°C

Table 24. Microchemical analysis of heavy ion (Fe^{++}) bombarded 0.1 % Y doped, AL-3 alloy with EDAX

	original composition wt%	Ion bombarded region				Masked region		
		matrix #1	pt. #2	pt. #3	pt. #4	matrix #5	pt. #6	pt. #7
Fe	58.35	58.68	3.09	50.81	32.80	58.15	31.74	58.86
Ni	25.63	25.44	1.26	22.88	39.09	26.34	12.63	25.62
Cr	8.66	8.96	0.72	7.56	3.68	8.87	5.60	8.88
Ti	3.28	2.95	70.20	2.52	4.40	3.22	34.25	2.98
Al	1.64	0.03	0	0.03	0.05	0.03	0.01	0.03
Mn	0.97	1.26	0.08	1.09	0.99	1.16	0.75	1.26
Mo	0.96	0.99	3.53	0	0.63	0.91	2.32	0.82
Si	0.31	0.28	0.24	0.65	0.67	0.39	0.35	0.39
Y	0.1	0	0	0	8.47	0	0	0
remainder	0.21							
Total	100.11	98.60	79.11	85.53	90.77	99.07	87.65	98.84

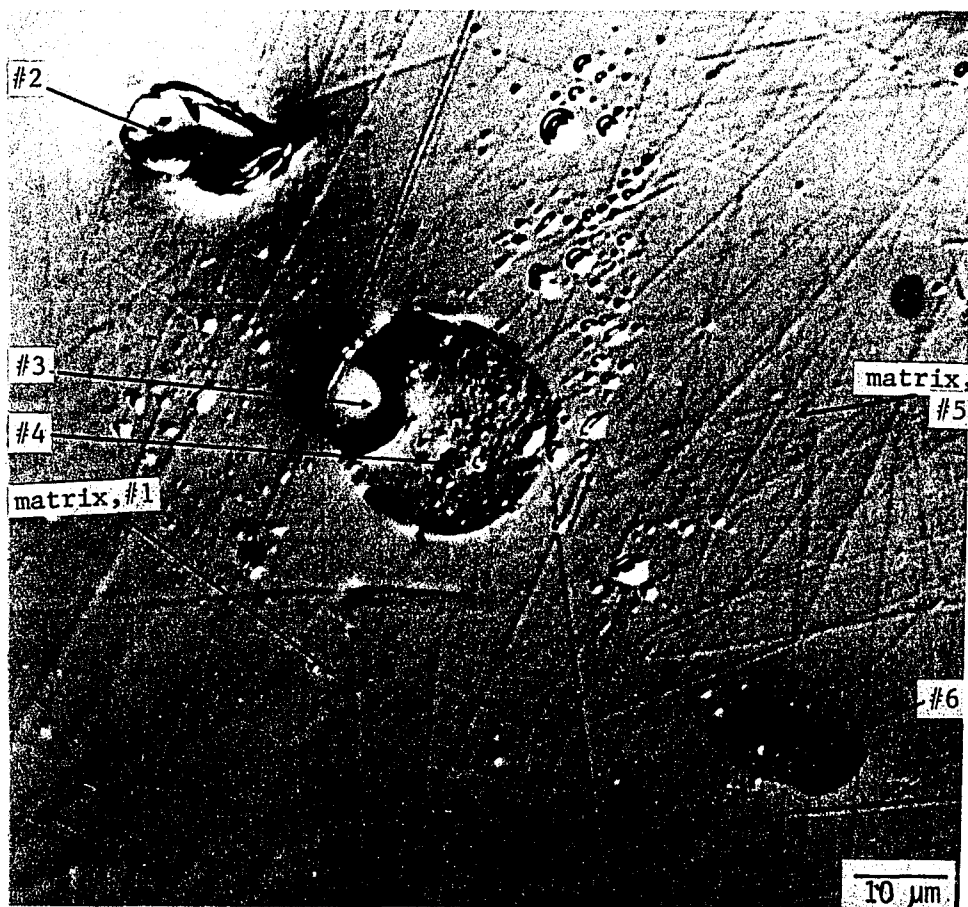


ion bombarded area ↑ masked area
boundary of mask

Fig. 76. AL-3 alloy, 0.1% yttrium-doped, partially masked and bombarded with 4 MeV Fe^{++} ions to 119 dpa at 600°C

Table 25. Microchemical analysis of heavy ion (Fe^{++}) bombarded 0.5 % Y doped, AL-4 alloy with EDAX

	original composition wt%	Ion bombarded region				Masked region	
		matrix #1	pt. #2	pt. #3	pt. #4	matrix #5	pt. #6
Fe	58.35	59.71	10.26	6.82	36.80	59.23	28.22
Ni	25.63	25.93	3.56	2.53	38.51	26.59	45.15
Cr	8.66	8.17	1.44	1.10	3.94	8.15	2.58
Ti	3.28	3.14	34.95	48.32	4.03	3.15	2.54
Al	1.64	0.03	0	0	0.04	0.03	0.06
Mn	0.97	0.89	0.22	0.08	0.69	0.86	0.59
Mo	0.96	1.02	0.52	0.90	1.02	0.98	0.62
Si	0.31	0.42	14.77	9.65	0.82	0.52	0.71
Y	0.5	0	2.04	0.73	9.90	0	14.10
remainder	0.21						
Total	100.51	99.30	67.77	70.13	95.75	99.50	94.56

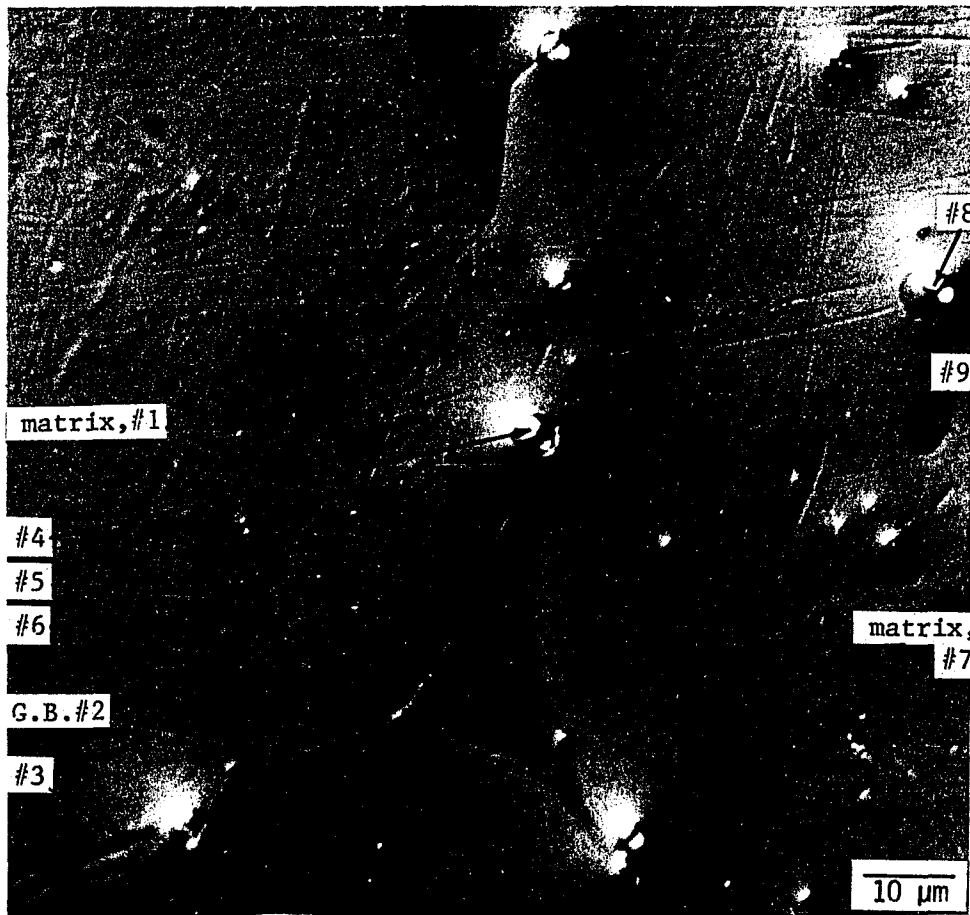


ion bombarded area | masked area
boundary of mask

Fig. 77. AL-4 alloy, 0.5% yttrium-doped, partially masked and bombarded with 4 MeV Fe^{++} ions to 87 dpa at 600°C

Table 26. Microchemical analysis of heavy ion (Fe^{++}) bombarded 1 % of Y doped, AL-5 alloy with EDAX

	original composition wt%	Ion bombarded region						Masked region		
		matrix #1	G.B.#2	pt.#3	pt.#4	pt.#5	pt.#6	matrix #7	pt.#8	pt.#9
Fe	58.35	58.84	57.59	25.52	4.77	27.89	27.71	58.60	9.94	25.71
Ni	25.63	23.17	24.83	44.51	5.45	42.41	42.66	23.53	3.55	46.24
Cr	8.66	9.10	8.91	2.68	0.77	2.64	2.74	9.05	2.11	2.86
Ti	3.28	2.87	3.10	2.41	60.70	2.29	2.37	2.89	59.71	2.40
Al	1.64	0.02	0.03	0.06	0	0.06	0.05	0.02	0	0.06
Mn	0.97	1.10	0.97	0.44	0.07	0.51	0.56	0.97	0.11	0.54
Mo	0.96	0.92	0.97	0.73	1.45	0.72	0.74	0.96	1.66	0.80
Si	0.31	0.25	0.29	0.34	1.17	0.16	0.29	0.30	0.61	0.34
Y	1.0	0	0	12.88	0.18	13.04	12.86	0	0	13.34
remainder	0.21									
Total	101.01	96.28	96.68	89.55	74.56	89.71	89.98	96.31	77.68	92.27

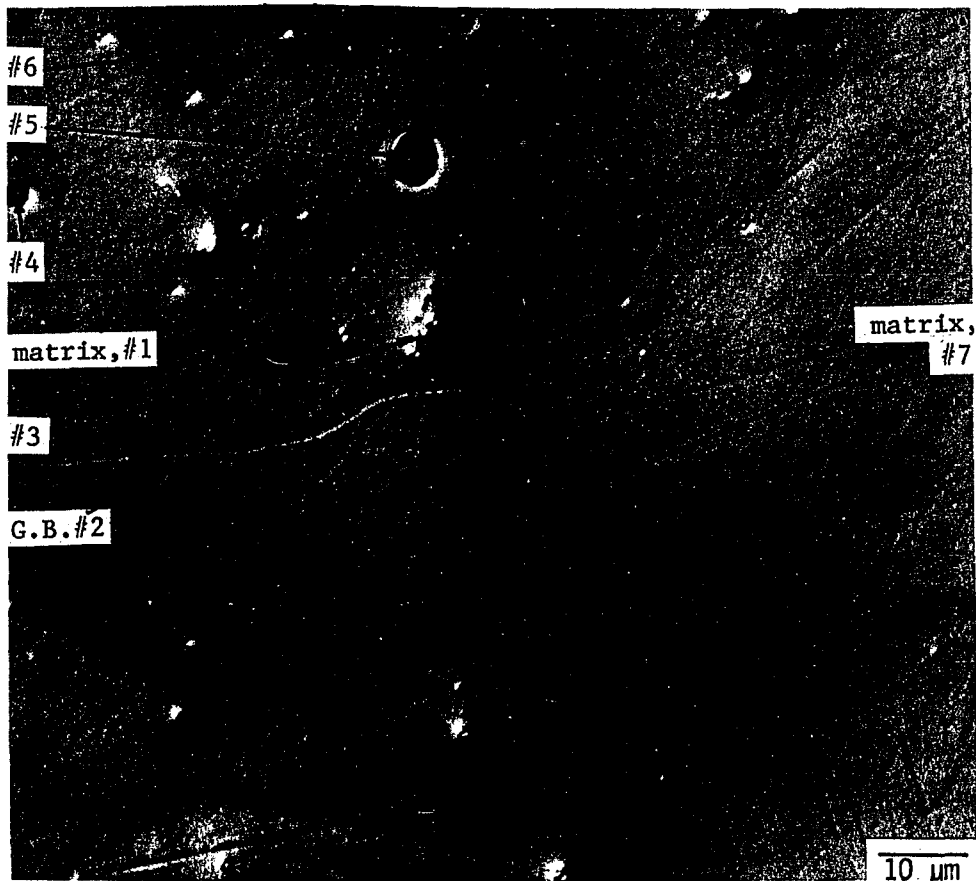


ion bombarded area | masked area
 ↑
 boundary of mask

Fig. 78. AL-5 alloy, 1.0% yttrium-doped, partially masked and bombarded with 4 MeV Fe^{++} ions to 108 dpa at 600°C

Table 27. Microchemical analysis of heavy ion (Fe^{++}) bombarded 0.05 % La doped, AL-6 alloy with EDAX

	original composition wt%	Ion bombarded region						Masked region
		matrix #1	G.B.#2	pt.#3	pt.#4	pt.#5	pt.#6	matrix #7
Fe	58.35	58.71	59.23	29.91	57.93	32.07	23.39	57.99
Ni	25.63	25.81	25.93	11.94	19.24	9.21	10.89	25.68
Cr	8.66	8.79	8.98	5.40	8.62	21.56	3.62	8.82
Ti	3.28	3.08	3.02	35.86	2.81	2.06	1.21	3.17
Al	1.64	0.03	0.03	0.01	0.01	0.16	0.02	0.03
Mn	0.97	1.39	1.25	0.80	1.29	1.25	0.51	1.20
Mo	0.96	0.90	1.02	3.44	0.34	0.68	0	0.90
Si	0.31	0.34	0.30	0.28	0.13	0.43	1.38	0.39
La	0.05	0.19	0	1.57	0	0	0	0
remainder	0.21							
Total	100.06	99.25	99.74	89.20	90.36	67.41	41.02	98.17



ion bombarded area ↑ masked area
boundary of mask

Fig. 79. AL-6 alloy, 0.05% lanthanum-doped, partially masked and bombarded with 4 MeV Fe^{++} ions to 119 dpa at 600°C

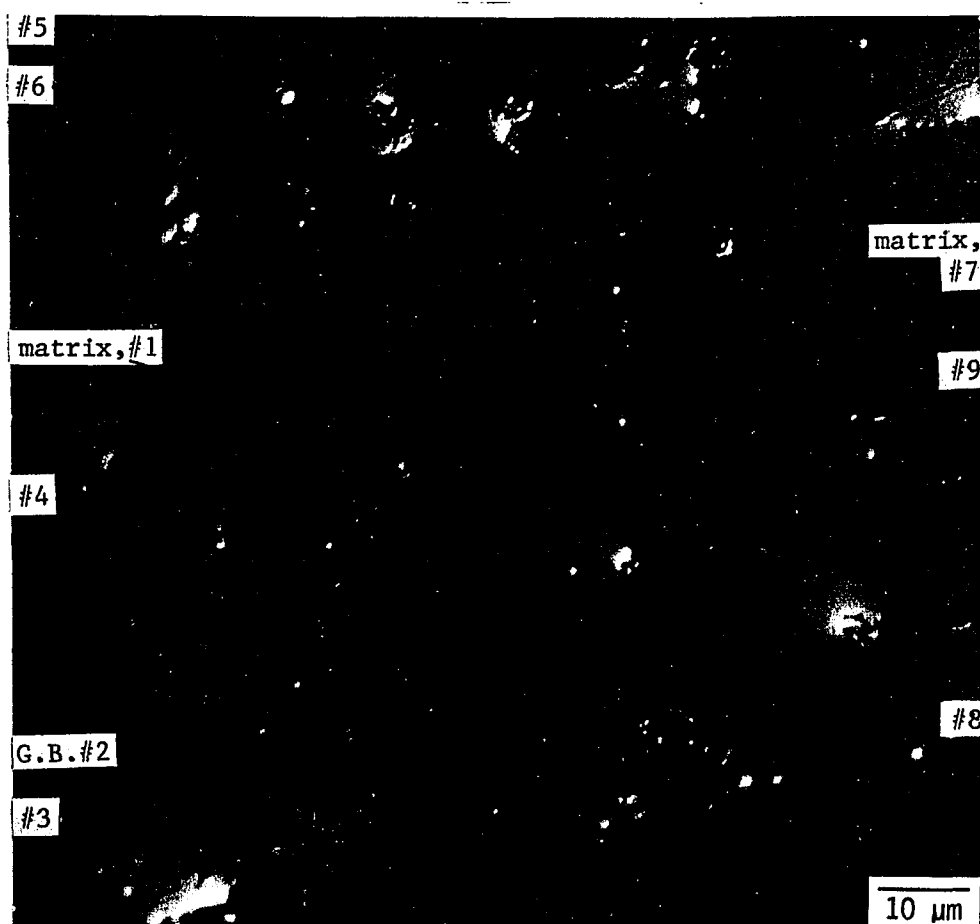
Table 28. Microchemical analysis of heavy ion (Fe^{++}) bombarded 0.1 % La doped, AL-7 alloy with EDAX

	original composition wt%	Ion bombarded region					Masked region			
		matrix #1	pt.#2	pt.#3	pt.#4	pt.#5	matrix #6	pt.#7	pt.#8	pt.#9
Fe	58.35	64.20	13.20	63.57	18.44	15.44	63.60	13.82	32.07	38.91
Ni	25.63	27.45	28.65	28.86	40.20	5.94	28.42	5.39	12.29	14.99
Cr	8.66	8.8	1.86	8.73	2.39	2.77	8.83	2.55	5.32	6.35
Ti	3.28	3.09	1.06	3.31	1.56	57.80	3.37	59.37	40.55	31.92
Al	1.64	0.03	0.07	0.05	0.09	0.01	0.04	0.01	0.02	0.01
Mn	0.97	1.19	0.59	1.04	0.72	0.37	1.23	0.31	0.62	0.76
Mo	0.96	0.87	1.76	0.87	0.96	3.41	0.96	4.26	1.80	3.23
Si	0.31	0.37	1.19	0.41	1.28	0.22	0.37	0.22	0.29	0.25
La	0.1	1.83	69.29	0	48.57	0	0	0.46	0	0.46
remainder	0.21									
Total	100.11	107.91	117.67	106.83	114.21	85.95	106.82	86.38	92.97	96.88

Fig. 80. AL-7 alloy, 0.1% lanthanum-doped, partially masked and bombarded with 4 MeV Fe^{++} ions to 103 dpa at 600°C

Table 29. Microchemical analysis of heavy ion (Fe^{++}) bombarded 0.5 % of La doped, AL-8 alloy with EDAX

	original composition wt%	Ion bombarded region						Masked region		
		matrix #1	G.B.#2	pt.#3	pt.#4	pt.#5	pt.#6	matrix #7	pt.#8	pt.#9
Fe	58.35	57.58	57.02	20.69	16.86	19.91	14.83	56.95	15.42	40.62
Ni	25.63	24.64	24.80	11.63	35.79	9.74	40.44	24.80	35.41	16.77
Cr	8.66	9.06	8.65	3.35	1.64	3.34	1.35	8.90	1.49	6.65
Ti	3.28	3.05	3.02	14.86	0.89	1.33	0.67	2.29	1.42	21.33
Al	1.64	0.03	0.03	0.14	0.07	1.00	0.07	0.03	0.06	0.02
Mn	0.97	1.24	1.25	0.23	0.56	0.39	0.43	1.18	0.39	0.76
Mo	0.96	0.94	0.89	1.30	0.43	0.59	0.50	0.90	0.94	2.05
Si	0.31	0.32	0.30	0.80	1.14	0.37	1.30	0.31	1.17	0.36
La	0.5	0.55	0.61	38.19	55.77	5.88	50.25	0.69	51.10	2.47
remainder	0.21									
Total	100.51	97.40	96.55	91.19	113.14	42.55	109.83	96.74	107.39	91.02

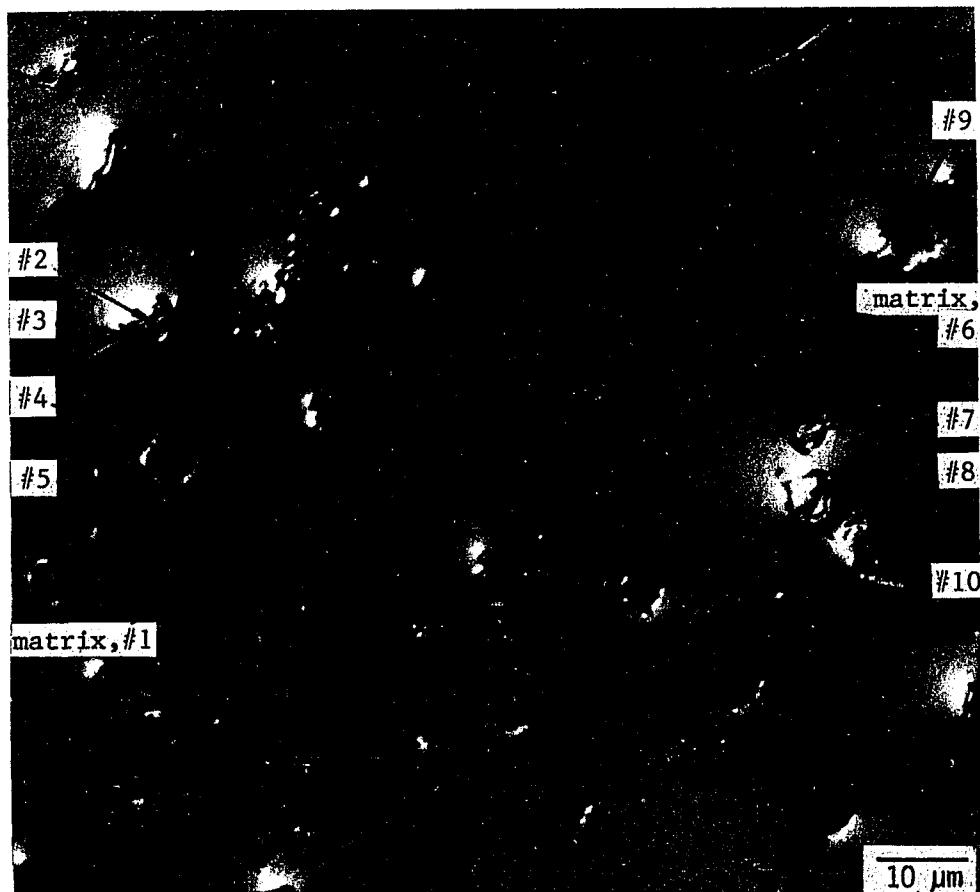


ion bombarded area | masked area
 boundary of mask

Fig. 81. AL-8 alloy, 0.5% lanthanum-doped, partially masked and bombarded with 4 MeV Fe^{++} ions to 108 dpa at 600°C

Table 30. Microchemical analysis of heavy ion (Fe^{++}) bombarded 1 % La doped, AL-9 alloy with EDAX

	original composition wt%	Ion bombarded region					Masked region			
		matrix #1	pt.#2	pt.#3	pt.#4	pt.#5	matrix #6	pt.#7	pt.#8	pt.#9
Fe	58.35	59.57	2.96	30.72	10.85	60.03	59.98	1.62	12.56	12.83
Ni	25.63	25.89	4.08	14.40	35.02	24.61	25.74	0.84	46.95	48.19
Cr	8.66	8.47	0.32	4.88	0.83	8.09	8.11	0.58	0.84	0.98
Ti	3.28	2.95	62.44	0.89	0	3.07	3.07	70.98	0.31	0
Al	1.64	0.03	0.01	0.02	0.05	0.03	0.03	0	0.07	0.07
Mn	0.97	0.90	0.12	0.46	0.38	0.99	1.09	0.09	0.24	0.29
Mo	0.96	0.93	2.29	1.88	0.10	0.94	0.91	6.15	0.12	0.12
Si	0.31	0.29	0.25	0.49	0.83	0.25	0.32	0.17	1.32	1.37
La	1.00	0.34	5.57	64.66	67.52	1.23	0	1.27	57.21	56.83
remainder	0.21									
Total	101.01	99.37	83.03	118.38	115.58	99.23	99.24	81.68	119.62	120.68

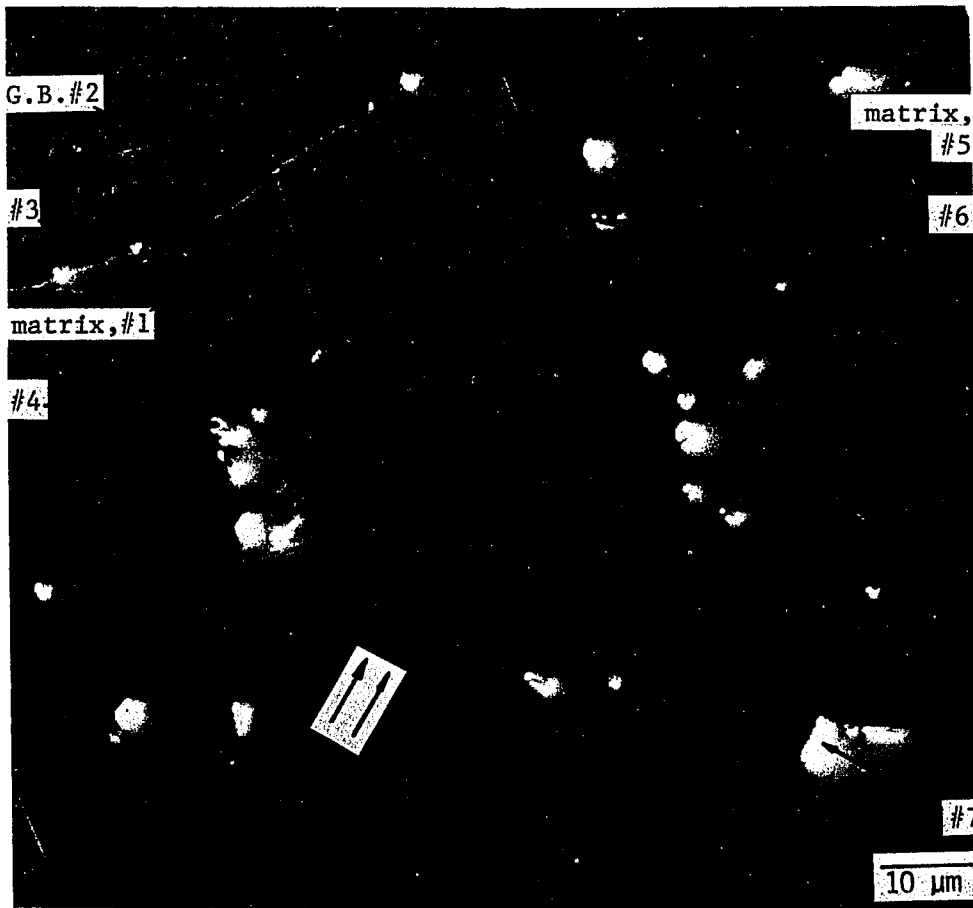


ion bombarded area ↑ masked area
boundary of mask

Fig. 82. AL-9 alloy, 1.0% lanthanum-doped, partially masked and bombarded with 4 MeV Fe^{++} ions to 100 dpa at 600°C

Table 31. Microchemical analysis of heavy ion (Fe^{++}) bombarded 0.05 % Ce doped, AL-10 alloy with EDAX

	original composition wt%	Ion bombarded region				Masked region		
		matrix #1	G.B. #2	pt. #3	pt. #4	matrix #5	pt. #6	pt. #7
Fe	58.35	59.21	58.04	33.73	21.73	58.64	27.87	48.40
Ni	25.63	25.51	25.73	28.41	8.10	24.95	25.45	21.69
Cr	8.66	8.90	8.91	5.76	3.92	8.76	4.82	7.52
Ti	3.28	3.02	3.04	4.80	46.42	2.87	3.12	2.69
Al	1.64	0.03	0.03	0.04	0.02	0.03	0.02	0.03
Mn	0.97	1.24	1.14	0.67	0.34	1.22	0.42	0.98
Mo	0.96	0.84	0.88	2.18	3.73	0.92	1.88	0.85
Si	0.31	0.32	0.35	1.67	0.21	0.35	0.70	0.36
Ce	0.05	0.20	0.27	20.54	0	0	42.21	0
remainder	0.21							
Total	100.06	99.25	98.38	97.81	84.47	97.74	106.49	82.51

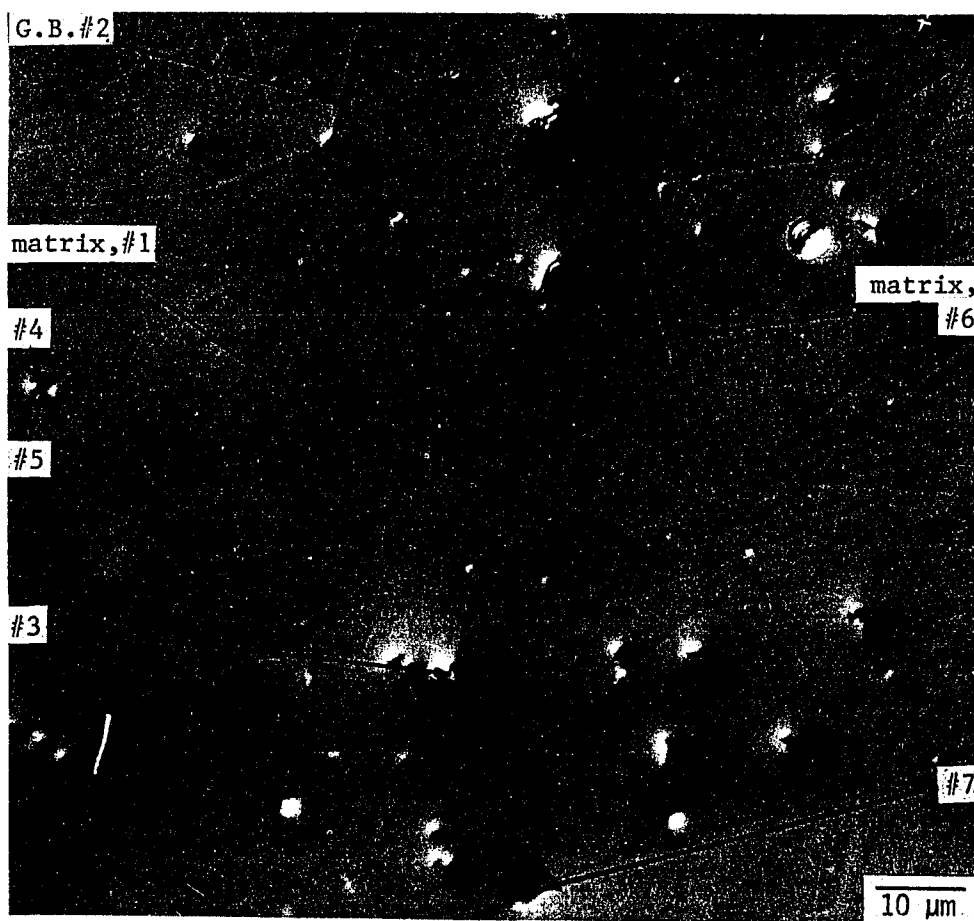


ion bombarded area ↑ masked area
boundary of mask

Fig. 83. AL-10 alloy, 0.05% cerium-doped, partially masked and bombarded with 4 MeV Fe^{++} ions to 108 dpa at 600°C

Table 32. Microchemical analysis of heavy ion (Fe^{++}) bombarded 0.1 % Ce doped, AL-11 alloy with EDAX

	original composition wt%	Ion bombarded region					Masked region	
		matrix #1	pt.#2	pt.#3	pt.#4	pt.#5	matrix #6	pt.#7
Fe	58.35	57.33	57.59	50.57	11.20	27.60	57.85	23.91
Ni	25.63	25.25	25.07	21.18	26.09	18.09	25.13	13.83
Cr	8.66	8.65	8.65	8.02	2.13	4.73	8.81	4.03
Ti	3.28	3.10	3.32	10.94	3.10	25.49	3.07	1.91
Al	1.64	0.03	0.03	0.03	0	0.02	0.03	0.98
Mn	0.97	1.22	1.08	1.02	0.05	0.57	1.18	0.59
Mo	0.96	0.87	1.30	1.56	2.38	2.19	0.91	0.82
Si	0.31	0.34	0.20	0.30	0.73	0.57	0.35	0.28
Ce	0.05	0	0	0	59.21	12.70	0	3.78
remainder	0.21							
Total	100.06	96.79	97.30	93.61	104.89	91.96	97.32	49.72



ion bombarded area | masked area
 boundary of mask

Fig. 84. AL-11 alloy, 0.1% cerium-doped, partially masked and bombarded with 4 NeV Fe^{++} ions to 116 dpa at 600°C

Table 33. Microchemical analysis of heavy ion (Fe^{++}) bombarded 0.5 % Ce doped, AL-12 alloy with EDAX

	original composition wt%	Ion bombarded region				Masked region				
		matrix #1	G.B.#2	pt.#3	pt.#4	matrix #5	pt.#6	pt.#7	pt.#8	pt.#9
Fe	58.35	59.81	59.81	18.83	16.43	59.73	3.57	14.99	20.80	18.00
Ni	25.63	26.07	26.13	45.05	45.90	25.94	2.11	26.71	48.01	47.15
Cr	8.66	8.09	8.00	2.22	1.10	7.96	0.64	1.81	2.28	1.51
Ti	3.28	3.07	2.94	0.96	0.68	3.00	67.89	0.89	1.14	0.79
Al	1.64	0.03	0.03	0.05	0.06	0.03	0	0.02	0.06	0.07
Mn	0.97	1.02	0.95	0.41	0.39	0.92	0	0.27	0.40	0.37
Mo	0.96	0.83	0.93	0.18	0	1.05	2.72	2.17	0.78	0
Si	0.31	0.30	0.26	1.53	1.40	0.30	0.19	1.14	1.30	1.38
Ce	0.5	0.14	0.27	39.83	46.97	0	0	66.72	38.28	46.85
remainder	0.21									
Total	100.51	99.34	99.31	109.05	112.93	97.92	77.11	114.71	113.35	116.12

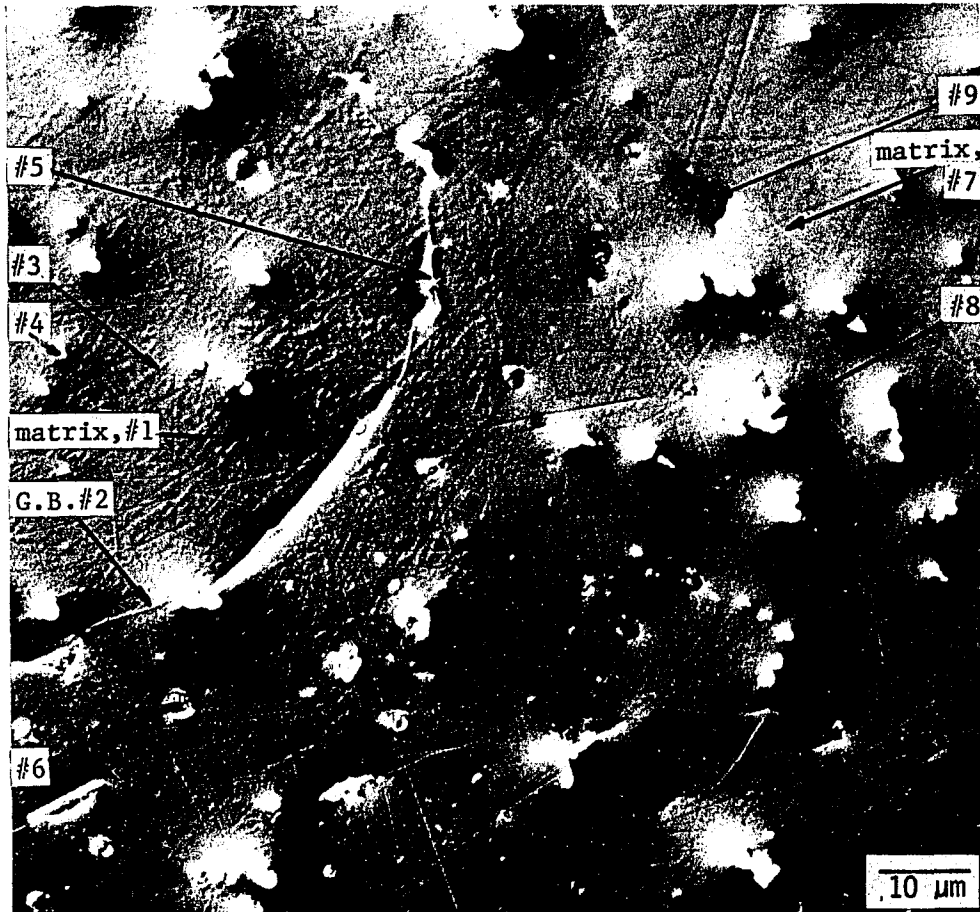


ion bombarded area | masked area
boundary of mask

Fig. 85. AL-12 alloy, 0.5% cerium-doped, partially masked and bombarded with 4 MeV Fe^{++} ions to 98 dpa at 600°C

Table 34. Microchemical analysis of heavy ion (Fe^{++}) bombarded 1% of Ce doped, AL-13 alloy with EDAX

	original composition wt%	Ion bombarded region						Masked region		
		matrix #1	G.B.#2	pt.#3	pt.#4	pt.#5	pt.#6	matrix #7	pt.#8	pt.#9
Fe	58.35	57.37	54.81	5.27	57.80	15.43	15.30	56.49	2.11	15.50
Ni	25.63	24.13	21.70	6.43	24.01	39.61	47.51	23.71	1.10	44.99
Cr	8.66	8.58	8.40	0.93	8.84	0.93	1.64	0.55	0.55	0.76
Ti	3.28	2.85	2.68	57.30	2.87	0.63	1.11	2.07	69.79	0.40
Al	1.64	0.03	0.19	0.01	0.03	0.07	0.06	0.03	0	0.06
Mn	0.97	1.22	1.08	0.08	1.13	0.31	0.38	1.11	0	0.36
Mo	0.96	0.84	0.87	2.63	0.90	0	0.11	0.90	2.13	0.13
Si	0.31	0.33	0.37	0.31	0.31	1.36	1.32	0.30	0.22	1.25
Ce	1.00	0.35	0.44	5.30	0.33	44.39	39.11	0.39	0.75	42.15
remainder	0.21									
Total	101.01	95.70	90.53	78.25	96.20	102.73	106.54	94.33	76.64	105.60



ion bombarded area | masked area
 boundary of mask

Fig. 86. AL-13 alloy, 1% cerium-doped, partially masked and bombarded with 4 MeV Fe^{++} ions to 107 dpa at 600°C

dual beam ($\text{Ni}^{++} + \text{He}^+$)
 bombarded area

shadowed area
 Ni^{++} ion bombarded

masked area

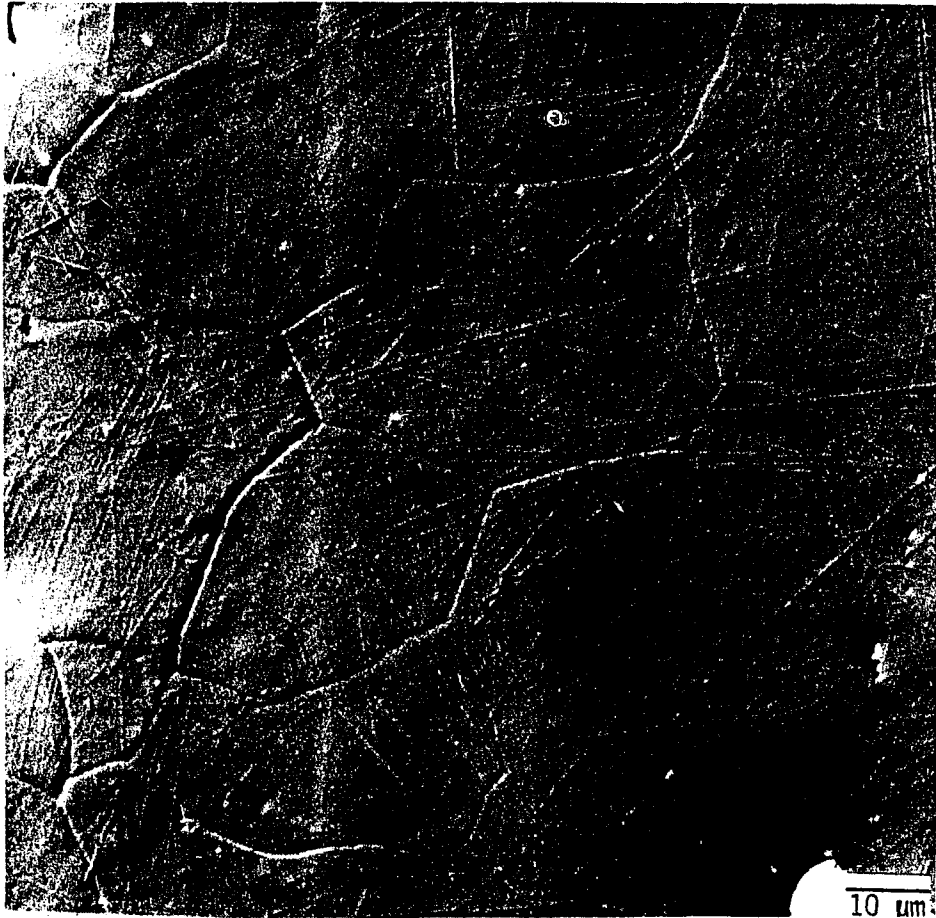


Fig. 87. AL-0 alloy, as-received, partially masked, shadowed single beam
 of Ni^{++} ions and dual beam of 4 MeV Ni^{++} and 0.4 MeV He^+ ions
 bombarded at to 114 dpa at 570°C

dual beam($\text{Ni}^{++}+\text{He}^+$)
 bombarded area

shadowed area
 Ni^{++} ion bombarded

masked area

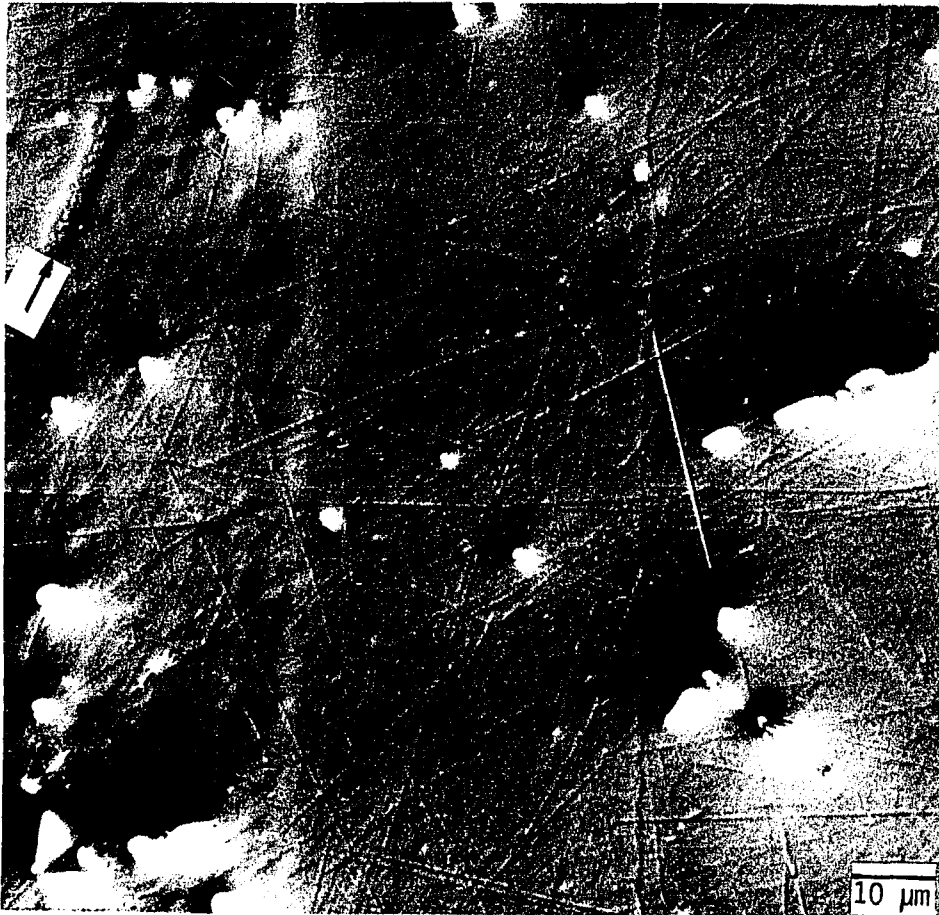


Fig. 89. AL-1 alloy, arc-melted, partially masked, shadowed single-beam
 of Ni^{++} ions and dual-beam of 4 MeV Ni^{++} and 0.4 MeV He^+ ions
 bombarded to 115 dpa at 570°C



Fig. 90. AL-2 alloy, 0.05% yttrium-doped, partially masked, shadowed single-beam of Ni⁺⁺ ions and dual-beam of 4 MeV Ni⁺⁺ and 0.4 MeV He⁺ ions bombarded to 115 dpa at 570°C

dual beam(Ni⁺⁺+He⁺)
bombarde d area

shadowed area
Ni⁺⁺ ion bombarde d

masked area

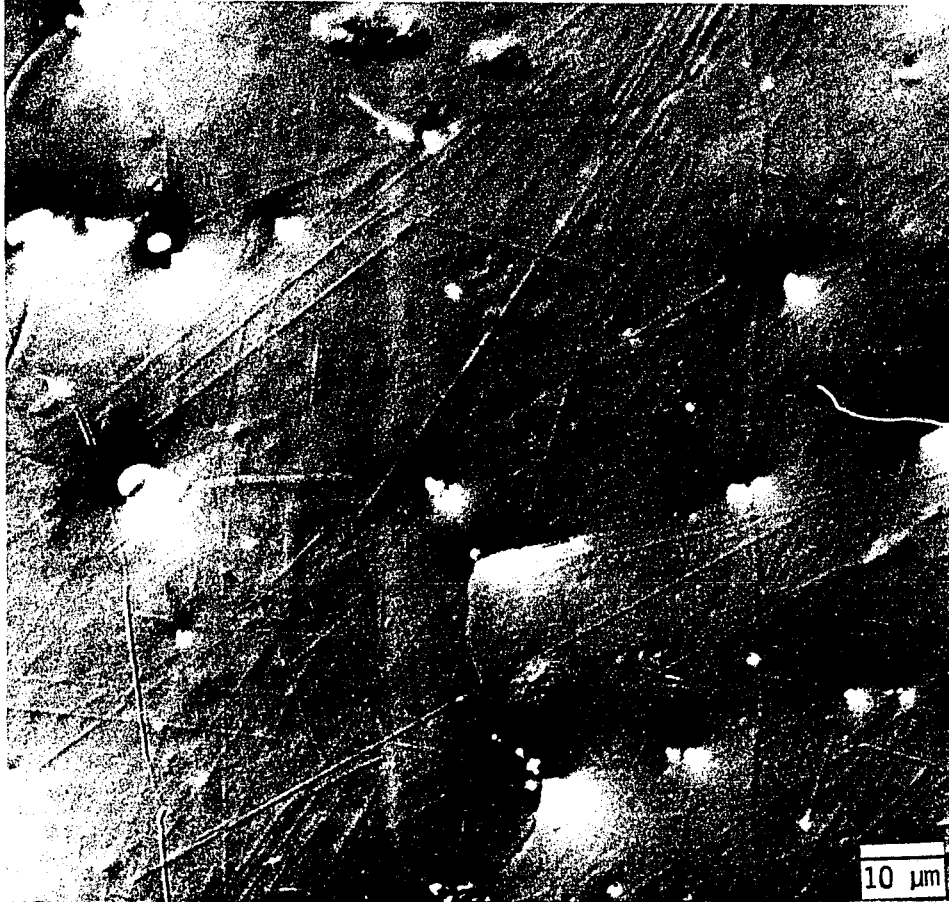


Fig. 91. AL-3 alloy, 0.1% yttrium-doped, partially masked, shadowed single-beam of Ni⁺⁺ ions and dual-beam of 4 MeV Ni⁺⁺ and 0.4 MeV He⁺ ions bombarded to 118 dpa at 570°C



dual beam(Ni⁺⁺+He⁺) bombarded area ← | → shadowed area Ni⁺⁺ion bombarded ← | → masked area

Fig. 92. AL-4 alloy, 0.5% yttrium-doped, partially masked, shadowed single-beam of Ni⁺⁺ ions and dual-beam of 4 MeV Ni⁺⁺ and 0.4 MeV He⁺ ions bombarded to 102 dpa at 570°C



Fig. 93. AL-5 alloy, 1.0% yttrium-doped, partially masked, shadowed single-beam of Ni^{++} ions and dual-beam of 4 MeV Ni^{++} and 0.4 MeV He^+ ions bombarded to 121 dpa at 570°C

dual beam($\text{Ni}^{++}+\text{He}^+$)
 bombarded area

shadowed area
 Ni^{++} ion bombarded

masked area

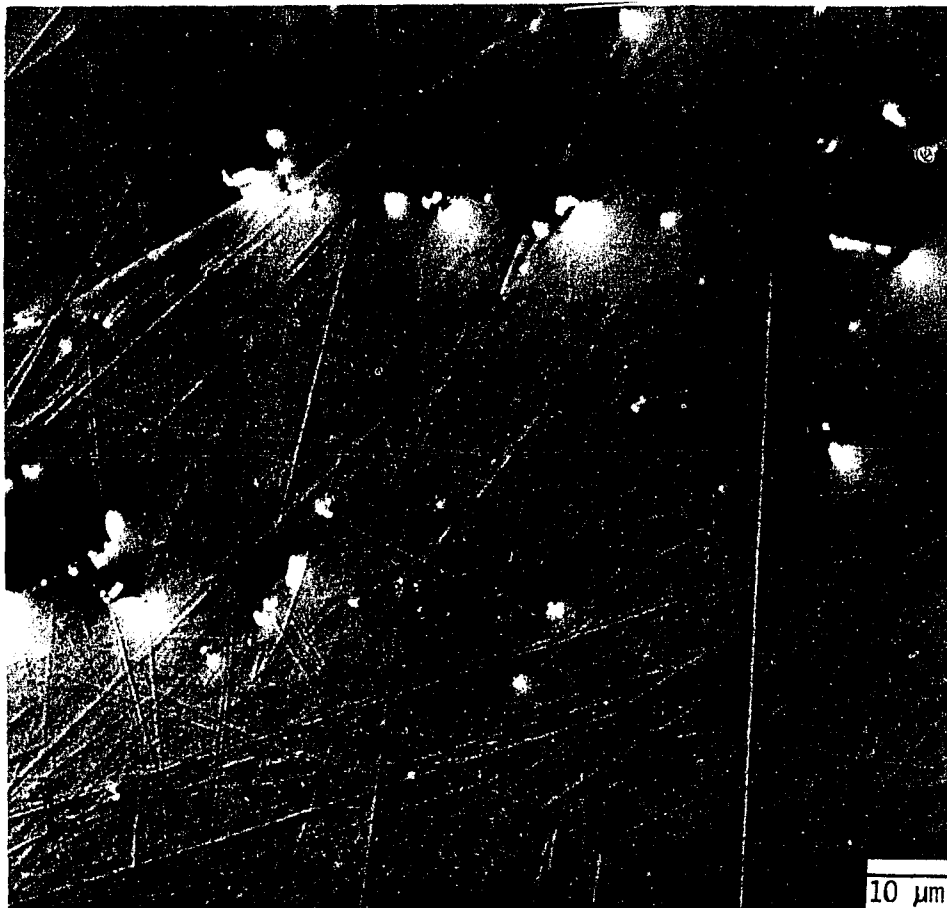


Fig. 94. AL-6 alloy, 0.05% lanthanum-doped, partially masked, shadowed single-beam of Ni^{++} ions and dual-beam of 4 MeV Ni^{++} and 0.4 MeV He^+ ions bombarded to 120 dpa at 570°C

dual beam($\text{Ni}^{++}+\text{He}^+$)
 bombarded area

shadowed area
 Ni^{++} ion bombarded

masked area

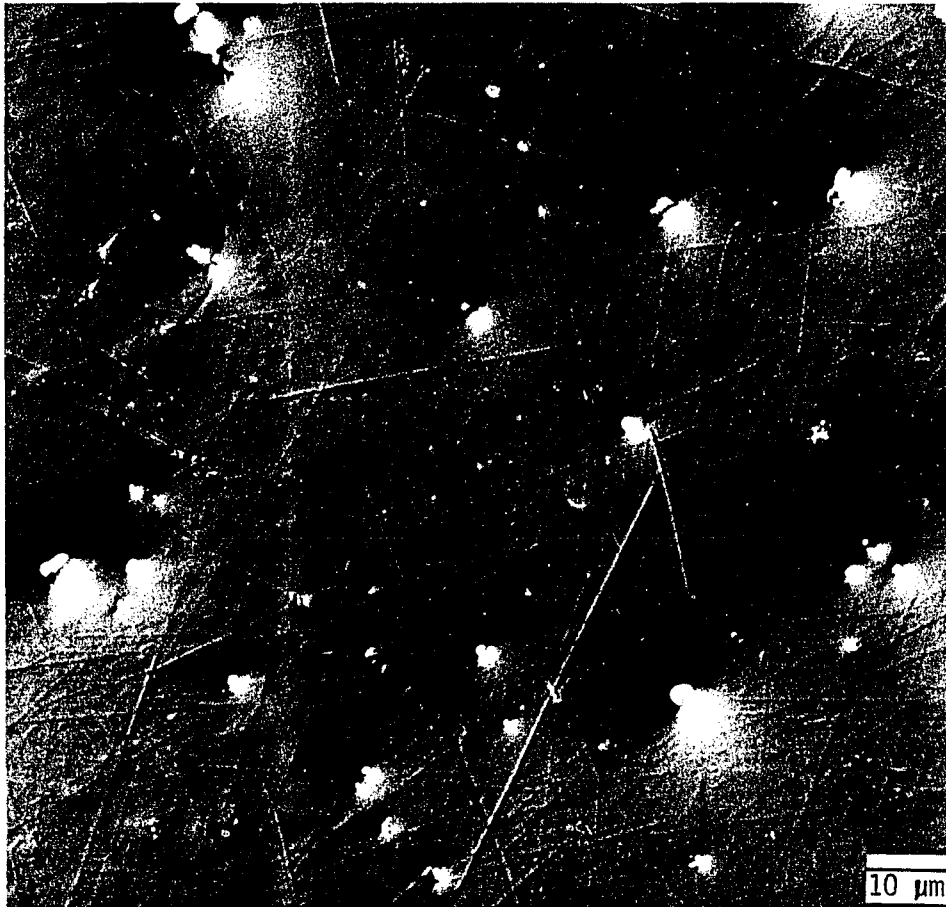


Fig. 95. AL-7 alloy, 0.1% lanthanum-doped, partially masked, shadowed single-beam of Ni^{++} ions and dual-beam of 4 MeV Ni^{++} and 0.4 MeV He^+ ions bombarded to 120 dpa at 570°C

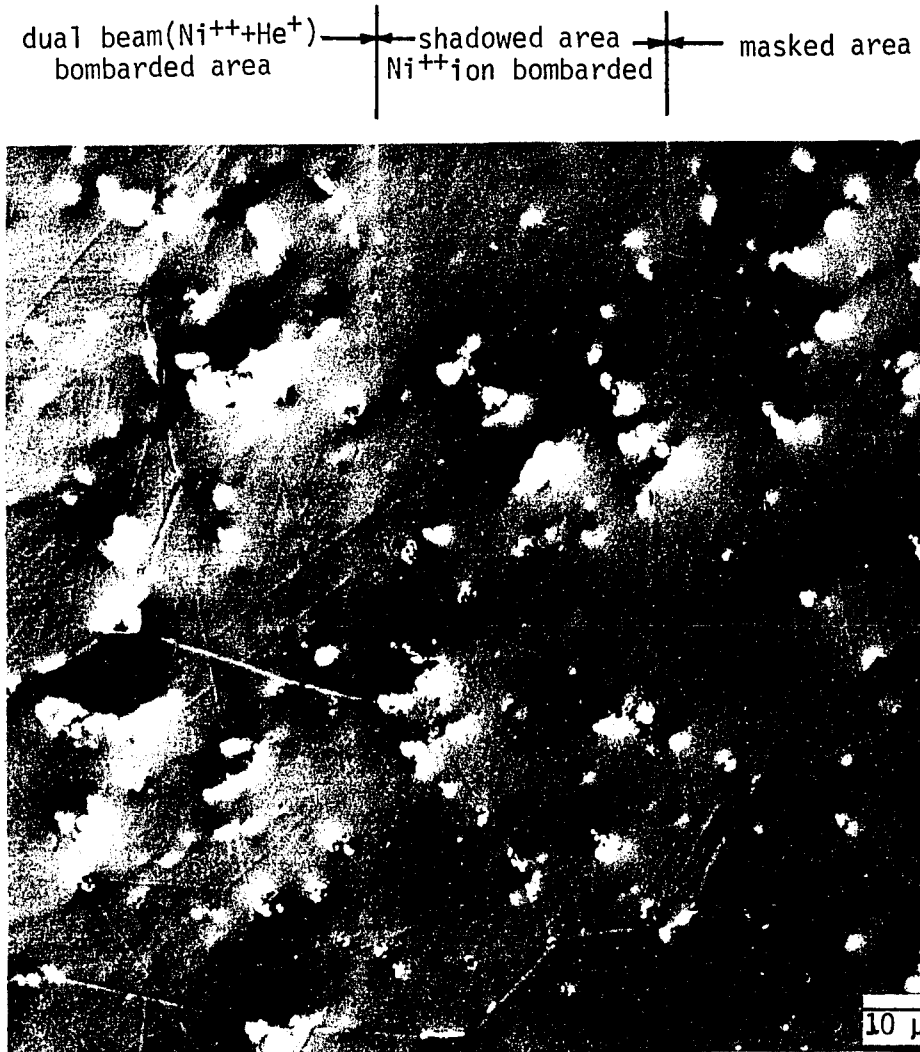


Fig. 96. AL-8-alloy, 0.5% lanthanum-doped, partially masked, shadowed single-beam of Ni^{++} ions and dual-beam of 4 MeV Ni^{++} and 0.4 MeV He^+ ions bombarded to 120 dpa at 570°C



Fig. 99. AL-11 alloy, 0.1% cerium-doped, partially masked, shadowed single-beam of Ni⁺⁺ ions and dual-beam of 4 MeV Ni⁺⁺ and 0.4 MeV H⁺ ions bombarded to 119 dpa at 570°C

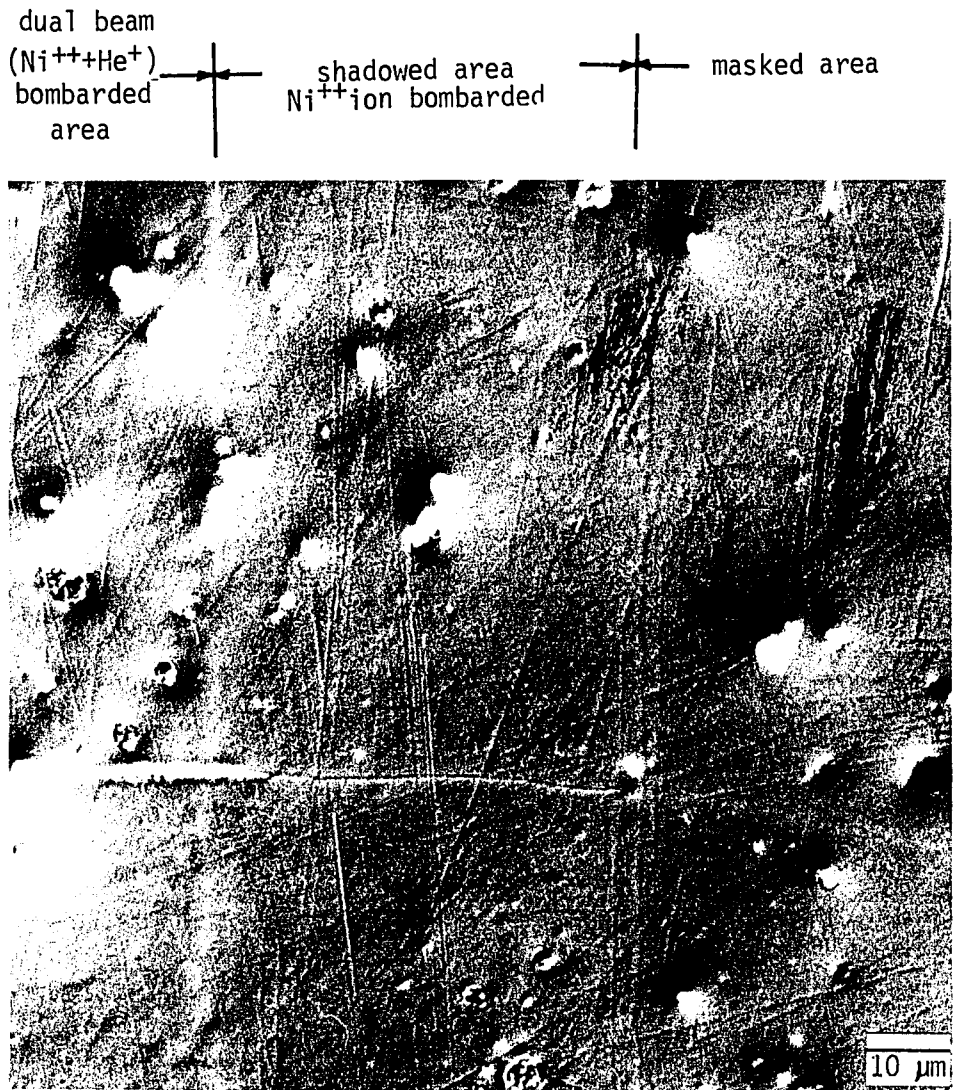


Fig. 100. AL-12 alloy, 0.5% cerium-doped, partially masked, shadowed single-beam of Ni⁺⁺ ions and dual-beam of 4 MeV Ni⁺⁺ and 0.4 MeV He⁺ ions bombarded to 105 dpa at 570°C

dual beam($\text{Ni}^{++}+\text{He}^+$)
 bombarded area

← shadowed area →
 Ni^{++} ion bombarded

← masked area

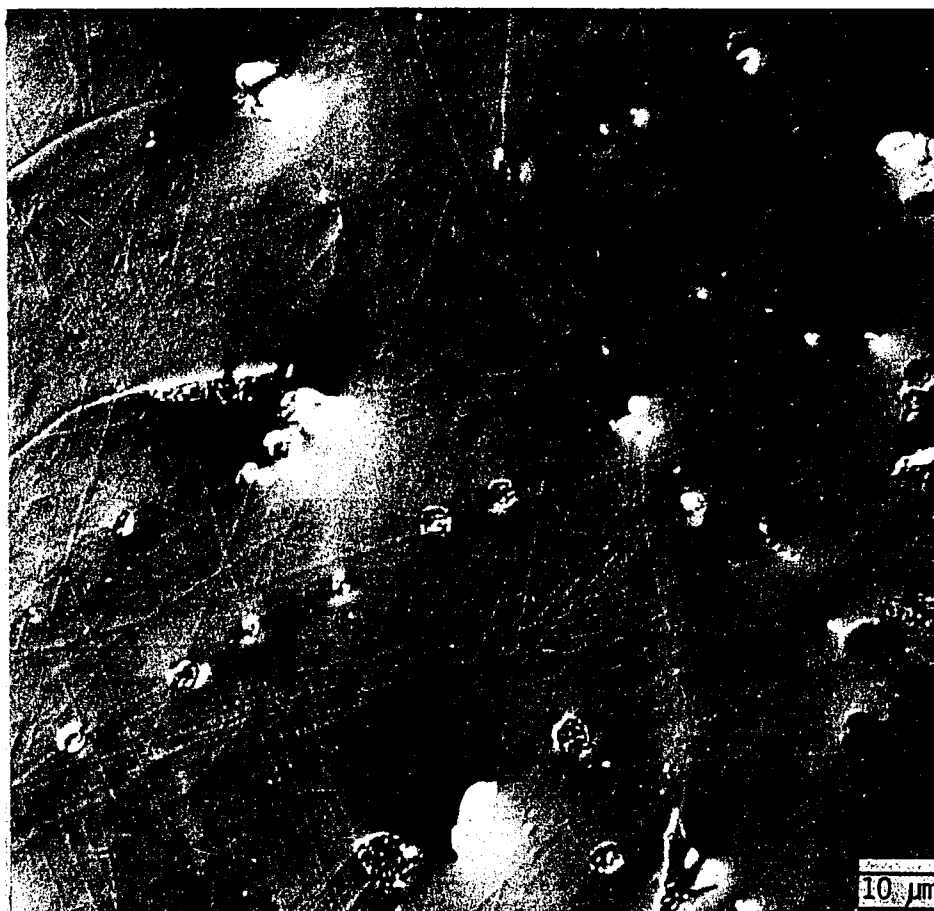


Fig. 101. AL-13 alloy, 1.0% cerium-doped, partially masked, shadowed
 single-beam of Ni^{++} ions and dual-beam of 4 MeV Ni^{++} and
 0.4 MeV He^+ ions bombarded to 114 dpa at 570°C

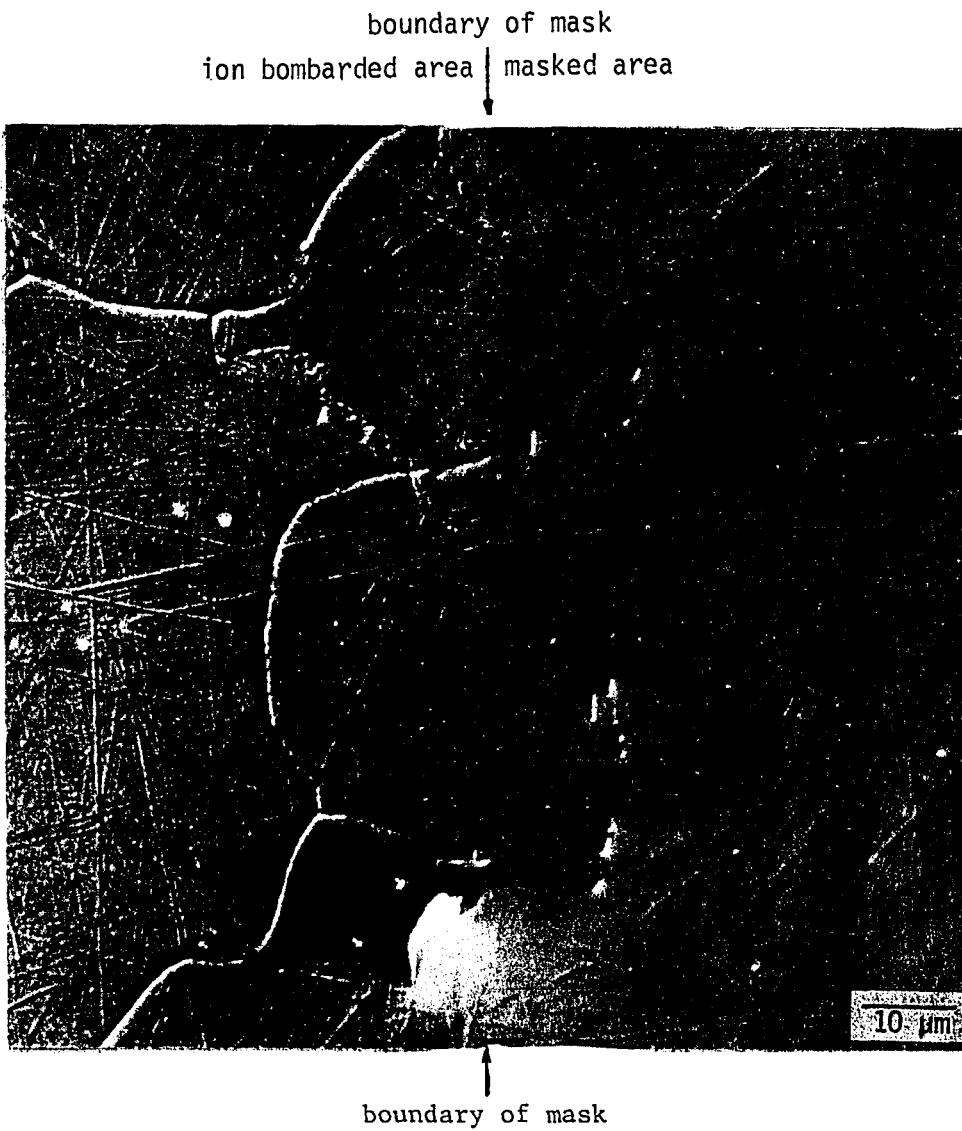


Fig. 102. AL-01, as-received, partially masked and bombarded with dual beam of 4 MeV Fe^{++} and 0.4 MeV He^+ ions to 135 dpa at 600°C

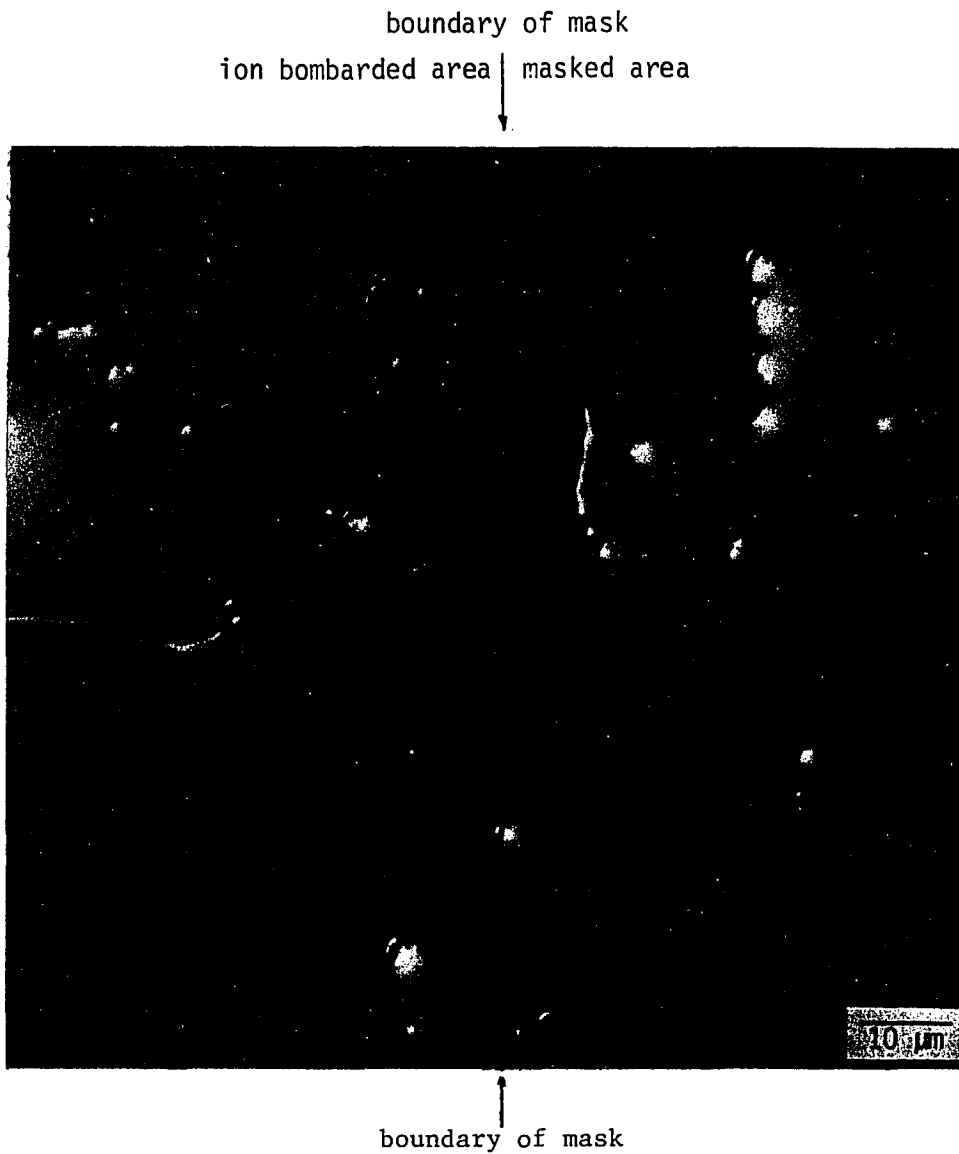


Fig. 103. AL-1, arc-melted, partially masked and bombarded with dual beam, 4 MeV Fe^{++} and 0.4 MeV He^+ ions to 139 dpa at 600°C

boundary of mask
on bombarded area | masked area



↑
boundary of mask

Fig. 104. AL-2, 0.05% yttrium-doped, partially masked and bombarded with dual beam of 4 MeV Fe^{++} and 0.4 MeV He^+ ions to 118 dpa at 600°C

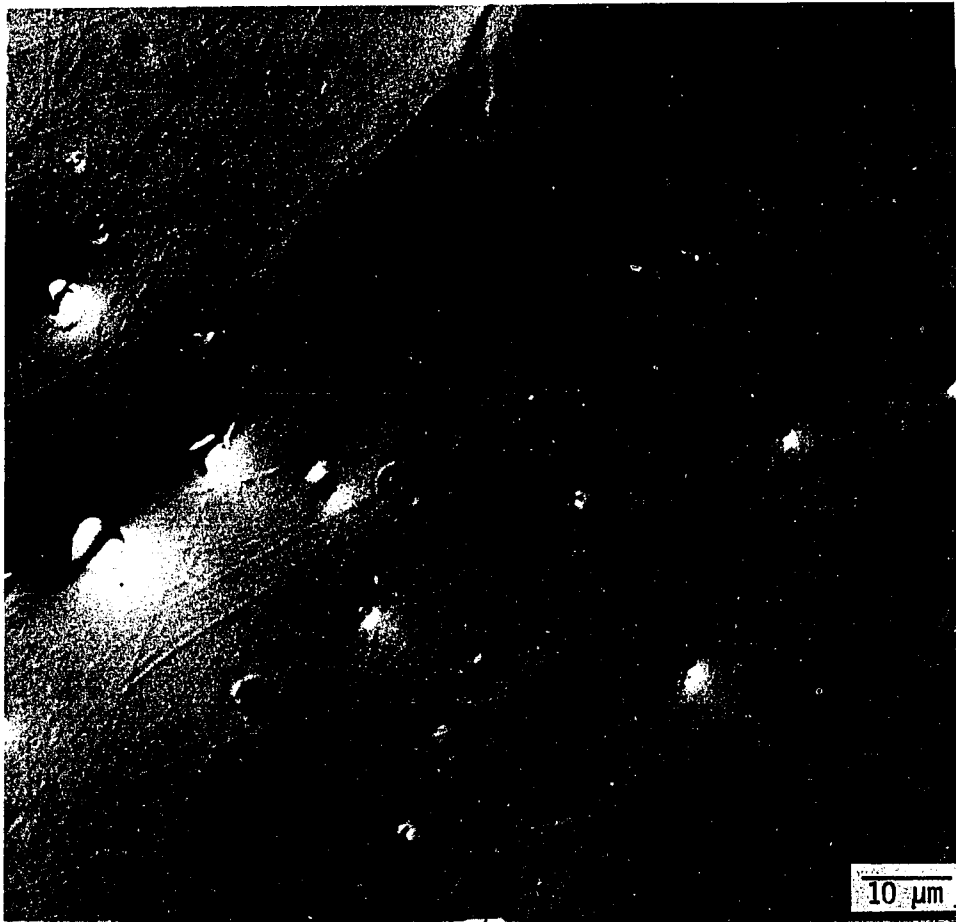
boundary of mask
ion bombarded area | masked area



boundary of mask

Fig. 105. AL-3, 0.1% yttrium-doped, partially masked and bombarded with dual beam of 4 MeV Fe^{++} and 0.4 MeV He^+ ions to 140 dpa at 600°C

boundary of mask
ion bombarded area | masked area



boundary of mask

Fig. 106. AL-4, 0.5% yttrium-doped, partially masked and bombarded with dual beam of 4 MeV Fe^{++} and 4 MeV He^+ ions to 118 dpa at 600°C

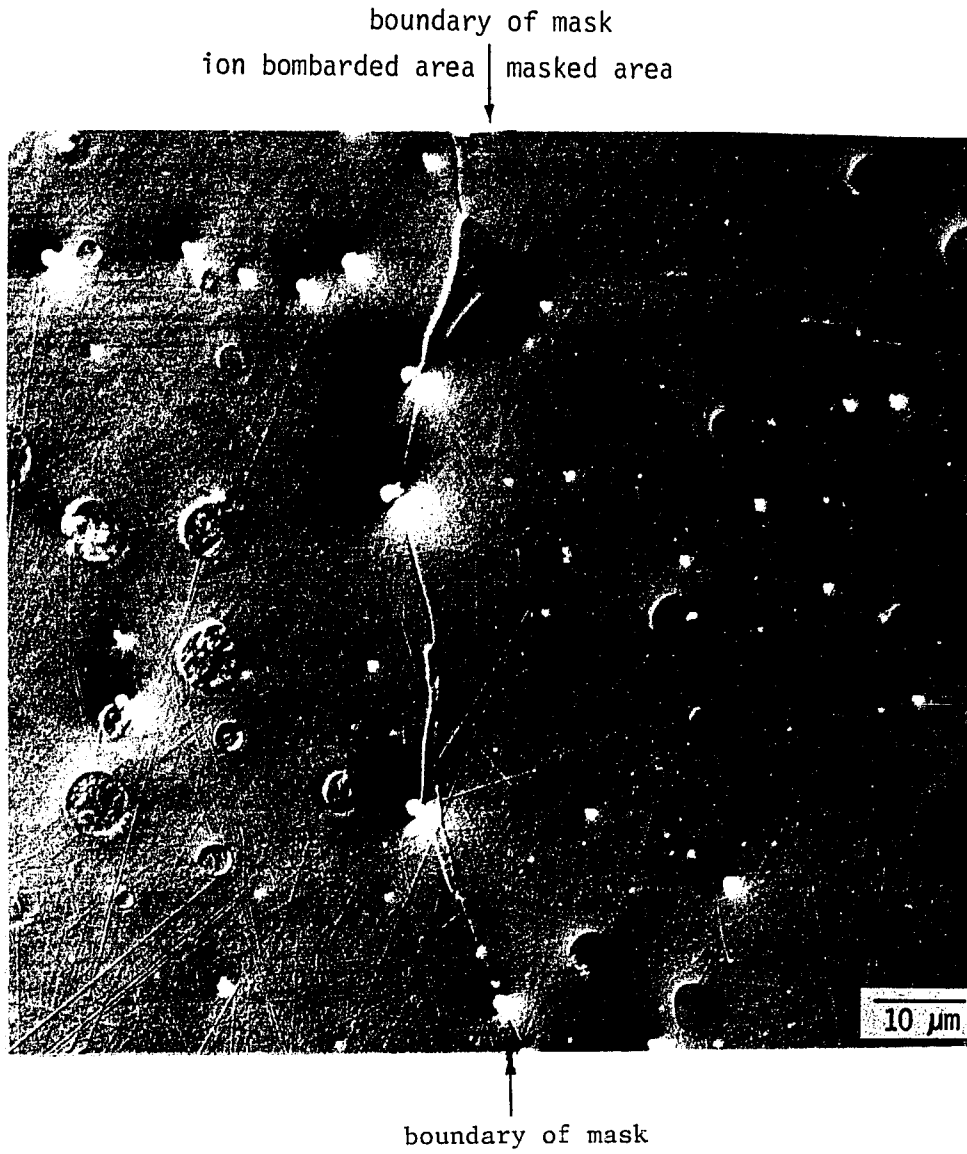


Fig. 107. AL-5, 1.0% yttrium-doped, partially masked and bombarded with dual beam of 4 MeV Fe^{++} and 0.4 MeV He^+ ions to 107 dpa at 600°C

boundary of mask
ion bombarded area | masked area
↓



↑
boundary of mask

Fig. 108. AL-6, 0.05% lanthanum-doped, partially masked and bombarded with dual beam of 4 MeV Fe^{++} and 0.4 MeV He^+ ions to 116 dpa at 600°C

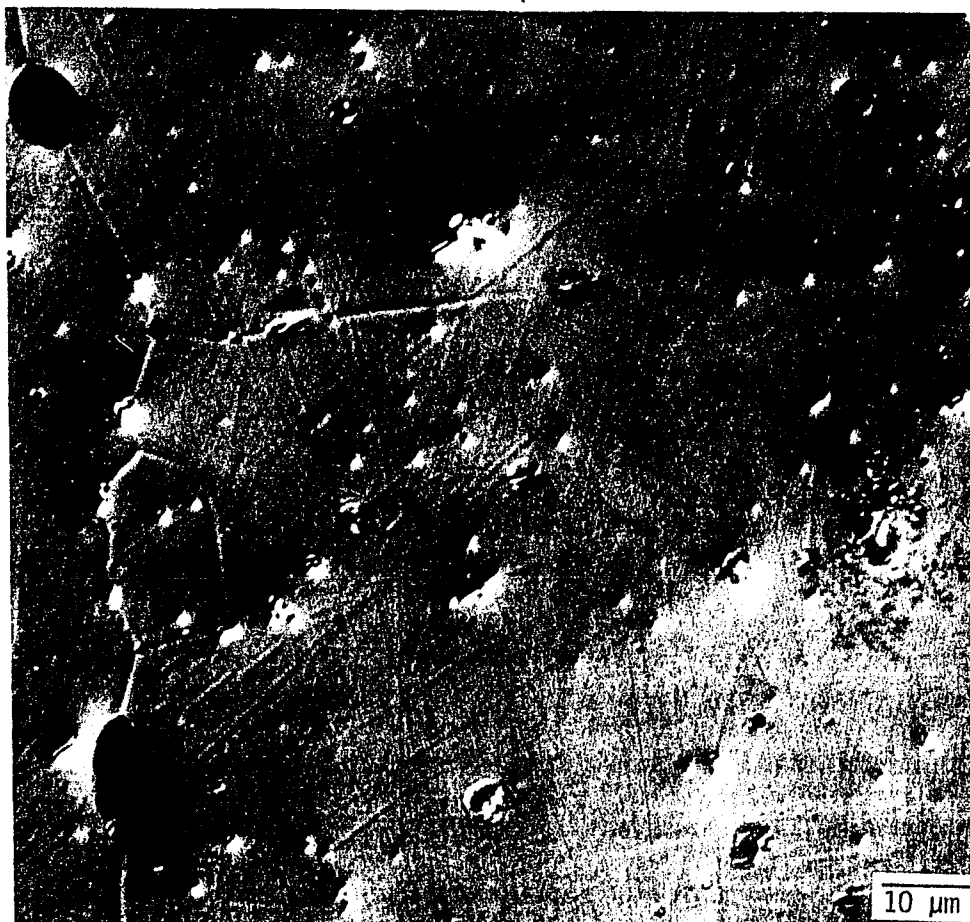
boundary of mask
ion bombarded area | masked area



↑
boundary of mask

Fig. 109. AL-7, 0.1% lanthanum-doped, partially masked and bombarded with dual beam of 4 MeV Fe^{++} and 0.4 MeV He^+ ions to 117 dpa at 600°C

boundary of mask
ion bombarded area | masked area



↑
boundary of mask

Fig. 110. AL-8, 0.5% lanthanum-doped, partially masked and bombarded with dual beam of 4 MeV Fe⁺⁺ and 0.4 MeV He⁺ ions to 97 dpa at 600°C

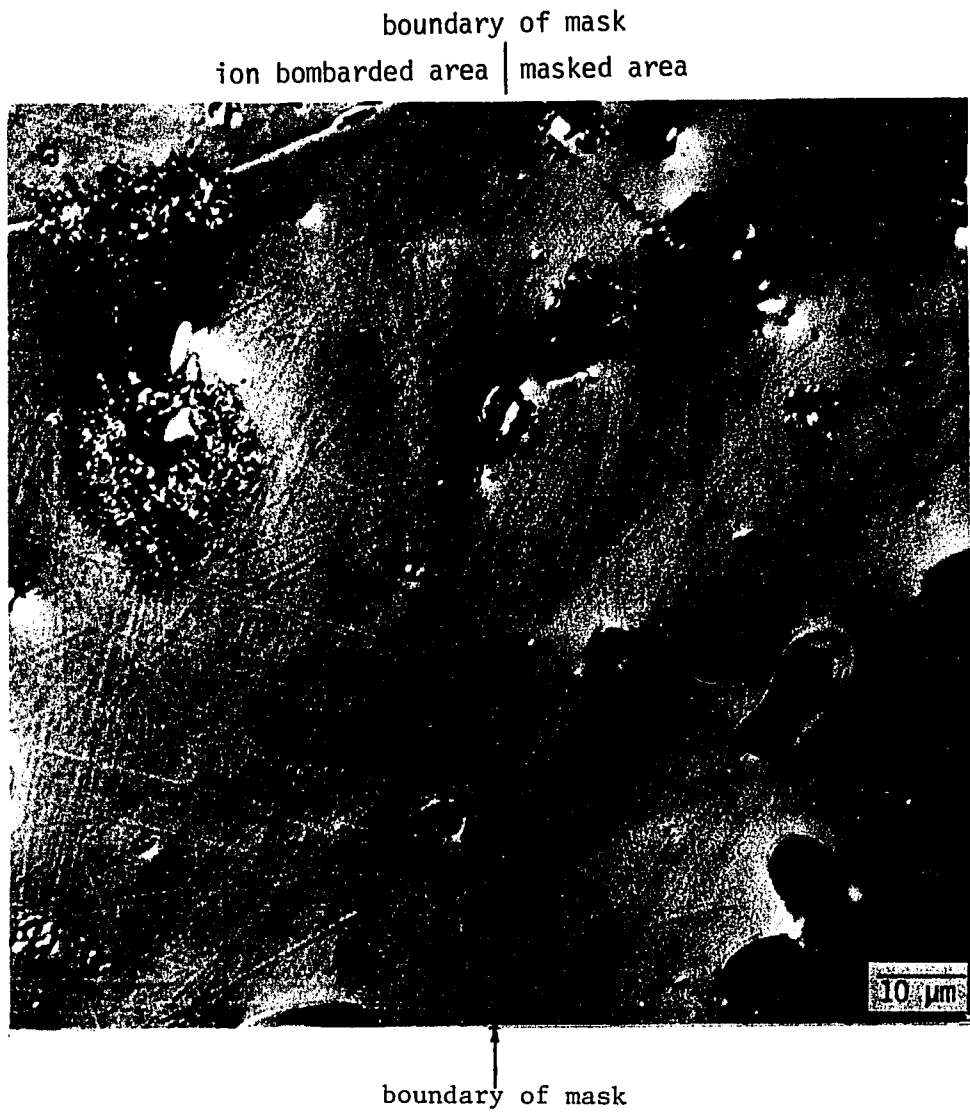


Fig. 111. AL-9, 1.0% lanthanum-doped, partially masked and bombarded with dual beam of 4 MeV Fe^{++} and 0.4 MeV He^+ ions to 116 dpa at 600°C

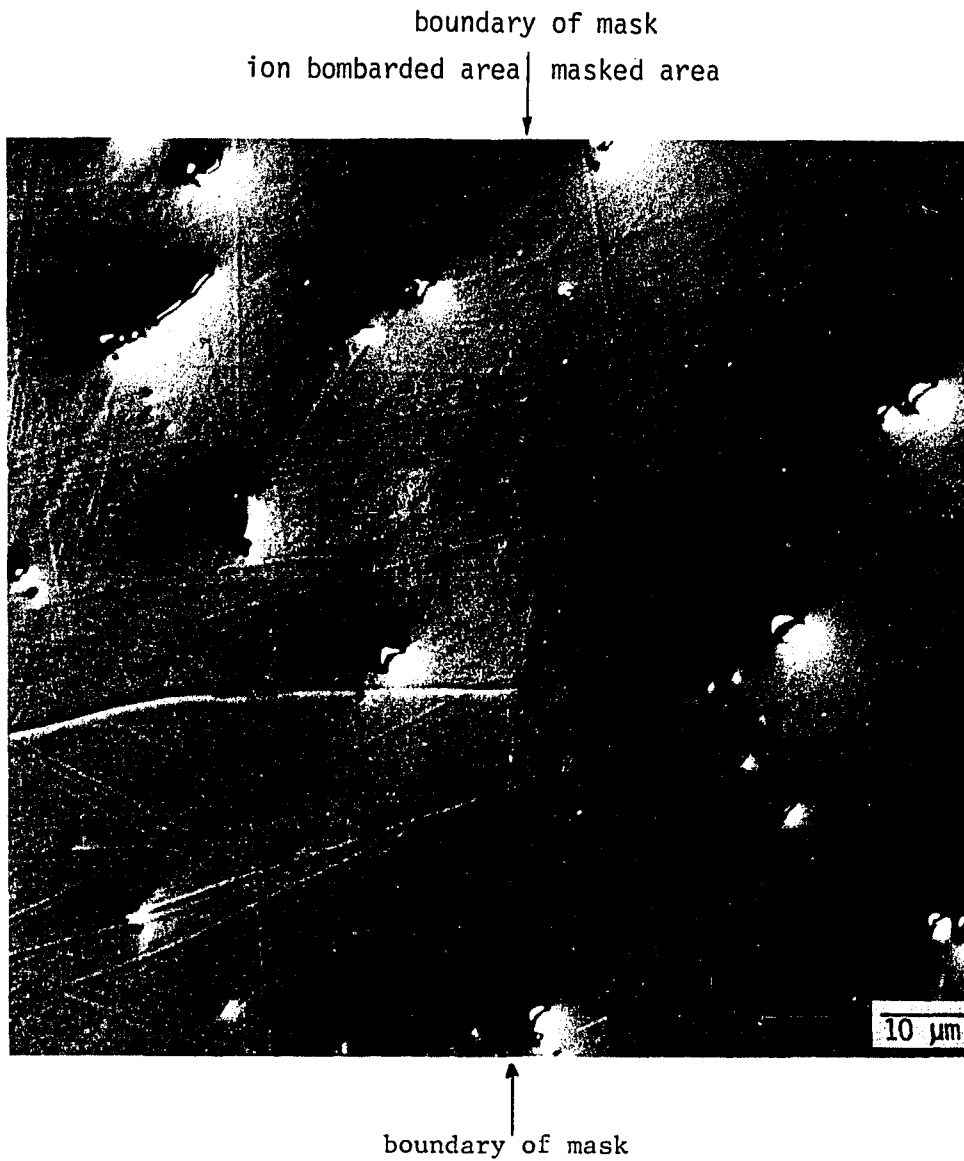


Fig. 112. AL-10, 0.05% cerium-doped, partially masked and bombarded with dual beam of 4 MeV Fe^{++} and 0.4 MeV He^{+} ions to 10^7 dpa at 600°C

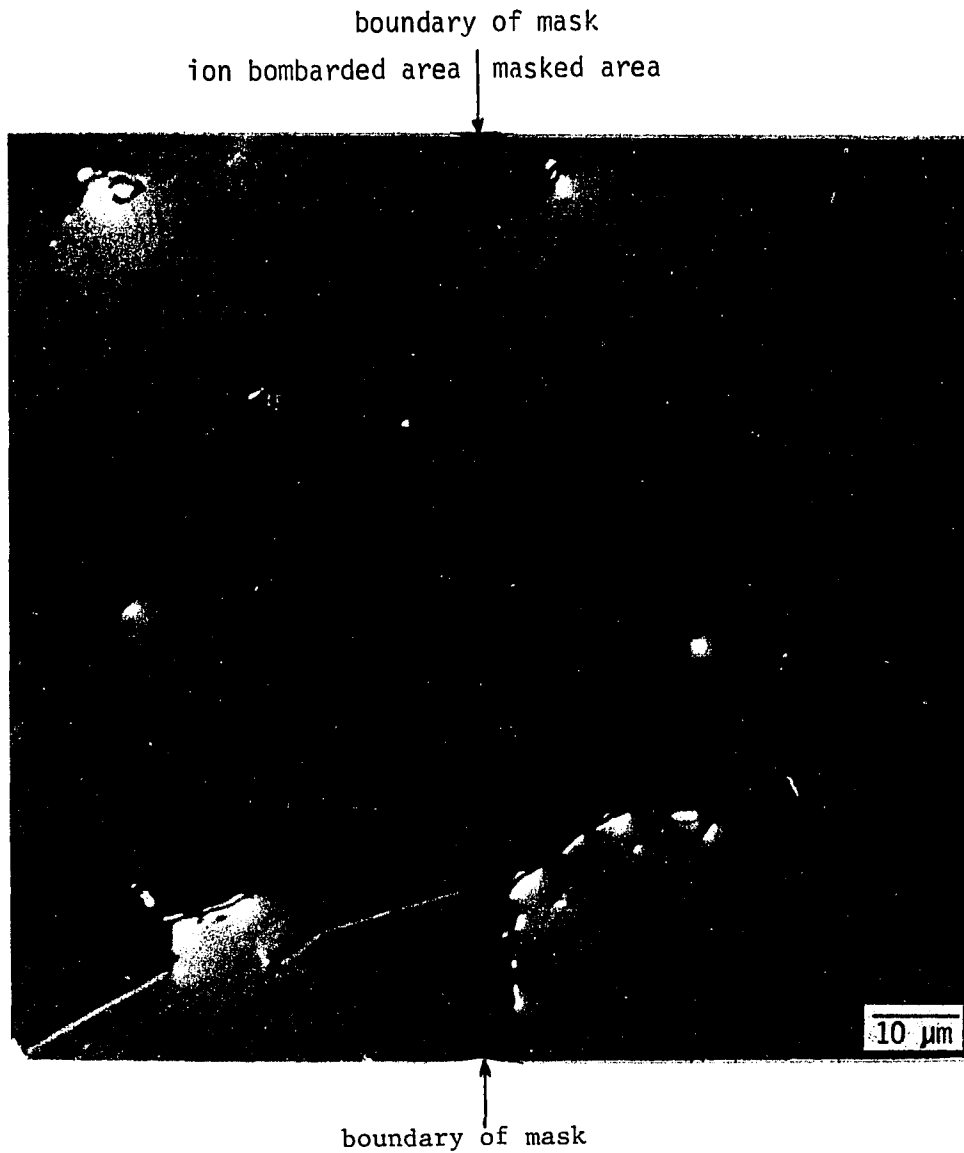
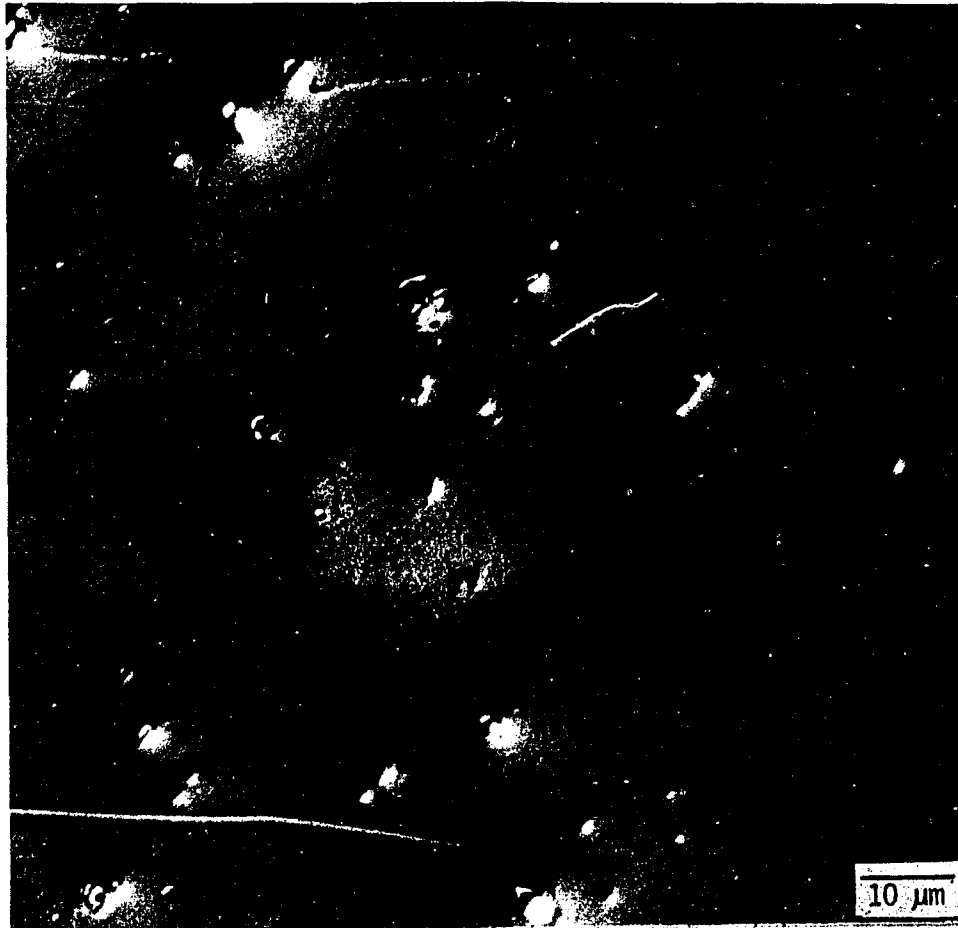


Fig. 113. AL-11, 0.1% cerium-doped, partially masked and bombarded with dual beam of 4 MeV Fe^{++} and 0.4 MeV He^+ ions to 130 dpa at 600°C

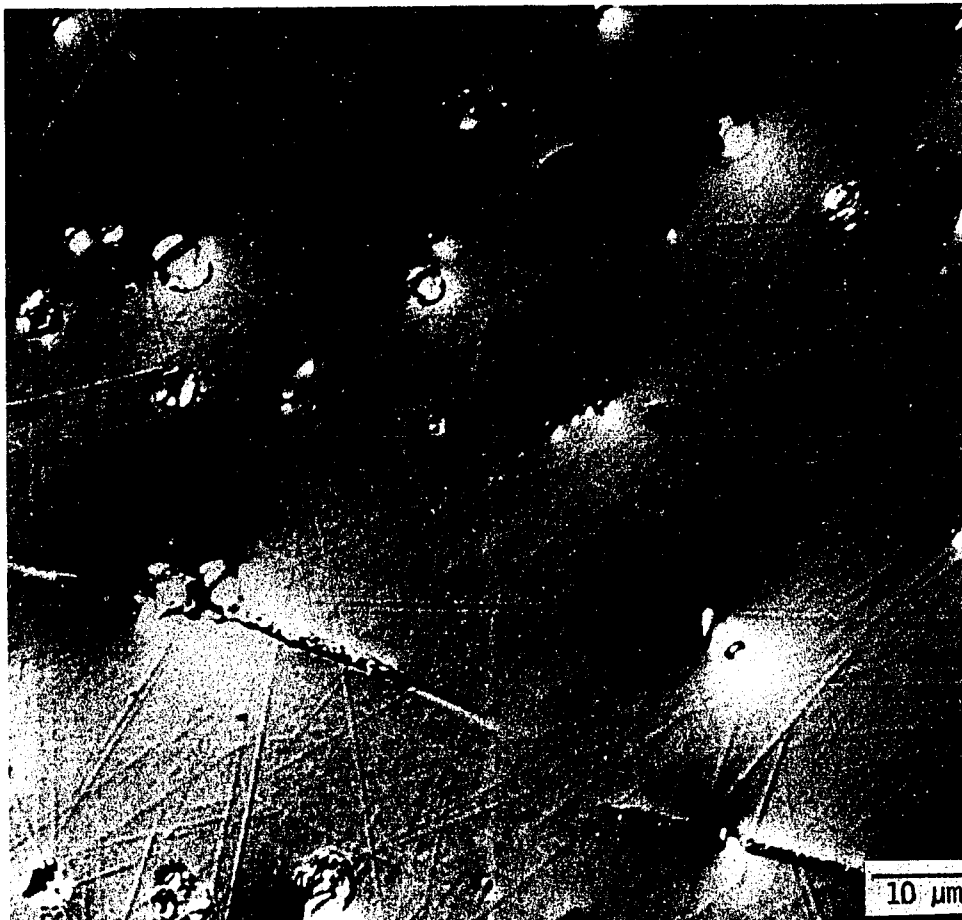
boundary of mask
ion bombarded area | masked area
↓



↑
boundary of mask

Fig. 114. AL-12, 0.5% cerium-doped, partially masked and bombarded with dual beam of 4 MeV Fe^{++} and 0.4 MeV He^+ ions to 112 dpa at 600°C

boundary of mask
ion bombarded area | masked area



↑
boundary of mask

Fig. 115. AL-13, 1.0% cerium-doped, partially masked and bombarded with dual beam of 4 MeV Fe^{++} and 0.4 MeV He^+ ions to 101 dpa at 600°C

Table 35. Approximated chemical composition of the typical second phase particles in the rare-earth doped and undoped AL alloys. See Tables 21-34 for detail

Alloy	Particle	Chemical formula ^a
Undoped AL	01-4	$Fe_{10}Ni_{10}Cr_2Ti_{22}Si_5(C)_n^b$
	01-6	$Ti(C)_n^b$
	01-7	$Ti(C)_n^b$
	1-3	$Fe_3NiTi_{10}Si_4(C)_n^b$
	1-6	$Fe_5Ni_2CrTi_{18}Al_4(C)_n^b$
Yttrium-doped AL	2-9	$Fe_{10}Ni_{11}Y_{24}$
	3-4	$Fe_{18}Cr_2Ni_{20}Y_3$
	4-4	Fe_6Ni_6Y
	4-6	$Fe_{15}Ni_{23}Y_5$
	5-3	Fe_3Ni_5Y
	5-5	$Fe_{10}Ni_{15}Y_3$
	5-6	Fe_6Ni_5Y
	5-9	Fe_3Ni_8Y
Lanthanum-doped AL	7-2	$FeNi_2La_2$
	7-4	$FeNi_2La$
	8-3	$Fe_{12}Ni_7La_9$
	8-6	$Fe_3Ni_6La_4$
	8-8	$Fe_3Ni_7La_4$
	9-4	$Fe_2Ni_6La_5$
	9-9	$FeNi_7La$
	10-3	$Fe_{25}Ni_{20}La_6$
	10-6	$Fe_{15}Ni_{13}La_9$
	11-4	$Fe_4Ni_9Ce_8$
Cerium-doped AL	12-3	$Fe_6Ni_{14}Ce_7$
	12-4	$Fe_6Ni_{16}Ce_7$
	12-7	$Fe_3Ni_5Ce_5$
	12-8	$Fe_4Ni_9Ce_4$
	12-9	$Fe_2Ni_5Ce_2$
	13-5	$Fe_2Ni_5Ce_5$
	13-6	$FeNi_3Ce$
	13-9	$Fe_2Ni_5Ce_2$

Sample Designation Key

Example: 01-4; 4 represents the particle number for a given alloy and 01 represents alloy number as described in the Table 14

^aLight materials such as H, C, N and O are not considered.

^bSupposed to be carbide.

measured, the total is sometimes below 100%, e.g., #6 and #7 in Table 21.

The standard P7 stainless steel shows high swelling of about 40-50% (Table 19) due to ion bombardment. The concentration of Ti in the matrix was determined for each alloy by the electron microprobe, as given in Table 36. These concentrations are plotted versus concentration of rare-earth addition and percent swelling in Figs. 116-118. The photomicrographs (Fig. 119) with interference light fringes show a grooved-shape grain boundary, contrary to a ridged-shape at low swelling. Johnston et al. [207] and Johnston and Rosolowski [208] observed a grooved-shape grain boundary with a ridge at its center, as shown as in Fig. 120, part 3.

Microstructure Analysis

After interferometry photographs were taken to measure swelling, the irradiated TEM specimens from the target assemblies D, E, F and G were used for the microstructure analysis by transmission electron microscopy. A part of the irradiated surface of each specimen was lacquered (for example, see Figs. 57 and 58) and the specimen was electropolished using the jet surface polishing rig (Fig. 43a) [197]. The electrolyte solution consisted of 9 parts acetic acid and 1 part perchloric acid at room temperature. A current of 200 mA at a voltage of about 40 V was applied for 1.8 sec to remove approximately 0.6 microns. Then, the specimen was cleaned with methanol and acetone. The step height between lacquered and

Table 36. The % swelling and composition of titanium in matrix

Alloy Designation	Alloy Description or Composition	% Swelling with 100 appm He	wt% of Ti in Matrix
AL0	As-received ^a	4	
AL01	Annealed	5.1	3.314
AL1	Arc-melted	3.8	3.168
AL2	AL + 0.05% Y	5.8	3.004
AL3	AL + 0.1 % Y	3.1	3.121
AL4	AL + 0.5 % Y	2.3	3.164
AL5	AL + 1.0 % Y	2.8	2.991
AL6	AL + 0.05% La	4.1	3.166
AL7	AL + 0.1 % La	4.2	3.009
AL8	AL + 0.5 % La	6.5	2.750
AL9	AL + 1.0 % La	5.2	3.031
AL10	AL + 0.05% Ce	5.0	2.990
AL11	AL + 0.1 % Ce	4.5	3.179
AL12	AL + 0.5 % Ce	3.1	3.077
AL13	AL + 1.0 % Ce	4.4	3.010

^aOverall concentration of Ti in the as-received alloy is 3.28%.

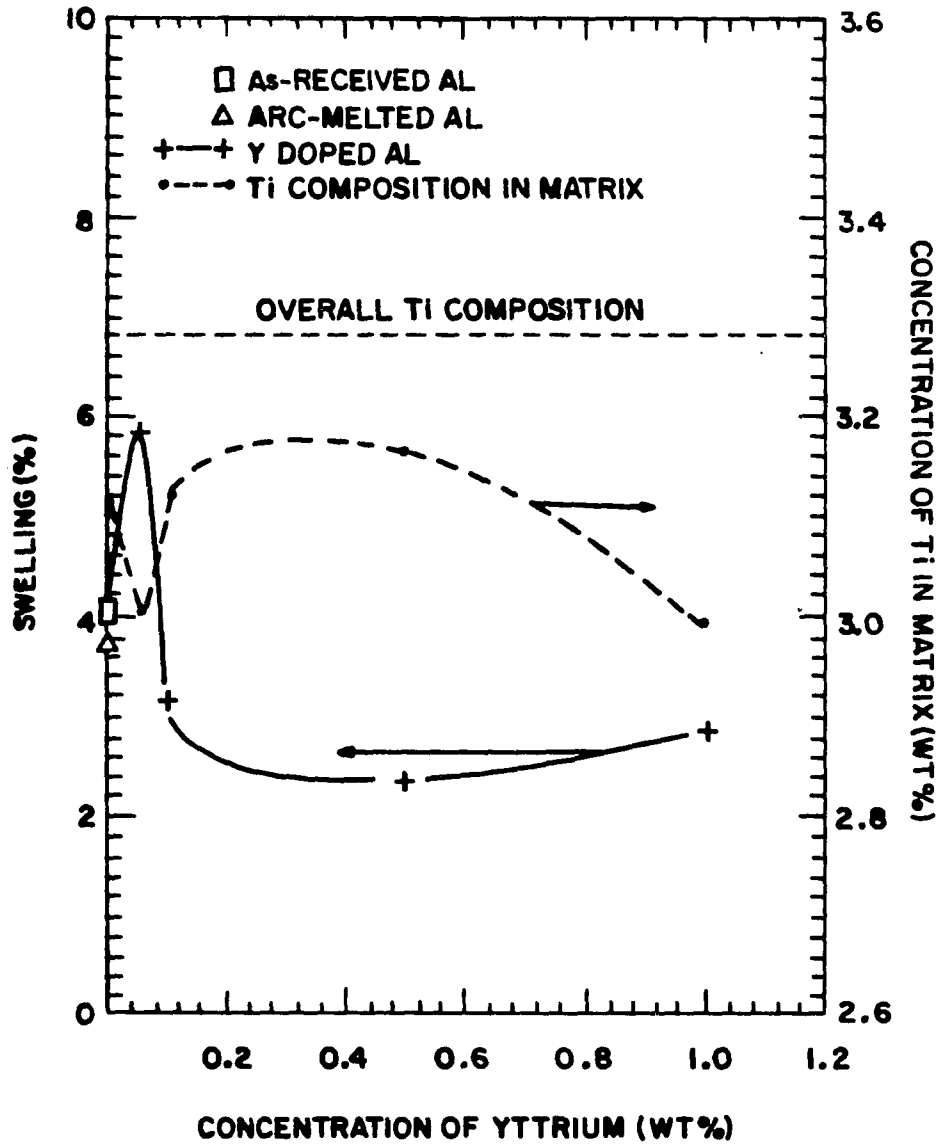


Fig. 116. Swelling and concentration of Ti in the matrix vs concentration of yttrium

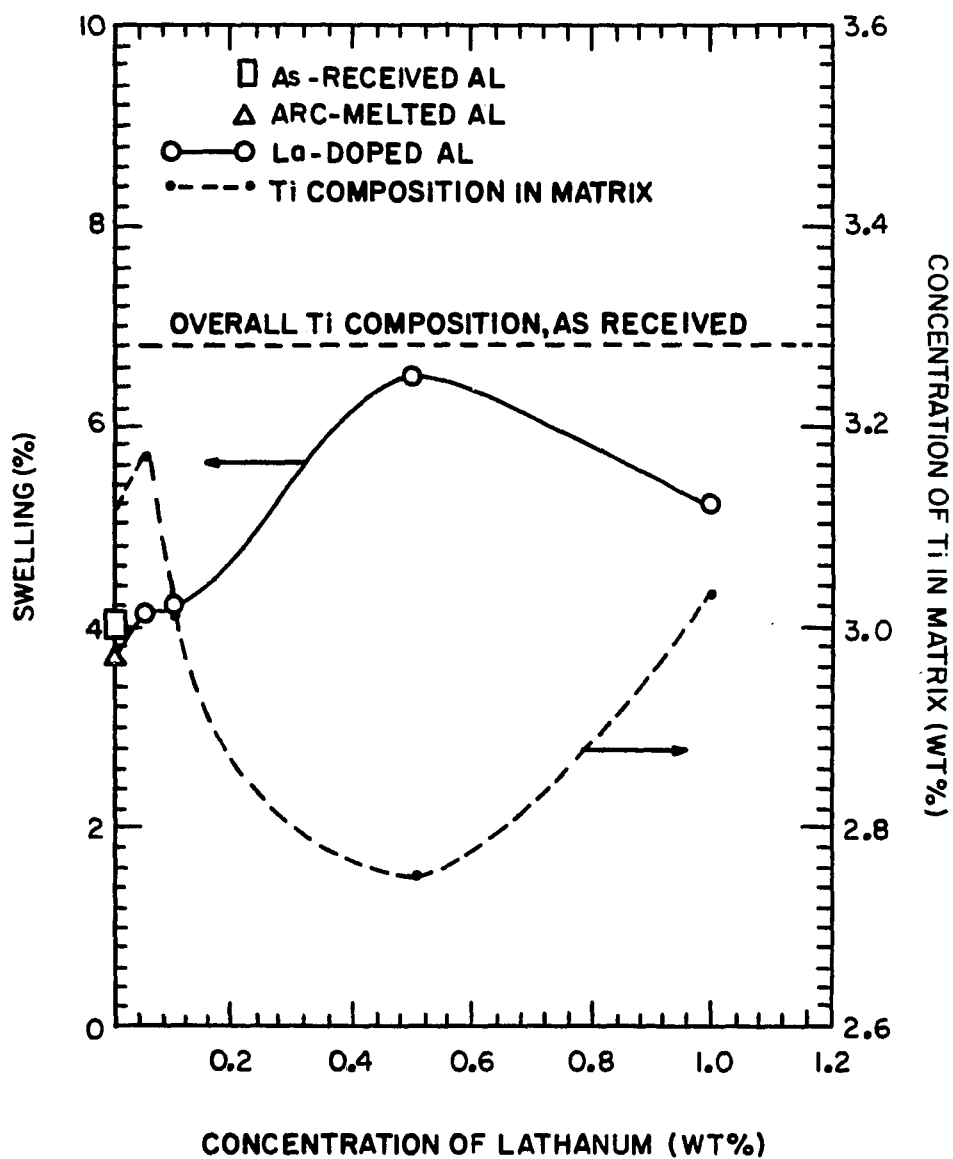


Fig. 117. Swelling and concentration of Ti in the matrix vs concentration of lanthanum

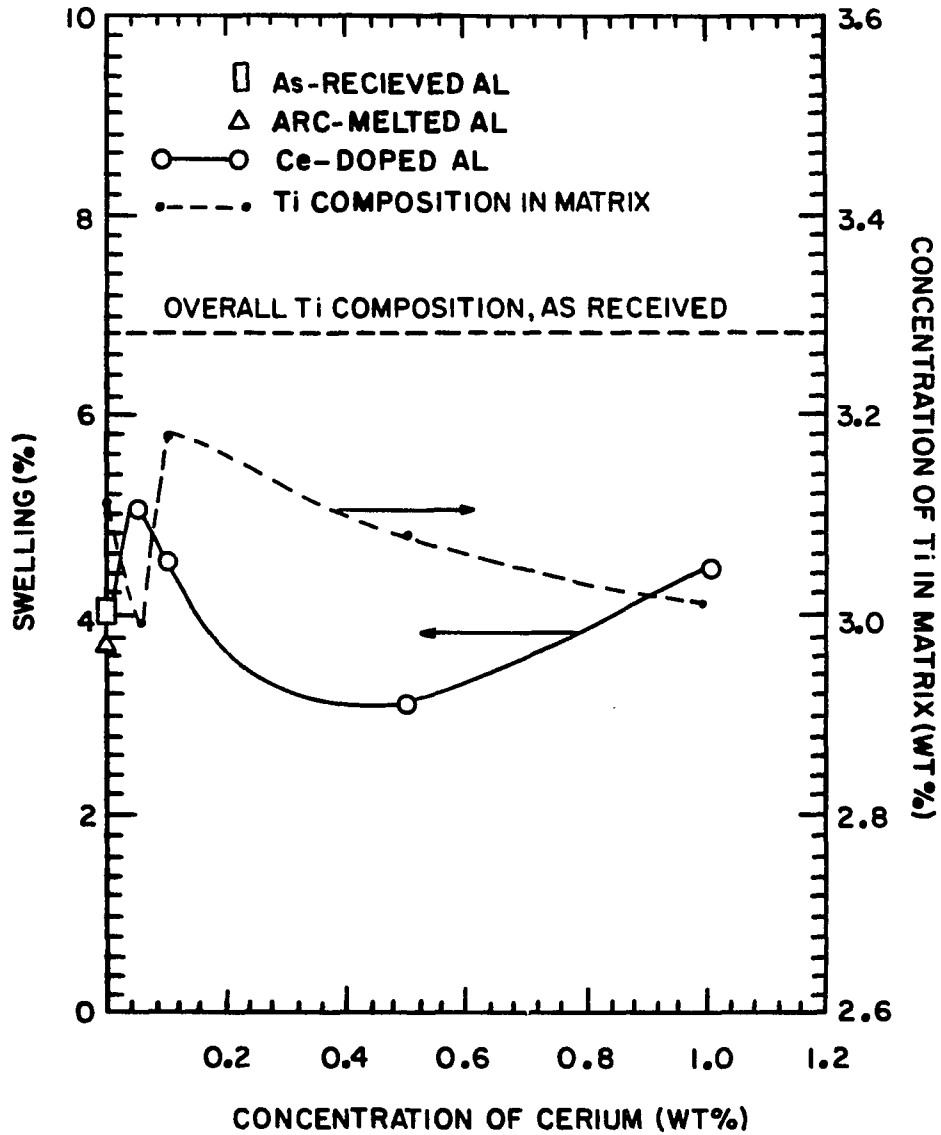


Fig. 118. Swelling and concentration of Ti in the matrix vs concentration of cerium

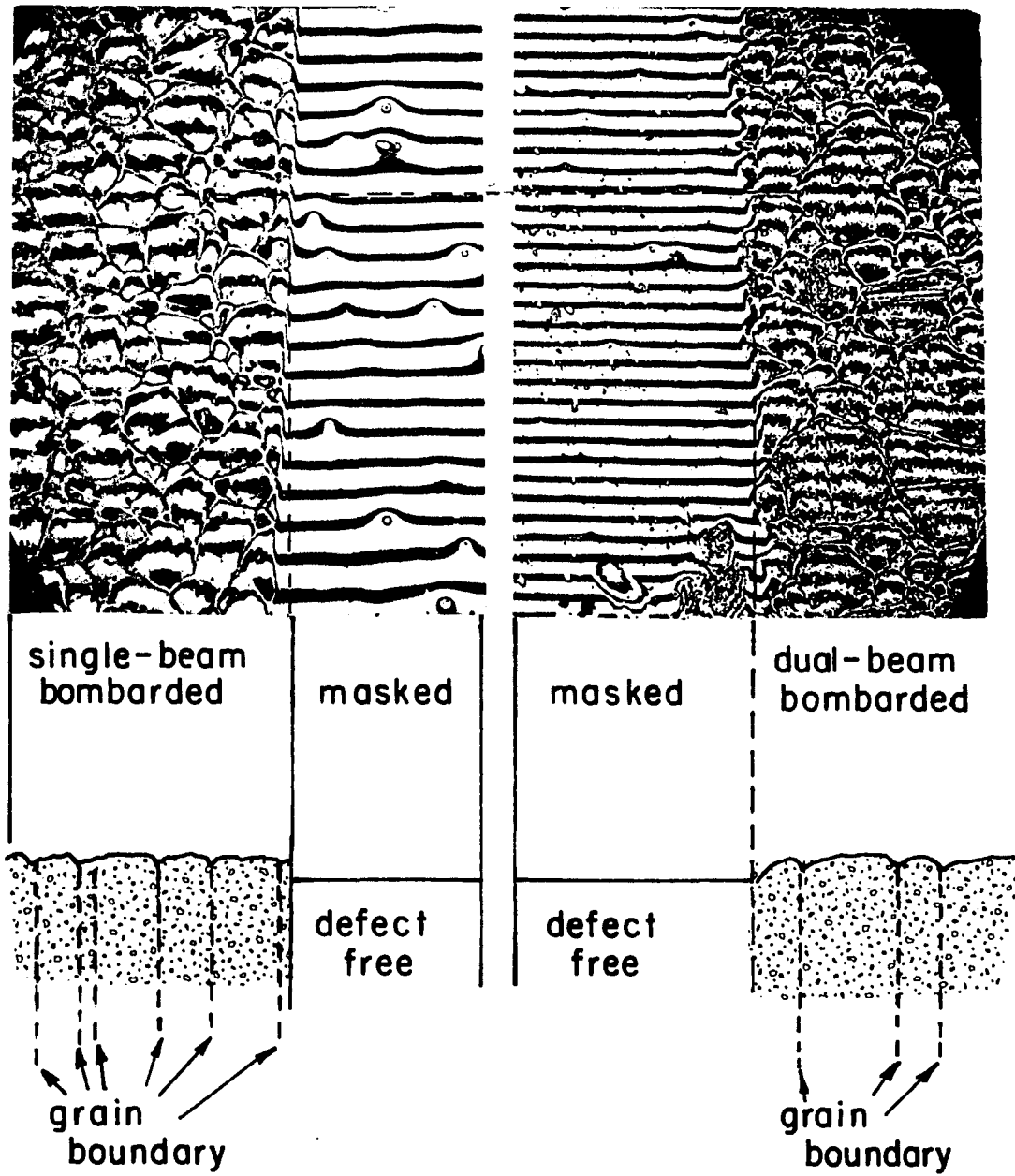


Fig. 119. Standard P7 stainless steel, irradiated with (a) dual-beam of 4 MeV Fe^{++} and 0.4 MeV He^+ ions to 106 dpa and (b) single-beam of 4 MeV Fe^+ ions to 116 dpa at 600°C

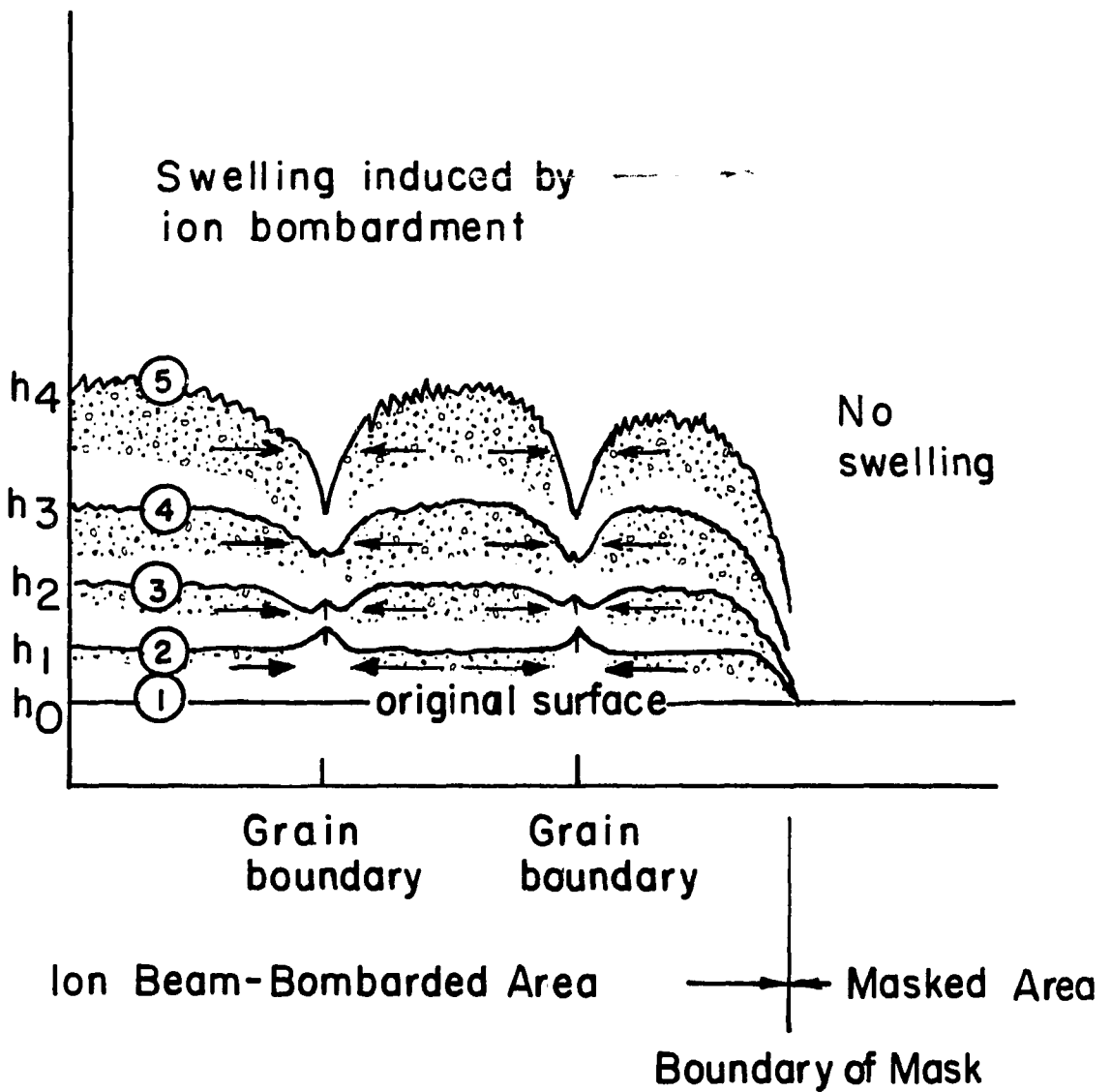
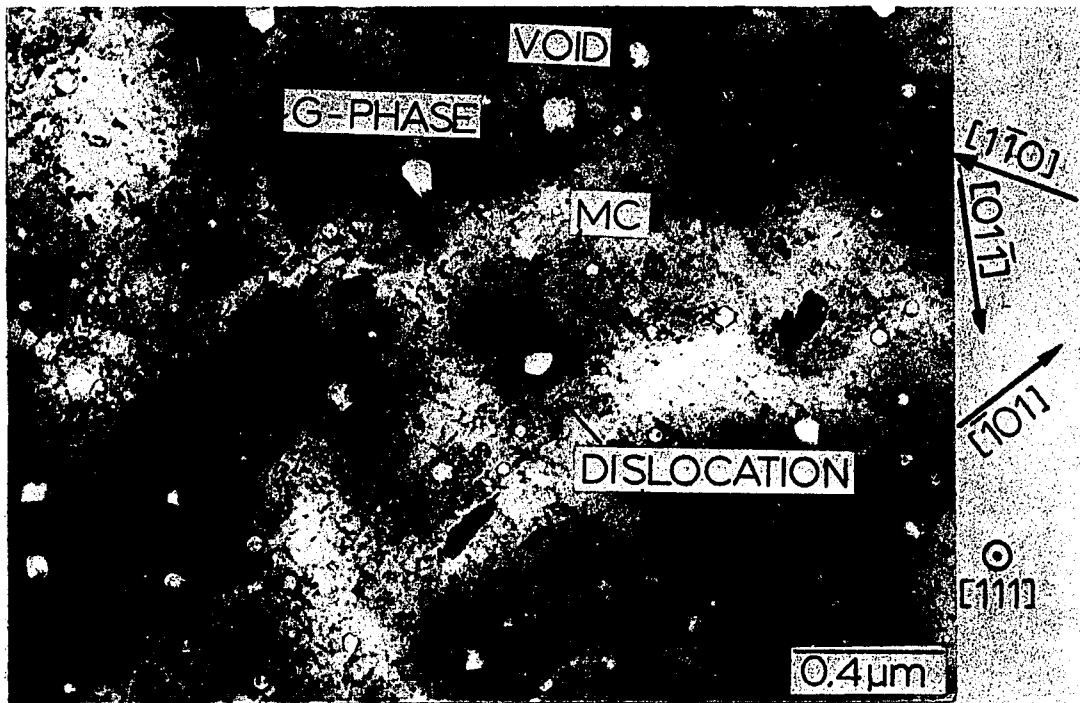


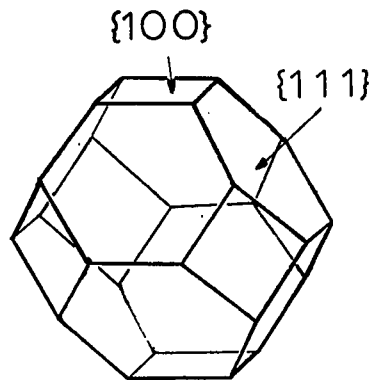
Fig. 120. Deformation of the grain boundary: 1) no swelling, 2) low swelling, 3) about 15% swelling, 4) higher swelling and 5) about 40% swelling

polished areas indicates the amount polished away (Fig. 60). The polished area was then also lacquered, and the backside was electropolished (backthinned) using the jet back-thinning rig (Fig. 43b) [197] and an electrolyte solution of 7 parts methanol and 1 part sulphuric acid at room temperature. A current of 30 mA was applied until a hole with a thin edge was developed. Some of the specimens were further ion milled, using a Polaron ion milling machine and argon gas. A current of about 0.2 mA at 4 KV was applied.

The electron microscope, JEOL 100CX, was used for the micro-structural analysis. To obtain high resolution, the [111] direction two-beam condition was applied to get bright field and dark field images at 20,000X magnification. The images were enlarged about 2.5 times (Figs. 121-132). Selected area diffraction patterns at a camera length of 46 cm were photographed.



(a)



(b)

Fig. 121. (a) Microstructure of AL-1, arc-melted, bombarded at 570° with dual beam of 4 MeV Ni^{++} and 0.4 MeV He^{+} ions to 83 dpa and 546 appm He and (b) configuration of the void structure, tetrakaidecahedron

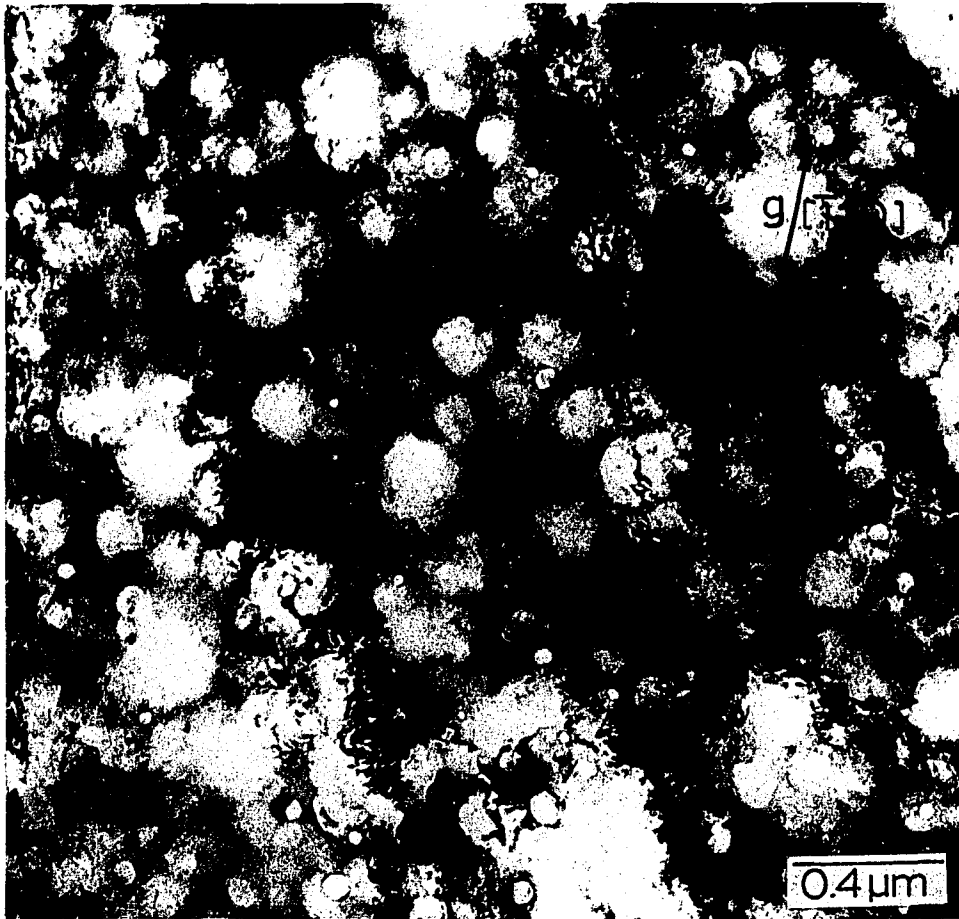


Fig. 122. Microstructure of AL-14, arc-melted, bombarded at 570°C with dual beam of 4 MeV Ni⁺⁺ and 0.4 MeV He⁺ ions to 96 dpa and 104 appm He

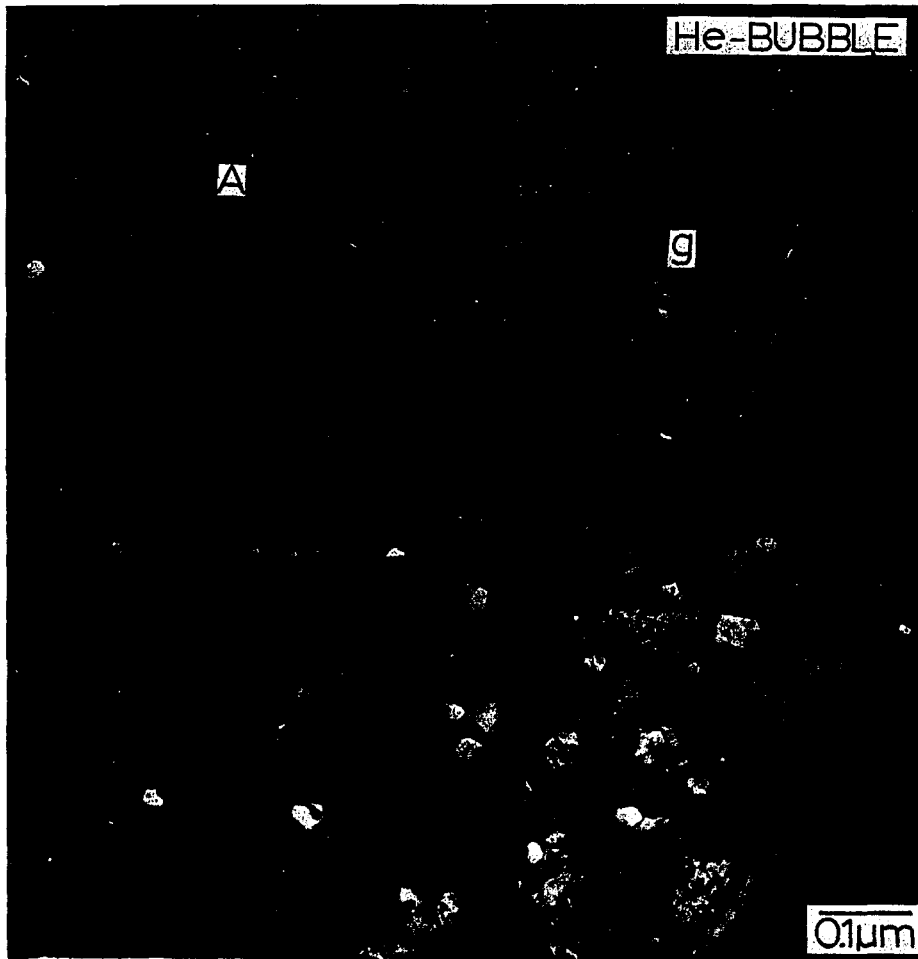


Fig. 123. Microstructure of AL-2, 0.05% yttrium doped, bombarded at 570°C with dual beam of 4 MeV Ni^{++} and 0.4 MeV He^+ ions to 135 dpa and 94 appm He

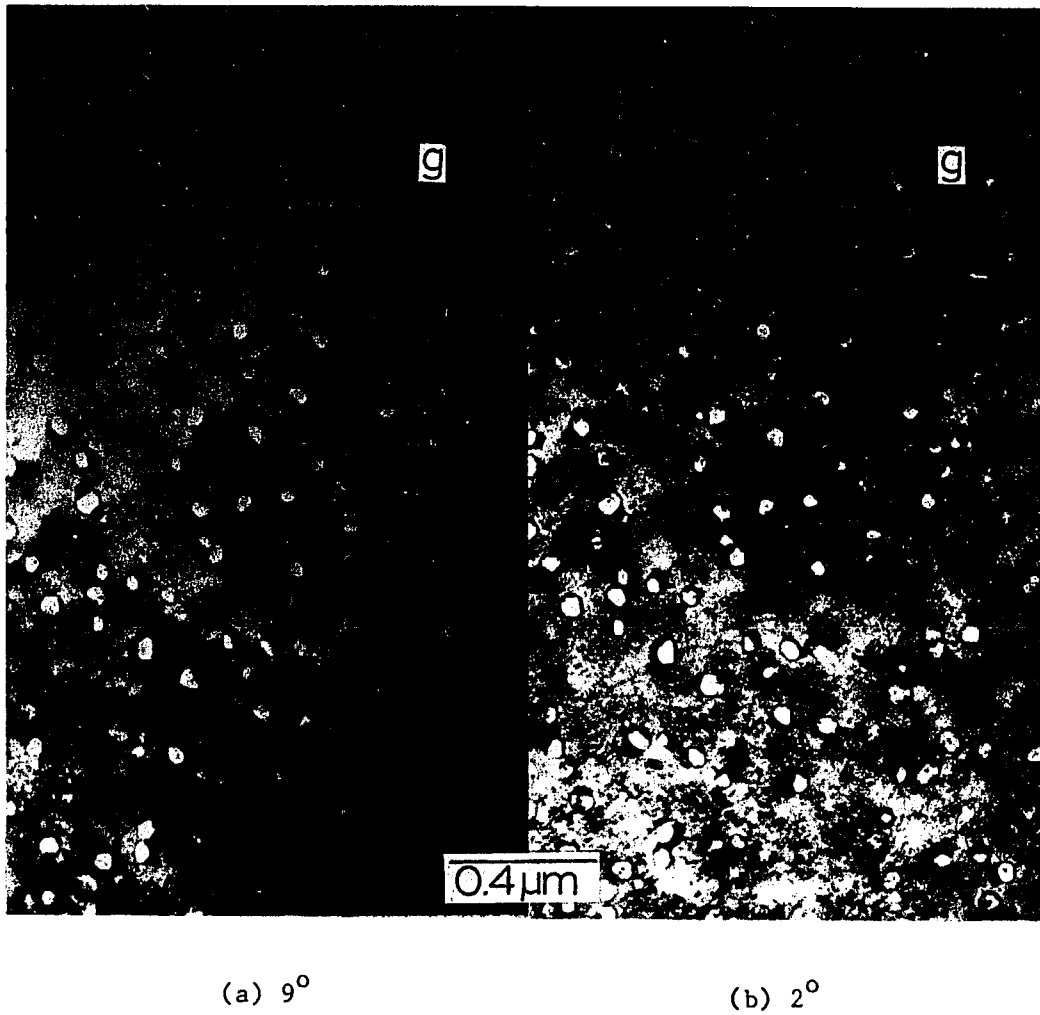
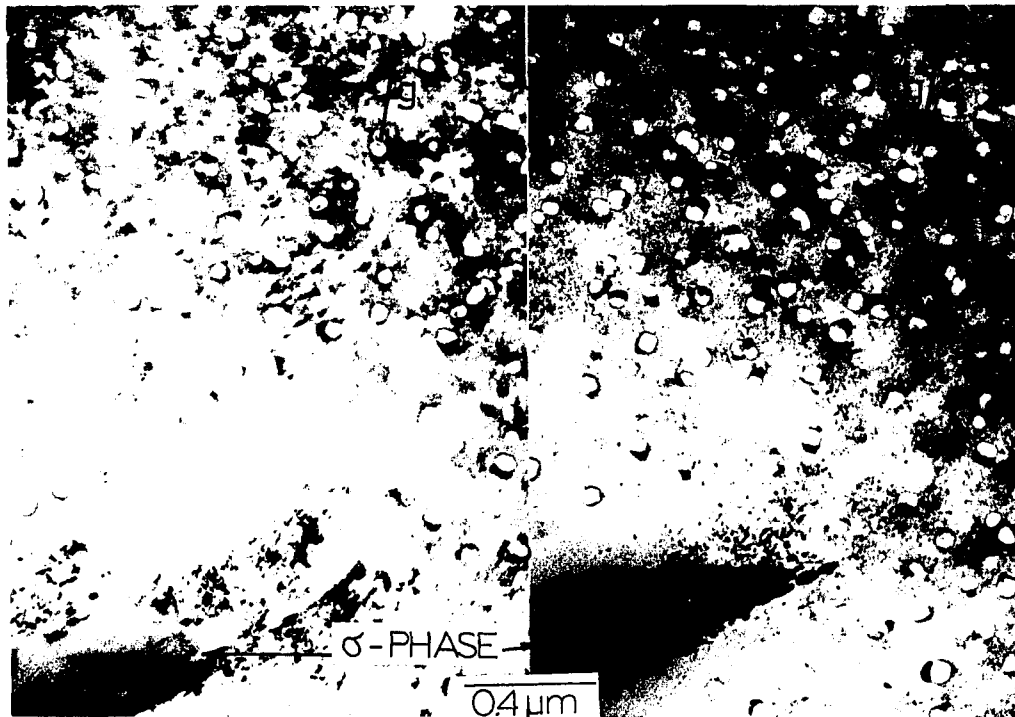
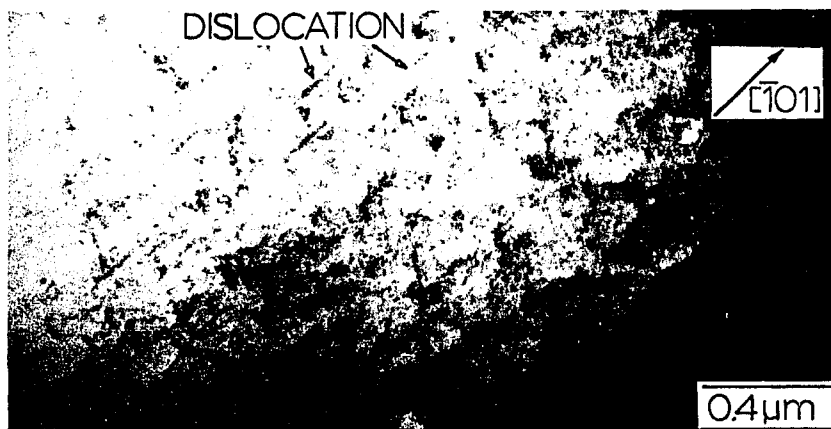


Fig. 124. Stereopair showing microstructure of AL-3, 0.1% yttrium doped, bombarded at 560°C with dual beam of 4 MeV Ni⁺⁺ and 0.4 MeV He⁺ ions to 106 dpa and 102 appm He. The angles are at (a) 9° and (b) 2° to the surface normal



(a)

(b)

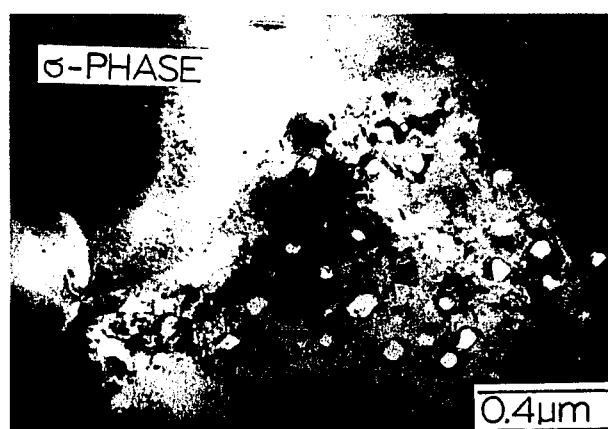


(c)

Fig. 125. Microstructure of AL-3, 0.1% yttrium doped, bombarded at 570°C with dual beam of 4 MeV Ni⁺⁺ and 0.4 MeV He⁺ ions to 106 dpa and 102 appm He at (a) -17° and (b) 3° to the normal direction of the specimen surface and (c) 73 dpa and 102 appm He at 570°C



(a)



(b)

Fig. 126. Microstructure of AL-4, 0.5% yttrium doped, bombarded at 570°C with dual beam of 4 MeV Ni^{++} and 0.4 MeV He^{+} ions to 102 dpa and 85 appm He. (a) Matrix region and (b) near the precipitate

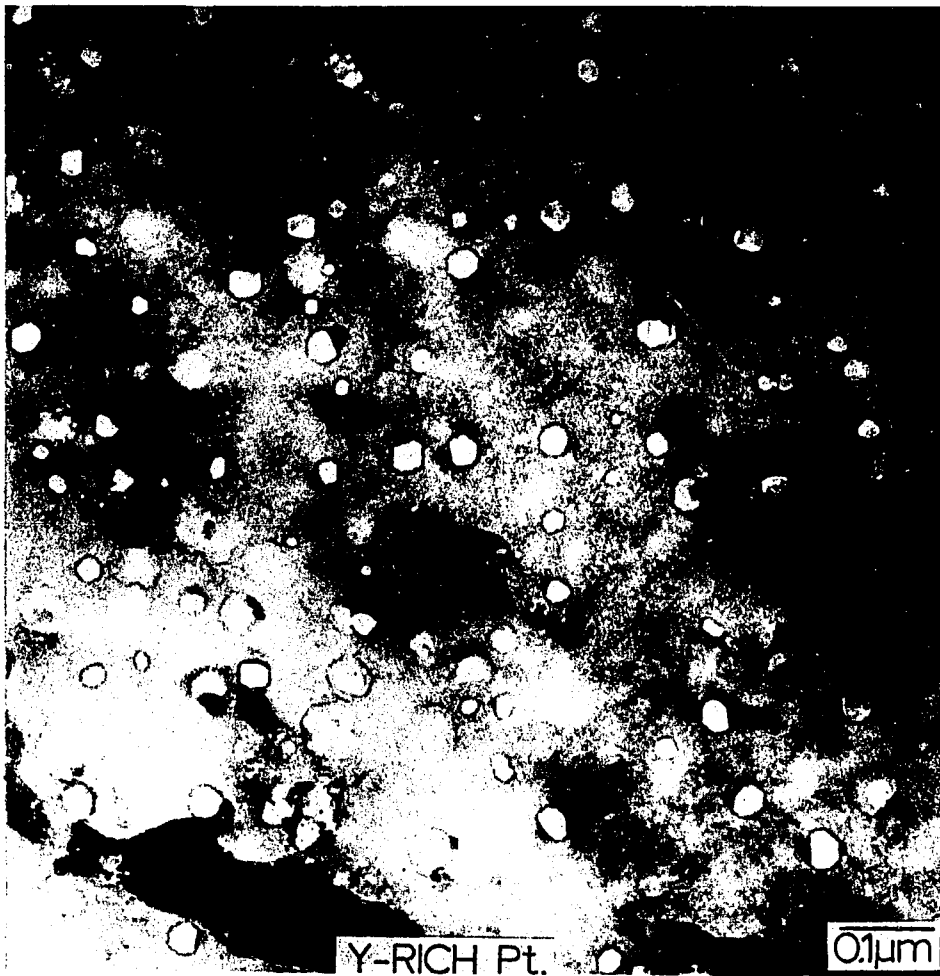


Fig. 127. Microstructure of Al-5, 1.0% yttrium doped, bombarded at 570°C with 4 MeV Ni⁺⁺ and 0.4 MeV He⁺ ions to 66 dpa and 546 appm He

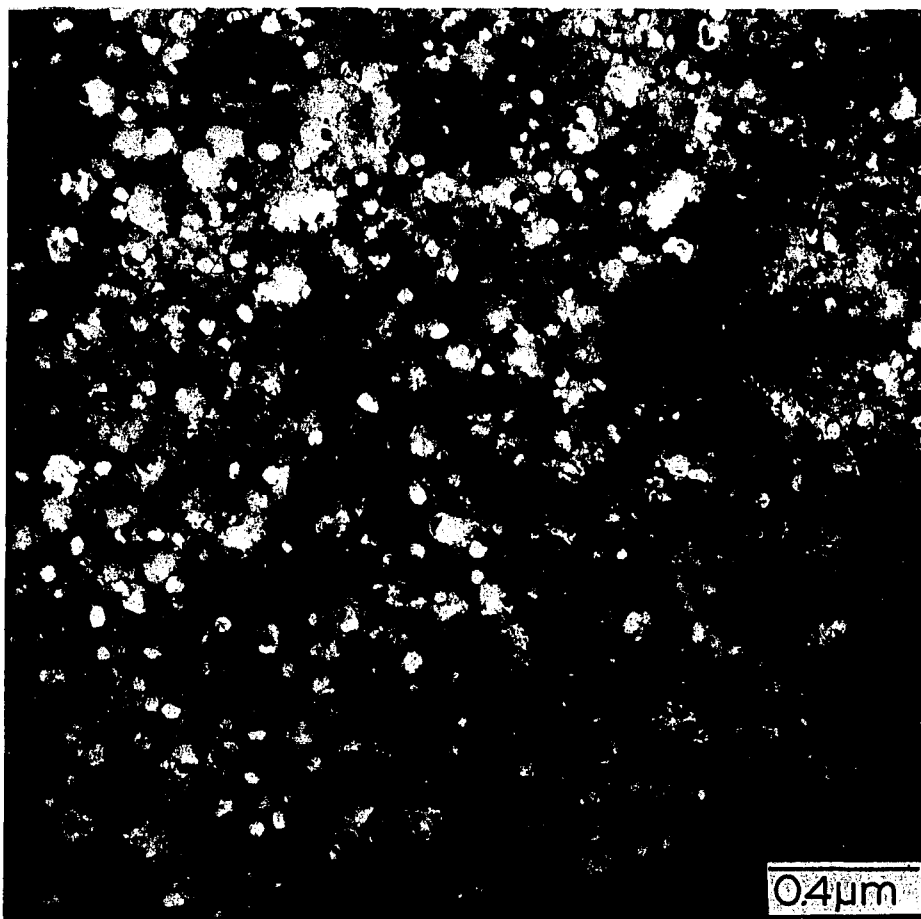


Fig. 128. Microstructure of AL-6, 0.05% lanthanum doped, bombarded at 570°C with 4 MeV Ni⁺⁺ and 0.4 MeV He⁺ ions to 83 dpa and 546 appm He

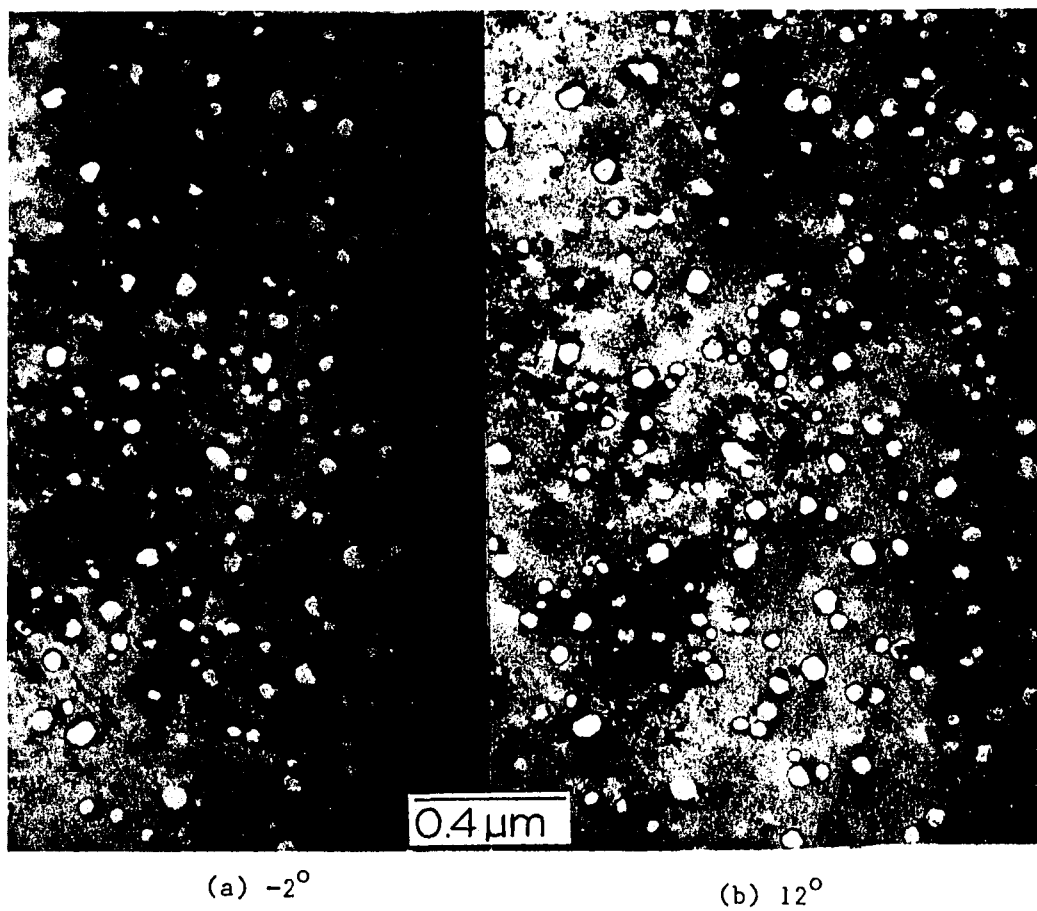
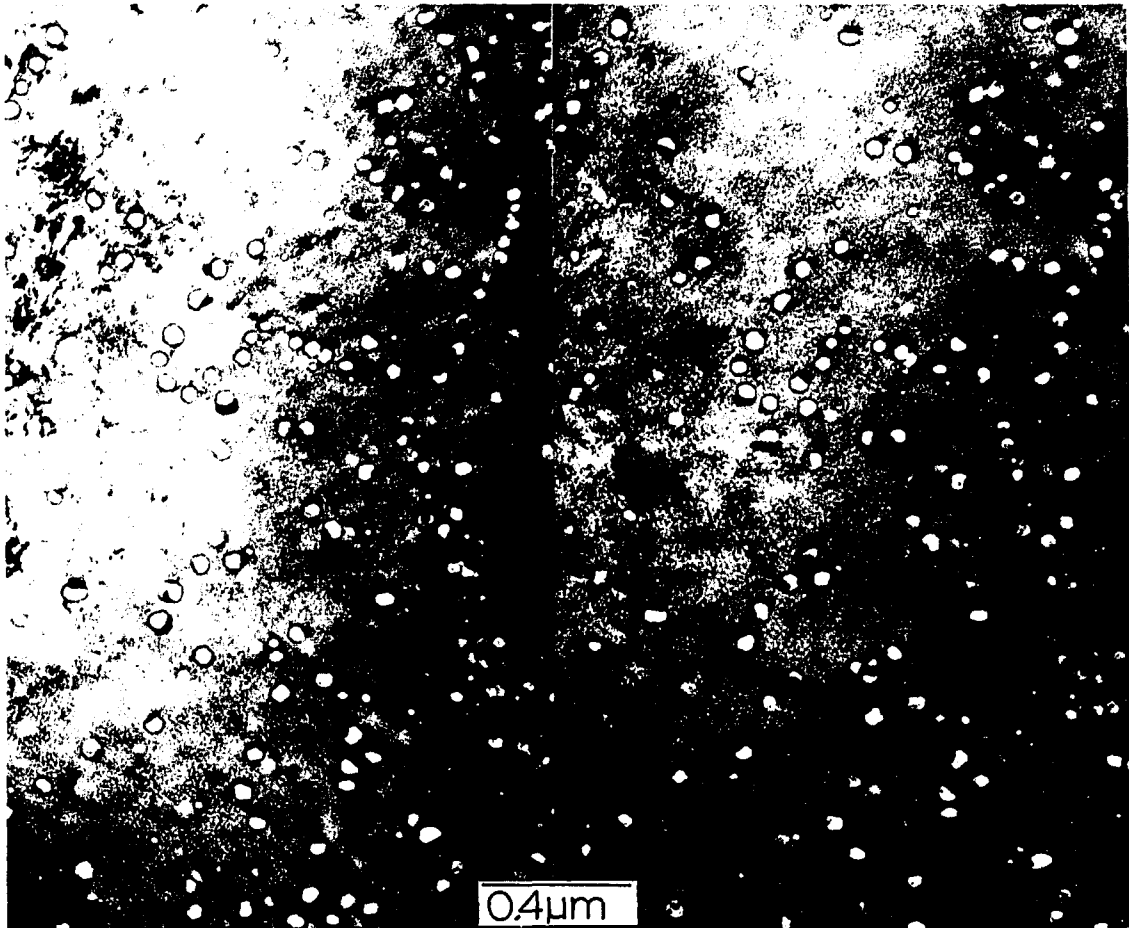


Fig. 129. Stereopairs showing microstructure of Al₃-8, 0.5% lanthanum doped, bombarded at 570°C with 4 MeV Ni⁺⁺ and 0.4 MeV He⁺ ions to 45 dpa and 546 appm He. The angles are at (a) 12° and (b) 2° to the surface normal



(a) -2°

(b) 12°

Fig. 130. Stereopairs showing microstructure of AL-11, 0.1% cerium doped, bombarded at 570°C with 4 MeV Ni^{++} and 0.4 MeV He^{+} ions to 116 dpa and 102 appm He. The angles are at (a) -2° and (b) 12° to the surface normal.

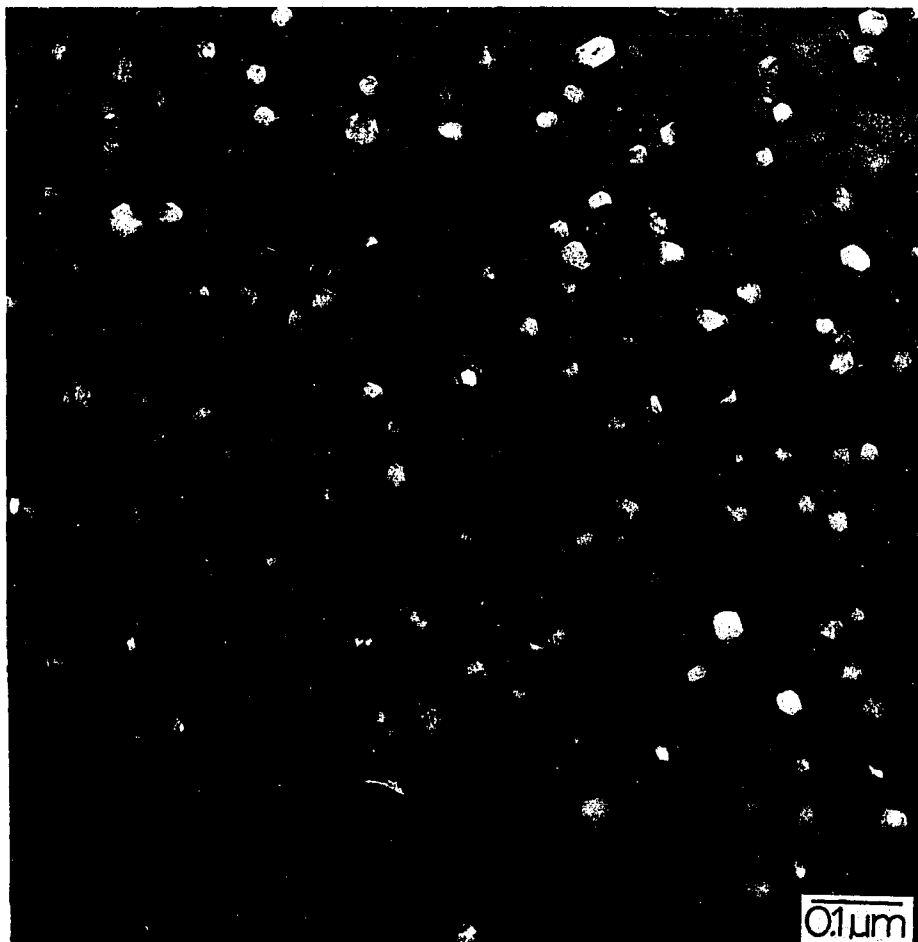
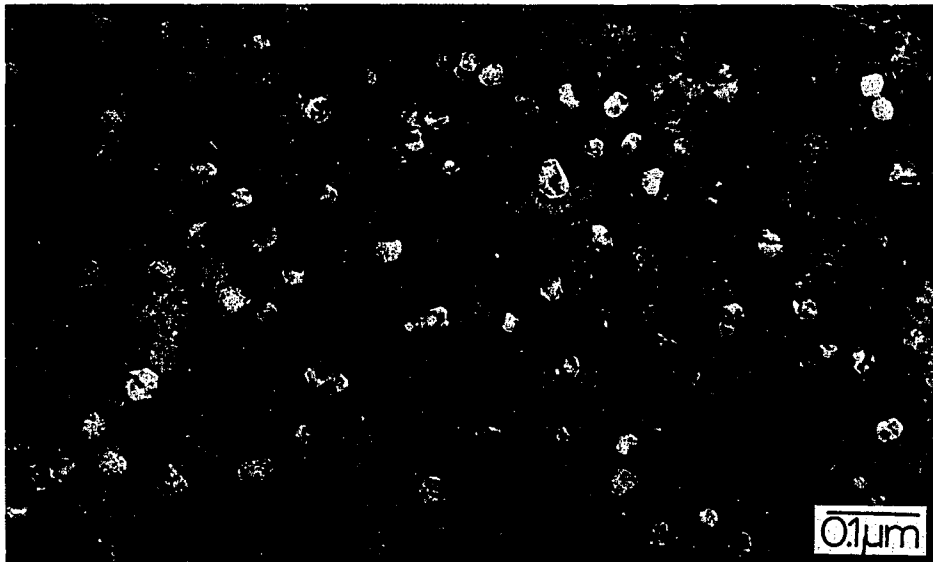
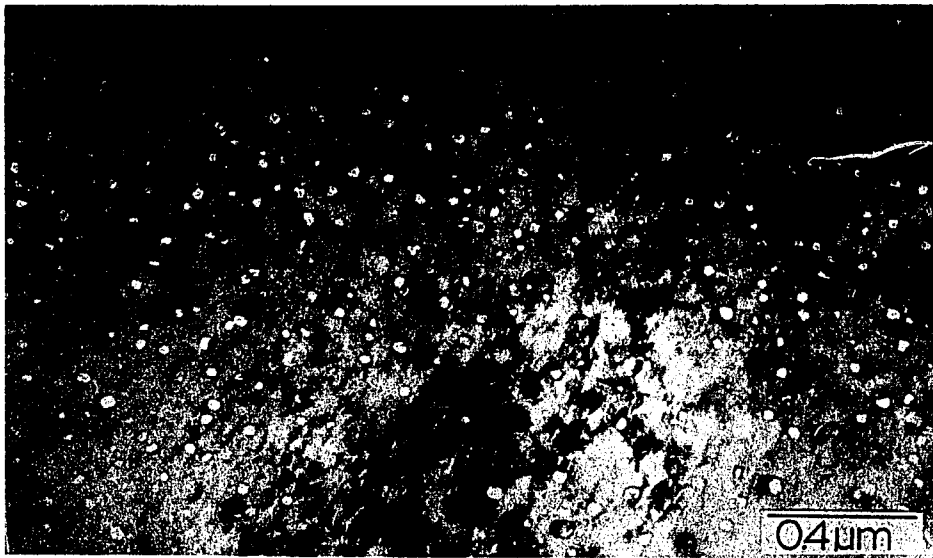


Fig. 131. Microstructure of AL-12, 0.5% cerium doped, bombarded at 570°C with 4 MeV Ni⁺⁺ and 0.4 MeV He⁺ ions to 60 dpa and 85 appm He ions



(a) 89 dpa and 546 appm He



(b) 98 dpa and 104 appm He

Fig. 132. Microstructure of AL-13, 1.0% cerium doped, bombarded at 570°C with 4 MeV Ni^{++} and 0.4 MeV He^+ ions to (a) 89 dpa and 546 appm He and (b) 98 dpa and 104 appm He

DISCUSSION

Structure and Lattice Parameter

At room temperature, the undoped and rare-earth doped AL alloys have the face-centered cubic (FCC) structure (Figs. 24-27). No additional peaks were observed indicating any other structure. The calculated lattice parameters (Figs. 28-30 and Table 10) give a mean of $3.5923 \pm 0.0009\text{\AA}$ and they do not vary as a function of the bulk concentration of the added rare-earth element to within experimental error. According to the microchemical analysis results (Tables 23-34), yttrium was not detectable in the matrix, but small amounts of lanthanum and cerium were detected to be dispersed in the matrix. Nevertheless, the lattice parameter does not vary with rare-earth alloying additions for all three alloying elements. The absence of a detectable change in lattice parameter upon adding Y, Ce, and La is perhaps not surprising, since rare earths are known to have very low solid solubilities in metals like Fe, Ni, and Cr.

Hardness

Microhardness of the as-received and annealed, arc-melted undoped and rare-earth doped AL alloys are compared in Table 11 and Fig. 31. The arc-melted undoped AL alloy shows a higher hardness (307.8 DPH) than the as-received and annealed AL alloy (256.7 DPH). The hardness of the arc-melted AL alloys does not significantly vary with addition of 0.05 and 0.1% yttrium, lanthanum and cerium. This result is consistent with

the absence of any change in lattice parameter, as discussed above.

Up to 1.0% addition of lanthanum and cerium, the hardness does not vary (Fig. 31). Addition of yttrium produces a linear decrease in hardness, at a rate of 10% decrease in DPH per 1% addition of yttrium. As previously discussed, the hardness is related to the microstructure of the solid. A change in microstructure due to the arc melting is expected. The results shown in Fig. 31 suggest, therefore, that the microstructure changes with the additions of 0.5 and 1.0% yttrium, but not with the additions of lanthanum and cerium. This is discussed further below.

Second Phase Particles

Figures 32-35 show that the smaller particles (smaller than 5 μ m) are much more numerous than the larger ones, but as shown in Figs. 36-40 and Table 12 they do not contribute significantly to the areal fraction.

The arc-melted AL alloy shows a reduction in the size of the larger particle and the total areal fraction and an increase in the population of the smaller particles as compared with the as-received AL alloy (Figs. 32 and 36, and Table 12). Hence, the arc-melting procedure is assumed to disintegrate the precipitate particles and increase the population of the smaller particles. The arc-melted AL alloy was shown to have higher hardness than the as-received AL alloy (Fig. 31). It appears that the arc-melting disintegration of the precipitate particles results in an increase of the hardness of the AL alloys.

As the amount of yttrium increases from 0.05 to 0.1%, the

precipitate particles are disintegrated and the population of the smaller articles increased (Figs. 33 and 37). But the hardness does not significantly change (Table 11 and Fig. 31) compared to the arc-melted AL alloy. As the amount of yttrium addition increases to 0.5 and 1.0%, the areal fraction, the biggest particle size and the population of the larger particles increases significantly and the concentration of small size particles and their hardness decrease. This may be due to enhanced formation of grain boundary precipitate. For the 0.5% yttrium alloy, the grain boundary precipitates are rather isolated at triple grain boundary junctions (for example, see Fig. 106), whereas for the 1.0% yttrium concentration, the grain boundary precipitates are more continuous (Fig. 78). The reduction in the population of the small size precipitate particles for the 0.5 and 1.0% yttrium additions is thought to be the reason for the decrease in hardness.

For lanthanum-doped alloys (Figs. 34 and 39), the population of small size particles does not depend on lanthanum concentration, but the population of larger particles increases with increasing amounts of lanthanum. The hardness does not change with the population of the larger particles and the amount of addition of the lanthanum. The lanthanum-doped alloys show much less grain boundary precipitate than the corresponding yttrium-doped alloys.

For cerium-doped alloys (Figs. 35 and 40), the population of small size particles shows an increase as the cerium concentration increases up to 0.5% and a decrease for the 1.0% cerium alloy. The 1% cerium-doped alloy also shows considerably more grain boundary precipitate.

Microchemical Analysis

The surfaces of the rare-earth doped and undoped alloys bombarded with 4 MeV Fe^{++} ions to 100 dpa, nominal, were microchemically analyzed using the electron microprobe. Matrix regions, grain boundaries, and a few typical precipitate particles in the ion-bombarded and masked areas of each alloy were investigated (Tables 21-34 and Figs. 73-86). For the overall alloys, the chemical compositions of the matrix and grain boundary regions are roughly the same.

Fig. 73 shows the optical micrograph for the 4 MeV Fe^{++} ions bombarded undoped as-received alloy. Points #4, #6 and #7 show typical precipitate particles. As shown in Tables 21 and 34, these particles are rich in Ti, and are probably sigma phase. For the undoped, arc-melted alloys (Tables 22 and 34 and Fig. 74), the precipitate particles #3, #4, #6, #7 and #9 are also rich in Ti, and to a smaller extent rich in Fe, Ni and Mo. The precipitate particle size appears to be smaller for the arc-melted undoped alloy than for the as-received alloy. The measured concentration of aluminum is much lower for all points than original bulk concentration. This low measured aluminum concentration is due to the characteristics of the electron microprobe which has lower resolution for the lighter elements.

For the yttrium-doped alloys (Tables 23-26, 34 and Figs. 75-78), yttrium is not present in the matrix. Instead, it appears to be accumulated in precipitate particles, regardless of the yttrium concentration. Even at bulk concentrations as low as 0.1% yttrium, precipitate particles with a high concentration of yttrium were found

(points #4 and #9 on Tables 23 and 35 and in Fig. 75). In the low composition 0.05 and 0.1% yttrium-doped alloys, the Ti-rich precipitate particles are refined (Tables 23, 24, 35 and Figs. 75, 76). At the yttrium-rich precipitate particles (Tables 23-26, 35 and Figs. 75-78), the iron and chromium tend to be reduced to about 1.5 to 4% from 8.66%, but nickel tends to increase in concentration. In Ti-rich particle, the chromium is lower than the bulk composition. However, the average size of the precipitate particles tends to decrease as the yttrium content increases up to 0.1% (Fig. 37), and tends to increase again as the yttrium addition increases above 0.5%. In the 0.5 and 1.0% yttrium-doped alloys, the average size of the yttrium-rich particles appears to increase. The Ti-rich particles also tend to increase in size (Tables 25, 26, 35 and Figs. 77, 78) but to a smaller extent.

Lanthanum appears in the precipitates as well as in the matrix (Tables 27-30, 35 and Figs. 79-82). The precipitate particles in the lanthanum-doped alloys have round shapes and are much smaller in size than for the corresponding yttrium-doped alloys (Figs. 79-82). The chromium concentration in the La-rich particles is much lower at about 0.5 to 5 wt% than in the bulk alloy. The precipitates in the lanthanum-doped alloys are not located in the grain, as was true for the precipitates in the yttrium alloys (Figs. 76-78).

Cerium appears in the matrix for the high concentration alloys (0.5 and 1.0%) (Tables 31-35 and Figs. 83-86). The cerium concentration at matrix point #1 in the 0.05% cerium alloy (Table 31 and Fig. 83) has the high value of 2.0%. This may be due to a hidden particle near the

surface, unseen in the optical microscope, but nevertheless detected by the EMP beam. The precipitate particles in the cerium-doped alloys are much smaller than those in the yttrium-doped alloys and a little smaller than those in the lanthanum-doped alloys (Figs. 79-82). The Ce-rich precipitate particles (Tables 31-35 and Figs. 83-86) are randomly dispersed in and near the grain boundary, contrary to the yttrium-rich precipitates which are agglomerated in the grain boundary. Also, the Ce-rich precipitates are often rich in Ti, and Ni, but not in Cr. The 1% Ce alloy shows considerably more grain boundary precipitates. Lanthanum, manganese, molybdenum, cerium and silicon are dispersed more or less in the matrix but yttrium does not.

Optical Metallographic Examination

The optical photomicrographs at 1250X magnification indicating the surface deformation induced by the irradiation and electropolishing are shown in Figs. 73-86 (single beam, Fe ions, 600°C), Figs. 61-63 and 87-101 (dual beam, Ni and He ions, 570°C), and Figs. 102-115 (dual beam, Fe and He ions, 600°C). The Nomarski diffraction interference contrast image shows the surface topographic condition even it may not be quantitative. For example, particle #4 in Fig. 73 shows bright and dark sides along the direction of the arrow. The particle contains a high concentration of Ti and is harder; and is therefore less polished than the matrix material. By examining the bright and dark sides along the arrow direction, the ridging and grooving of the grain boundary, grooving of the polishing scratches and surface deformation in the matrix region

are quantitatively determined.

Matrix

Taken as a whole for all the rare-earth doped and undoped AL alloys, the ion bombarded area appeared to be deformed and swelled. The matrix area bombarded with single-beam Fe ions at 600°C (Figs. 73-83) is not greatly changed, although there are often regions that show some surface upheaval reminiscent of rows of blisters, as shown for example in Fig. 83 at the two parallel arrows. The amount of swelling for the rare-earth doped and undoped specimens bombarded at 600°C is negligible compared to that for the specimens bombarded at 570°C. The region bombarded at 570°C with the shadowed single beam of Fe ions (Figs. 87-101 and Table 19) is swelled even though the amount of swelling is apparently small compared to the region bombarded with the dual beam. For the TEM (Figs. 61-64 and Table 20), and the stacked-edge-on specimens bombarded with dual beam at 570°C (Figs. 87-101 and Table 19), the swelling at the shadowed single-beam bombarded region is apparently high and sometimes is comparable with the dual-beam-induced swelling. From these observations, it is concluded that, the helium increases the swelling but it is not essential to the swelling.

Some of the specimens, e.g., arc-melted undoped (Fig. 89), 0.05% (Fig. 90) and 0.1% (Fig. 91) yttrium doped, 0.05% (Fig. 94), 0.1% (Fig. 95) and 0.5% (Fig. 96) lanthanum doped and cerium doped (Figs. 98-101) AL alloys, show square-bottomed grooves. These are twin bands [207,208]. Johnston et al. [207], Johnston and Rosolowski [208] suggested that the

amount of swelling of each grain depends upon the grain orientation. Since the orientations of the twinned and matrix regions are different, they undergo different amounts of swelling, which results in the square-bottomed groove.

For the standard P7 stainless steel specimens, irradiation with dual and single beams at 570°C as well as at 600°C induces surface deformation and swelling which is readily apparent by optical microscopy and interferometry.

Grain boundary

For the irradiated rare-earth doped and undoped AL alloys, grain boundaries were observed to be swelled by the irradiation. The grain boundaries have a ridge-shape and are different than the stair-shaped grain boundaries induced by chemical etching and the groove-shaped grain boundaries of the irradiated standard P7 stainless steel (Fig. 116). The grain boundary ridging upon swelling seems to be a general phenomenon in the AL alloys, regardless of the concentration of the rare-earth addition, single or dual beam bombardment, and irradiation temperature in the range from 570 C to 600 C (Figs. 73-115). The ridges range from 100Å to 300Å in height above the swelled matrix surface.

All of the alloys studied show a large amount of grain boundary ridging (Figs. 87, 88, 90, 91, 94-102, 104, 105, 108-115), although somewhat less ridging is observed for the dual beam bombarded arc-melted undoped alloy (Fig. 103) and the 0.5% yttrium (Figs. 92 and 106) and 1.0% yttrium (Figs. 93 and 107) alloys. This is perhaps consistent with the

observation that the amount of grain boundary precipitation was approximately the same for all La and Ce concentrations. The grain boundary in the arc-melted alloy (Figs. 89 and 103) had slightly lower ridging than that in the as-received (Fig. 87) and annealed (Figs. 88 and 102) AL alloys, but nearly the same (about 300\AA) as for the other rare-earth doped alloys. Anyhow, the ridging of the grain boundaries hardly depended on the irradiation temperature in the range of 570°C to 600° and the helium ion bombardment. Nevertheless, the matrix region did show an apparent dependence on temperature and helium bombardment, as mentioned above.

Contrary to the grain boundary ridging in the AL alloys, the highly swelled standard P7 stainless steel shows a groove-shaped grain boundary (Fig. 116). Following the discussion of Johnston et al. [207], the irradiation behavior of the grain boundary can be shown as in the Fig. 117. At the first stage, as shown as 1 in Fig. 117, the matrix region swells and the surface elevates from level h_0 to h_1 . Near the grain boundary, the defects diffuse to the grain boundary and the area becomes relatively low in defects and is less swelled than the middle of the grain as shown as Stage 2 in Fig. 117.

The grain boundary with relatively less efficient packing and higher energy behaves as a sink for the defects and swells forming a ridge-shaped grain boundary. Johnston et al. [207], Johnston and Rosolowski [208] discussed the ridging mechanism, postulating that the ridges may be an effect of extrusion due to the lateral constraints on the very thin layer of about 1 micron that experiences void swelling. But they do not

give an explanation for the ridging at very low swelling. In general, however, the mechanism is not well established yet.

Relating to Fig. 14[172], the defects are shown to occur in the layer of about 1 micron in 4 Mev Ni ion bombarded nickel and stainless steels. However, the peak swelling occurs at a depth of about 0.1 micron beneath the surface. At low swelling (Stage 2 in Fig. 117), the surface elevates to level h_1 from the original level of h_0 . As the swelling is three dimensional, the inner matrix with defects expands horizontally as well as vertically. At the region near the grain boundary, defects diffuse to and are annihilated at the grain boundary. Therefore, the region near the grain boundary is softer than it is deep within the grain. Hence, the grain boundary region is extruded upwards due to the lateral constraints on the very thin layer of about 0.2 microns and this forms a ridge-shaped grain boundary. As the swelling proceeds to Stage 3 in Fig. 117, the inner surface of the grain elevates to the level h_2 . And also, the peak swelling layer moves up to about the same level as the surface of the grain boundary region. At this stage, the extrusion force due to the horizontal surface expansion as a result of swelling does not affect the grain boundary as much as at Stage 2. This is because the direction of force (arrows, Fig. 117) is at about the same level as the surface of the grain boundary, and therefore the grain boundary ridging does not proceed further. As the swelling proceeds to Stage 4 in Fig. 117, the middle of the grain swells continuously to level h_3 . But the region near the grain boundary remains unswelled. The peak swelling point is well above the region near the grain boundary. Hence, no more

extrusion effect resulting in ridging occurs at the grain boundary, and the expansion of the surface causes the grain boundary to be narrow and grooved. So, grooving and ridging coexist at the grain boundary (Stage 4 in Fig. 117). With more swelling (Stage 5), the surface of matrix elevates to level h_4 and the ridges at the grain boundary disappear. At this stage, the volume change is about 40%. Materials with such a high swelling may not be acceptable for the commercial breeder reactor. However, the differential swelling between grain boundary and matrix regions may cause special microstructural problems and this appears to be worthwhile for a more detailed study.

Second phase particle swelling

The effect of irradiation on second phase particles is shown optically in Figs. 73-115. Ti-rich particles, for example, #4 and #6 in Fig. 73, seem to be harder than the matrix, since they are above the matrix surface and remain unpolished through the mechanical polishing. They are probably to be sigma phase [36]. Their swelling behavior is not optically apparent. The yttrium-rich second phase particles show apparent swelling, as shown by points #5 and #6 in Fig. 78, and the similar shaped particles in Figs. 92, 93, 106 and 107. In Fig. 78, a part of a particle, #5, was unirradiated and the other part, #6, was bombarded with Fe ions at 600°C. By comparing these two parts, the particle of the part #6 is clearly swelled to a greater extent. For more dramatic evidence of particle swelling, note the particles in Fig 106. Here, the left part was bombarded with a dual beam of Fe and He ions at

600°C, and the other part was not bombarded. Fig. 106 shows the clear evidence of much more swelling of the yttrium-rich particle than the matrix region. Comparing the particles in the Figs. 78, 92 and 106, the yttrium-rich particles swell more at the higher temperature of 600°C than at 570°C, and more with dual-beam irradiation than with single beam irradiation.

The lanthanum-rich particles appear to be softer than the matrix, as shown at #9 in Fig. 82, which was not bombarded and its surface is quite below the matrix surface. Point #4 in Fig. 82 irradiated with the single beam at 600°C seems to be a little elevated and to have rough surface, which suggests the swelling of the particle. Around the particle, a round halo is apparent. The area of the halo has the same chemical composition as matrix area (Table 30), and it lies a little below the matrix area. The formation of the round halo may be because defects in the region diffuse to the particle and the halo region remains unswelled.

The cerium-rich particles, such as particles #3, #4, #7, #8 and #9 in Fig. 85, #5, #6 and #9 in Fig. 86, and in Figs. 100, 101, 114 and 115, are shown to be softer than the matrix, since the particles at the unirradiated area have a lower surface than for the matrix region. These particles at the ion bombarded region show deformation at the particle surface and at the boundary between the particle and matrix. Elevation of the particle surface does not appear to be significant even at the dual beam bombarded region where the matrix swelled to 5.3%.

Electropolishing behavior

In Figs. 61-63, dual beam bombarded and electropolished areas (section #4 and #6 in Fig. 60) show a rougher surface condition than the unpolished areas (section #1, #2 and #3 in Fig. 62b) and the masked and electropolished area (section #5 in Fig. 62b). Through the electropolishing, a boundary between the shadowed single beam bombarded area (section #5 in Fig. 63) and the dual beam bombarded area (section #6 in Fig. 63) is revealed, which is not shown in the unpolished state (between section #3' and #3 in Fig. 63). Contrary to the boundary between the shadowed single beam bombarded and the dual beam bombarded areas, the boundary between the masked area (#2) and shadowed single beam bombarded areas (#3') in Fig. 63 becomes ambiguous following the electropolishing, as shown at the boundary between areas #5 and #5' in Fig. 63. At the dual beam bombarded area, voids, defect clusters and helium bubbles are known to be present. Meanwhile, at the shadowed single beam bombarded area the helium bubble is not developed. Based on these observations and step height measurements (Table 20), the topographic configuration of the cross section of the masked (unbombarded), shadowed single beam bombarded, and dual beam bombarded areas can be shown as in Fig. 64.

The surface roughness and less removal of the dual beam bombarded area are assumed to be because of the different electropolishing behavior between the masked and single beam bombarded areas. The lesser removal of the surface layer of the dual beam bombarded area (sections #3 and #6) than the single beam bombarded area (sections #3' and #5') shows higher electrical resistivity at sections #3 and #6 than at sections #3' and

#5'. Kelly [55] suggested that the change in electrical resistivity due to the radiation damage is because of the introduction of scattering centers for the conduction electrons and new electronic states changing the band structure. He discussed a number of calculations of the resistivity change in metals due to the interstitials and vacancies, and mentioned 0.6 to 4 $\mu\Omega$ -cm per 1% vacancies and 0.75 to 11.5 $\mu\Omega$ -cm per 1% interstitials. The similar amount of surface layer removal at the shadowed single beam bombarded (sections #3' and #5') and the unbombarded (sections #2 and #5) areas shows the similar electropolishing properties, i.e., similar electrical resistivities, even though the shadowed single beam bombarded area shows high and nearly the same amount of swelling as the dual-beam bombarded area. Hence, the heavy ion beam alone produces defect clusters and voids but helium bubbles and is considered not to change the microstructural or electrical states. Only the helium bubble accompanied with heavy ion bombardment induces this damage changing the electrical resistivity. After electropolishing, a clear distinct boundary developed between the single beam bombarded (section #5') and dual beam bombarded (section #6) areas. This shows the clear difference in the microstructural or electrical states. The clear boundary between the unbombarded (section #2) and shadowed single beam bombarded (section #3') areas becomes ambiguous (section #5 and #5') after the electropolishing. This shows the similarity in the microstructural and electrical states between the unirradiated and single beam bombarded areas.

Swelling

The rare-earth doped and undoped AL alloys bombarded with the dual beam and with the single beam at 600°C do not show any significant swelling (Figs. 73-83, 102-115) as analyzed quantitatively using the interference microscope (Figs. 54 and 55). The low swelling is likely to be due to the high irradiation temperature, 600°C, compared to the peak swelling temperature of about 575°C [34]. However, the AL alloys bombarded with the dual beam at 570°C do show significant swelling (Figs. 58, 59, 84-101 and Table 19). A normalized value of swelling (Tables 18 and 19) corresponding to 100 dpa obtained using the least-square best fits and the swelling data for each specimen (Figs. 58, 59, Tables 18 and 19) are used to compare the swelling response of the alloys.

The as-received alloy (AL-0) bombarded with Ni and 94 appm He ions shows 4% swelling (Fig. 59, Table 19). As a result of pre-irradiation annealing for 2 hours at 1200°C, the alloy (AL-01) shows an increased swelling of 5.1% (Figs. 58, 59, Tables 18, 19). This increase in swelling is because of the reduction of sinks due to the larger grain size, agglomeration of the second phase precipitates or reduction of the internal stress induced by cold working. The arc-melted alloy (AL-1) shows slightly lower swelling of 3.8%. This reduction is supposed to be because of the segregation and the more homogenized dispersion of the second phase precipitates (Figs. 32, 36, 41 and Table 10).

For the yttrium-doped AL alloys (Fig. 59, Table 19), the 0.05% yttrium alloy (AL-2) shows higher swelling of 5.8% than the as-received

alloy (AL-0), but the 0.1% yttrium alloy (AL-3) shows lower swelling of 3.1%. As the composition of yttrium in both alloys and the amount of the swelling are relatively low for a high dpa of 100 dpa, the reason for the difference in swelling of the AL-1, AL-2 and AL-3 alloys may not be simple to explain. The particle size analysis (Figs. 32, 33 and 37) shows that the AL-3 alloy has more disintegrated smaller precipitates, and the total areal fraction is smaller than for the AL-2 alloy. This may be the partial reason for the reduction in the swelling as the yttrium composition increases from 0.05% to 0.1%. As the concentration of yttrium increases to 0.5% (AL-4) and 1.0% (AL-5), the swelling reduces to 2.3% and increases to 2.8%, respectively (Fig. 59 and Table 19). These values of swelling are for the matrix region.

The higher areal fraction of the yttrium-rich precipitates (5.2% for AL-4 and 16% for AL-5 in Fig. 41 and Table 10) and their greater swelling may be responsible for the greater overall swelling. Hence, about 0.3% of yttrium is considered to be the optimum concentration to suppress swelling. Aluminum is used in the AL alloy at 1.6 weight percent or 3.4 atomic percent because of its strong affinity for gaseous atoms, such as oxygen, nitrogen and hydrogen. Normally, rare-earth materials have higher affinity for these gaseous atoms than aluminum. Fig. 6, Ref. 19, shows that aluminum increases the swelling slightly. Hence, 0.3 weight percent of yttrium is considered to be able to replace the aluminum and suppress swelling.

Titanium is also an important low-level alloying addition to Fe-Ni-Cr cladding alloys, and in our AL alloy its bulk concentration is

3.3 wt%. It is known that Ti in solid solution suppresses swelling [19,145]. The concentrations of Ti in the matrix for the yttrium-doped AL alloys is given in Table 36. Also, Fig. 116 shows Ti concentration in the matrix and swelling as a function of yttrium concentration. It is seen that there is a strong correlation between decrease in swelling and increase in Ti concentration in solid solution. As to the reason for the effect of Y on Ti in solid solution, Fig. 116 shows that much of the bulk Ti is not in solid solution, and it is suggested that much of the Ti is present as TiO_2 , which is a very stable compound. For the 0.05% Y alloy, some of the Ti may form complexes with Y, which reduces the Ti in the matrix. For higher Y concentrations, the Y may take oxygen from the TiO_2 , which causes Ti to go back into solid solution, as shown in Fig. 116. For La and Ce alloys, Figs. 117 and 118, respectively, show a similar correlation between decrease in matrix Ti and increase in swelling, but not to as great an extent as for Y alloys.

On the lanthanum-doped alloys (AL-6, AL-7, AL-8, and AL-9), the low concentration of 0.05 and 0.1% lanthanum does not change the swelling behavior (Fig. 59 and Table 19). As the concentration increases to 0.5% and 1.0%, the swelling increases to 6.5% and then decreases to 5.2%. The particle size analysis shows a monotonic increase in population precipitates and in their total areal fraction (Figs. 34, 39, 41 and Table 10) as the lanthanum concentration increases to 0.05, 0.1, 0.5 and 1.0% successively. This result gives some clue for the explanation of the irradiation behavior. Anyhow, the lanthanum-doped alloy has a tendency to increase and then decrease the swelling as the lanthanum

concentration increases to 0.5% and 1.0%.

The cerium-doped alloys (AL-10, AL-11, AL-12 and AL-13) have a similar relation of swelling to the composition as for the yttrium-doped alloys (Fig. 59). With 0.05% cerium (AL-10), swelling increases to 5%. Then, with 0.1% cerium (AL-11), the swelling decreases to 4.5%. The difference of these two values of swelling may not be significant considering the high dose of 100 dpa and the complexity of the irradiation experimental procedure. At any rate, the particle size analysis shows that the population of the smaller segregated precipitates increases as the cerium composition increases to 0.05, 0.1 and 0.5%, and then it decreases as the cerium concentration increases to 1.0% (Fig. 35). Hence, the swelling of the cerium-doped alloys depends on the population of the smaller size precipitates even through the particle size analysis is based on the precipitates larger than 0.4 μ m in diameter.

It is mentioned above that TEM assembly D inadvertently received a complex irradiation treatment in which helium was coimplanted to 81 appm for the first 264 minutes and then implanted to an additional 465 appm He during the last 15 minutes, giving a total of 546 appm He. The irradiation temperature was 570°C. The samples subjected to this treatment showed higher swelling. For example, the arc-melted undoped alloy (AL-1) showed higher swelling of 5.2%, as compared to 3.2% swelling for only 94 appm implanted helium, or an increase of about 2% swelling. Hence, it is considered that the helium stimulates the swelling even during the last 15 minutes of bombardment at the near-peak swelling temperature, 570°C. For the case of the 1.0% yttrium alloy (AL-5)

bombarded with the higher fluence of He ions, one specimen (AL5-R) shows negligible but the other specimen (AL5-S) shows higher swelling of 4.6% at 66 dpa than the same alloy (AL-5) bombarded with the low fluence of He ions (Table 19). Another example is the 0.05% La alloy, which shows higher swelling of 6.1% (AL6-V and AL6-W, Table 19), as compared to 4.1% for only 94 appm implanted helium (AL6-D, -E, and -F, Table 19). This is again an increase of about 2% swelling due to the higher He fluence, similar to that experienced by the arc-melted alloy, AL-1. However, the 1.0% Ce alloy (AL-13) shows slightly lower swelling of 3.9% for the higher He fluence, as compared to 4.4% for the lower He fluence case. This apparent inverse effect may not lie outside experimental error. Anyhow, all the alloys bombarded with the higher fluence of He ions (AL-1, AL-5, AL-6, and AL-13) show swelling in the range of 3.9 to 6.5%, and the increase due to the higher He fluence is 2% or less.

Microstructure

The TEM microphotographs (Figs. 121-132) of the rare-earth doped and undoped AL(Fe-25.6%Ni-8.7%Cr) alloys bombarded with dual-beam of Ni and He ions illustrate the microstructure of the alloy and permit a comparison with the optically measured swelling data (Table 19). The arc-melted undoped alloy irradiated to 124 dpa and 546 appm He and swelled to 6.5% (Fig. 121a and Table 19) shows voids of bimodal sizes of about 1000\AA and 400\AA in diameter. The alloy also exhibits dislocation segments and bubbles. Many of the voids shown in Fig. 118a have hexagonal shapes with sides $\langle 110 \rangle$. As stated in the Introduction,

the three dimensional shape of voids in austenitic stainless steels is represented by a tetrakaidecahedron, which is illustrated in Fig. 121b. The {111} surfaces of the tetrakaidecahedron are regular hexagons with $\langle 110 \rangle$ sides, consistent with the voids shown in Fig. 121a. The larger size voids are normally accompanied by precipitates of about 400\AA in diameter, which are likely to be G-phase [36]. The smaller size voids appear to be associated with the Ti-carbide. Thus, the Ti-carbide is a more favorable microstructure than the G-phase from the point of view of suppressing swelling. The same arc-melted undoped alloy but bombarded to the lower displacement concentration of 96 dpa and lower He concentration of 94 appm shows an irregular polished surface (Fig. 122) which prevents even a qualitative evaluation of the amount of swelling. However, the step height observations do show that, when the swelling is normalized to 100 dpa, the higher helium concentration of 546 appm resulted in 5.2% swelling (specimens AL1-B and C, Table 19) as compared to 3.8% swelling for 94 appm He (specimens AL1-D, -E, and -F). It is interesting that the effect of the higher helium concentration was manifested in higher swelling despite the fact that 465 appm He of the total of 546 appm He was implanted in only the last 15 minutes of the total irradiation period of 279 minutes.

The 0.05% yttrium-doped alloy with 109 dpa and 94 appm He (specimen AL2-F, Table 19 and Fig. 123) shows voids associated with precipitates. The precipitates are about 300\AA in diameter and are likely to be G-phase. The number of voids and precipitate particles is remarkably high compared to that for the undoped alloy (Figs. 121a and 122). So,

the 0.5% yttrium produced more precipitates and hence, promoted swelling. Also, He bubbles of about 30\AA in diameter appear to be dispersed homogeneously.

A pair of stereo photomicrographs with 7° difference in viewing angle (Fig. 124a and b) of 0.1% yttrium-doped alloy, bombarded to 106 dpa and 102 appm He and swelled only 1.9%, shows a reduction of the G-phase and the more uniform voids of about 600\AA compared to the 0.05% yttrium alloy (Fig. 123). Hopson [34] also observed a decrease in swelling for the 0.1% yttrium alloy. The low population of the G-phase is considered to be the main reason for the low swelling. Figs. 125a and b show a sigma phase particle (lower left hand corners) [36]. Close inspection of the particle in Fig. 125a indicates a homogeneous distribution of small bubbles with diameters of $30\text{-}40\text{\AA}$. In the immediate vicinity of the sigma phase particle, the microstructure does not indicate any voids. This denudation of voids near the particle suggests that it serves as a sink for vacancies. This does not have any effect on the bulk swelling, however, since the density of sigma phase particles is quite low. Fig. 125c shows the same 0.1% yttrium alloy irradiated to lower fluences of Ni and He ions (73 dpa and 102 appm He, specimen AL3-K, Table 19). In this case, the swelling was quite low (below the limit of resolution of about 1%). A few voids are seen in Fig. 125c and a larger number of small bubbles mostly aligned within dislocation segments. There is also a rather homogeneous distribution of small black dots, assumed to be metallic carbides [36,144], but no G-phase is apparent.

The 0.5% yttrium-doped alloy bombarded with Ni ions to 102 dpa and He ions of 85 appm (AL4-N, Table 19 and Fig. 125a) shows a bimodal distribution of voids of about 400\AA and 800\AA in diameter. The larger size voids are normally not attached to the G-phase particles. The ratio of the numbers of G-phase particles and voids is lower than that for the 0.05% yttrium-doped alloy (Fig. 123). The Ti-rich precipitates likely to be sigma phase often contain homogeneously distributed bubbles, although they cannot be seen in Fig. 125b. The 1.0% yttrium-doped alloy bombarded with Ni ions to 66 dpa and He ions to 546 appm swelled to 4.6% (specimen AL5-S, Table 19). The microstructure shows a significant reduction in the population of the G-phase. However, another unknown phase likely to be an yttrium-rich precipitate appears, as seen in Fig. 127, lower left corner. Around the particle, many voids are located.

To summarize concerning the effect of yttrium additions, in the 0.05% yttrium alloy the amount of G-phase is increased and the void swelling is greater. As seen in Fig. 123, almost every void has a G-phase particle associated with it. As the yttrium concentration increases to 0.1% and 0.5%, the population of G-phase particles and the void swelling are reduced. At 0.5% yttrium, a new yttrium-rich precipitate begins to appear. At 1% yttrium, the areal fraction of this precipitate is increased to about 16% (Fig. 41 and Table 12, alloy #5), and the swelling increases again. The G-phase is known to have the general formula $T_6Ni_{16}Si_7$, where T is a transition element such as Ti, Mn, Cr, Zr, Nb, Ta, Hf, or Nb [36]. Because of the high Ni

content in the G-phase particle, one expects the Ni concentration in the vicinity if the particle is to be reduced. As shown in Figs. 4 and 5, a reduction in Ni is likely to cause an increase in the amount of swelling. Greater swelling is also observed when the yttrium-rich precipitate is present in the 1% yttrium material. As shown in Table 26, the yttrium-rich precipitate (points #3, 5, and 6 Table 26) is rich in nickel, as is also true for the G-phase particle. Thus, the presence of Ni-rich particles appears to promote swelling.

The 0.05% lanthanum-doped alloy bombarded with Ni ions to 83 dpa and He ions to 546 appm is shown in Fig. 128. The specimen shown was observed to have swelled 5.9% (specimen AL6-V, Table 19). A bimodal is seen in Fig. 125. The predominating sizes are at about 500 \AA and about 1000 \AA . Voids at both sizes are frequently associated with G-phase particles. The high population of the G-phase is the same as for the case of the 0.05% yttrium-doped alloy. The high value of swelling is considered to be because of the high fluence of He ions and the higher population of the G-phase.

Fig. 129 shows a pair of stereo photomicrographs with 10 $^{\circ}$ difference in angle of view for the 0.5% lanthanum-doped alloy bombarded with Ni ions to 45 dpa and He ions to 546 appm. The alloy swelled 6.4% (specimen AL8-h, Table 19). This high swelling is again accompanied by a fairly high concentration of G-phase.

Figure 130 shows a pair of stereo photomicrographs of the 0.1% cerium-doped alloy bombarded with Ni ions to 116 dpa and He ions to 102 appm, which gave swelling to 6.1% (specimen AL11-2, Table 19). However,

the swelling of the alloy normalized to 100 dpa is about 4.5%. Fig. 130 again shows that many of the voids are associated with G-phase particles.

The 0.5% cerium-doped alloy was bombarded with Ni ions to 60 dpa and He ions to 85 appm, and it swelled to 3% (specimen AL12-9, Table 19).

Fig. 131 shows homogeneously dispersed voids of about 300\AA in diameter. The lower population of G-phase is considered to be the reason of the low swelling.

Figure 132 shows 1.0% cerium-doped alloy bombarded with (a) Ni ions to 89 dpa and He ions to 546 dpa, giving swelling of 3.5% and (b) Ni ions to 98 dpa and He ions to 104 dpa, giving swelling of 4.4%. The homogeneous distribution of voids and their small size of about 300\AA in diameter for both specimens is consistent with the low swelling. There is also a reduction in the number of G-phase particles.

In summary, a number of factors make difficult the analysis and interpretation of the TEM micrographs. These factors include the strong depth dependence of the size and number density of voids and bubbles (as illustrated in Fig. 14), the variation in electropolishing properties from one alloy to another and from one precipitate to another, and the complex nature of the effects of irradiation. Nevertheless, some general conclusions can be drawn. For the yttrium alloys, the void formation appears to be strongly correlated with the G-phase, i.e., void swelling increases with the amount of G-phase present in the microstructure. The greatest swelling occurs for 0.05% yttrium, and for this alloy G-phase precipitate particles are particularly abundant (Fig. 123). As the yttrium concentration increases to 0.1 and 0.5%, the amount of G-phase

decreases and so does the swelling. For 1.0% yttrium, a new yttrium-rich precipitate develops and the swelling increases again. The G-phase does not appear to be reduced upon the addition of lanthanum, and there is no reduction in swelling (Fig. 59). For the case of cerium, the G-phase is reduced as the cerium content increases to 0.05, 0.1, 0.5, and 1.0%, and the voids become smaller in size. Thus, it appears that the G-phase is a major determinant as to whether or not swelling occurs in the undoped and rare-earth-doped AL alloys. The reason for the critical influence of the G-phase may be associated with the distribution of nickel. It is generally known that swelling in Fe-Ni-Cr alloys becomes greater as the nickel concentration is reduced, as illustrated in Fig. 5 [17-19]. Also, the G-phase is quite rich in nickel, corresponding to concentrations as high as about 48 wt % Ni [36]. It seems likely, therefore, that nickel is scavenged from the vicinity of the G-phase, which leaves this region more susceptible to void formation. It is interesting that the yttrium-rich precipitate in the 1% yttrium alloy is also rich in nickel at about 43 wt % Ni, as seen in Table 26 for points #3, 5, and 6. This is consistent with the somewhat larger swelling for the 1% yttrium alloy as compared to that for the 0.5% yttrium alloy (Fig. 59). Although the above discussion emphasizes the role of the G-phase, it should be stated that several other phases in these complex irradiated alloys may also influence void formation. Titanium carbide and MC-type carbides, in general, are thought to suppress swelling since, when they are present, they are finely distributed throughout the matrix, as seen in Fig. 118. Sigma phase, on the other hand, appears as a coarse structure and,

furthermore, it has a low nickel content (as low as 5 wt %, according to [36]). Sigma phase particles, therefore, do tend to suppress swelling.

CONCLUSIONS

The study of the microstructure and irradiation effects for the 0.05, 0.1, 0.5 and 1.0 wt % yttrium-, lanthanum- and cerium-doped and undoped AL(Fe-25.7Ni-8.7Cr-3.3Ti-1.6Al) alloys shows the following:

1. At room temperature, the alloys have, basically, the face-centered-cubic (FCC) structure characteristic of austenitic stainless steel. The addition of rare earth elements does not introduce any additional X-ray diffraction peaks. The mean lattice parameter of the alloy is $3.5923 \pm 0.0009 \text{ \AA}$ and it does not vary with the rare-earth alloying additions up to 1%.
2. The hardness of the undoped AL alloy increases to 308 DPH from 257 DPH as a result of refinement of particles though the arc-melting and it does not change significantly with the addition of up to 1.0% of lanthanum or cerium. But the addition of yttrium produces a linear decrease in hardness at the rate of 10% decrease in DPH per 1% addition of yttrium. This decrease is considered to be due to the ability of yttrium to act as an efficient getter for interstitial impurities.
3. As a result of arc melting, the Ti-rich precipitates likely to be sigma phase in the undoped AL alloys are reduced in size and in the total areal fraction. Thus, Ti atoms are drawn into solution in the matrix and swelling is slightly

decreased. Annealing the as-received alloy for 2 hours at 1200°C increases swelling from 4% to 5.1%. This is reasonable since the as-received alloy was in cold-worked condition.

4. The introduction of yttrium in the alloy changes the amount of G-phase precipitate present, and this, in turn, affects the amount of swelling. For 0.05% yttrium, the amount of G-phase precipitate is high and there is considerable swelling. As the Y content increases to 0.1 and 0.5%, the G-phase precipitate number density is decreased and so is the swelling. For the 1% Y alloy, Y-rich precipitates are formed, and the swelling increases again. The increase in swelling with increasing G-phase and Y-rich precipitates is considered to be due to the scavenging of nickel into the precipitates, leaving the matrix adjacent to the precipitates poor in nickel and susceptible to void formation. Another possible factor is the influence of Y on the titanium distribution. Titanium in solid solution is thought to have a swelling suppression effect. When Y is added, it may replace Ti in titanium-rich precipitates and thus increase the amount of Ti in solid solution, which decreases the swelling.
5. Lanthanum up to 1 wt % does not suppress the swelling.
6. As the cerium content increases to 0.05%, 0.1% and 0.5%, the Ti-rich particles become smaller and swelling is

decreased. As the cerium content increases from 0.5% to 1.0%, new globular-shaped Ce-rich particles appear. These particles themselves exhibit swelling and there is an increase in matrix swelling also. The minimum swelling occurs at about 0.4% cerium.

7. Ion implanted helium atoms form into bubbles which facilitates but is not essential for swelling.
8. At low swelling up to 5%, the grain boundary swells more than the matrix and forms a ridge shape. As the swelling proceeds, the grain boundary becomes a groove shape with a ridge at the center. Then, at higher swelling of about 40%, the ridge is no longer present. The ridging at low swelling is due to the radiation induced matrix swelling, which extrudes material in the grain boundary area. Radiation defects are annihilated in the grain boundary area and this area is therefore softer than the matrix. The grooving is due to the elevation of the grain bodies above the grain boundary region.
9. Aluminum of 1.64 wt % is included in the base alloy to improve the mechanical properties because of its strong affinity with O, N and C, but it has an adverse effect on swelling. About 0.3% of yttrium is the optimum composition to suppress swelling to about 2% and can replace the aluminum.

BIBLIOGRAPHY

1. "A National Plan for Energy RD&D: Creating Energy Choices for the Future." ERDA 76-1, 1976.
2. A. M. Judd. Fast Breeder Reactor, an Engineering Introduction. Pergamon Press Inc., Oxford, England, 1981.
3. B. R. Leonard, Jr. "A Review of Fusion-Fission (Hybrid) Concepts." Nuc. Tech., 20 (Dec. 1973), 161-178.
4. G. A. Moses. "Summary of the Fusion-Fission Hybrid Fuel Cycle Analysis (Tritiumless Hybrids ?)." UWFDM-337, (1979).
5. C. Cawthorne and E. J. Fulton. "Voids in Irradiated Stainless Steels." Nature 216 (1967), 576.
6. J. M. Dupouy. "French Program on LMFBR Cladding Materials Development." In Radiation Damage in Breeder Structural Materials. Edited by M. L. Bleiberg and J. W. Bennett, Proc. of American Institute of Mining, Metallurgical and Petroleum Engineers International Conference, Scottsdale, Arizona, June 19-23, 1977, AIME, New York, N.Y., 1977, 1-11.
7. D. R. Harries. "The UKAEA Fast Reactor Project Research and Development Programs on Fuel Element Cladding and Sub-Assembly Wrapper Materials." In Radiation Damage in Breeder Structural Materials. Edited by M. L. Bleiberg and J. W. Bennett. Proc. of American Institute of Mining, Metallurgical and Petroleum Engineers International Conference, Scottsdale, Arizona, June 19-23, 1977. AIME, New York, N.Y., 1977, pages 27-40.
8. J. J. Laidler, J. J. Holmes and J. W. Bennett. "U.S. Programs on Reference and Advanced Cladding/Duct Materials." In Radiation Damage in Breeder Structural Materials. Edited by M. L. Bleiberg and J. W. Bennett. Proc. of American Institute of Mechanical Engineers International Conference, Scottsdale, Arizona, June 19-23, 1977. AIME, New York, N.Y., 1977, pages 41-51.
9. W. Dietz, K. Ehrlich and J. J. Het. "Research and Development Programme in the Debene - Area for Fast Breeder Material Development." In Radiation Damage in Breeder Structural Materials. Edited by M. L. Bleiberg and J. W. Bennett. Proc. of American Institute of Mining, Metallurgical and Petroleum Engineers International Conference, Scottsdale, Arizona, June 19-23, 1977. AIME, New York, N.Y., 1977, pages 13-25.

10. J. W. Bennett and K. E. Horton. "Materials Requirements for Liquid Metal Fast Breeder Reactor." *Met. Trans. A*, 9A (1978), 143-149.
11. C. J. McHargue and J. L. Scott. "Materials Requirements for French Reactors." *Met. Trans. A*, 9A (1976), 151-159.
12. J. L. Scott. "Materials for Fusion Reactors." *Met. Prog.* 114 (July 1978), 40-49.
13. P. Behrisch. "Surface Erosion from Plasma Materials Interaction." *J. Nucl. Mater.*, 85 & 86 (1979), 1047-1061.
14. J. Bodhansky, J. Roth and F. Brossa. "Formation of Various Coating and Their Behavior under Particle Bombardment." *J. Nucl. Mater.*, 85 & 86 (1979) 1145-1150.
15. R. Bullough, B. L. Eyre and G. L. Kulcinski. "A Systematic Approach to the Radiation Damage Problem." *J. Nucl. Mater.*, 68 (1977), 168-178.
16. P. J. Maziasz, D. N. Braski, J. M. Vitek, F. W. Wiffen, R. L. Klueh, M. L. Grossbeck and E. E. Bloom. "Progress in Alloy Development in the Fusion Materials Program." *J. Nucl. Mater.*, 108 & 109 (1982), 296-298.
17. W. G. Johnston, J. H. Rosolowski, A. M. Turkalo and T. Lauritzen. "An Experimental Survey of Swelling in Commercial Fe-Cr-Ni Alloys Bombarded with 5 MeV Ni Ions." *J. Mat.*, Mat 54 (1974), 24-40.
18. R. B. T. Frost. "Radiation Damage Considerations." In Fundamental Aspects of Structural Alloy Design. Presented at the Battelle Colloquium Seattle, Washington and Harrison Hot Springs, B.C., Canada, (Sept. 15-19, 1975), pages 1-24.
19. W. G. Johnston, J. Lauritzen, J. H. Rosolowski and A. M. Turkalo. "Void Swelling in Fast Reactor Materials - A Metallurgical Problem." *J. Metals*, 28 (June 1976), 19-24.
20. E. E. Bloom, J. O. Stiegler, A. W. Rowcliffe and J. M. Leitneker, "Austenitic Stainless Steels with Improved Resistance to Radiation Induced Swelling." *Scripta Met.*, 10 (1976), 303-308.
21. "Metals Handbook: Metallography, Structures and Phase Diagram." 8th ed. American Society for Metals, Metals Park, Ohio, 1973.
22. R. Bajaj and M. S. Wechsler. "Defect Clusters in Neutron-Irradiated Vanadium Containing Oxygen." *Met. Trans.* 7A (March 1976), 351-358.

23. K. Kippenhan and K. A. Gschneidner, Jr. "Rare-Earth Metals in Steels." Rare-Earth Information Center, Institute for Atomic Research, Iowa State University, IS-RIC-4, 1970.
24. A. C. Roberts, D. R. Harries, D. R. Arkell, A. D. Dewey and J. D. H. Hughes. "Effects of Yttrium on the Structure and Post Irradiation Tensile Properties of an Iron-Chromium-Aluminum Alloy." ASTM STP-457,(1969), 313-328.
25. J. M. Francis. "Structure of Surface Oxides formed of an Yttrium-Bearing 20% Cr/25% Ni/Nb - Stabilized Steel in Carbon Dioxide at High Temperatures." Brit. Corr. J. 3 (1968), 113-119.
26. A. A. Babakov and T. V. Ostapenko. "Effect of Rare-Earth Metals on the Tendency of OOKh128N11 Steel to Intercrystalline Corrosion." Translated from Zashchita Metallov, 10 (3), (1974), 292-284 (262-263).
27. S. L. Chistyakov, E. D. Mokhiv and S. K. Filatov. "Effect of Cerium on the Structure and Properties of OKh33Ni18 Steel." Eng. Trans. Stal. (11 26) in English (1966), 925-927.
28. K. A. Gschneidner, Jr., N. A. Kippenhan and O. D. McMasters. "Thermochemistry of the Rare-Earth, Part I. Rare Earth Oxides, Part II. Rare-Earth Oxysulfides, Part III. Rare Earth Compounds with B, Sn, Pb, P, As, Sb, Bi, Cu and Ag." Rare-Earth Information Center, Institute for Atomic Research, Iowa State University, IS-RIC-6, 1973.
29. W. G. Wilson, D. A. R. Kay and A. Vahed. "The Use of Thermodynamics and Phase Equilibrium to Predict the Behavior of the Rare-Earth Element in Steel." J. Metals, 26 (1974), 14-23.
30. A. Raman. "Uses of Rare-Earth Metals and Alloys in Metallurgy: Part 1. Applications in Ferrous Materials." Sonderdruck aus Zeitschrift für Metallkunde, 67 (1976), 780-789.
31. P. I. Krivets, V. S. Basik, A. P. Polyakova and V. N. Reveka. "Influence of Soaking at Quenching Temperature on the Mechanical Properties of G13L Steel." Metal Science and Heat Treatment, (1967), 294-297.
32. M. B. Lewis, N. H. Packan, G. F. Wels and R. A. Buhl. "Improved Techniques for Heavy-Ion Simulation of Neutron Radiation Damage." Nucl. Instr. and Meth. 167 (1979), 233-247.
33. N. H. Packan and R. A. Buhl. "A Multispecimen Dual-Beam Irradiation Damage Chamber." ORNL TM-7226, (1980).
34. R. D. Hopson. "The Effect of Yttrium Additions on Void Swelling in Liquid Metal Fast Breeder Reactor Candidate Cladding Alloys." M.S. thesis. Iowa State University, Ames, Iowa, 1981.

35. M. Z. Shah-Khan. "The Effect of Yttrium Additions on the Tensile Properties and Hardness of an Iron-Nickel-Chromium Alloy." M.S. thesis, Iowa State University, Ames, Iowa, 1981.
36. E. H. Lee, P. J. Maziasz and A. W. Rowcliffe. "The Structure and Composition of Phase Occuring in Austentic Stainless Steels in Thermal and Irradiation Environments." In Phase Stability During Irradiation. Edited by J. R. Holland, L. K. Mansur and D. I. Potter. Proc. of Symposium sponsored by the Nuc. Met. Comm., Fall meeting of the Metallurgical Society of AIME, Pittsburgh, Penn. (Oct. 5-9, 1980), 191-218.
37. A. F. Rowcliffe and E. H. Lee. "High Temperature Radiation Damage Phenomena in Complex Alloys." J. Nucl. Mater., 108&109 (1982), 306-318.
38. J. Friedel. Dislocations. Pergamon Press Inc., Oxford, England 1964.
39. D. Hull. Introduction to Dislocations, Sec. 10.4. Pergamon Press Inc., Oxford, England, 1965.
40. A. T. Churchman, I. Mogford and A. H. Cottrell. "The Hardening and Embrittlement of Steel by Irradiation with Neutrons." Phil. Mag. 2 (1957), 1271.
41. M. A. Adams and P. R. B. Higgins. "The Hardening of Copper by Neutron Irradiation." Phil. Mag. 4 (1959), 777.
42. A. A. Johnson. "The Embrittlement of Molybdenum by Neutron Irradiation." Phil. Mag. 5 (1960), 413-416.
43. T. H. Blewitt, R. R. Coltman, R. E. Jamison and J. K. Redman. "Radiation Hardening of Copper Single Crystals." J. Nucl. Mater., 2 (1960), 277.
44. B. L. Eyre. "Direct Observations of Neutron Irradiation Damage in α -iron." Phil. Mag. 7 (1962), 2107-2113.
45. M. E. Downey and B. L. Eyre. "Neutron Irradiation Damage in Molybdenum." Phil. Mag. 17 (1965), 53-70.
46. B. L. Eyre and A. F. Bartlett. "An Electron Microscope Study of Neutron Irradiation Damage in Alpha-Iron." Phil. Mag. 12 (1965), 261-272.
47. C. Cawthorne and E. J. Fulton. "The Influence of Irradiation Temperatures on the Defect Structures in Stainless Steel." In The Nature of Small Defect Clusters. Edited by M. J. Makin. Vol. 2 of Report of a Consultants Symposium held at UKAERE Harwell, England, July 4-6, 1966.

48. J. H. Gittus, Irradiation Effects in Crystalline Solids. Appl. Sci. Pub. London, England, 1978.
49. M. W. Thompson, Defects and Radiation Damage in Metals. Cambridge Univ. Press, Cambridge, England, 1969.
50. J. W. Corbett, Electron Radiation Damage in Semiconductors and Metals. Academic Press, N.Y., 1966.
51. A. L. Bement. "Void Formation in Irradiated Stainless Steels." Advan. Nucl. Sci. Technol., 7 (1973), 1.
52. D. I. R. Norris. "Voids in Irradiated Metals." Radiat. Eff. 14 (1972), 1.
53. D. R. Olander. Fundamental Aspects of Nuclear Reactor Fuel Elements. TID-26711-P1, 1976.
54. R. Bullough and R. S. Nelson. "Voids in Irradiated Metals." Phys. in Technol. 5 (No. 1) (1974), 29.
55. B. T. Kelly. Irradiation Damage to Solids. Pergamon Press Inc., Oxford, England, 1966.
56. American Society for Testing and Materials. Effects of Radiation on Structural Metals. A Symposium (STP 426), Atlantic City, N.J. June 26-July 1, 1966. ASTM, Philadelphia, Pa., 1966.
57. W. F. Sheely, ed. Radiation Effects. Proc. of American Institute of Mechanical Engineers Symposium, American Metallurgical Society Conferences V. 37, Goldon and Beach, New York, 1967.
58. American Society for Testing and Materials. Irradiation Effects in Structural Alloys for Thermal and Fast Reactors. A Symposium (STP-457), San Francisco, California, June 23-28, 1968. ASTM. Philadelphia, Pa., 1968.
59. International Atomic Energy Agency. Radiation Damage in Reactor Materials, 2 vols. Proc. of a Symposium, Vienna, Austria, June 2-9 (1969). International Atomic Energy Agency, 1969.
60. American Society for Testing and Materials. Irradiation Effects on Structural Alloys for Nuclear Reactor Applications. Edited by A. L. Bement, Proc. of Symposium, Niagara Fall, Ont. ASTM, Philadelphia, Pa., 1971.
61. American Society for Testing and Materials. Irradiation Effects on Structural Alloys for Nuclear Reactor Applications. Edited by A. L. Bement, Proc. of Symposium, Philadelphia, Penn. ASTM, Philadelphia, Pa., 1971.

62. S. F. Pugh, M. M. Loretto and D. I. R. Norris, eds. Voids Formed by Irradiation of Reactor Materials. Proc. of the British Nuclear Energy Society European Conference, Reading, England, March 24-25, 1971, 1972.
63. J. W. Corbett and L. C. Ianniello, eds. Radiation-Induced Voids in Metals. Proc. of International Conference, Albany, N. Y., June 9-11, 1971, 1972.
64. R. S. Nelson, ed. The Physics of Irradiation Produced Voids. Consultant Symposium, Harwell, England, Sept. 9-11, 1974, 1975.
65. N. L. Peterson and S. D. Harkness, eds. Radiation Damage in Metals. ASM, Metals Park, Ohio, Nov. 9-10, 1975.
66. C. H. S. Dupouy, ed. Radiation Damage Processes in Materials. Proc. of the NATO Advanced Study Institute, Corsica, France, Aug. 27-Sept. 9, 1973. Leyden Noordhoff Co., France, 1975.
67. American Society for Testing and Materials. Irradiation Effects on the Microstructure and Properties of Metals. Proc. of International Symposium (STP 611). St. Louis, Missouri, 1976.
68. J. S. Watson and F. W. Wiffen, eds. Radiation Effects and Tritium Technology for Fusion Reactors. 4 vols. Proc. of an International Conference, Gatlinburg, Tenn., Oct. 1-3, 1975.
69. M. T. Robinson and F. W. Young, Jr., eds. Fundamental Aspects of Radiation Damage in Metals. 2 vols. Proc. of an International Conference, Gatlinburg, Tenn., Oct. 6-10, 1975.
70. M. L. Bleiberg and J. W. Bennett, eds. Radiation Effects in Breeder Reactor Structural Materials. Proc. of American Institute of Mining, Metallurgical and Petroleum Engineers International Conference, Scottsdale, Arizona, June 19-23, 1977. AIME, New York, N.Y., 1977.
71. N. L. Peterson and R. W. Siegel, eds. Properties of Atomic Defects in Metals, Proc. of the International Conference; Argonne, Ill., Oct. 18-22, 1976, North-Holland Pub. Co. Netherlands, 1978.
72. F. W. Wiffen, J. H. DeVan and J. O. Stiegler, eds. Fusion Reactor Materials. Proc. of the First Topical Meeting, Miami Beach, Florida, Jan. 29-31, 1979, North-Holland Pub. Co., Netherlands, 1979.
73. R. E. Nygren, R. E. Gold and R. H. Jones, eds. Fusion Reactor Materials. Proc. of the Second Topical Meeting, Seattle, Washington, Aug. 9-12, 1981, North-Holland Pub. Co. Netherlands, 1982.

74. M. A. Kirk, ed. Neutron Irradiation Effects in Solids. Proc. of the International Conference, Argonne, Ill., 9-12 Nov. 1981, ANL, Argonne, Ill., 1982.
75. W. K. Appleby, E. E. Bloom, J. E. Flinn and F. A. Garner. "Swelling in Neutron-Irradiated 300-Series." In Radiation Damage in Breeder Structural Materials. Edited by M. L. Bleiberg and J. W. Bennett. Proc. of American Institute of Mining, Metallurgical and Petroleum Engineers International Conference, Scottsdale, Arizona, June 19-23, 1977. AIME, New York, N.Y., 1977, 509-528.
76. J. F. Bates and M. K. Korenko. "Empirical Development of Irradiation-Induced Swelling Design Equations." Nucl. Technol., 48 (1979), 303-322.
77. M. J. Makin, S. N. Buckley and G. P. Walters. "The determination of the displacement energy in type 316 austenitic steel." J. Nucl. Mater., 68 (1977), 161-167.
78. M. B. Lewis, Private communication. Metals and Ceramics Division, Oak Ridge National Laboratory, Oak Ridge, Tennessee, January 5, 1983.
79. Annual Book of ASTM Standards. Part 45 E-521 (1977), 991-999.
80. M. S. Wechsler. "Neutron Cross Sections: The Field of Radiation Damage." in N.B.S. Special Pub. 299, (1968), 67-83.
81. C. O. Smith. Nuclear Reactor Materials. Addison-Wesley Pub. Co., Reading, Mass., 1967.
82. G. H. Kinchin and R. S. Pease. "The Displacement of Atoms in Solids by Radiation." Prog. Phys. 18 (1955), 1-51.
83. B. S. Billington and J. H. Crawford, Jr. Radiation Damage in Solids, Princeton University Press, Princeton, Ca., 1961.
84. J. T. E. Nihoul. "Radiation Damage and Recovery in Metals." IAEA-SM-120/A-1 (1960), 3-31.
85. J. W. Corbett. Electron Radiation Damage in Semiconductors. Academic Press, New York, 1966.
86. D. H. Holmes. "Radiation Damage in Non-Fissionable Metals." in The Interaction of Radiation with Solids. Edited by F. Strumane, J. N. Nihoul, R. Gevers and A. Amelinckx, 1964. Proc. of the International Summer School on Solid State Physics, Mol, Belgium, Aug. 12-31, 1963.

87. S. Takamura. "Recovery of Lattice Defects after Plastic Deformation and Neutron Irradiation at Low Temperature." JERI-M4707, Japan, 1972.
88. W. Schilling, P. Ehrhart and K. Sonnenberg. "Interpretation of Defect Reactions in Irradiated Metals by the One Interstitial Model." In Fundamental Aspects of Radiation Damage in Metals. 2 vols. Proc. of an International Conference, Gatlinburg, Tenn., Oct. 6-10, 1975, pages 470-492.
89. L. K. Mansur and E. E. Bloom. "Radiation Effects in Reactor Structural Alloys." J. Metals, 34 (Oct. 1982), 23-31.
90. L. K. Mansur. "Effects of Point Defect Trapping and Solute Segregation on Irradiation Induced Swelling and Creep." J. Nucl. Mater., 83 (1979), 109-127.
91. D. G. Doran, G. R. Odette, L. K. Mansur and R. L. Simons. "Damage Correlation in Theory and Practice." In Radiation Damage in Breeder Structural Materials. Edited by M. L. Bleiberg and J. W. Bennett. Proc. of American Institute of Mining, Metallurgical and Petroleum Engineers International Conference, Scottsdale, Arizona, June 19-23 1977. AIME, New York, N.Y., 1977, pages 591-611.
92. J. R. Beeler, Jr. "Computer Experiments on Radiation-Induced Defect Production and Defect Annealing." ANS Winter Meeting, San Francisco, CA, Nov. 27, 1977. Trans. Am. Nucl. Soc., 27 (1977), 314-315.
93. H. L. Heinrisch and J. O. Schiffgens. "The Application of Dynamic Computer Models to High Energy Cascades." J. Nucl. Mater., 85 & 86 (1979), 607-610.
94. J. R. Beeler, Jr. and M. F. Beeler. "Computer Experiment Studies on Mechanisms for Irradiation Induced Defect Production and Annealing Processes, Final Report." ORD-3912-101-112 (June 1979) 885.
95. E. P. Simonen and J. L. Brimhall. "Computing Helium Deposition and Helium Promotion of Void Nucleation during Accelerator Experiments." Trans. Am. Nuc. Soc., 27 (1977), 329-330.
96. D. G. Doran and R. L. Simons. "Computer Simulation and Damage Function Analysis." Trans. Am. Nuc. Soc., 27 (1977), 315-316.
97. M. I. Baskes. "Computer Simulation of Helium-Assisted Bubble Nucleation." Trans. Am. Nuc. Soc., 27 (1977), 320-321.
98. D. G. Doran and R. L. Simons. "Computer Simulation and Damage Function Analysis." HEDL-SA-1335, (1977), 18.

99. R. S. Walker and D. A. Thompson. "Computer Simulation of Iron Bombardment Collision Cascades." *Radiat. Eff.*, 37 (Nos. 1-2) (June 1978), 113-120.
100. H. W. Bertini and M. P. Guthrie. "New Item, Results from Medium Energy Intranuclear-Cascade Calculation." *Nuc. Phys., A*, 169 (1971), 670-672.
101. L. P. Kubin and J. L. Martin. "In-Situ Deformation Experiments in the H.V.E.M." In *Proc. of International Conference on Strength of Metals and Alloys, Aachen, F. R. Germany, Aug. 27-31, 1979*.
102. D. S. Gelles, L. E. Thomas and R. W. Powell. "HVEM In-Situ Deformation of Neutron Irradiated Fe-0.3%Cu." *HEDL-SA-1937*, (Jan., 1980), 14.
103. W. A. Jessen. "In-Situ HVEM Investigations under the Influence of Ion Beams." *Krist. Tech.*, 14 (No. 11) (Nov. 1979), 1393-1398.
104. M. Kiritani and K. Urban. "Submicroscopic Defects in Metals and Their Influence on HVEM In-Situ Experiments." *Krist. Tech.*, 14 (No. 11) (Nov. 1979), 1413-1417.
105. S. C. Agarwell, G. Ayrault, D. I. Potter, A. Taylor and F. V. Nolfi, Jr. "Microstructure of Single and Dual-Ion Irradiated Fe-20Ni-15Cr and Fe-6Al-4V alloys." *J. Nucl. Mater.*, 85 & 86 (1979), 653-657.
106. I. R. Bires and W. E. Ellis. "A New Source of Helium in Cladding Materials." In *Void Formed by Irradiation of Reactor Materials*, BNES European Conference, Reading, England, Mar. 24-25, 1971, pages 339-345.
107. G. L. Kulcinski. "Radiation Damage by Neutrons to Materials in DT Fusion Reactors." *IAEA-CN-33/S 3-1*, (1969), 251-273.
108. T. A. Gabriel, B. L. Bishop and F. W. Wiffen. "Calculated Irradiation Response of Materials Using Fission Spectra." *ORNL TM-6361, Conf. No. W-7405-eng-26*, 1979.
109. G. P. Scheidler, M. J. Makin, F. J. Minter and W. F. Schilling. "The Effect of Irradiation Temperature on the Formation of Clusters in Neutron Irradiated Copper." *UKAERE-R 5269*, 1966.
110. E. E. Bloom. "Nucleation and Growth of Voids in Stainless Steels during Fast Neutron Irradiation." In *Radiation-Induced Voids in Metals*. *Proc. of International Conference, Albany, N.Y., June 9-11, 1971, 1972*, pages 1-30.

111. J. L. Brimhall, H. E. Kissinger and G. L. Kulcinski. "The Effect of Temperature on Void Formation in Irradiated Pure and Impure Metals." In Radiation-Induced Voids in Metals. USAEC, Washington, D. C., 1972, pages 338-362.
112. K. Farrell. "Experimental Observations of Effects of Inert Gas on Cavity Formation during Irradiation." In Consultant Symposium on Rare Gases in Metals and Ionic Solids, ORNL-TM-7193 Harwell, England, Sept. 10-14, 1979.
113. K. O. Bagley, J. I. Bramman and C. Cawthorne. "The Neutron Induced Voids in Non-Fissile Materials and Alloys Review." In Voids Formed by Irradiation of Reactor Materials. Proc. of the British Nuclear Energy Society European Conference, Reading, England, March 24-25, 1971, 1972, pages 1-26.
114. J. L. Brimhall and E. P. Simonen. "Effect of Helium on Void Formation in Nickel." J. Nucl. Mater., 68 (1977), 235-243.
115. V. Levy, N. Azam, L. Le Naour, G. Didout and J. Delaplace. "Effect of Structure and Alloying Elements on Void Formation in Austenitic Steels and Nickel Alloys." In Effect on Structure and Alloying Elements on Void Formation in Austenitic Steels and Nickel Alloys. Edited by L. M. Bleiberg and J. W. Bennett. AIME, New York, N. Y., 1977, pages 709-725.
116. B. N. Singh and A. J. E. Foreman. "An Assessment of Void Formation by Gas Atoms during Irradiation." J. Nucl. Mater. 103 & 104 (1981), 389-394.
117. D. K. Brice. "Hydrogen Trapping in Fusion Materials due to Ion Irradiation; Implications for Neutron Irradiation." J. Nucl. Mater., 108 & 109 (1982), 389-394.
118. D. J. Mazey and R. S. Nelson. "Bubble-Void Transition Effects in Ni Alloys." J. Nucl. Mater., 85 & 86 (1979), 671-675.
119. J. A. Spitznagel, W. J. Choyke, N. J. Doyle, R. B. Irwin, J. R. Townsend and J. N. McGruer. "Critical Cavity Sizes in Dual-Ion Bombarded 304 SS, Part I; Experiment." J. Nucl. Mater., 108 & 109 (1982), 537-543.
120. J. R. Townsend. "Critical Cavity Sizes in Dual-Ion Bombarded 304 SS, Part II; Theoretical." J. Nucl. Mater., 108 & 109 (1982), 1053-1058.

121. K. C. Russell. "Effects of Irradiation on Stability of Alloy Phases." In Radiation Damage in Breeder Structural Materials. Edited by M. L. Bleiberg and J. W. Bennett. Proc. of American Institute of Mining, Metallurgical and Petroleum Engineers International Conference, Scottsdale, Arizona, June 19-23, 1977. AIME, New York, N.Y., 1977, pages 821-840.
122. M. Shimada and H. Kamei. "Ion Irradiation Mode Effects on Void Formation." J. Nucl. Mater., 103 & 104 (1981), 1481-1486.
123. K. Shiraishi, T. Aruga and Y. Katamo. "Void Swelling in Nitrogen-Ion Irradiated 316 Stainless Steel." J. Nucl. Mater. 103 & 104 (1981), 1053-1058.
124. E. A. Kenik and E. H. Lee. "Influence of Injected Helium on the Phase Instability of Iron-Irradiated Stainless Steel." In the Proc. of Symposium on Irradiation Phase Stability, AIME Fall Meeting, Pittsburgh, Penn., Oct. 1980.
125. W. J. Choyke, J. N. McGruer, J. R. Townsend, J. A. Spitznagel, N. J. Doyle and F. J. Venskytis. "Helium Effects in Ion-Bombarded 304 Stainless Steel." J. Nucl. Mater., 85 & 86 (1979), 647-651.
126. P. J. Maziasz. "Some Effects of Increased Helium Content on Void Formation and Solute Segregation in Neutron Irradiated Type 316 Stainless Steel." J. Nucl. Mater., 108 & 109 (1982), 359-384.
127. P. J. Maziasz and T. K. Roche. "Preirradiation Microstructural Development Designed for Minimize Properties Degradation during Irradiation in Austenitic Alloys." J. Nucl. Mater., 103 & 104 (1981), 797-802.
128. B. B. Glasgow, A. Si-Ahmed, W. G. Wolfer and F. A. Garner. "Helium Bubble Formation and Swelling in Metals." J. Nucl. Mater., 103 & 104 (1981), 981-986.
129. J. Rothant and H. Schroeder. "Influence of Temperature, Stress and Time on the Formation of Helium Bubbles in Type 316 Stainless Steel." J. Nucl. Mater., 103 & 104 (1981), 1023-1034.
130. L. K. Mansur, M. R. Hayns and E. H. Lee. "Mechanism Affecting Swelling in Alloys with Precipitates." In Proc. of Symposium on Irradiation Phase Stability, AIME Fall Meeting, Pittsburgh, Penn., Oct. 1980.

131. L. Arnberg, J. Megusa, D. Imeson, H. J. Frost, J. B. Vander Sande, O. K. Harling and N. J. Grant. "The Microstructure of of Neutron Irradiated Rapidly Solidified Path A Prime Candidate Alloys." *J. Nucl. Mater.*, 103 & 104 (1981), 1005-1010.
132. T. M. Williams, J. M. Titchmarsh and D. R. Arkell. "Void-Swelling and Precipitation in a Neutron-Irradiated Niobium Stabilized Austenitic Stainless Steel." *J. Nucl. Mater.*, 107 (1982), 222-244.
133. A. F. Rowcliffe, E. H. Lee and P. S. Sklad. "The Effect of Phase Instabilities on the Correlation of Nickel Ion and Neutron Irradiated Swelling in solution Annealed 316 Stainless Steels." In Proc. of International Conference on Irradiation Behavior of Metallic Materials for Fast Reactor Core Arrangement. Ajaccio, Corsica, June 1979.
134. M. Terasawa, S. Nakahigashi and H. Kamei. "Void Swelling and Microstructural Segregation in Ion-Irradiated 316 Stainless Steel." *J. Nucl. Mater.*, 108 & 109 (1982), 1017-1022.
135. G. Ayrault, H. A. Hoff, F. V. Nolfi, Jr. and A. P. L. Turner. "Influence of He Injection Rate on the Microstructure of Dual-Ion Irradiated Type 316 Stainless Steel." *J. Nucl. Mater.*, 103 & 104 (1981), 1035-1040.
136. W. G. Johnson, T. Lauritzen, J. H. Rosolowski and A. M. Turkalo. "The Effect of Metallurgical Variables on Void Swelling." In Radiation Damage in Metals. Edited by N. L. Petersen and S. D. Harkness. ASM, Metals Park, Ohio, 1976.
137. M. Snykers, F. Biermans and J. Cornelis. "The Influence of an Oxide Dispersion Strengthened Ferritic Alloy in a HVEM." *J. Nucl. Mater.*, 103 & 104 (1981), 1079-1084.
138. H. Kawanishi, M. Yamada, K. Fukuya and S. Ichino. "Effect of Titanium on Microstructural Changes in SUS 316 Stainless Steels." *J. Nucl. Mater.*, 103 & 104 (1981), 1097-1101.
139. R. W. Chickerling, R. Bajaj and J. S. Lally. "A Comparison of the Irradiation Effects of Swelling and Microstructure in Commercial Alloy A-286 and a Simpler Fe-25Ni-15Cr Gamma Prime Hardened Alloy." In Radiation Damage in Breeder Structural Materials Edited by M. L. Bleiberg and J. W. Bennett. Proc. of American Institute of Mining, Metallurgical and Petroleum Engineers International Conference, Scottsdale, Arizona, June 19-23, 1977. AIME, New York, N.Y., 1977, pages 405-414.

140. J. Megusar, L. Arnberg, J. B. Vander Sande and N. J. Grant, "Microstructure of Rapidly Solidified PATH A Prime Candidate Alloys." *J. Nucl. Mater.*, 103 & 104 (1981), 1103-1107.
141. W. Kesternich and J. Rothant. "Reduction of Helium Embrittlement in Stainless Steel by Finely Dispersed TiC Precipitates." *J. Nucl. Mater.*, 103 & 104 (1981), 845-852.
142. L. Arnberg, J. B. Vander Sande, H. J. Frost and O. K. Harling. "The Microstructure of Rapidly Solidified Path A Prime Candidate Alloys Following Irradiation with Fe and He Ions." *J. Nucl. Mater.*, 103 & 104 (1981), 1069-1073.
143. N. Kanani, L. Anberg and O. K. Harling. "Pre-Irradiation Spatial Distribution and Stability of Boride Particles in Rapidly Solidified Boron Doped Stainless Steel." *J. Nucl. Mater.*, 103 & 104 (1981), 1115-1119.
144. E. H. Lee, A. F. Rowcliffe and L. K. Mansur. "Precipitation and Cavity Formation in Austenitic Stainless Steels during Irradiation." In Fusion Reactor Materials. R. E. Nygren, R. E. Gold and R. H. Jones, eds. Proc. of the Second Topical Meeting, Seattle, Washington, August 9-12, 1981. North-Holland Pub. Co., Netherlands, 1982.
145. M. Terasawa, M. Shimada, T. Kakuma, t. Yukitoshi, K. Shiraishi, and K. Uematsu. "The Influence of Metallurgical Variables on Void Swelling in Type 316 Steel." In Radiation Damage in Breeder Structural Materials. Edited by M. L. Bleiberg and J. W. Bennett. Proc. of American Institute of Mining, Metallurgical and Petroleum Engineers International Conference, Scottsdale, Arizona, June 19-23, 1977. AIME, New York, N.Y., 1977, pages 687-707.
146. H. R. Brager and F. A. Garner. "Comparison of the Swelling and the Microstructural/Microchemical Evolution of AISI 316 Irradiated in EBR-II and HFIR." *J. Nucl. Mater.*, 103 & 104 (1981), 993-997.
147. J. F. Bates, F. A. Garner and F. M. Mann. "The Effect of Solid Transmutation Products on Swelling in 316 Stainless Steel." *J. Nucl. Mater.*, 103 & 104 (1981), 999-1004.
148. G. R. Odette. "Modelling of Microstructural Evolution under Irradiation." *J. Nucl. Mater.*, 85 & 86 (1979), 533-545.
149. E. H. Lee, N. H. Packan and L. K. Mansur. "Effects of Pulsed Dual-Ion Irradiation on Phase Transformations and Microstructure in Ti-Modified Austenitic Alloy." [to be published.]

150. N. H. Packan. "Effects of Pulsed Dual-Ion Irradiation on Microstructural Development." *J. Nucl. Mater.*, 103 & 104 (1981), 1029-1034.
151. L. K. Mansur. "Void Swelling in Metals and Alloys under Irradiation: An Assessment of the Theory." *Nuc. Tech.*, 40 (Aug. 1979), 5-34.
152. H. Wiedersich. "Theory of Defect Clustering and Void Formation." In Radiation Damage in Metals. N. L. Peterson and S. D. Harkness, eds. ASM, Metals Park, Ohio, Nov. 9-10, 1975, 157-193.
153. L. K. Mansur and M. H. Yoo. "Advance in the Theory of Swelling in Irradiated Metals and Alloys." *J. Nucl. Mater.*, 85 & 86 (1979), 523-532.
154. S. Ishino, S. Iwata, Y. Matsutami and S. Tanaka. "Computer Simulation and Neutron, Heavy-Ion and Electron." In Radiation Damage in Breeder Structural Materials. Edited by M. L. Bleiberg and J. W. Bennett. Proc. of American Institute of Mining, Metallurgical and Petroleum Engineers International Conference, Scottsdale, Arizona, June 19-23, 1977. AIME, New York, N.Y., 1977, pages 879-898.
155. W. Daenner. "A Comparison of AISI Type 316 and German Type DIN 1.4970 Stainless Steel with Regard to the First-Wall Lifetime." *J. Nucl. Mater.*, 103 & 104 (1981), 121-126.
156. B. O. Hall. "Effect of Simultaneous Helium Injection on Defect Cluster Nucleation in Irradiated Metals." *J. Nucl. Mater.*, 85 & 86 (1979), 565-569.
157. D. G. Doran. "Fundamental Radiation Effects Studies in the Fusion Materials Program." *J. Nucl. Mater.*, 108 & 109 (1982), 277-295.
158. J. J. Holmes and J. L. Straalsund. "Irradiation Sources for Fusion Materials Development." *J. Nucl. Mater.*, 85 & 86 (1979), 447-451.
159. E. W. Pottmeyer, Jr. "The Fusion Materials Irradiation Test Facility at Hanford." *J. Nucl. Mater.*, 85 & 86 (1979), 463-465.
160. K. Farrell, M. B. Lewis and N. H. Packan. "Simultaneous Bombardment with Helium, Hydrogen, and Heavy Ions to Simulate Microstructural Damage from Fission or Fusion Neutrons." *Scripta Met.*, 12 (1978), 1121-1124.

161. R. S. Nelson, D. J. Mazey and J. A. Hudson. "Voids Formed by Irradiation of Reactor Materials." In Voids Formed by Irradiation of Reactor Materials. Edited by S. f. Pugh, M. M. Loretto and D. I. R. Norris. Proc. of the British Nuclear Energy Society European Conference, Reading, England, March 24-25, 1971, pages 191-201.
162. F. A. Smidt, J. R. Reed and J. A. Sprague. "A Comparison of the Swelling Produced in Nickel by Neutron Irradiated and by Ion Bombardment." In Radiation Damage in Breeder Structural Materials Edited by M. L. Bleiberg and J. W. Bennett. Proc. of American Institute of Mining, Metallurgical and Petroleum Engineers International Conference, Scottsdale, Arizona, June 19-23, 1977. AIME, New York, N.Y., 1977, pages 337-346.
163. N. H. Packan, K. Farrell and J. O. Stiegler. "Correlation of Neutron and Heavy-Ion Damage, I. The influence of dose rate and injected helium on swelling in pure nickel." J. Nucl. Mater., 78 (1978), 143-155.
164. L. K. Mansur. "Correlation of Neutron and Heavy Ion Damage - Part II. The predicted temperature shift of swelling with changes in radiation dose rate." J. Nucl. Mater., 108 & 109 (1982)3, 156-160.
165. M. H. Yoo and L. K. Mansur. "The Influence of Mobile Helium in a Rate Theory of Void Swelling." J. Nucl. Mater., 85 & 86 (1979), 571-575.
166. E. H. Lee, L. K. Mansur and M. H. Yoo. "Spatial Variation in Void Volume during Charged Particle Bombardment - The Effects of Injected Interstitials." J. Nucl. Mater., 85 & 86 (1979), 577-581.
167. F. A. Garner, J. J. Laidler and G. L. Guthrie. "Development and Evaluation of a Stress-Free Swelling Correlating for 20% CW 316 Stainless Steel." ASTM STP, 611 (1976), 208.
168. F. A. Garner, R. W. Powell, S. Diamond, T. Lauritzen, A. F. Rowcliffe, J. A. Sprague and D. Keefer. "Simulation of High Fluence Swelling Behavior in Technological Materials." In Radiation Damage in Breeder Structural Materials. Edited by M. L. Bleiberg and J. W. Bennett. Proc. of American Institute of Mining, Metallurgical and Petroleum Engineers International Conference, Scottsdale, Arizona, June 19-23, 1977. AIME, New York, N.Y., 1977, pages 543-569.
169. I. Maning and G. P. Mueller. "Depth Distribution of Energy Deposition by Ion Bombardment." Comp. Phy. Comm., 1 (1974), 85-94.

170. K. Farrell, N. H. Packan and J. T. Houston. "Depth Profiles of Nickel Ion Damage in Helium-Implanted Nickel." *Radiat. Eff.*, 62 (1982), 39-52.
171. J. B. Whitley, G. L. Kulcinski, P. Wilkes and H. V. Smith, Jr. "The Depth Dependent Damage Profile in Nickel Irradiated with Nickel or Copper Ions." *J. Nucl. Mater.*, 79 (1979), 159-169.
172. N. H. Packan, private communication. Metals and Ceramic Division, Oak Ridge National Laboratory, September 1, 1982.
173. R. Bullough and M. R. Hayns. "The Free Surface Effect on Swelling." *J. Nucl. Mater.*, 68 (1977), 286-293.
174. E. H. Lee, L. K. Mansur and M. H. Yoo. "Spatial Variation in Void Volume during Charged Particle Bombardment - The Effects of Injected Interstitials." *J. Nucl. Mater.*, 85 & 86 (1979), 577-581.
175. N. H. Packan and K. Farrell. "Simulation of First Wall Damage: Effects of the Method of Gas Implantation." *J. Nucl. Mater.*, 103 & 104 (1981), 677-681.
176. K. Farrell and N. H. Packan. "A Helium-Induced Shift in the Temperature Dependence of Swelling, *J. Nucl. Mater.*, 103 & 104 (1981), 683-687.
177. ANSI/ASTM. 1980, Powder Diffraction File, Inorganic Phases, American Society for Testing and Materials, Philadelphia, Pa., 1980.
178. R. C. Weast and M. J. Astle. CRC Handbook of Chemistry and Physics. CRC Press, Inc., Cleveland, Ohio, 1980.
179. J. B. Nelson and D. P. Riley. "An Experimental Investigation of Extrapolation Methods in the Derivation of Accurate Unit-Cell Dimensions of Crystals." *Proc. Phys. Soc. London*, 57 (1945), 160-177.
180. S. R. Williams. Hardness and Hardness Measurements. American Society for Metals, Cleveland, Ohio, 1942.
181. D. Tabor. "The Hardness and Strength of Metals." *J. Inst. Met.* 79 (No. 1) (1951), 1-18.
182. R. A. George, S. Dinda and A. S. Kasper. "Estimating Yield Strength from Hardness Data." *Metal Progress*, 109 (1976), 30-35.

183. D. R. Tate. "A Comparison of Microhardness Indentation Tests." Trans. Am. Soc. Metals, 35 (1945), 374.
184. M. C. Saw and G. J. Desalvo, "On the Plastic Flow Beneath a Blunt Axisymmetric Indenter." J. Trans. ASME, J. Eng. Ind., 92 (1970), 481.
185. E. E. Underwood. "Creep Properties from Short Time Tests." Mater. Meth., 15 (1957), 129.
186. A. G. Atkins and D. Tabor. "The Plastic Deformation of Crossed Cylinders and Wedges." J. Inst. Met., 94 (1966), 107.
187. F. b. Bens. "Hardness Testing of Metals and Alloys at Elevated Temperatures." Trans. ASME, 38 (1947), 505.
188. J. Moteff, R. K. Bhargarva and W. L. McCullough. "Correlation of the Hot-Hardness with the Tensile Strength of 304 Stainless Steel to Temperature of 1200°C." Met. Trans. A, 6A (1975), 1101.
189. G. A. Geach. "Hardness and Temperature." Int. Met. Rev., 19 (1974), 255-267.
190. J. L. Kamphouse, D. A. Nyers and J. Moteff. "Hot Microhardness Values for Metals and Alloys (Irradiated and Unirradiated)." GEMP-716, 1969.
191. M. J. Hill and D. J. Rowcliffe. "Deformation of Silicon at Low Temperatures." J. Mater. Sci., 9 (1974), 1569.
192. E. D. Harmer. The Testing of Engineering Materials. McGraw-Hill Book co., New York, 1982, p. 195.
193. N. H. Polakowski and E. J. Ripling. Strength and Structure of Engineering Materials. Prentice Hall Inc., Englewood Cliffs, N.J., 1966.
194. Annual ASTM Standards. 10 ANSI/ASTM Std. E92-72, ASTM, Philadelphia, Penn., 1975.
195. Annual ASTM Standards. 11 ANSI/ASTM 384-73, ASTM, Philadelphia, Penn., 1976.
196. J. T. Houston and K. Farrell. "Procedure for Preparing Specimens for Ion Bombardment." ORNL CF-80/302, 1980.

197. E. H. Lee and A. F. Rowcliffe. "Multiple Sectioning and Perforation Techniques for TEM Sub-Surface Studies." *Micro. Sci.*, 7 (1979), 403.
198. M. B. Lewis. "A Method for Simulating Fusion Reactor Radiation Damage Using Triple Ion Beams." *IEEE Trans. Nuc. Sci.*, NS-26, No. 1, (Feb. 1979), 1320-1322.
199. C. H. Johnson. "A Ring Lens for Focusing Ion Beams to Uniform Densities." *Nucl. Instr. & Methods*, 127 (1975), 163.
200. P. G. T. Howell. "Taking, Presenting and Treating Stereo Data from the SEM." *Scan. Elec. Micro.*, 1 (1975), 679.
201. F. J. Minter and R. C. Piller. "A computerized graphical method of analyzing stereophotomicrographs." UK AERE-R8570, 1976.
202. W. G. Johnston, J. H. Rosolowski, A. M. Turkalo and K. D. Challenger. "Surface Observation on Nickel Ion Bombarded Stainless Steels." *Scripta Met.*, 6 (1972), 999-1006.
203. G. R. Gessel. "Effect of Minor Alloying Additions on the Strength and Swelling Behavior of an Austenitic Stainless Steel." ORNL/TM-6359, 1978.
204. R. C. Gifkins. Optical Microscopy of Metals. American Elsevier Pub. Co. Inc., New York, N.Y., 1970.
205. H. E. Knechtel, W. F. Kindle, J. L. McCall and R. D. Buchheit, "Metallography." In Tools and Techniques in Physical Metallurgy Edited by F. Weinberg. Marcel Dekker, Inc., New York, N.Y., 1970.
206. SAS Institute. SAS User's Guide 1979 Edition. SAS Institute, Cary, N.C., 1979.
207. W. G. Johnston, J. H. Rosolowski and A. M. Turkalo. "Void Swelling Produced by 5 MeV Nickel Ions." In The Physics of Irradiation Produced Voids. Edited by R. S. Nelson. Consultant Symposium Harwell, England, Sept. 9-11, 1974, 1975, pages 101-118.
208. W. G. Johnston and J. H. Rosolowski, "Ion Beams in the Study of Void Formation." *Inst. Phys. Conf. Ser. No. 28*, (1976), 228-239.

ACKNOWLEDGEMENTS

The author would like to express his sincerest gratitude to his major professor, Dr. M. S. Wechsler, for his constant direction, patient consultation and sincere interest throughout the course of this investigation and for his steadfast assistance in the long, arduous task of preparing this manuscript.

This research was carried out in the Metallurgy Division of the Ames Laboratory, USDOE, at Iowa State University and the ion bombardment was carried out in the Metals and Ceramic Division of Oak Ridge National Laboratory. The author is grateful for the opportunity to perform this investigation at the laboratories, where the expertise and facilities are available. Special appreciation is expressed to Drs. J. J. Laidler and J. L. Straalsund of Hanford Engineering Development Laboratory for providing the starting alloy stock, to Professor K. A. Gschneidner, Jr, for his endless guide to and supply of the rare-earth elements, Mr. W. E. Alexander and B. J. Beaudry and R. E. Whetstone, Jr., for the alloy preparation, Mr. L. P. Lincoln and F. A. Schmidt for heat treatment, Dr. J. E. Benson and Professor F. X. Kayser for consultation on X-ray analysis, Mr. H. H. Baker for the photomicrographs, Mr. F. C. Laabs for TEM work and Mr. G. Wells for his sincere technical expertise on the specimen preparation. And also, special thanks are extended to Dr. M. B. Lewis and Mr. S. W. Cook for the ion bombardment, Dr. K. Farrell for consultation and the suggestion to use the stacked-edge-on multispecimen

holders, Dr. N. H. Packan as the consultant on the step profile of the irradiation damage and Dr. E. H. Lee for his kind consultation on the analysis of the radiation induced defects and specimen treatment techniques.

The author would like to express special gratitude to Professors R. A. Danofsky, D. M. Roberts, and D. K. Finnemore for their academic guidance as well as consultation on this work.

The author is sincerely grateful to Rebecca Shivers and Young Sook Lee for the typed manuscript.

I sincerely appreciate the many years of moral support and encouragement provided by my family, especially my mother O-Bong, friends and professors at Iowa State University and Seoul National University.

The author is a member of the Korea Advanced Energy Research Institute and is grateful for the financial support.

The author is grateful to the Ames Laboratory, USDOE and Iowa State University for the assistantship provided for the study.

And lastly, I am very grateful to my wife, Duck Hee, for her support, encouragement, and understanding. A special thanks go to my sons, Gyu Hyun, Gyu Tae and Gyu Jin for their patience and understanding.

APPENDIX

```

10 OPEN4,4
20 DIMQ2(4),Q3(4),Q4(4),T(4)
21 PRINT"ASSEMBLY NUMBER ?"
22 INPUTCC
24 PRINT#4,"=====
25 PRINT#4," ASSEMBLY #"CC
26 PRINT#4,"=====
30 FORI=1TO2
40 PRINT"Q11,Q12,Q22 ?"
51 IFI=2GOTO56
52 PRINTI"STEP-HEIGHT SHAPE-MATRIX ?"
53 PRINT#4,"STEP-HEIGHT SHAPE-MATRIX :S-S"
55 GOTO60
56 PRINTI"SHAPE-MATRIX OF DPA ?"
57 PRINT#4,"DPA SHAPE-MATRIX ; FARADAY CUP"
60 INPUT Q2(I),Q3(I),Q4(I)
70 X=Q2(I)2+4*Q3(I)2-2*Q2(I)*Q4(I)+Q4(I)2
80 Y=(Q4(I)-Q2(I)+SQR(X))/2/Q3(I)
90 T1(I)=ATN(Y)
100 Y=(Q4(I)-Q2(I)-SQR(X))/2/Q3(I)
110 T2(I)=ATN(Y)
125 PRINT#4," Q11 ="Q2(I)" ,Q12 ="Q3(I)
130 PRINT#4," Q21 ="Q3(I)" ,Q22 ="Q4(I)
131 PRINT#4
140 T0=T1(I)*2
150 Z1=2*(Q4(I)-Q2(I))*COS(T0)-2*Q3(I)*SIN(T0)
160 T0=T2(I)*2
170 Z2=2*(Q4(I)-Q2(I))*COS(T0)-2*Q3(I)*SIN(T0)
172 T5=T1(I)*180/π
173 T6=T2(I)*180/π
175 PRINT#4,"THETA1 ="T1(I)"RAD : "T5"DEG"
176 PRINT#4,"THETA2 ="T2(I)"RAD : "T6"DEG"
180 PRINT#4,"D2(C/R2)THETA1 ="Z1
190 PRINT#4,"D2(C/R2)THETA2 ="Z2
195 PRINT#4
200 IFZ1>0THEN240
210 IFZ2<0THEN350
220 T(I)=T2(I)
230 GOTO260
240 IFZ2>0THEN350
250 T(I)=T1(I)
260 PRINT#4,"ANGLE BTWN MAJOR- & X-AXIS : "T(I)"RAD"
280 PRINT#4,"-----"
290 NEXTI

```

Fig. A1. Basic computer program (PET 2001) written to calculate the beam intensity distribution

```

300 TH=T(1)-T(2)
301 PRINT#4,"TRANSFORM-ANGLE : "TH"RAD"
310 PRINT#4,"TRANSFORM-MATRIX (IN RAD) ;"
320 PRINT#4,"  COS("TH")  SIN("TH")"
325 PRINT#4," -SIN("TH")  COS("TH")"
327 PRINT#4,"    OR"
329 G1=COS(TH)
330 G2=SIN(TH)
332 G3=-SIN(TH)
333 PRINT#4,"  "G1"  ,"G2
334 PRINT#4,"  "G3"  ,"G1
335 PRINT#4,"=====
340 GOTO455
350 PRINT#4,"THIS PROBLEM MAY NOT CORRECT"
370 GOTO600
380 PRINT#4
382 PRINT"PEAK POINT OF STEP-HEIGHT ,(B1,B2) ?"
385 INPUTB1,B2
386 PRINT#4,"PEAK PT.OF STEP-HEIGHT ("B1","B2")"
390 PRINT"PEAK VALUE OF DPA ?"
391 INPUTD0
392 PRINT#4,"PEAK VALUE OF DPA      : "D0
393 PRINT#4
394 PRINT#4,"-----"
395 PRINT#4
396 PRINT#4," #      X1      X2      DPA"
397 PRINT#4
398 PRINT#4,"-----"
400 FORI=1TO100
402 IFI=1THEN411
403 PRINTI"("X1", X2 ) FOR DPA "
405 INPUTX2
406 IFX2=0THEN600
407 IFX2=1THEN394
410 GOTO415
411 PRINTI"(" X1,X2 ) FOR DPA "
412 INPUTX1,X2
415 X0=(X1-B1)*COS(TH)-(X2-B2)*SIN(TH)
416 Y0=(X1-B1)*SIN(TH)+(X2-B2)*COS(TH)
420 DD=Q2(2)*X0↑2+2*Q3(2)*X0*Y0+Q4(2)*Y0↑2
423 DD=D0*EXP(-DD)
425 DD=INT(DD)
433 IFI>9THEN445
440 PRINT#4,I" "X1""X2" "DD

```

Fig. A1. (Continued)

```

443 GOTO450
445 PRINT#4, I""X1""X2" "DD
450 NEXTI
452 GOTO600
455 T2=TH*2
457 S2=Q2(2)*COS(TH) T2-Q3(2)*SIN(T2)+Q4(2)*SIN(TH) T2
459 S3=(Q2(2)-Q4(2))/2*SIN(T2)+Q3(2)*COS(T2)
461 S4=Q2(2)*SIN(TH) T2+Q3(2)*SIN(T2)+Q4(2)*COS(TH) T2
463 X0=SQR(S2 T2+4*S3 T2-2*S2*S4+S4 T2)
465 X1=(S4-S2+X0)/2/S3
467 X2=(S4-S2-X0)/2/S3
469 X1=ATN(X1)
471 X2=ATN(X2)
473 PRINT#4, "TRANSFORMED SHAPE-MATRIX"
475 PRINT#4, S2" , "S3
477 PRINT#4, S3" , "S4
479 PRINT#4
481 PRINT#4, "THETA1 ="X1
483 PRINT#4, "THETA2 ="X2
485 X4=X1*2
487 ZZ=2*(Q4(2)-Q2(2))*COS(X4)-2*Q3(2)*SIN(X4)
489 PRINT#4
491 PRINT#4, "ANGLE BTWN MAJOR- AND X-AXIS IS"
493 IFZZ>0THEN499
495 PRINT#4, X1"RAD"
497 GOTO380
499 PRINT#4, X2"RAD"
500 GOTO380
600 CLOSE4:END
READY.

```

Fig. A1. (Continued)